

# Magnetic states and spin-wave modes in single ferromagnetic nanotubes

THÈSE N° 6316 (2014)

PRÉSENTÉE LE 14 NOVEMBRE 2014

À LA FACULTÉ DES SCIENCES ET TECHNIQUES DE L'INGÉNIEUR  
LABORATOIRE DES MATÉRIAUX SEMICONDUCTEURS  
PROGRAMME DOCTORAL EN PHYSIQUE

ÉCOLE POLYTECHNIQUE FÉDÉRALE DE LAUSANNE

POUR L'OBTENTION DU GRADE DE DOCTEUR ÈS SCIENCES

PAR

Daniel RÜFFER

acceptée sur proposition du jury:

Prof. V. Savona, président du jury  
Prof. A. Fontcuberta i Morral, directrice de thèse  
Prof. C. H. Back, rapporteur  
Dr V. Cros, rapporteur  
Dr S. Rusponi, rapporteur



ÉCOLE POLYTECHNIQUE  
FÉDÉRALE DE LAUSANNE

Suisse  
2014



To Despoina...





# Acknowledgements

I would like to express my gratitude to everyone who supported me throughout the course of my thesis and made my time as a PhD student a great and unforgettable experience. In particular, I would like to thank:

**Prof. Anna Fontcuberta i Morral**, first of all for giving me the opportunity to join your group. I really appreciate your guidance and continuous support. I would also like to thank you for giving me the liberty to develop and pursue my own research interest and at the same time for providing invaluable advice and ideas where necessary. Thank you for everything!

**Prof. Dirk Grundler**, for your continuous support and advice during my thesis (and before). I am grateful for your generous offer to collaborate with you and your group and for the many hours of stimulating and fruitful discussion. Your optimism and contagious passion for Physics were a constant source of inspiration and motivation. Thank you also very much for the rigorous proofreading of my thesis draft.

**Prof. Christian H. Back**, **Dr. Vincent Cros** and **Dr. Stefano Rusponi** for having accepted to comprise my PhD examination committee and **Prof. Vincenzo Savona** for presiding it.

**Florian Brandl**, **Florian Heimbach**, **Rupert Huber** and **Thomas Schwarze** at E10 in Munich for the smooth and successful collaboration in general and the deposition processes in particular. I thank the entire E10 for the welcoming atmosphere and support during my visits.

**Arne Buchter**, **Prof. Dieter Kölle**, **Joachim Nagel**, **Prof. Martino Poggio** and **Dennis Weber** for a productive collaboration on cantilever magnetometry and nanoSQUID sensing.

**Prof. Jordi Arbiol**, **Prof. Rafal Dunin-Borkowski**, **András Kovács** and **Reza R. Zamani**, for performing the transmission electron microscopy studies of our nanotubes.

the prospective junior researchers **Christian Dette**, **Kevin Keim**, **Johannes Mendil**, **Marlou Slot**, **Tobias Stückler** and **Shengda Wang** whom I had the pleasure to (co-)supervise. Thank you for your well-targeted ideas, helping hands, positive attitude and great work.

**Prof. Pedro Landeros Silva** and **Jorge Otálora Arias** for the interesting discussions on ferromagnetic nanotubes.

the entire staff of CMi for doing a downright amazing job and providing a professional and friendly work environment. Without your professional advice and support, the sample fabrication would have been much more painful. In particular, I would like to thank **Zdenek Benes**, **Guy-François Clerc**, **Anthony Guillet**, **Cyrille Hibert**, **Philippe Langlet**, **Patrick Alain Madliger**, **László Pethő** and **Joffrey Pernollet**.

## Acknowledgements

---

the technical staff at ICMP and the IMX workshops for your skilled support and your helping hands. Thank you, **Claude Amendola, Philippe Cuanillon, Philippe Cordey, Gilles Grandjean, Adrien Grisendi, Olivier Haldimann, Nicolas Leiser, Damien** and **Yoan Trolliet**.

all my colleagues at LMSC, **Esther Alarcón-Lladó, Francesca Amaduzzi, Alberto Casadei, Sonia Conesa Boj, Carlo Colombo, Anna Dalmau Mallorquí, Yannik Fontana, Martin Heiss, Bernt Ketterer, Heidi Potts, Eleonora Russo-Averchi, Gözde Tütüncüoglu**, and all the visiting students and researchers. Thank you very much for a great time in the lab and outside, e.g. on the ski slope or the lake. Thank you also accepting the “intruding” magnetism guy and bearing my long explanations on such a different topic. Thank you **Yannik** for the help with the abstract and two million other French documents.

**Yvonne Cotting** and **Monika Salas-Tesar** who helped me a thousand times to solve the administrative problems within and outside EPFL. Thank you very much for all the translations and for the patience while trying to cope with my horrible French.

---

**Arndt von Bieren, Alina Deac, Andreas Mann** and **Antonio Vetrò** for the amazing time we had together after arriving in Lausanne and for being a great team and sticking together when times got less amazing.

the doctoral school of EPFL and particular members of EPFL for offering astounding support through some difficult moments. In particular, I would like to thank **Alexander Verkhovsky**, my PhD mentor, for your advice and for listening patiently to concerns at that time. I am also indebted and would like to express my sincere gratitude to **Prof. Jean-Philippe Ansermet, Prof. Jacques Giovanola, Susan Kiliyas, Prof. Thomas Rizzo, Prof. Wolf-Dieter Schneider**.

**Prof. Mathias Kläui** for hiring me and allowing my personal and professional path to pass through EPFL and the beautiful Lake Geneva Region.

**Chantal Roulin** and **Florence Grandjean** for all the help when I arrived and during my time at ICMP.

all my former colleagues at University of Konstanz, ICMP and PSI for their support and the fun.

---

**Burak Boyaci** for being a formidable flatmate and a good friend.

**my friends** for providing emotional support and keeping me grounded.

**meinen Eltern und meinem Bruder David**, für eure bedingungslose Unterstützung. Vielen Dank, dass ihr mir das alles ermöglicht habt! Ihr wart immer für mich da und eine unglaublich wichtige moralische Stütze.

**Despoina**, σε ευχαριστώ Δέσποινα που είσαι στη ζωή, που με αγαπάς και με στηρίζεις κάθε στιγμή και σε κάθε προσπάθεια. Ιδιαίτερα σου είμαι ευγνώμων για την υποστηριξή σου καθόλη την διάρκεια που ετοίμαζα την διδακτορική μου διατριβή. Πραγματικά χωρίς εσένα δεν θα μπορούσα να αντέξω στις δύσκολες στιγμές.

Lausanne, 20th August 2014

Daniel

# Abstract

In this thesis the electrical properties, magnetic states and spin wave resonances of individual magnetically hollow ferromagnetic nanotubes have been studied. They were prepared from the different materials Nickel (Ni), Permalloy (Py) and Cobalt-Iron-Boron (CoFeB), deposited as shells onto non-magnetic Gallium-Arsenide (GaAs) semiconductor nanowires via Atomic Layer Deposition (ALD), thermal evaporation and magnetron sputtering, respectively. The resulting nanotubes had lengths between 10 to 20  $\mu\text{m}$ , diameters of 150 to 400 nm and tube walls (shells) which were 20 to 40 nm thick. Structural analysis of the tubes by Transmission Electron Microscopy revealed a poly(nano)crystalline (Ni, Py) and amorphous (CoFeB) structure.

Electrical transport experiments as a function of temperature revealed different transport mechanisms for each of the materials. Electron-phonon scattering dominated the temperature dependence of the resistivity in Ni, while a clear evidence for electron magnon scattering was observed in Py. Electron-electron interaction in granular and amorphous media was identified as the major contribution to the temperature dependence in CoFeB. The Anisotropic Magnetoresistance (AMR) ratios have been determined for all tubes and different temperatures. Ni nanotubes exhibited a large relative AMR effect of 1.4% at room temperature. The AMR measurements provided information about the magnetic configurations as well as the magnetization reversal mechanism. Indications for the formation of vortex segments in Ni tubes were found for the magnetization reversal when the magnetic field was perpendicular to the nanotube axis.

In cooperation with the Poggio group in Basel, cantilever magnetometry has been used for the further characterization of the nanotube magnetization. The magnetization curves were compared to the AMR measurements and finite element method (FEM) micromagnetic simulations. The comparison between the experimental results and the simulations suggested that the roughness of Ni tubes gave rise to segmented magnetic switching. An almost perfect axial alignment of the remanent magnetization has been observed in Py and CoFeB nanotubes. The influence of the inhomogeneous internal field in transverse magnetic fields was investigated by simulation. The segment-wise alignment of spins with the field direction is argued to provoke characteristic kinks in the hysteresis curve and measured AMR effect. Magnetothermal spatial mapping experiments using the anomalous Nernst effect (ANE) complemented the magnetotransport experiments in cooperation with the group of Prof. Grundler in Munich. Here, first evidence of end-vortices entering the nanotube before reversal could be found.

Electrically detected spin wave resonance experiments have been performed in cooperation with the group of Prof. Grundler on individual nanotubes. The detected voltage, generated by

## Abstract

---

the spin rectification effect, revealed multiple resonances in the GHz frequency. The experimentally observed resonances were compared to calculated ones extracted from dynamic simulations. With this comparison, the signatures could be attributed to azimuthally confined spin-wave modes. The deduced dispersion relation suggested the quantization of exchange-dominated spin waves in that resonance frequencies follow roughly a quadratic dependence on the wave vector.

Key words: ferromagnetic nanotubes, micromagnetics, magnetoresistance, magnetothermal effects, magnonics, microwave photovoltage, Ni, Py, CoFeB

# Zusammenfassung

In dieser Arbeit wurden die elektrischen Eigenschaften, die magnetischen Zustände und die Spinwellen Eigenmoden in einzelnen ferromagnetischen Nanoröhren untersucht. Dazu wurden Nickel (Ni), Permalloy (Py) und Cobalt-Eisen-Boron (CoFeB) Filme auf Halbleiter-Nanodrähte mittels Atomlagenabscheidung (ALD), thermischen Bedampfen oder Magnetron-sputtern aufgebracht. Die Nanoröhren hatten Längen zwischen 10 und 20  $\mu\text{m}$ , Durchmesser im Bereich von 150 und 400 nm und Wandstärken von 20 bis 40 nm. Die Strukturanalyse per Transmission Elektronen Mikroskop (TEM) ergab, dass die Filme der Ni und Py Röhren polykristallin und die der CoFeB Röhren amorph waren.

Temperaturabhängige Experimente zeigten unterschiedliche Transportmechanismen für die verschiedenen Materialien. Während für Ni die Streuung von Elektronen an Phononen den Temperaturverlauf zwischen 2 K und 300 K bestimmte, lies sich das Verhalten von Py mit Elektron-Magnon Streuung erklären. Die Elektron-Elektron Wechselwirkung in granularen und amorphen Materialien wurde als dominanter Beitrag zum Widerstand in CoFeB Röhren identifiziert. Weiterhin wurde die Stärke des anisotropen magnetoresistiven Effekts (AMR) in allen Materialien und für unterschiedliche Temperaturen bestimmt. Ni Nanoröhren zeigten einen grossen relativen AMR von 1.4 % bei Raumtemperatur. Mittels AMR Messungen konnten Informationen über die magnetischen Zustände und die Mechanismen, die das Umschalten der Magnetisierung bestimmen, gesammelt werden. Im Umschaltprozess unter Querfeld wurden Hinweise auf Vortexbildung gefunden.

In Zusammenarbeit mit der Forschungsgruppe um Prof. Martino Poggio in Basel wurde eine zusätzliche Charakterisierung der Nanoröhren Magnetisierung durch Cantilever Magnetometry vorgenommen. Die Magnetisierungskurven wurden mit AMR Daten und mikromagnetischen Finite-Elemente-Methode (FEM) Simulationen verglichen. Der Vergleich deutete darauf hin, dass die Rauigkeit der Ni Röhren zu einem segmentierten Schalten führt. Die Magnetisierung in Py and CoFeB Röhren wies eine nahezu perfekte axiale Ausrichtung auf. Es wurde weiterhin der Einfluss des inhomogenen internen Feldes im Querfeld in Simulationen untersucht. Das segmentweise Ausrichten der Spins entlang des internen Feldes führte zu charakteristischen Knicks in der Hysteresekurve und dem gemessenen AMR Signal. Die Magnetotransport-Messungen wurden in Zusammenarbeit mit der Münchner Gruppe von Prof. Grundler um orts-aufgelöste magnetothermische Experimente erweitert. In diesen Versuchen wurden erste Hinweise auf das Eindringen von End-Vortices vor dem Umschalten gefunden.

Zusammen mit der Gruppe von Prof. Grundler wurden auch elektrisch detektierte Spinwellen-

## Zusammenfassung

---

Resonanz Versuche durchgeführt. Die Gleichrichtung des induzierten Mikrowellenstroms erzeugte eine Photospannung, die mehrere Eigenmoden in der Nanoröhre aufweist. Der Vergleich zu dynamischen Simulationen identifizierte diese als entlang des Umfangs stehende Spinwellen. Die abgeleitete Dispersionrelation zeigte quadratische Abhängigkeit vom Wellenvektor und bestätigte somit den Austausch-Charakter der Spinwellen.

Stichwörter: ferromagnetische Nanoröhren, Mikromagnetismus, magnetothermische Effekte, Magnetwiderstand, Magnonik, Mikrowellen-Photospannung, Ni, Py, CoFeB

# Résumé

Cette thèse présente l'étude expérimentale des propriétés électriques, des états magnétiques et des résonances des ondes de spins de nanotubes magnétiques individuels. Les nanotubes ont été préparés à partir de nickel (Ni), de permalloy (Py) et d'un alliage cobalt-fer-bore (CoFeB) déposés de manière à former une enveloppe autour de nanofils d'arsenure de gallium (GaAs) amagnétiques. Les dépositions ont été effectuées respectivement par dépôt de couches minces atomiques (atomic layer deposition, ALD), par évaporation thermique et par pulvérisation cathodique magnétron. Les nanotubes ainsi obtenus ont une longueur comprise entre 10 et 20  $\mu\text{m}$ , pour des diamètres entre 100 et 400 nm. Les parois des nanotubes varient entre 20 et 40 nm d'épaisseur (épaisseur de l'enveloppe). L'analyse structurale par microscope électronique en transmission a révélé des enveloppes ayant des microstructures polycristalline à l'échelle nanométrique (Ni, Py) et amorphe (CoFeB).

Les expériences de conductivité en fonction de la température ont permis de mettre à jour des mécanismes de transport différents pour chaque matériau : Si pour les enveloppes Ni la diffusion résultant des interactions entre électrons et phonons domine la dépendance en température, des preuves claires de diffusions par interaction électron-magnon ont été observées dans le cas d'enveloppes de Py. Les interactions électron-électron présentes dans matériaux granulaires et amorphes ont été identifiées comme contribution majoritaire à la résistivité dans le cas du CoFeB sur la plage de températures observée, entre 2 K et 300 K. Les ratios de magnétorésistance anisotrope (AMR) ont été déterminés pour tous les types de tubes et à différentes températures. Les nanotubes de Ni ont présenté un effet AMR important, 1.4%, à température ambiante. L'utilisation de l'AMR a permis d'obtenir d'informations sur la configuration magnétique et l'inversion de cette dernière. Les phénomènes d'inversion dans le cas de champs magnétiques transverses à l'axe principale des nanotubes indiquent la formation de segments comprenant des vortex magnétiques.

En collaboration avec le groupe du prof. Poggio à l'université de Bâle, des mesures de magnétométrie par cantilever ont été réalisées afin de mieux caractériser les phénomènes de magnétisation dans les nanotubes. Les courbes de magnétisation comparées à des simulations micromagnétiques utilisant la méthode des éléments finis (FEM) ont suggéré que la rugosité des tubes de Ni engendre une inversion magnétique segmentée. Un alignement axial uniforme et quasiment parfait a été observé pour les enveloppes de Py et CoFeB. L'influence d'un champ magnétique interne inhomogène dans un champ transverse a été étudiée par simulations. L'alignement des spins dans la direction du champ magnétique, segment par segment, est considéré comme étant la cause d'irrégularités caractéristiques dans la courbe d'hystérèse

## Résumé

---

et dans les mesures de l'effet d'AMR. De manière complémentaire aux expériences de transport électrique, des mesures réalisées en collaboration avec le groupe du Prof. Grundler à Munich ont permis d'établir une cartographie spatiale magnétothermique basée sur l'effet Nernst anormal (ANE). Ces mesures se sont montrées consistantes avec l'existence de vortex terminaux avant l'inversion.

Des expériences portant sur la détection électrique de résonances des ondes de spins ont aussi été réalisées en collaboration avec le groupe du Prof. Grundler sur des nanotubes individuels. Le voltage, généré par un effet de redressement des spins, laisse apercevoir de nombreuses résonances à des fréquences de l'ordre du Ghz. La comparaison avec des simulations dynamiques permet d'attribuer ces signatures à des modes azimutaux confinés d'ondes de spins. La relation de dispersion déduite de ces mesures, dans le sens où elle suit approximativement une dépendance quadratique par rapport au vecteur d'onde, suggère le caractère quantifié des ondes de spins dominées par des effets d'échange.

Mots clefs : nanotubes ferromagnétiques, micromagnétisme, magnéto-résistance, effets magnétothermiques, magnonique, micro-ondes photovoltage, Ni, Py, CoFeB



# List of Publications

Parts of this thesis have been published in peer-reviewed journals. I was the principal responsible for the majority of the experimental work as well as data analysis and writing of the manuscript. The publications are reproduced in Chap. 6 with permission of the corresponding publisher. A draft version of a third manuscript is reproduced in Chap. 8. Throughout this thesis the published papers are referred to by Pub. A-I to A-III.

## **A-I. Magnetic states of an individual Ni nanotube probed by anisotropic magnetoresistance**

D. Ruffer, R. Huber, P. Berberich, S. Albert, E. Russo-Averchi, M. Heiss, J. Arbiol, A. Fontcuberta i Morral and D. Grundler

*Nanoscale*, 2012, 4, 4989-4995

doi: 10.1039/C2NR31086D

*I designed the experiment, conducted largely the sample preparation (cf. Sec. 5), coordinated the data acquisition and analyzed the data. I wrote the draft version of the manuscript.*

## **A-II. Anisotropic magnetoresistance of individual CoFeB and Ni nanotubes with values of up to 1.4% at room temperature**

D. Ruffer, M. Slot, R. Huber, T. Schwarze, F. Heimbach, G. Tütüncüoğlu, F. Matteini, E. Russo-Averchi, A. Kovács, R. Dunin-Borkowski, R. R. Zamani, J. R. Morante, J. Arbiol, A. Fontcuberta i Morral, and D. Grundler

*APL Mat.* 2, 076112 (2014)

doi: 10.1063/1.4891276

*I designed the experiment, conducted largely the sample preparation (cf. Sec. 5), coordinated the data acquisition and analyzed the data. The magnetotransport measurements were performed by the Master student Marlou Slot, supervised by myself. I wrote the draft version of the manuscript.*

## **A-III. Quantized exchange spin waves in ferromagnetic nanotubes**

D. Ruffer, J. Mendil, S. Wang, T. Stückler, R. Huber, T. Schwarze, F. Heimbach, G. Tütüncüoğlu, F. Matteini, E. Russo-Averchi, R. R. Zamani, J. R. Morante, J. Arbiol, A. Fontcuberta i Morral, and D. Grundler

Draft

*I designed the experiment and the relevant parts of the measurement when visiting the group Prof Dirk Grundler in Munich. I coordinated and conducted largely the sample*

## List of Publications

---

*preparation and pushed the data analysis and interpretation. The simulations were conducted and analyzed by myself.*

The following papers were co-authored by me and are relevant for the topic of the thesis. I did participate actively in the discussion and interpretation of the data, e.g. by supplying micromagnetic simulations. As I did not participate in the actual experiments and was not the principal author of the manuscript, the publications are reproduced in the App. D with permission of the corresponding publishers. The papers are referred to as Pub. B-I and B-II in the thesis. The findings which are relevant for the discussion of the nanotubes are summarized in Sec. 6.4 and Sec. 6.5.

### **B-I. Cantilever Magnetometry of Individual Ni Nanotubes**

D. P. Weber, D. Ruffer, A. Buchter, F. Xue, E. Russo-Averchi, R. Huber, P. Berberich, J. Arbiol, A. Fontcuberta i Morral, D. Grundler, and M. Poggio  
*Nano Letters*, 2012, 12 (12), 6139–6144

*I participated actively in the discussion and interpretation. The experiment and the modeling were done by Arne Buchter, Prof. Martino Poggio and Dennis Weber, who wrote the majority of the manuscript.*

### **B-II. Reversal Mechanism of an Individual Ni Nanotube Simultaneously Studied by Torque and SQUID Magnetometry**

A. Buchter, J. Nagel, D. Ruffer, F. Xue, D. P. Weber, O. F. Kieler, T. Weimann, J. Kohlmann, A. B. Zorin, E. Russo-Averchi, R. Huber, P. Berberich, A. Fontcuberta i Morral, M. Kemmler, R. Kleiner, D. Koelle, D. Grundler, and M. Poggio  
*Phys. Rev. Lett.*, 2013, 111, 067202

*I participated actively in the discussion and interpretation. The experiment and the analysis of the measurements were done by Arne Buchter, Prof. Dieter Kölle, Joachim Nagel, Prof. Martino Poggio and Dennis Weber, who wrote the majority of the manuscript. I conducted and analyzed the micromagnetic simulations.*

# List of Figures

2.1	Sketches of theoretically predicted modes in a solid magnetic cylinder . . . . .	9
2.2	Sketches of reversal via transverse and vortex domain wall . . . . .	10
2.3	Depiction of the axial, the vortex and the mixed state . . . . .	11
3.1	Geometry for the calculation of $N_M$ in prism and hollow cylinder . . . . .	18
3.2	Spin wave dispersion relations for a planar thin film . . . . .	23
3.3	Phasediagram of axial and vortex state . . . . .	24
3.4	Phasediagram of axial, vortex and mixed state . . . . .	25
3.5	Phasediagram for transition from transverse to vortex wall . . . . .	27
3.6	Switching field as function of angle and of tube wall thickness . . . . .	28
3.7	Spin wave dispersion relations in thin nanotubes . . . . .	30
4.1	Depiction of field in cryostat . . . . .	33
4.2	Depiction of field in vector magnets . . . . .	34
4.3	Cantilver magnetometry experiment . . . . .	36
4.4	Angle dependence of spin-rectification . . . . .	38
4.5	Quasi-periodic boundary conditions in Nmag . . . . .	41
4.6	Pulse shape and field geometry in dynamic simulations . . . . .	42
5.1	Schematic of the $Al_2O_3$ ALD process . . . . .	47
5.2	Pattern layout for automatized nanotube localization and lithography . . . . .	49
5.3	SEM images of nanotube bundling and pairing . . . . .	50
5.4	Graphical User Interface of the software tool . . . . .	51
5.5	Lithography patterns for contacting or rf injection . . . . .	53
5.6	SEM images of tube contacts . . . . .	54
6.1	SEM and TEM images and EELS analysis of Ni nanotubes . . . . .	61
6.2	Magnetotransport data of Ni tube in large fields, normal and parallel . . . . .	62
6.3	Magnetotransport data for field perpendicular to axis in small range . . . . .	64
6.4	AMR in thin films and resistance of relevant states . . . . .	65
6.5	Reversal process attributed to resistance data . . . . .	67
6.6	TEM analysis of Ni and CoFeB tubes . . . . .	71
6.7	SEM images of contacted Ni and CoFeB tubes . . . . .	72
6.8	Resistance as function of field in Ni and CoFeB tubes . . . . .	73

## List of Figures

---

6.9	Resistance and AMR as function of temperature . . . . .	75
6.10	Resistance as function of temperature in Py tubes . . . . .	78
6.11	Magnetotransport data of Py tube in parallel and normal field . . . . .	79
6.12	Magnetotransport data of Py tube for small parallel fields . . . . .	79
7.1	Schematic of local AMR and ANE mapping . . . . .	84
7.2	Segment-wise AMR data in CoFeB tube in axial field . . . . .	84
7.3	Segment-wise AMR data for CoFeB tube in perpendicular field . . . . .	85
7.4	Sketch and data of ANE experiment . . . . .	86
7.5	Spatial magnetothermal mapping . . . . .	87
7.6	Theoretical and experimental switching field . . . . .	87
7.7	Cross-sectional schematic of a cylindrical and hexagonal nanotube . . . . .	90
7.8	Simulated demagnetization field in cylindrical and hexagonal tube . . . . .	91
7.9	Averaged magnetization and second derivative . . . . .	92
7.10	Points of curvature change in hysteresis as function of $\beta$ . . . . .	93
7.11	Magnetotransport data of a CoFeB tube at 180 K . . . . .	94
7.12	Schematic for the prism approximation of nanotubes in transverse field . . . . .	95
8.1	TEM and SEM images of Py tube, 3D depiction of a mode . . . . .	98
8.2	Spin rectification signal as function of the angle between field and axis . . . . .	99
8.3	Rectified voltage as function of the field strength at parrallel alignment . . . . .	100
8.4	Simulated mode spectrum and spatial maps . . . . .	101
8.5	Dispersionrelation as extracted from simulation . . . . .	102
A.1	Data used for the AMR calculation of CFBM1 . . . . .	131
A.2	Field sweep raw data at room temperature for samples given in Tab. A.1. . . . .	132
A.3	Resistance of the Py sample as function of the angle between axis and field . . . . .	133
A.4	Resistance as function of the field strength at parallel alignment . . . . .	133
A.5	<b>a</b> $V(f, H)$ for a 12.0 $\mu\text{m}$ Nickel tube with film thickness of 40 nm and $D = 310 - 390$ nm, as well as for <b>b</b> a 16.5 $\mu\text{m}$ CoFeB tube with a 30 nm film and total diameter of between 210 and 250 nm. . . . .	134
B.1	Magnetotransport data for sample NiS1 at RT . . . . .	135
B.2	Magnetotransport data for sample NiL1 in normal field . . . . .	135
B.3	Magnetotransport data for sample CFBS2 at RT . . . . .	136
B.4	Add. magnetotransport data for sample CFBS2 in normal field . . . . .	136
C.1	Detailed mask layout for automated nanotube detection . . . . .	138

# List of Tables

4.1	Simulation parameters . . . . .	43
6.1	Calculated exchange length $\lambda_{\text{ex}}$ . . . . .	81
7.1	Position-dependent chirality of the azimuthal orientation . . . . .	89
A.1	Geometrical dimensions and measured values for Samples of Pub.A-II . . . . .	132



# Contents

<b>Acknowledgements</b>	<b>v</b>
<b>Abstract (English/Français/Deutsch)</b>	<b>vii</b>
<b>List of Publications</b>	<b>xiii</b>
<b>List of Figures</b>	<b>xv</b>
<b>List of Tables</b>	<b>xvii</b>
<b>Table of Contents</b>	<b>xix</b>
<b>I Introductory chapters</b>	<b>1</b>
<b>1 Introduction</b>	<b>3</b>
1.1 Scope of the thesis . . . . .	4
1.2 Overview of the thesis . . . . .	4
1.3 Contributions . . . . .	5
<b>2 Literature review</b>	<b>7</b>
2.1 Reported techniques for ferromagnetic tube fabrication . . . . .	7
2.2 Magnetic states and reversal . . . . .	8
2.3 Domain wall motion in nanotubes . . . . .	11
2.4 Spin waves in nanotubes . . . . .	11
<b>3 Theoretical background</b>	<b>13</b>
3.1 Ferromagnetism . . . . .	13
3.2 Micromagnetics . . . . .	14
3.3 Magnetization dynamics . . . . .	20
3.4 Effects of tubular geometry . . . . .	23
<b>4 Methods</b>	<b>33</b>
4.1 Experimental techniques . . . . .	33
4.2 Micromagnetic simulations . . . . .	40
	<b>xix</b>

## Contents

---

<b>5</b>	<b>Sample fabrication</b>	<b>45</b>
5.1	Ferromagnetic tube fabrication based on nanowire templates . . . . .	45
5.2	Fabrication of samples for electrical measurements . . . . .	48
<b>II</b>	<b>Results &amp; Discussion</b>	<b>55</b>
<b>6</b>	<b>Characterization of ferromagnetic nanotubes</b>	<b>57</b>
6.1	Pub. A-I: Magnetic states of an individual Ni nanotube probed by AMR . . . . .	57
6.2	Pub. A-II: Anisotropic magnetoresistance of individual CoFeB and Ni [...] . . . . .	69
6.3	Resistivity and AMR of Permalloy nanotubes . . . . .	78
6.4	Saturation magnetization . . . . .	80
6.5	Magnetization reversal in Ni nanotubes under axial field . . . . .	81
<b>7</b>	<b>Magnetization reversal in CoFeB tubes</b>	<b>83</b>
7.1	Magnetization reversal [...] probed via AMR and ANE . . . . .	83
7.2	Influence of the inhomogeneous demagnetization field [...] . . . . .	90
<b>8</b>	<b>Pub. A-III: Quantized exchange spin waves in ferromagnetic nanotubes</b>	<b>97</b>
<b>9</b>	<b>Summary</b>	<b>105</b>
9.1	Ferromagnetic nanotubes . . . . .	105
9.2	Magnetic states and reversal . . . . .	106
9.3	Spin wave resonances . . . . .	108
	<b>Bibliography</b>	<b>109</b>
	<b>Appendix</b>	<b>129</b>
<b>A</b>	<b>Supplementary Information</b>	<b>131</b>
A.1	Pub. A-II: Supplementary Information . . . . .	131
A.2	Pub. A-III: Supplementary Information . . . . .	133
<b>B</b>	<b>Additional data</b>	<b>135</b>
B.1	Ni tubes . . . . .	135
B.2	CoFeB tube . . . . .	136
<b>C</b>	<b>Parameters &amp; Values</b>	<b>137</b>
C.1	Lithography mask fabrication by e-beam lithography . . . . .	137
C.2	Process flows for the sample fabrication . . . . .	137
<b>D</b>	<b>Co-authored papers</b>	<b>143</b>
	<b>Curriculum Vitae</b>	<b>157</b>



# Introductory chapters **Part I**



# 1 Introduction

During the last decades the digital revolution has transformed the daily life. Our ways of living, working and communicating have been recast drastically by the emergence of mass storage and high-speed logic. The enormous advances in the amount of available digital memory and computing power have been achieved on the shoulders of two fundamental principles: first, the scaling ability of semiconductor device fabrication, sometimes called die shrink. The significance of scaling lies in the fact that the shrinkage goes along with an increase in performance and lower power consumption, while the same time reducing the manufacturing cost per unit [M<sup>+</sup>65]. A second key-element of the success has been magnetic memory devices for high-density random-access data storage. From the humble magnetic-core memory, in which wires are fed through macroscopic magnetic toroids, to modern day hard disc drives (HDDs) with giant or tunneling magnetoresistive read-heads, information has been stored in ever more tiny magnetic domains. Both technologies are matured and reach the end of further improvement: transistor gates reach dimensions in which tunneling processes and thermal limitations severely hamper performance. In HDDs the small size of the magnetic domains provokes the superparamagnetic limit, for which the domains become susceptible to inadvertent switching because of thermal effects [GAB74]. To overcome this intrinsic limit, new paths have been envisaged. One potential path to further increase the density is to leave the planar technology and venture into the third dimension. One particular example is the racetrack memory [PHT08], in which magnetic domain walls are moved along vertically standing ferromagnetic wires. Here, a key parameter of device performance is the speed of the domain walls when subject to external fields or spin polarized currents. It has been predicted that the speed is particularly high in *ferromagnetic nanotubes* [LNn10, YAK<sup>+</sup>11]. Interestingly, such ferromagnetic nanotubes can be fabricated in arrays using a bottom-up approach [NCRK05], facilitating three-dimensional device fabrication. The peculiar tubular structure of such ferromagnetic nanotubes makes them also promising candidates in very different applications. For example, large potential is found in medical applications, such as drug delivery or immunobinding [SRH<sup>+</sup>05]. Due to their magnetization they can be guided by external magnetic fields. Their hollow structure allows for capturing or releasing species. Because of their high surface to volume ratio, nanotubes are effective geometries for surface

functionalization. Numerous theoretical works on magnetic states in nanotubes can be found in literature. Despite their interesting geometry and their potential as building block in future applications, experimental investigations on individual nanotubes were however scarce in recent years.

### 1.1 Scope of the thesis

The goal of this thesis is to gain an understanding of the microscopic details of the magnetic states, the magnetization reversal and spin dynamics in individual nanotubes prepared from ferromagnetic metals.

In the past, most publications focused on the reversal of magnetization in nanotubes under a magnetic field along their axis. By investigating the mechanism of reversal upon the application of a magnetic field perpendicular to the nanotube axis, we aim at elucidating the role of the inhomogeneous internal field in the magnetization reversal. We also want to explore if a stable vortex state with minimum stray field is possible. Answering this question is important for the potential of these nanostructures as memory elements.

Theoretical work has established the notion of a mixed state, in which the magnetic moments align along the axis for most of the nanotube length and curl at its ends to minimize the stray field [WLL<sup>+</sup>05, CUBG07, LSS<sup>+</sup>07, LSCV09, CGG10]. Calculations suggest that the reversal is greatly influenced by the mixed state. We want to elaborate experimentally this state.

To the best of our knowledge there are no studies on the spin wave dynamics in single ferromagnetic nanotubes. Previous studies addressed ensembles of short nanotubes [WLL<sup>+</sup>05] or rolled-up membranes with micron-radii [MPT<sup>+</sup>08, BMK<sup>+</sup>10, BJH<sup>+</sup>12, BBJ<sup>+</sup>13, BNM13]. With the study of spin dynamics in ferromagnetic nanotubes we want to answer the questions of how spin waves interact and what resonant modes exist in the tubular geometry. The thesis aims at experiments addressing the magnetic properties of individual magnetic tubes from DC to GHz frequencies.

We use nanotubes from three different materials, i.e. poly(nano)crystalline Nickel (Ni), Ni<sub>80</sub>Fe<sub>20</sub> (Py) and amorphous Cobalt-Iron-Boron (CoFeB). Avoiding magnetocrystalline anisotropy, we intend to study the role of the tubular shape on the magnetic properties of the nanostructures.

### 1.2 Overview of the thesis

Please note that the measurements, the fabrication and structural analysis were embedded in a large collaboration with colleagues from Barcelona, Basel, Jülich and Munich. The contributions are listed in Sec. 1.3 and in the list of publications in the preface. Parts of the thesis have been published in peer-reviewed journals and are reproduced with permission of the

publisher.

An extensive review of the existing literature on ferromagnetic nanotubes is given in Chap. 2. The following Chapter 3 gives an introduction to the theory on ferromagnetism, micromagnetics and spin dynamics. It will also summarize the effects of the tubular geometry on the magnetic behavior. The experimental methods and the sample fabrication are described in Chap. 4 and Chap. 5, respectively. The characterization of Ni, CoFeB and Py nanotubes and is presented in Chap. 6. Here, we also discuss the reversal process in individual Ni nanotubes. Chapter 7 is devoted to the study of reversal in CoFeB nanotubes. The dynamic measurements and simulations are discussed in Chap. 8. Finally, the thesis is concluded with a summary in Chap. 9.

## 1.3 Contributions

The experiments were embedded in a larger collaboration with colleagues from Barcelona, Basel, Jülich and Munich. Individual contributions other than mine were:

### Measurements:

- Transmission electron microscopy images and their analysis were conducted by Jordi Arbiol<sup>1,2</sup>, Rafal Dunin-Borkowski<sup>3</sup>, András Kovács<sup>3</sup>, Joan R. Morante<sup>4</sup> and Reza R. Zamani<sup>1,4</sup>.
- Marlou Slot and I performed the high field magnetotransport experiments from ~2 K to room temperature (cf. Sec. 6.2).
- Cantilever magnetometry experiments and their analysis via analytical modelling were done by Arne Buchter<sup>5</sup>, Martino Poggio<sup>5</sup> and Dennis Weber<sup>5</sup>. I performed the micro-magnetic simulations. The setup was extended by Arne Buchter<sup>5</sup>, Prof. Dieter Kölle<sup>6</sup> and Joachim Nagel<sup>6</sup> to include a nanoSQUID flux sensor.
- The setup for dynamic measurements was built and run in the group of Dirk Grundler<sup>7</sup>. I modified the setup for electrically detected spin wave spectroscopy and wrote the control software. The experimental setup was further improved by Florian Brandl<sup>7</sup> and Johannes Mendil<sup>7</sup>. Florian Heimbach<sup>7</sup>, Johannes Mendil<sup>7</sup>, Tobias Stückler<sup>7</sup> and Shengda Wang<sup>7</sup> and I conducted the dynamic measurements.

---

<sup>1</sup>Institut de Ciència de Materials de Barcelona (ICMAB-CSIC), Campus de la UAB, 08193 Bellaterra, CAT, Spain

<sup>2</sup>Institució Catalana de Recerca i Estudis Avançats (ICREA), 08019 Barcelona, CAT, Spain

<sup>3</sup>Ernst Ruska-Centre for Microscopy and Spectroscopy with Electrons and Peter Grünberg Institute, Forschungszentrum Jülich, D-52425 Jülich, Germany

<sup>4</sup>Catalonia Institute for Energy Research (IREC), Barcelona 08930, Spain

<sup>5</sup>Department of Physics, University of Basel, 4056 Basel, Switzerland

<sup>6</sup>Physikalisches Institut and Center for Collective Quantum Phenomena in LISA<sup>+</sup>, Universität Tübingen, 72076 Tübingen, Germany

<sup>7</sup>Lehrstuhl für Physik funktionaler Schichtsysteme, Physik Department E10, Technische Universität München, 85747 Garching, Germany

## Chapter 1. Introduction

---

- Florian Brandl<sup>7</sup> and Johannes Mendil<sup>7</sup> designed the setup for magnetothermal mapping and conducted the measurements on nanotubes with specifically designed microwave antennas and electrical contacts fabricated by me. Ioannis Stasinopoulos<sup>7</sup> optimized the design parameters of the co-planar waveguides.

### Sample fabrication:

- The semiconductor nanowires were grown by Martin Heiss<sup>8</sup>, Federico Matteini<sup>8</sup>, Eleonora Russo-Averchi<sup>8</sup>, Gözde Tütüçüoğlu<sup>8</sup> and me. Particularly, Federico Matteini<sup>8</sup> and Eleonora Russo-Averchi<sup>8</sup> optimized the growth parameters for the given requirements. The software control system of the MBE system and the related tools for automation and monitoring were developed by Martin Heiss<sup>8</sup> and me.
- The Atomic Layer Deposition (ALD) process in Munich was developed by Rupert Huber<sup>7</sup>. The initial processes were performed by Rupert Huber<sup>7</sup> and me, subsequent deposition was executed by Rupert Huber<sup>7</sup> and Thomas Schwarze<sup>7</sup>.
- The setups for thermal evaporation of Py and magnetron sputtering of CoFeB were devised by Thomas Rapp<sup>7</sup>. The modifications for deposition under an angle and with rotation was planned by Florian Heimbach<sup>7</sup> and Thomas Rapp<sup>7</sup>. The depositions were conducted by Florian Heimbach<sup>7</sup>.

---

<sup>8</sup>Laboratoire des Matériaux Semiconducteurs, Institut des Matériaux, Ecole Polytechnique Fédérale de Lausanne, 1015 Lausanne, Switzerland

## 2 Literature review

Although Frei *et al.* and Aharoni and Shtrikman theoretically treated the magnetization reversal of infinite, solid cylinders already in 1957 [FST57] and 1958 [AS58], respectively, it took nearly four decades until these theories were extended to hollow tubes [CLY94, LC96]. Since then, a multitude and increasing amount of theoretical and experimental work has been conducted in the field of magnetic nanotubes. In the following, an overview of the state-of-the-art and published research results is given. The literature review is divided into three topical sections: Sec. 2.1 treats the progress in the fabrication of ferromagnetic nanotubes. Publications on static magnetization behavior and reversal in tubes are discussed in Sec. 2.2 considering both, theoretical and experimental works. Section 2.3 focuses on studies about domain wall motion. Finally, Sec. 2.4 summarizes the publications about spin waves in tubular geometries. Details of the most important theories will be discussed in Sec. 3.4 of Chap. 3.

### 2.1 Reported techniques for ferromagnetic tube fabrication

During the late 1990s and early 2000s research focused on the development of processes to fabricate ferromagnetic tubes. Mertig *et al.* [MKP98] performed electroless Co and Ni plating of biomolecular microtubules. The tobacco mosaic virus as a template for iron oxide mineralization was chosen by Shenton *et al.* [SDY<sup>+</sup>99]. The electrochemical fabrication of nanotubes was reported by Tourillon *et al.* in 2000 [TPLL00]. They deposited Fe and Co into track-etched polycarbonate membranes. In contrast, Bao *et al.* [BTX<sup>+</sup>01] used porous alumina membranes, in which the Ni was deposited with pulsed and dc electrodeposition. In such porous alumina membranes, metal salt was successfully decomposed in hydrogen to form FePt and Fe<sub>3</sub>O<sub>4</sub> nanotubes (Sui *et al.* [SSSS04]) or Co/Polymer multilayers formed by thermal decomposition (Nielsch *et al.* [NCM<sup>+</sup>05]). The use of Atomic Layer Deposition (ALD) to fabricate Ni, Co and Fe<sub>3</sub>O<sub>4</sub> tubes into anodic alumina membranes was pioneered in 2007 [DKGN07, BJK<sup>+</sup>07, NBD<sup>+</sup>07, EBJ<sup>+</sup>08, BEP<sup>+</sup>09, AZA<sup>+</sup>11]. Amongst various other publications related to the fabrication via electrodeposition, e.g. [TGJ<sup>+</sup>06, CSA<sup>+</sup>13], further techniques can be found in literature: Kirkendall diffusion [WGW<sup>+</sup>10], liquid phase deposition [YC11], nanoparticle assembly [CST<sup>+</sup>07], a hydrothermal, coordination-assisted

dissolution process [JSY<sup>+</sup>05, LXWS08] or particle coating of carbon nanotubes [SYL<sup>+</sup>05].

With the epitaxial growth of Fe<sub>3</sub>O<sub>4</sub> core-shell nanowires, Zhang and co-workers pioneered the usage of bottom-up grown nanowire templates [ZLH<sup>+</sup>04, LZH<sup>+</sup>05]. For the shell deposition, pulsed laser deposition was chosen. In contrast, Rudolph *et al.* [RSK<sup>+</sup>09] employed Molecular Beam Epitaxy (MBE) to fabricate both, the GaAs nanowire core and the GaMnAs shell.

Efforts to fabricate magnetic nanotubes with well established lithography methods have also been undertaken. Khizroev and co-workers have fabricated short nanotubes with rectangular cross-section by Focused-Ion-Beam (FIB) etching on top of a pillar [KKLT02]. A different technique for low aspect-ratio tubes was developed by Huang *et al.* only recently [HKS<sup>+</sup>12]. They succeeded to create nanotube stubs by coating lithographically fabricated resist pillars with Py and subsequent ion-beam milling. AC dielectrophoretic assembly of a poly(3,4-ethylenedioxythiophene) PEDOT nanowire on prefabricated electrodes and subsequent electrodeposition was employed to overcome the difficult post-growth contacting problem in the publication by Hangarter *et al.* [HRSM11]. In this approach, the ferromagnetic coating of the contacts influenced the nanotube behavior and thus made the analysis of the tube properties problematic. Nevertheless, a refined process could be interesting for future top-down fabrication.

Within the last decade a method to fabricate rolled-up tubular structures was developed: when removing a sacrificial layer in a strained thin-film stack, the upper layers are released and roll up into a tube-like structure [SE01]. By strain engineering one can choose the diameter and by lithography define the length of such tubes. Mendach *et al.* [MPT<sup>+</sup>08] fabricated Rolled-Up Permalloy Tubes (RUPTs) from planar thin films. Using thin-film techniques gives rise to good material quality and allow for integration with other circuitry. The diameters are usually larger than 1  $\mu\text{m}$  [UMC<sup>+</sup>09, BJH<sup>+</sup>12, BBJ<sup>+</sup>13, BNM13, SHK<sup>+</sup>14].

## 2.2 Magnetic states and reversal

Frei *et al.* [FST57] suggested three modes of magnetization reversal for infinite, solid cylinders: below a critical radius reversal of the axially aligned magnetization occurs by *coherent rotation* [Fig. 2.1 (a)]. For intermediate radii, the so called *buckling* is the energetically preferred route to reversal [Fig. 2.1 (b)]. For wider cylinders, the magnetization reverses through the so called *curling* state [Fig. 2.1 (c)]. In the latter case, the magnetization forms a global vortex state. In a solid cylinder, this state involves a line singularity in the center. Note that the vortex state is singularity-free in a tubular geometry, lowering its energy and making it more favorable. The transition from curling to coherent reversal as a function of angle between axis and field was proposed and discussed by Han *et al.* [HZLW03] and followed by other works [HSS<sup>+</sup>09, HRSJY<sup>+</sup>09, SLS<sup>+</sup>09, ZZW<sup>+</sup>13]. All these works assume a solid infinite cylinder to calculate the coercive field  $H_c$ . They assume a single-domain behavior for the coherent rotation as well as for the curling mode.



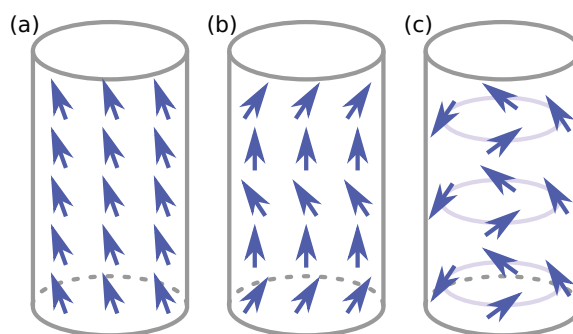


Figure 2.1 – Sketches of theoretically predicted mode in a solid ferromagnetic cylinder (a) coherent reversal, (b) reversal buckling and (c) curling, which involves a global vortex state.

In a pioneering work Landeros *et al.* [LAE<sup>+</sup>07] introduced the notion of a domain-wall mitigated reversal. In this model, a domain wall is nucleated at the end and propagates through the tube. Depending on the geometry it can be a vortex or transverse domain wall [Fig. 2.2]. The model will be reviewed in Sec. 3.4.2. Escrig and co-workers extended this work to calculate nucleation fields  $H_n$  of the different modes. They consider hollow nanotubes, the influence of finite length and the reversal via domain walls. They predicted a change in reversal depending on both, the orientation of the applied field [EDL<sup>+</sup>07, AEA<sup>+</sup>08] and the thickness  $t$  of the film [EBJ<sup>+</sup>08, BEP<sup>+</sup>09]. For both dependencies experimental evidence was reported in SQUID studies [EBJ<sup>+</sup>08, BEP<sup>+</sup>09, AZA<sup>+</sup>11]. An introduction to the model is given in Sec. 3.4.3. Considering nanotube arrays, they included the effect of mutual stray field. This led to a reduction of the coercive field due to dipolar coupling with adjacent tubes [EBJ<sup>+</sup>08, BEP<sup>+</sup>09].

In a similar approach, the phase diagram for the static equilibrium in finite-length nanotubes has been calculated by Escrig *et al.* [ELA<sup>+</sup>07]. The authors compared the energies of the axial configuration [Fig. 2.3 (a)] and the stray-field free vortex state [Fig. 2.3 (b)]. Because the curvature comprises an exchange energy penalty for the vortex configuration, it is more likely to be found in tubes with large diameters. In addition, a mixed state has been postulated [WLL<sup>+</sup>05, CUBG07, LSS<sup>+</sup>07, LSCV09]. In this state, depicted in Fig. 2.3 (c), the magnetization curls at the end of a tube to minimize the stray field and aligns axially in the center to minimize the exchange energy involved with curvature. The state was reported by Wang *et al.* [WLL<sup>+</sup>05], who performed numerical simulations in 2005. Such mixed states were found numerically by Chen *et al.* [CUBG07] and Lee *et al.* [LSS<sup>+</sup>07] two years later. A corresponding phase diagram was developed analytically by Landeros *et al.* [LSCV09] only shortly thereafter. In Sec. 3.4.1 we discuss this model in further detail. It has been evaluated numerically that the relative chirality, i.e. the rotational senses, of the end-vortices depends on the ratio  $t/r_0$  of thickness  $t$  to outer radius  $r_0$ . The reason is a stronger stray field interaction for tubes with larger  $t$ . Tubes with  $t/r_0 < 0.2$  exhibit end-vortices with the same chirality and thicker tubes show opposite rotational senses [CGG10, CGG11].

Most of the experimental work, e.g. Ref. [HZLW03, CDM<sup>+</sup>05, WWL<sup>+</sup>06, TGJ<sup>+</sup>06, DKG07, ZCWL07, LTBL08, SSM<sup>+</sup>08, EBJ<sup>+</sup>08, HRSJY<sup>+</sup>09, HSS<sup>+</sup>09, SLS<sup>+</sup>09, BEP<sup>+</sup>09, HTH<sup>+</sup>09, ZWZ<sup>+</sup>11,

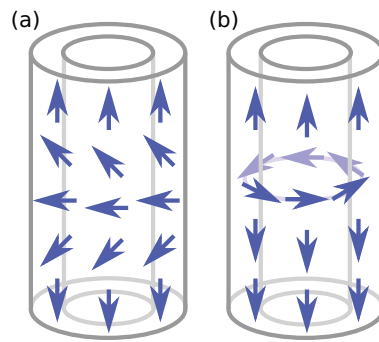


Figure 2.2 – Sketches of magnetization reversal in a magnetic nanotube, mediated by a (a) transverse or (b) vortex domain wall

[ZZW<sup>+</sup>13, SSS<sup>+</sup>13], have been limited to studies on arrays of magnetic tubes using either superconducting quantum interference devices (SQUIDs) or vibrating sample magnetometers (VSMs). So far the magnetic properties of individual magnetic nanotubes have been explored by a small number of publications. Magnetotransport experiments on individual tubes were pioneered by Zhang *et al.* [ZLH<sup>+</sup>04] in 2004, when they presented magnetoresistance studies in MgO/Fe<sub>3</sub>O<sub>4</sub> core-shell nanowires. Since then, few works have been reported. Notably, Li *et al.* [LTBL08] extended their SQUID investigation on arrays of Co tubes by Magnetic Force Microscopy (MFM) images of a single tube. They interpret the almost vanishing MFM signal and the very small remanent magnetization as an indication for a global vortex state. Comparison of the involved energy densities support their finding. During the course of the thesis, further groups published work on individual tubes. They treated either epitaxially grown materials [ZLH<sup>+</sup>04, BRR<sup>+</sup>13], observing magnetocrystalline anisotropy, or microtubes with comparably large diameters [SLE<sup>+</sup>12, LWP<sup>+</sup>12].

Magnetic imaging of ferromagnetic nanotubes is challenging due to their dimensions and curvature. Nevertheless, recent advances in X-ray Magnetic Circular Dichroism PhotoEmission Electron Microscopy (XMCD PEEM) are a promising basis for future investigations. In such experiments, the magnetic pattern is extracted from the x-ray shadow with high resolution and material selectivity. Results of a first study on Ni-Fe<sub>3</sub>O<sub>4</sub> core-shell structures [KKM<sup>+</sup>11] with diameters of about 100 nm supported a model of two distinct switching events of core and shell, presented by Chong *et al.* [CGM<sup>+</sup>10]: while the shell curls, the core switches via a domain wall. Very recent the same method was employed to image transverse and bloch-point walls in solid nanowires with diameters below and above 70-90 nm, respectively [DCJR<sup>+</sup>14]. Finally, the uniform axial, the global vortex state and two vortices with opposing chirality were measured with the same technique in rolled-up microtubes with diameters above 1 μm and multiple windings [SHK<sup>+</sup>14]. The results indicate that tightly wound tubes, similar to the ones studied dynamically (cf. Sec. 2.4), can be considered as a hollow tube with continuous tube walls. Another promising method for future high resolution, 3D imaging is the Lorentz transmission electron microscopy (LTEM) [YDH<sup>+</sup>13b].

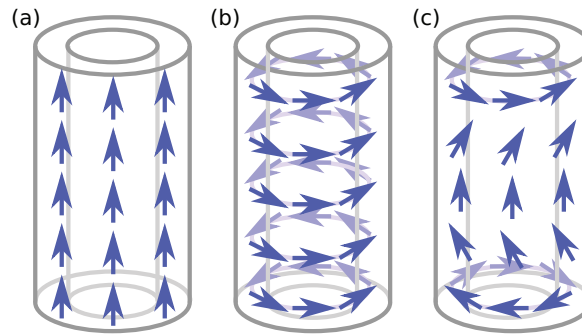


Figure 2.3 – Depiction of the (a) axial, the (b) vortex and (c) mixed state

## 2.3 Domain wall motion in nanotubes

After Landeros *et al.* [LAE<sup>+</sup>07] proposed that vortex walls mediate the reversal of uni-axially magnetized and not too thin nanotubes (cf. Sec. 3.4.2), multiple theoretical studies on their motion were published. The predicted velocities of more than 1 km/s are interesting for future applications as memory or logic devices [LNn10, YAK<sup>+</sup>11, OLLVL12, OLLNnL12, YAK<sup>+</sup>12, YKAH13]. It is still under discussion whether a phenomena similar to the Walker breakdown [SW74], exists in magnetic nanotubes. While analytic models by Landeros and co-workers predict a decrease in velocity after a certain threshold [LNn10, OLLVL12, OLLNnL12], simulations by Yan *et al.* [YAK<sup>+</sup>11, YAK<sup>+</sup>12, YKAH13] claim the suppression of the breakdown, at least in certain geometric dimensions. If this is the case, the domain wall velocities could reach the phase velocity regime, which in turn would lead to Cherenkov-like spin wave emission [YAK<sup>+</sup>11, YKAH13]. Furthermore it was observed that the left-right symmetry of the domain wall dynamics is broken [OLLVL12, YAK<sup>+</sup>12]. This chiral symmetry breaking results in different mobility for vortex walls with different rotational sense. This peculiar observation might be relevant for technological applications. At the time of this thesis and to the authors knowledge, no successful experiments on domain wall motion have been published in literature.

## 2.4 Spin waves in nanotubes

Arias and Mills developed a theory for axially propagating dipole-exchange spin waves in solid cylinders [AM01]. The dispersion relation of axially propagating spin waves in a hollow magnetic tube was presented for the special case of  $t \rightarrow 0$  by Leblond and Veerakumar [LV04]. In their model, an increase in the exchange energy for all fields and wave vectors is introduced by the cylindrical coordinate system. Further aspects of the model are given in Sec. 3.4.4.

The first experimental results were published in 2005 by Wang *et al.* [WLL<sup>+</sup>05], who performed BLS experiments on arrays of 150 nm long nanorings. The rings, which have an outer diameter of 80 nm, are spaced 105 nm apart. They extended the Arias-Mills theory to include an effective radial component and also found an additional term in the dispersion relation which accounts

for the effect of curvature on the exchange energy. Furthermore, they perform OOMMF simulations to obtain the equilibrium state and the fundamental spin wave mode. Motivated by this work, Nguyen and Cottam reported results for a nanotube composed of hexagonally ordered spins [NC06]. Their model is microscopic and based on a spin Hamiltonian. By solving the system numerically, they found dispersion relations for axial field comprising minima at finite wave vectors and evidence of mode-repulsion and -mixing. Das and Cottam reported numerical solutions of magnetostatic modes [DC07] for particular dimensions of a Py nanotube. They consider propagation along the axis and a quantized azimuthal wave vector component  $k_\phi$ . Later the same authors extended their numerical calculations to include dipole-exchange spin waves and radial confinement [DC11]. In the investigated EuS and Ni tubes, they find mode-mixing of the radially quantized bulk modes and the modified magnetostatic surface modes. The spin wave spectra of infinitely long, cylindrical nanotubes with or without vortex wall were calculated by Gonzalez *et al.* [GLNn10] by minimization of the corresponding energy functional and linearization of the Landau-Lifshitz-Gilbert equation [cf. Eq. 3.32]. Because they assume radially homogeneous magnetization, the calculation are applicable to thin wall tubes with small  $t$ . They find that spin waves dispersion is modified by a domain wall. Also, spin waves propagating along the tube axis are scattered by the domain wall.

Mendach *et al.* [MPT<sup>+</sup>08] conducted an experimental study on spin waves in single micrometric Rolled-Up Permalloy Tubes (RUPTs) in 2008. Due to the large diameters, curvature only influences the dipolar exchange in these tubes. It is thus possible, to describe the observations using modified thin-film models. In such a model the curvature can be included by a dynamic demagnetization field. Later works by Balhorn *et al.* observed azimuthal and axial confinement [BMK<sup>+</sup>10, BJH<sup>+</sup>12, BBJ<sup>+</sup>13, BNM13]. Further details of the applied model are given in Sec. 3.4.4.

Hai-Peng *et al.* [HPMGLLJ11] reported recently the dynamic response of Ni-P nanotube/-paraffin composites. Because of the random dispersion of the tubes in the paraffin, little information about an individual nanotube could be extracted.

## 3 Theoretical background

In this chapter the essential theoretical background for the presented research is introduced. In Sec. 3.1 the term ferromagnetism is defined, followed by a brief overview over relevant micromagnetic aspects. Section 3.3 summarizes dynamic effects in magnetic materials. Finally, the concepts are applied to the tubular geometry in order to outline the most important aspects of ferromagnetic nanotubes.

### 3.1 Ferromagnetism

Magnetism in materials is a macroscopic manifestation of quantum mechanical angular momenta. The magnetic moment  $\mu$  is proportional to the angular momenta of atoms and electrons. The proportionality factor is called the gyromagnetic ratio  $\gamma$  and takes the value  $1.761 \times 10^{11} \frac{\text{rad}}{\text{sT}}$  for an electron in vacuum [nis]. As a magnetic body contains a large number of magnetic moments, it comes handy to define the magnetization  $\mathbf{M}$  as the volume density of the total magnetic moments. On most realistic length scales, one can neglect the quantized character of the individual magnetic moments. In this, so called 'continuum approach',  $\mathbf{M}$  is a smooth and continuous vector field over the entire magnetic body. In free space, the magnetic flux density  $\mathbf{B}$  scales linearly with the magnetic field  $\mathbf{H}$ . In presence of a magnetic body,  $\mathbf{M}$  and  $\mathbf{H}$  add vectorially:

$$\mathbf{B} = \mu_0 (\mathbf{H} + \mathbf{M}) \quad (3.1)$$

Here  $\mu_0 = 4\pi \times 10^{-7} \text{ H/m}$  is the vacuum permeability.

Magnetic materials can be classified by their response to external fields. For this one usually considers the tensor components of the magnetic volume susceptibility

$$\chi_{ij} = \frac{\partial M_i}{\partial H_j}. \quad (3.2)$$

Often  $\chi_{ij}$  is considered to be a scalar  $\chi = \chi_{ij}$ . In certain materials and for sufficiently small

$H$ , we observe a linear relation and thus  $\chi = \text{const.} \forall H$ . If  $\chi > 0$  and small we speak of paramagnetism. Here the magnetic moments line up with the applied field and give rise to an increased flux density  $\mathbf{B}$ . If  $\mathbf{H}$  induces a magnetic moment in a material such that it opposes the applied field, which is equivalent to  $-1 < \chi < 0$ , the material is called diamagnetic. In a number of materials, the magnetic moments order spontaneously below a certain critical temperature  $T_c$ . One possibility is the anti-parallel ordering of two sublattices of magnetic moments. If the magnetic moments are of similar strength we speak of antiferromagnetism and of ferrimagnetism in case of disparate moments.

Ferromagnetism is characterized by parallel ordering of the magnetic moments. This leads to a remanent magnetization even at vanishing field and usually to a strong amplification of the magnetic flux. A ferromagnet is often described by  $\chi \gg 1$ . Please note that this is only applicable in soft ferromagnets with negligible remanence. In case of remanent behavior, the relation between  $\mathbf{M}$  and  $\mathbf{H}$  is neither linear nor single-valued.  $\mathbf{M}$  depends on the history of the sample, it has a hysteretic behavior. The maximal magnitude  $\mathbf{M}$  is defined as the saturation magnetization  $M_s$ . At room temperature Fe, Co and Ni are the only three chemical elements that are ferromagnetic. There is however a plethora of alloys which show ferromagnetism. Throughout the thesis, the elemental ferromagnet Ni and the two alloys Permalloy (Py, Ni<sub>80</sub>Fe<sub>20</sub>) and Cobalt-Iron-Boron (CoFeB, typically Co<sub>20</sub>Fe<sub>60</sub>B<sub>20</sub>) are used.

### 3.2 Micromagnetics

To describe the magnetic behavior of objects on the micrometric scale, one usually employs the micromagnetic model, pioneered by Brown [Bro40, Bro63]. Instead of considering the microscopic origin of magnetism, this model considers the influence of different physical effects by including multiple phenomenological energy contribution. It is further assumed that the material is spontaneously saturated in each point to the same magnitude  $|\mathbf{M}| = M_s$  but that the direction of the magnetization vector varies.

In the following the thermodynamic treatment of magnetostatics (cf. Sec. 3.2.1), the relevant energies (cf. Sec. 3.2.2) and the equations of motion (cf. Sec. 3.3) are presented.

#### 3.2.1 Magnetostatics

To find the thermal equilibrium of the system the correct thermodynamic potential has to be utilized. Considering that the externally applied magnetic field  $\mathbf{H}_{\text{ext}}$  is a free variable, the Gibbs free energy

$$G(\mathbf{H}_{\text{ext}}, T) = U - TS - \int \mu_0 \mathbf{H}_{\text{ext}} \cdot \mathbf{M} dV \quad (3.3)$$

is the correct thermodynamic potential to describe a system with Volume  $V$ . Here  $S$  denotes the entropy,  $T$  the temperature and  $U$  the inner energy of the system. Per definition of  $G$  and

a well-defined thermal equilibrium,  $\mathbf{M}$  has to be uniquely defined by the free variables  $\mathbf{H}_{\text{ext}}$  and  $T$ :  $\mathbf{M} = \mathbf{M}(\mathbf{H}_{\text{ext}}, T)$ . On the other hand it is well known, that a magnetic body can have multiple meta-stables states, i.e. local minima in the free energy. A typical manifestation of this is the familiar hysteresis curve. In the framework of non-equilibrium thermodynamics, the metastable states of a body with Volume  $V$  can be taken into account for by a generalized version of the total Gibbs free energy where the inner energy is a function of  $\mathbf{M}$ :

$$G_{\text{tot}}(\mathbf{H}_{\text{ext}}, T, \mathbf{M}) = U(\mathbf{M}) - \int \mu_0 \mathbf{H}_{\text{ext}} \cdot \mathbf{M} dV - TS \quad (3.4)$$

$$= E_{\text{tot}}(\mathbf{H}_{\text{ext}}, \mathbf{M}) - TS \quad (3.5)$$

At fixed  $T$  the metastable equilibrium can be determined by minimizing the total energy  $E_{\text{tot}}$ , composed of multiple energy terms described in the following chapter.

The energy contributions can also be understood as an effective magnetic field  $\mathbf{H}_{\text{eff}}$ , acting on the magnetization. It is defined as the derivative of the energy density with respect to orientation of  $\mathbf{M}$ . It can be written as

$$\mathbf{H}_{\text{eff}} = -\frac{1}{\mu_0} \frac{d}{d\mathbf{M}} \frac{dE_{\text{tot}}}{dV}. \quad (3.6)$$

In this picture, a metastable state is reached, when the torque exerted by  $\mathbf{H}_{\text{eff}}$  on  $\mathbf{M}$  vanishes. In other words, the magnetization aims to align with the effective field. One can express Brown's equations as [Bro78]

$$\mathbf{M} \times \mathbf{H}_{\text{eff}} = 0 \quad (3.7)$$

$$\left. \frac{\partial \mathbf{M}}{\partial \mathbf{n}} \right|_{\Omega} = 0 \quad (3.8)$$

The second equation defines the boundary condition at the surface boundary  $\Omega$  with normal vector  $\mathbf{n}$ .

### 3.2.2 Energies in a micromagnetic systems

The free energy of a magnetic system consists of multiple extrinsic and intrinsic contributions. In addition to the Zeeman energy,  $E_z$ , one usually considers the exchange energy  $E_{\text{ex}}$ , the dipolar energy  $E_d$  and the crystalline anisotropy  $E_{\text{ani}}$ . These terms add up to

$$E_{\text{tot}} = E_z + E_{\text{ex}} + E_d + E_{\text{ani}} \quad (3.9)$$

and are explained in the following.

### 3.2.2.1 Zeeman Energy

The second term in Eq. 3.4 is the Zeeman energy:

$$E_z = -\mu_0 \int \mathbf{H}_{\text{ext}} \cdot \mathbf{M} dV \quad (3.10)$$

It states that the energy of a magnetic moment in an external field is minimal when aligned parallel.

### 3.2.2.2 Exchange energy

The quantum mechanical exchange is the fundamental force behind ferromagnetism. The Pauli exclusion principle states that two identical fermions cannot occupy the same quantum state. Two atoms minimize the energy by a parallel alignment of their spins  $\mathbf{S}_i$  and  $\mathbf{S}_j$  due to the Coulomb interaction. The exchange energy of localized individual magnetic moments can be written as

$$E_{\text{ex}} = -J_{ij} \sum_{i,j} \mathbf{S}_i \cdot \mathbf{S}_j = -2J_{ij} \sum_{i<j} \mathbf{S}_i \cdot \mathbf{S}_j, \quad (3.11)$$

where  $J_{ij}$  is the exchange integral. For a ferromagnet  $J_{ij} > 0$ . The exchange energy is responsible for spontaneous and long-range ordering of magnetic moments. Please note that the exchange interaction strength decreases rapidly with increasing distance. For this reason it is often sufficient to consider only neighboring spins.

In the continuum approximation,  $E_{\text{ex}}$  can be reformulated as [HK51]

$$E_{\text{ex}} = \frac{A}{M_s^2} \int (\nabla \mathbf{M})^2 dV. \quad (3.12)$$

In this formulation, the exchange stiffness or coupling constant  $A$ , which is related to  $J_{ij}$  is assumed position independent. The exchange energy is sensitive to the gradient of  $\mathbf{M}$  and is large for non-uniform magnetization<sup>1</sup>.

### 3.2.2.3 Dipolar Energy

The dipolar coupling, with which two magnetic moments couple to each other, is basically the force of the stray field of a spin on another one. Considering Gauss' law of magnetism a

---

<sup>1</sup>Please note that  $(\nabla \mathbf{M})^2 = \sum_{i=x,y,z} (\nabla M_i)^2$  is the squared gradient of the magnetization and not the divergence.



divergence in  $\mathbf{M}$  leads to the generation of a stray field  $\mathbf{H}_d$ :

$$\nabla \cdot \mathbf{B} = 0 \quad (3.13)$$

$$\mu_0 \nabla \cdot (\mathbf{H}_d + \mathbf{M}) = 0 \quad (3.14)$$

$$\Rightarrow \nabla \cdot \mathbf{M} = -\nabla \cdot \mathbf{H}_d \quad (3.15)$$

It can be seen that  $\mathbf{H}_d$  opposes the magnetization in a body with homogeneous magnetization. For this it is dubbed the demagnetization field. In absence of free currents and assuming the electric displacement field to be constant over time, Ampère's circuital law reads

$$\nabla \times \mathbf{H}_d = 0 \quad (3.16)$$

It follows thus that we can introduce the magnetic scalar potential  $\phi$  that solves the Poisson's equation

$$\Delta \phi = \rho_m \quad (3.17)$$

by

$$\mathbf{H}_d = -\nabla \phi \quad (3.18)$$

with the magnetic charge density  $\rho_m = -\nabla \cdot \mathbf{M}$ . It is important to understand that  $|\mathbf{M}| = M_s$  inside the magnetic body and  $|\mathbf{M}| = 0$  everywhere else. The finite extent of the ferromagnetic region implies that  $|\mathbf{H}_d| \rightarrow 0$  for  $|\mathbf{x}| \rightarrow \infty$ . This demands the scalar potential  $\phi$  to be constant far away from the magnetic body. Usually one chooses

$$\lim_{|\mathbf{x}| \rightarrow \infty} \phi = 0 \quad (3.19)$$

which defines an open boundary condition. One can calculate the dipolar energy of the stray field  $\mathbf{H}_d$  which is generated by  $\rho_m$  via

$$E_d = \frac{\mu_0}{2} \int \mathbf{H}_d^2 dV \quad (3.20)$$

The integration over the entire space can be replaced by one over the magnetic body:

$$E_d = -\frac{\mu_0}{2} \int_V \mathbf{H}_d \cdot \mathbf{M} dV \quad (3.21)$$

The general expression for  $\phi$  can be derived as [Aha96]

$$\phi(\mathbf{x}) = \frac{1}{4\pi} \int_V \frac{\rho_m(\mathbf{x}')}{|\mathbf{x} - \mathbf{x}'|} dV + \frac{1}{4\pi} \int_\Omega \frac{\sigma_m(\mathbf{x}')}{|\mathbf{x} - \mathbf{x}'|} d\Omega. \quad (3.22)$$

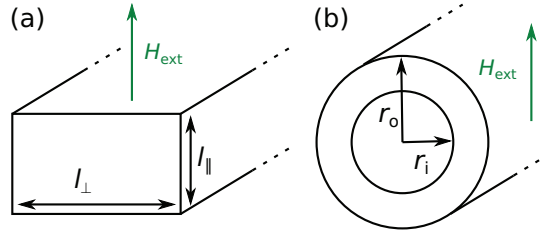


Figure 3.1 – Illustration of the geometry and the parameters for the calculation of the demagnetization factor of (a) a rectangular prism and (b) a hollow cylinder in transverse field.

In addition to the left term, which gives the contribution of the magnetic charge density in the volume, one obtains a term due to the discontinuity of  $\mathbf{M}$  at the surface  $\Omega$ . The discontinuity effectively gives rise to an effective magnetic surface charge  $\sigma_m = \mathbf{n} \cdot \mathbf{M}$ .

The calculation of  $\mathbf{H}_d$  can be very complex and is not analytically possible in the general case. A relatively simple relation can be given for uniformly magnetized ellipsoids using the demagnetization tensor  $\hat{N}$ :

$$\mathbf{H}_d = -\hat{N}\mathbf{M} \quad (3.23)$$

The tensor is diagonal in the coordinate system of the ellipsoid's principal axes and can be written as

$$\hat{N} = \begin{pmatrix} N_x & 0 & 0 \\ 0 & N_y & 0 \\ 0 & 0 & N_z \end{pmatrix} \quad (3.24)$$

For the degenerate shapes of an ellipsoid, such as e.g. spheres, long rods or films, the tensor can be analytically solved. For a thin-film with its normal vector along  $\mathbf{e}_z$  the demagnetization factors read  $N_x = N_y = 0$  and  $N_z = 1$ , in a sphere they are  $N_x = N_y = N_z = 1/3$  and in a solid, infinitely long cylinder with  $\mathbf{e}_z$  along the axis they are  $N_x = N_y = 1/2$  and  $N_z = 0$ . Because of the inhomogeneity of  $\mathbf{H}_d$  for non-ellipsoidal bodies, we cannot define a general demagnetization tensor. Effective demagnetization tensors, employing some kind of averaging, are defined and used in literature. Common definitions are the magnetometric demagnetization tensor

$$\hat{N}_M = -\frac{1}{V} \int_V \hat{N}_P dV \quad (3.25)$$

and the ballistic demagnetization tensor

$$\hat{N}_B = -\frac{1}{M^2} \int_{\Omega} \mathbf{H}_d \cdot \mathbf{M} d\Omega \quad (3.26)$$

with the point-function demagnetization tensor  $\hat{N}_P$  defined as  $\mathbf{H}_d(\mathbf{x}) = -\hat{N}_P(\mathbf{x})\mathbf{M}$ . In both cases uniform magnetization is assumed [MDT66].

As a technologically relevant example, one can solve analytically the magnetometric demagnetization factor for a rectangular prism. For the special case of a stripe, infinitely elongated along  $y$ , Aharoni has calculated it to be [Aha98]

$$N_{M,r} = \frac{1}{\pi} \left[ \frac{1-p_r^2}{2p_r} \ln(1+p_r^2) + p_r \cdot \ln(p_r) + 2 \arctan(p_r^{-1}) \right] \quad (3.27)$$

for a field along the  $z$ -axis and  $p_r = l_{\parallel}/l_{\perp}$  the ratio of the rectangle's respective sides [Fig. 3.1 (a)]. Recently, Prat-Camps *et al.* [PCNCS12] determined the analytic solution as function of  $\chi$  for a cylindrical tube in transverse fields. For the ballistic and the magnetometric demagnetization tensor [cf. Eq. 3.26] they obtained

$$N_{B,PC} = \frac{1-\beta}{2} \quad (3.28)$$

and

$$N_{M,PC} = \frac{1}{2} \left( 1 - \beta^2 \frac{\chi}{\chi+2} \right), \quad (3.29)$$

respectively. Here  $\beta = r_i/r_o$  is the ratio of inner and outer radii [Fig. 3.1 (b)].

### 3.2.2.4 Crystalline anisotropies

In crystalline materials  $\mathbf{M}$  preferentially aligns along certain crystallographic directions. Microscopically, the magnetocrystalline anisotropy arises from spin-orbit coupling which links the electron orbits to the lattice structure. It can be expressed by an energy term  $E_{\text{ani}}$ , whose structure depends on the underlying lattice symmetry. This thesis focuses on amorphous and polycrystalline materials.  $E_{\text{ani}}$  is thus neglected when analyzing the data and not further discussed in the following.

### 3.2.3 Equations of motion

To describe the dynamic behavior of  $\mathbf{M}$  in the continuum approach one makes use of the *Landau-Lifshitz equation* of [LL35]:

$$\frac{d\mathbf{M}}{dt} = -\gamma\mu_0\mathbf{M} \times \mathbf{H}_{\text{eff}} + \lambda_{\text{LL}}\mathbf{M} \times (\mathbf{M} \times \mathbf{H}_{\text{eff}}). \quad (3.30)$$

Here,  $\lambda_{\text{LL}}$  is the phenomenological Landau-Lifshitz damping parameter. A physically more sound formulation was given by Gilbert in 1955 by adding a 'viscous' force in a Lagrangian formulation [Gil04]. The resulting *Gilbert equation* has a damping term which depends on the time derivative of the magnetization:

$$\frac{d\mathbf{M}}{dt} = -\gamma\mu_0\mathbf{M} \times \mathbf{H}_{\text{eff}} + \frac{\alpha}{M_s}\mathbf{M} \times \frac{d\mathbf{M}}{dt} \quad (3.31)$$

## Chapter 3. Theoretical background

---

The Gilbert damping parameter  $\alpha$  is again a phenomenological constant to be determined by experiments. Although more realistic, the Gilbert equation is numerically more challenging. The time derivative appears in the damping term, while it appears only on the left-hand side in the Landau-Lifshitz equation. Because both formulas are mathematically equivalent, one can reformulate the Gilbert equation to resemble the form of the Landau-Lifshitz equation:

$$\frac{d\mathbf{M}}{dt} = -\frac{\gamma\mu_0}{1+\alpha^2}\mathbf{M} \times \mathbf{H}_{\text{eff}} + \frac{\alpha\gamma\mu_0}{M_s(1+\alpha^2)}\mathbf{M} \times (\mathbf{M} \times \mathbf{H}_{\text{eff}}) \quad (3.32)$$

In this form it usually referred to as *Landau-Lifshitz-Gilbert* (LLG) equation. The LLG equation can equally be used to relax the system to its equilibrium state and to follow the evolution of  $\mathbf{M}$  in time. From a numerical point of view it is by far easier to implement. For this reason it usually employed to describe magnetization dynamics.

### 3.3 Magnetization dynamics

The LLG describes a damped precessional motion of the magnetization after pulsed excitation. Although a general analytic solution of Eq. 3.32 is not conceivable, special cases can be described analytically. The ones relevant for this thesis will be presented in the following. First the ferromagnetic resonance (FMR) is explained, followed by the extension of the theory towards spin-exchange waves. Finally, a brief introduction to spin wave confinement in thin films is given.

#### 3.3.1 Ferromagnetic resonance

A solution of the equations of motion was found by Kittel in 1948 [Kit48] for an ellipsoid which is homogeneously magnetized in direction of the static external field  $\langle \mathbf{H}_{\text{ext}} \rangle = \mathbf{H}_0 = H_0 \mathbf{e}_z$ . The exciting external radio frequency (rf) field  $\mathbf{h}_{\text{rf}} = h_{\text{rf}} \mathbf{e}_x$  is chosen to be perpendicular to the static field. Additionally, damping is neglected and a *macrospin model* employed, in which the magnetization is assumed to be uniform over the entire sample and for all times:

$$\mathbf{M}(\mathbf{x}, t) = \mathbf{M}. \quad (3.33)$$

This means, according to Eq. 3.12, that the exchange energy contribution vanishes. Furthermore  $E_{\text{ani}} = 0$  in isotropic materials and thus the only other contribution to the effective field is  $\mathbf{H}_{\text{d}} = -\hat{N}\mathbf{M}$ . With  $M_x(t), M_y(t) \ll M_z \approx M_s$  and  $|h_{\text{rf}}| \ll |H_0|$  the equation of motion, Eq. 3.32, simplifies to

$$\frac{dM_x}{dt} = \gamma\mu_0 [H_0 + (N_y - N_z) M_s] M_y \quad (3.34)$$

$$\frac{dM_y}{dt} = \gamma\mu_0 [h_{\text{rf}} M_s - H_0 M_x - (N_x - N_z) M_x M_s] \quad (3.35)$$

and  $\frac{dM_z}{dt} \approx 0$ . Using  $M_x, M_y \sim \exp(i\omega t)$  and solving the set of equations, one yields a resonance condition in the magnetic susceptibility tensor component  $\chi_{xx}$  with a resonance frequency described by the *Kittel formula*:

$$\omega_0 = \gamma\mu_0 \sqrt{[H_0 + (N_y - N_z) M_s][H_0 + (N_x - N_z) M_s]}. \quad (3.36)$$

This solution, called the *ferromagnetic resonance* (FMR), describes the uniform precession of the entire magnetization. It corresponds to a wave with infinite wavelength  $\lambda$  or, similarly, a wave vector  $\mathbf{k} = 0$ . In the special case of a sphere (cf. Sec. 3.2.2.3) Eq. 3.36 becomes independent of  $M_s$  and simplifies to  $\omega_0 = \gamma H_0$ .

### 3.3.2 Dipole-exchange spin waves

For waves with  $\mathbf{k} \neq 0$ , the assumption of the previous section that the exchange can be neglected does not hold true. Per definition, a phase shift between neighboring spins exists, giving rise to  $(\nabla \mathbf{M})^2 \neq 0$  and  $E_{\text{ex}} \neq 0$  [cf. Eq. 3.12]. Obviously,  $\mathbf{M}$  comprises a static component  $\mathbf{M}_0$  with  $|\mathbf{M}_0| = M_s$  and a dynamic component  $\mathbf{m}(\mathbf{x}, t)$  that is a function of the position. For small precession angles,  $\mathbf{m}(\mathbf{x}, t)$  can be expanded in a series of plane waves with amplitude  $\mathbf{m}_k$ :

$$\mathbf{M}(\mathbf{x}, t) = \mathbf{M}_0 + \mathbf{m}(\mathbf{x}, t) = \mathbf{M}_0 + \sum_k \mathbf{m}_k(t) \exp(i\mathbf{k} \cdot \mathbf{r}). \quad (3.37)$$

Inserting into Eqs. 3.12 and 3.6, the exchange field can be calculated to be

$$\mathbf{H}_{\text{ex}} = \frac{2A}{\mu_0 M_s^2} \nabla^2 \mathbf{M} = \frac{2A}{\mu_0 M_s^2} k^2 \mathbf{m}(\mathbf{x}, t). \quad (3.38)$$

Inserting into the equation of motion, Eq. 3.32, assuming  $\mathbf{M}_0 = M_0 \mathbf{e}_z$  and linearizing the set of equations one obtains the *Herring-Kittel formula* [HK51]

$$\omega_0 = \gamma\mu_0 \sqrt{\left(H_{\text{int}} + \frac{2A}{\mu_0 M_s} k^2\right) \left(H_{\text{int}} + \frac{2A}{\mu_0 M_s} k^2 + M_s \sin^2 \vartheta_{\text{HK}}\right)} \quad (3.39)$$

$$= \gamma\mu_0 \sqrt{(H_{\text{int}} + \lambda_{\text{ex}}^2 M_s k^2) (H_{\text{int}} + \lambda_{\text{ex}}^2 M_s k^2 + M_s \sin^2 \vartheta_{\text{HK}})}. \quad (3.40)$$

Here  $\vartheta_{\text{HK}}$  is the angle between  $\mathbf{M}$  and the propagation direction. The internal field is composed of the external field and the demagnetizing field,  $\mathbf{H}_{\text{int}} = \mathbf{H}_{\text{ext}} + \mathbf{H}_{\text{d}}$ . In general it could also include the influence of magnetocrystalline anisotropies. We define the *spin exchange length*  $\lambda_{\text{ex}}$  as

$$\lambda_{\text{ex}} = \sqrt{\frac{2A}{\mu_0 M_s^2}} \quad (3.41)$$

Equation 3.40 represents the dispersion relation of spin waves in an unbound media. For  $\lambda_{\text{ex}}^2 k^2 \ll 1$  the influence of the exchange term  $\lambda_{\text{ex}}^2 M_s k^2$  can be neglected and the dispersion  $\omega_0(k)$  is independent of  $k$ . In this regime we speak of *magnetostatic waves* or *dipolar spin waves*. For larger  $k$ , the solutions are called *exchange spin waves* or *dipolar-exchange spin waves*. In this regime  $\omega_0$  becomes a function of  $k$  and has a finite value even for zero field. For very large  $k$ , one observes  $\omega_0 \propto k^2$ .

### 3.3.3 Spin waves in thin films

In a thin film with thickness  $t$ , the spin waves are confined in one dimension and the wave vector can be split into an in-plane and an out-of-plane component  $\mathbf{k} = \mathbf{k}_{\text{ip}} + \mathbf{k}_{\text{op}}$ . The dispersion relation for this case has been computed by Kalinikos and Slavin [KS86] to be

$$\omega_0 = \gamma \mu_0 \sqrt{(H_{\text{int}} + \lambda_{\text{ex}}^2 M_s k^2) (H_{\text{int}} + \lambda_{\text{ex}}^2 M_s k^2 + M_s F_{nn}(k, H_{\text{int}}))} \quad (3.42)$$

with

$$F_{nn}(k, H_{\text{int}}) = P_{nn} + \sin^2 \vartheta \left[ 1 - P_{nn} (1 + \cos^2 \varphi_{\text{KS}}) + \frac{P_{nn} (1 - P_{nn}) M_s \sin^2 \varphi_{\text{KS}}}{H_{\text{int}} + \lambda_{\text{ex}}^2 M_s k^2} \right] \quad (3.43)$$

as the dipolar matrix element.  $\vartheta$  is the angle between  $\mathbf{M}$  and the film normal and  $\varphi_{\text{KS}}$  is the angle between the in-plane component of  $\mathbf{M}$  and the propagation direction<sup>2</sup>. The latter coincides with the film plane. The exact form of the matrix element depends on the pinning condition of  $\mathbf{M}$  at the surfaces [KS86]. The confinement along the film normal leads to the condition  $k_{\text{op}} = \pi n / t$ . For the special case of totally pinned surface spins,  $P_{nn}$  reads

$$P_{nn} = \frac{k_{\text{ip}}^2}{k^2} + \frac{2k_{\text{ip}} k_{\text{op}}^2}{t k^4} [1 - (-1)^n \exp(-t k_{\text{ip}})] \quad (3.44)$$

with  $n = 1, 2, 3 \dots$ . For totally unpinned surface spins it is modified to

$$P_{nn} = \frac{k_{\text{ip}}^2}{k^2} - \frac{2k_{\text{ip}}^3}{t k^4} \frac{1}{1 + \delta_{0n}} [1 - (-1)^n \exp(-t k_{\text{ip}})] \quad (3.45)$$

and  $n = 0, 1, 2 \dots$ . Neglecting the exchange term  $\lambda_{\text{ex}}^2 M_s k^2$ , the spin waves are called magnetostatic modes or dipolar spin waves. In a thin film one usually considers three types of modes [DHS01]:  $\mathbf{M}$  in-plane and  $\mathbf{k} \perp \mathbf{M}$  gives rise to so called magnetostatic surface modes or Damon-Eshbach Modes (DE) [DE61]. Magnetostatic backward volume modes (MSBV) for  $\mathbf{k} \parallel \mathbf{M}$  and both in-plane. The backward volume modes exhibits negative group velocity. Finally, the magnetostatic forward volume (MSFV) waves describe waves propagating in the plane when  $\mathbf{M}$  is normal to the surface. As an example, the spin wave dispersion of each mode is plotted for  $H_{\text{int}} = M_s$  and  $k_{\text{op}} = 0$  in Fig. 3.2. The reader is referred to Refs. [DHS01, KDG10] for further reading.

---

<sup>2</sup>Please note that  $\varphi_{\text{KS}}$  is only equal to  $\varphi_{\text{HK}}$  of the Herring-Kittel formula, if the magnetization is aligned in-plane

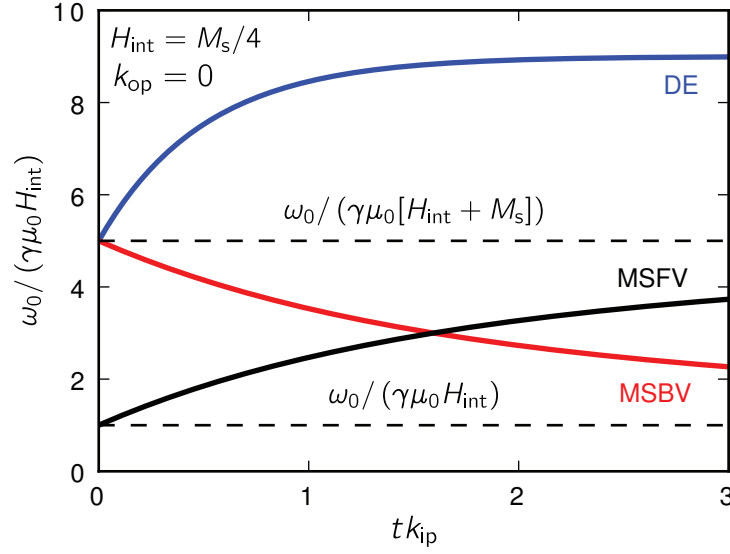


Figure 3.2 – Dispersion relations for spin waves propagating in a planar thin film for an internal field of  $H_{\text{int}} = M_s$  and  $k_{\text{op}} = 0$  under various field orientation.

### 3.4 Effects of tubular geometry

The concepts introduced before will now be applied to the tubular geometry. In the following analytic models found in literature are summarized for the convenience of the reader. Although they are limited to special cases or perfect geometries, they are essential for an understanding of the fundamental physics that govern the magnetic behavior in ferromagnetic nanotubes.

#### 3.4.1 Equilibrium states

In the following we will discuss possible magnetization configurations in a ferromagnetic nanotube. First, two configurations which are uniform over the entire length of the nanotubes are considered: the uniform axial alignment [Fig. 2.3 (a)] and the global vortex configuration [Fig. 2.3 (b)].

The parallel alignment minimizes the gradient in magnetization at the cost of dipolar energy due to the stray field at the ends. The dipolar energy of the axial alignment  $E_d^{\text{ax}}$  can be calculated [ELA<sup>+</sup>07] by expanding  $|\mathbf{x} - \mathbf{x}'|^{-1}$  in the magnetic scalar potential  $\phi$  [cf. Eq. 3.22] and combining Eqs. 3.18 and 3.21 to

$$E_d^{\text{ax}} = \pi\mu_0 M_s^2 r_o^3 \int_0^\infty \frac{1 - \exp(-yL/r_o)}{y^2} [J_1(y) - \beta J_1(\beta y)]^2 dy, \quad (3.46)$$

where  $L$  is the length of the nanotube,  $\beta = r_i/r_o$  the ratio of inner to outer diameter,  $J_1$  is a

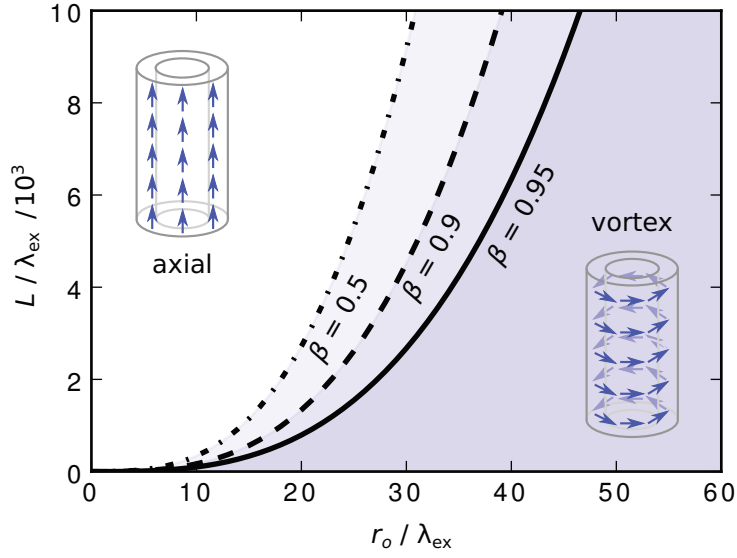


Figure 3.3 – Phasediagram for the transition from axial to vortex state as function of the normalized outer radius  $r_o/\lambda_{\text{ex}}$  and the normalized tube length  $L/\lambda_{\text{ex}}$  for  $\beta = 0.5, 0.9$  and  $0.95$  (after [ELA<sup>+</sup>07]).

Bessel function of the first type. For large  $L/r_o$  this can be approximated as [ELA<sup>+</sup>07]

$$E_{\text{d}}^{\text{ax}} \approx \pi\mu_0 M_{\text{s}}^2 r_o^3 \left[ \frac{4}{3\pi} (1 + \beta^3) - \beta^2 F_{21}(\beta) \right]. \quad (3.47)$$

Here  $F_{21}(\beta) = F_{21}[-\frac{1}{2}, \frac{1}{2}, 2, \beta^2]$  denotes a hypergeometric function. From  $\nabla\mathbf{M} = 0$  and Eq. 3.12 it follows that the exchange energy is  $E_{\text{ex}}^{\text{ax}} = 0$ . The total energy of the axial alignment is thus determined only by its dipolar energy.

The complete flux closure of the vortex results in zero stray field  $E_{\text{d}}^{\text{v}} = 0$  but significant exchange energy due to bending. Inserting  $\mathbf{M}(\mathbf{x}) = M_{\text{s}}\mathbf{e}_{\vartheta}$ , where  $\vartheta$  is the azimuthal coordinate in a cylindrical coordinate system, into Eq. 3.12 and considering that  $(\nabla\mathbf{M})^2 = -\mathbf{M} \cdot \Delta\mathbf{M} = M_{\text{s}}^2 r^{-2}$  [BRH93], one yields [ELA<sup>+</sup>07]

$$E_{\text{ex}}^{\text{v}} = A \int_0^{2\pi} d\vartheta \int_0^L dz \int_{r_i}^{r_o} r^{-1} dr = 2\pi L A \ln(\beta^{-1}). \quad (3.48)$$

It can be seen from Eq. 3.47 that for fixed  $\beta$ ,  $E_{\text{d}}^{\text{ax}}$  increases with  $r_o$  while  $E_{\text{ex}}^{\text{v}}$  is constant. On the other hand,  $E_{\text{d}}^{\text{ax}}$  does not depend on the tube length for large  $L/r_o$ , while  $E_{\text{ex}}^{\text{v}}$  is a linear function of  $L$ . This means that long and thin nanotubes will have an axial alignment as equilibrium configuration and thick short tubes a vortex state. This can be understood, considering that larger  $r_o$  is equal to less curvature, which implies smaller  $\nabla\mathbf{M}$  and smaller  $E_{\text{ex}}$ . At the same time larger radii result in larger surfaces at the ends and thus increased stray field. To determine the critical parameters we can compare the energies of Eqs. 3.47 and 3.48. The vortex will



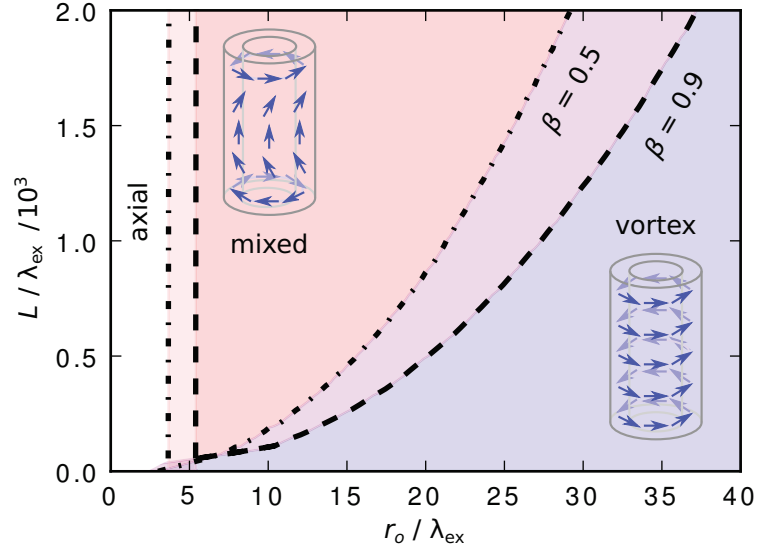


Figure 3.4 – Phasediagram for the transition from axial to mixed and finally vortex state as function of the normalized outer radius  $r_o/\lambda_{\text{ex}}$  and the normalized tube length  $L/\lambda_{\text{ex}}$  for  $\beta = 0.5$  and  $0.9$  (after [LSCV09]).

dominate for

$$E_{\text{ex}}^{\text{v}} < E_{\text{d}}^{\text{ax}} \quad (3.49)$$

$$2\pi L A \ln(\beta^{-1}) < \pi \mu_0 M_s^2 r_o^3 \left[ \frac{4}{3\pi} (1 + \beta^3) - \beta^2 F_{21}(\beta) \right]. \quad (3.50)$$

Rearranging and utilizing the exchange length  $\lambda_{\text{ex}} = \sqrt{\frac{2A}{\mu_0 M_s^2}}$  we can write this condition for the vortex state as

$$\frac{L/\lambda_{\text{ex}}}{(r_o/\lambda_{\text{ex}})^3} < \frac{1}{\ln(\beta^{-1})} \left[ \frac{4}{3\pi} (1 + \beta^3) - \beta^2 F_{21}(\beta) \right]. \quad (3.51)$$

Figure 3.3 depicts the phasediagram corresponding to Eq. 3.51.

If one relaxes the constraint that the magnetization has to be uniform over the whole tube, one can imagine another configuration. In the mixed state, first observed in numerical simulations by Chen *et al.* [CUBG07] in 2007, the stray field is minimized by the magnetization curling at the ends of the tube while being parallel aligned over the rest of the length [Fig. 2.3 (c)]. For the detailed analytic calculations performed by Landeros *et al.* the reader is kindly referred to Ref. [LSCV09]. The phasediagram including this state is reproduced in Fig. 3.4. It follows that the mixed state dominates in high aspect ratio nanotubes with negligible magnetocrystalline anisotropy over a wide range of radii.

### 3.4.2 Domain walls

Considering a tube with axial alignment of the magnetization, one can think of two domain wall types: the transverse [Fig. 2.2 (a)] and the vortex wall [Fig. 2.2 (b)]. Similar to the calculations presented in Sec. 3.4.1, one can determine the energies related to the two types of walls and determine a phase diagram. In principal the vortex wall avoids the surface magnetic charges, which occur for a transverse wall, and has thus a lower dipolar energy. On the other hand the gradient in magnetization related to the vortex wall increases the exchange energy. For detailed calculations we refer to Landeros *et al.* [LAE<sup>+</sup>07] and summarize the most important results of a simpler thin shell model developed by Landeros and Núñez [LNn10]<sup>3</sup>. In this model the minimal energy difference for the existence of a domain wall in respect to a homogeneous axial configuration can be expressed as

$$\Delta E^w = \frac{4\pi r_o^2 (1 - \beta^2) A}{w} \quad (3.52)$$

with the domain wall width  $w$ , which is

$$w = w_{vw} = \sqrt{\frac{(1 - \beta^2)}{2 \ln(\beta^{-1})}} r_o \quad (3.53)$$

for the vortex wall and

$$w = w_{tw} = \sqrt{2} \lambda_{ex} \quad (3.54)$$

in case of a transverse wall. It can already be seen that the domain wall width is the critical parameter in Eq. 3.52: smaller walls cost more energy. The width of the vortex wall scales linearly with the outer radius of the tube. In contrast the transverse wall width is independent of the geometrical dimensions. For this reason it is clear that above a certain critical radius only vortex walls will exist. From an energy comparison one yields the condition for vortex walls,

$$\frac{r_o}{\lambda_{ex}} > 2 \sqrt{\frac{\ln(\beta^{-1})}{1 - \beta^2}} \quad (3.55)$$

which is plotted in Fig. 3.5. Considering that the typical exchange length is in the order of a few to a few tens of nanometers, it is evident that in tubes with dimension of this work, the vortex wall is expected.

Calculations and simulations predict that moving the vortex walls with external fields [LNn10, YAK<sup>+</sup>11, OLLVL12] or electrical pulse [OLLNnL12] takes place at very high velocities. In Py it can reach multiple km/s [LNn10]. A Walker breakdown [SW74] like phenomenon is predicted to occur above a certain threshold, leading to periodic switching of the chirality, i.e. the

---

<sup>3</sup>Please note that the thin shell model is similar to the more complete calculation for large  $\beta \gtrsim 0.7$ . The qualitative picture holds true in any case.

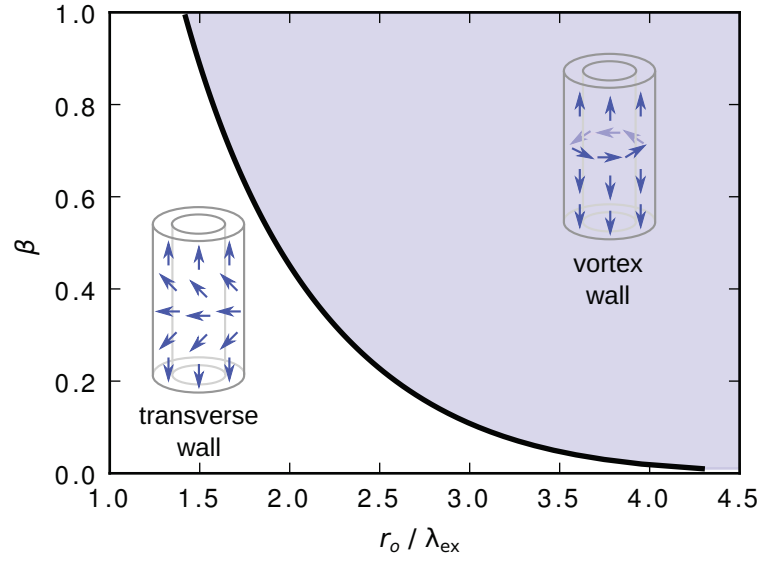


Figure 3.5 – Phasediagram for the transition from transverse to vortex wall as function of the normalized outer radius  $r_o / \lambda_{ex}$  and the radii ratio  $\beta$  (after [LNn10]).

rotational sense [LNn10, OLLVL12, OLLNnL12]. Interestingly the chiral symmetry of domain wall motion is broken in magnetic nanotubes [OLLVL12, YAK<sup>+</sup>12]. Employing the correct pulse strength and length of the field or the current, it is expected that the chirality can be switched in a predictable manner [OLLNnL12, OLLVL12]. On the other hand simulations show that, at least for specific geometrical dimensions, the Walker breakdown can be suppressed [YAK<sup>+</sup>11] and speeds of the phase velocity of magnons are reached, leading to Cherenkov-like spin wave emission [YAK<sup>+</sup>11, YKAH13].

### 3.4.3 Switching field

First experimental investigations analyzed the dependence of the switching field<sup>4</sup>  $H_s$  as function of either the angle  $\theta$  between the external field and the tube axis or the tube wall thickness  $t$ . In a first model, only curling or coherent reversal processes were considered and the calculations for an infinite and solid cylinder employed [HZLW03, SSM<sup>+</sup>08, HRSJY<sup>+</sup>09, HSS<sup>+</sup>09, SLS<sup>+</sup>09]. Escrig and co-workers introduced the possibility of magnetization reversal via transverse or vortex walls [EDL<sup>+</sup>07, EBJ<sup>+</sup>08, AEA<sup>+</sup>08, BEP<sup>+</sup>09, AZA<sup>+</sup>11].

All models are based on either a theory of coherent rotation derived by Stoner and Wohlfarth [SW48] or Aharoni's calculation for the curling reversal [Aha97]. The Stoner-Wohlfarth model is a macrospin model based on energy minimization and includes the Zeeman and the dipolar energy (cf. Sec. 3.2.1). It allows the determination of the characteristic jumps of

<sup>4</sup>The switching field is defined as the field at which  $\mathbf{M}$  performs a spontaneous jump. The coercive field is the field at which the projection of the magnetization along the field is zero. The terms switching field and coercive field are often interchanged, because in most cases switching causes the magnetization to cross zero.

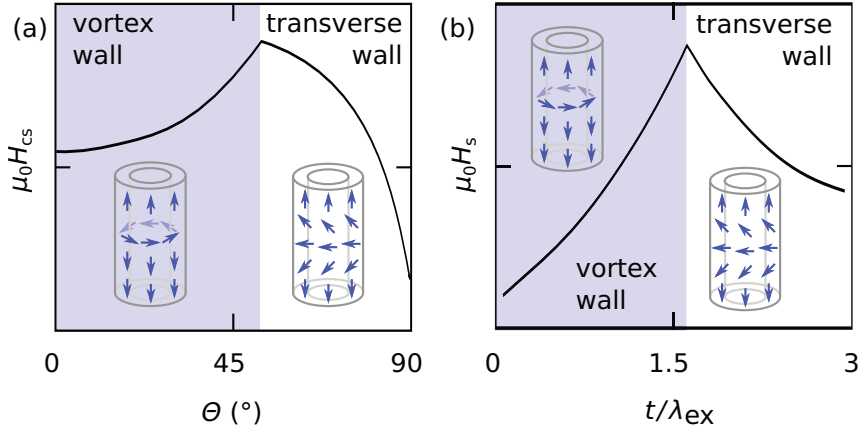


Figure 3.6 – Switching field as function of (a) the angle between field and axis,  $\theta$ , and (b) the normalized tube wall thickness  $t/\lambda_{\text{ex}}$ . Please note that the graphs are using values of Refs. [AEA<sup>+</sup>08, EBJ<sup>+</sup>08]. They depict the behavior of (a) Ni tubes and (b) Fe<sub>3</sub>O<sub>4</sub> tubes with  $r_1 = 25$  nm and typical material parameters. The exact shape and critical values depend on the actual material and geometry.

**M.** At this switching field  $H_s^{\text{coh}}$ , **M** coherently rotates into a new energy minimum. Escrig *et al.* [EDL<sup>+</sup>07] extended the model to the tubular geometry by employing the demagnetization factor in a long tube [cf. Eq. 3.46]

$$H_s^{\text{coh}} = -\frac{1 - 3N_z(L)}{2} \frac{\sqrt{1 - \tan^2(\theta) + \tan^4(\theta)}}{1 + \tan^2(\theta)} \quad (3.56)$$

with the demagnetization factor

$$N_z(L) = \frac{2r_o}{L(1 - \beta^2)} \int_0^\infty \frac{1 - \exp(-yL/r_o)}{y^2} [J_1(y) - \beta J_1(\beta y)]^2 dy \quad (3.57)$$

Here  $J_1$  is a Bessel function of the first type. Shortly after, Escrig *et al.* [EBJ<sup>+</sup>08, AEA<sup>+</sup>08] argued that the nucleation field of a transverse wall with width  $w_{\text{tw}}$  is similar to the switching field of a tube with length  $w_{\text{tw}}$ . The nucleation field is thus  $H_n^{\text{tw}} = H_s^{\text{coh}}(L = w_{\text{tw}})$ .

Chang *et al.* [CLY94] calculated the nucleation field  $H_n^{\text{cur}}$  for the curling mode in an infinite hollow cylinder using the model of Frei *et al.* [Aha97]. In this model, the Brown equation [cf. Eq. 3.7] is employed  $H_n^{\text{cur}}$  can then be found solving the equation assuming a solution with azimuthal magnetization component. Escrig *et al.* [EDL<sup>+</sup>07] modified  $H_n^{\text{cur}}$  in order to describe its dependence on  $\theta$ . For this they extended the expression found in prolate spheroids [Aha97] to include the effect of curvature as derived by Chang *et al.*:

$$H_n^{\text{cur}} = M_s \frac{\left(N_z - \frac{\alpha(\beta)\lambda_{\text{ex}}^2}{r_o^2}\right) \left(N_x - \frac{\alpha(\beta)\lambda_{\text{ex}}^2}{r_o^2}\right)}{\sqrt{\left(N_z - \frac{\alpha(\beta)\lambda_{\text{ex}}^2}{r_o^2}\right)^2 \sin^2(\theta) + \left(N_x - \frac{\alpha(\beta)\lambda_{\text{ex}}^2}{r_o^2}\right)^2 \cos^2(\theta)}}, \quad (3.58)$$

where the function  $\alpha(\beta) = q^2$  satisfies [CLY94]

$$\frac{qJ_0(q) - J_1(q)}{qY_0(q) - Y_1(q)} - \frac{\beta qJ_0(\beta q) - J_1(\beta q)}{\beta qY_0(\beta q) - Y_1(\beta q)} = 0. \quad (3.59)$$

$J_i$  and  $Y_i$  are Bessel functions of the first and second kind, respectively.  $\alpha(\beta)$  can be approximated using a Ritz model to [EDL<sup>+</sup>07]

$$\alpha(\beta) = \frac{8}{3} \frac{(14 - 13\beta^2 + 5\beta^4)}{(11 + 11\beta^2 - 7\beta^4 + \beta^6)}. \quad (3.60)$$

Equation 3.58 simplifies to

$$H_n^{\text{cur}} = \alpha(\beta) \frac{\lambda_{\text{ex}}^2}{r_0^2} \quad (3.61)$$

In this model, employed in Ref. [EDL<sup>+</sup>07, AEA<sup>+</sup>08, EBJ<sup>+</sup>08, BEP<sup>+</sup>09, AZA<sup>+</sup>11], the nucleation field of the curling mode is used as switching field for a reversal via vortex domain wall. This implies two assumptions: first, it has to be assumed that the curling nucleation occurs at the same energy as the nucleation of a domain wall. Second, the switching field of the vortex wall reversal  $H_s^{\text{vw}}$  has to be assumed equal to the absolute of the nucleation field  $|H_n^{\text{vw}}|$ .

The resulting  $H_s$  as function of (a)  $\theta$  and (b)  $t$  are illustrated in Fig. 3.6. The observed trend can be understood if one considers that a higher nucleation field corresponds to a configuration with higher energies. The transverse wall is supported by the Zeeman energy for approximately transverse fields. Because of the curvature, a vortex wall induces more exchange energy if  $\beta = r_i/r_0 = 1 - t/r_0$  becomes smaller. At the same time, the dipolar energy of the void in the center a transverse wall diminishes with decreasing  $\beta$ .

Please note that the model is only valid in the axial phase:<sup>5</sup> Landeros *et al.* [LSCV09] showed that tubes which support mixed states, reverse by first nucleating the incomplete end-vortices. In negative fields, which differ in strength from the nucleation field,  $H_n \neq |H_s|$ , the end-vortices expand and reversal starts. It is assumed that once the end-vortices extend further than the length of a vortex domain wall, such a wall is nucleated. The domain wall then propagates along the tube axis and causes the reversal. It was shown by numerical simulations, that in shorter tubes, the end-vortices extend until they touch. At this point they are separated by a Néel-type domain wall [CGG10, BNR<sup>+</sup>13].

#### 3.4.4 Spin waves

A general analytic solution for tubes with arbitrary inner radius  $r_i$  and film thickness  $t$  is very complex and has not yet been developed up to today. Nevertheless, solutions for special cases have been discussed in literature. Most notably, Leblond and Veerakumar [LV04] solved the

<sup>5</sup>The radii at which the axial state is supported roughly correspond to the ones, where transverse walls are possible (cf. Fig. 3.4 and 3.5).

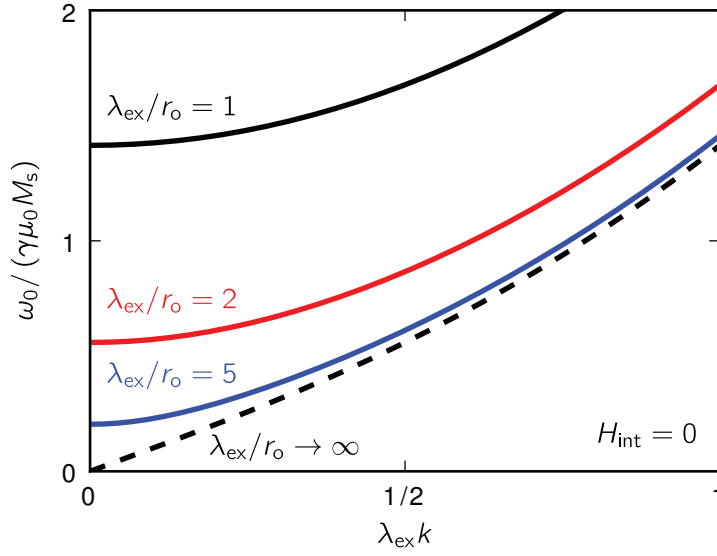


Figure 3.7 – Dispersion relations for spin waves in an infinite ( $L \rightarrow \infty$ ) and thin walled ( $t \rightarrow 0$ ) nanotube with axial alignment [cf. Eq. 3.62] for  $H_{\text{int}} = 0$  and various normalized curvatures  $\lambda_{\text{ex}}/r_0$ .

Landau-Lifshitz equation and the magnetostatic Maxwell equations for an infinite tube ( $L \rightarrow \infty$ ) in the thin wall limit ( $t \rightarrow 0$  or  $r_i \rightarrow r_o$ ) with uniform axial alignment of  $\mathbf{M}_0$ . They consider spin waves propagating along the axis of the tube and neglect any azimuthal confinement. Under these constraints they obtain

$$\omega_0 = \gamma\mu_0 \sqrt{[H_0 + \lambda_{\text{ex}}^2 M_s (k^2 + r_o^{-2})] [H_0 + \lambda_{\text{ex}}^2 M_s (k^2 + r_o^{-2}) + M_s]}. \quad (3.62)$$

Interestingly, and in contrast to the bulk case,  $\omega_0$  is always non-zero, even for vanishing magnetic field and  $k = 0$  [Fig. 3.7]. This is a direct effect of the exchange energy related to the misalignment of the spins on the curved surface of the tube. In a tube, exchange effects can only be neglected for  $\lambda_{\text{ex}}^2 (k^2 + r_o^{-2}) \ll 1$ . This means that the modes are exchange dominated for much smaller  $k$  than in planar samples.

In case the magnetic tube is large enough, so that the exchange effect of curvature itself can be neglected, one can model the system using the thin film dispersion equation, Eq. 3.42, and assume periodic boundary conditions. Balhorn *et al.* [BMK<sup>+</sup>10] used the model to interpret the spin wave resonances found in Rolled-Up Permalloy Tubes (RUPTs). Under the experimental conditions, the magnetization is parallel to the axis and the spin waves are considered to propagate in-plane and perpendicular to  $\mathbf{M}$ . This means that  $\varphi_{\text{KS}} = \vartheta = \pi/2$  in Eq. 3.43. Considering only the fundamental out-of-plane mode,  $n = 0$ , the wave vector becomes  $k = k_{\text{ip}}$ .

Assuming further unpinned surface spins Eqs. 3.43 and 3.45 simplify to

$$F(k, H_{\text{int}}) = 1 - P(k, t) [1 - P(k, t)] \frac{M_s}{H_{\text{int}} + \lambda_{\text{ex}}^2 M_s k^2} \quad (3.63)$$

and

$$P(k, t) = 1 - \frac{1}{tk} [1 - \exp(-tk)]. \quad (3.64)$$

The periodic boundary condition demands a quantization of the azimuthal wavevector. This can be expressed as

$$k = 2m/d \quad (3.65)$$

with  $m = 0, 1, 2, \dots$ .

The authors argue that precession in a curved system lead to magnetization pointing normal to surfaces. This is the source of a dynamic demagnetization field. Balhorn *et al.* [BMK<sup>+</sup>10] include this effect by adding it to the externally applied field. Its magnitude can be estimated by measurement in transverse field. When the external field and the opposing demagnetization field cancel each other, minimal frequency is expected. In practice, it is employed as an additional fit parameter. It should be noted that this model only holds true as long as the curvature is small and the wave lengths are large, i.e.  $\lambda_{\text{ex}}^2 (k^2 + r_0^{-2}) \ll 1$ .





## 4 Methods

The present chapter gives an overview of methods which were employed in the framework of the thesis. First, in Sec. 4.1.1, an overview of the employed experimental techniques is given. Section 4.2 gives a brief description of the micromagnetic simulations.

### 4.1 Experimental techniques

#### 4.1.1 Magnetic field generation

Electrical measurements were performed either in a cryostat with superconducting magnet coils or room temperature setups with resistive 2D vector magnets. The superconducting coils deliver high enough fields to saturate the magnetization in all directions within a large temperature range. Complementary to this, resistive magnets allow for small field steps with negligible field hysteresis. All setups comprise the possibility to contact the samples with multiple low frequency lines which are contacted to a break-out-box.

**Cryostat** A liquid helium bath-cryostat with superconducting coils, Variable Temperature Insert (VTI) and rotatable sample platform has been installed at the EPFL. The system is fabricated by *Cryogenic LTD* and provides magnetic fields up to 9 T in a fixed direction. By cooling a superconducting switch a persistent field can be frozen-in. The sample temperature can be adjusted within a range between 1.6 and 300 K using gas cooling and resistive heaters in the VTI and the sample platform. The rotatable sample platform, which rotates through 320°, comprises a Cermet potentiometer linked to the platform. By reading the voltage drop in a four terminal configuration, the angle can be determined. The rotation is controlled with a stepper motor

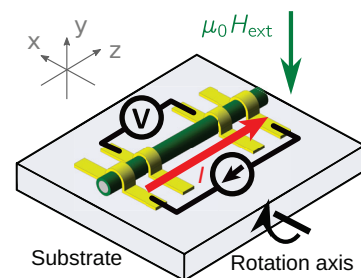


Figure 4.1 – In the cryostat the substrate plane can be rotated through 320° in a fixed magnetic field of up to 9 T.

to a angle accuracy  $\leq 0.5^\circ$ . A custom software, developed in the course of the thesis, allows for the full control and scripting of the cryostat. While the superconducting coils provide high magnetic fields at a wide range of temperatures, they have some intrinsic trade-offs: flux trapping in the superconducting coils gives rise to a hysteretic behavior of few mT. Furthermore, stabilizing on a field value can take substantial time (up to 2 min for that particular system) and the field resolution is only in the range of half a mT.

**Resistive 2D vector magnet coils**

The cryostat has been supplemented by room temperature setups in the group of Prof. Dirk Grundler at the *Technical University Munich (TUM)*, Germany. The setups comprise two pairs of resistive coils around pole shoes which are fed by bipolar power supplies. The magnetic field can be rotated freely by  $360^\circ$  in the substrate plane by adequate superposition of the two generated fields. The maximal field amplitude is 100 mT

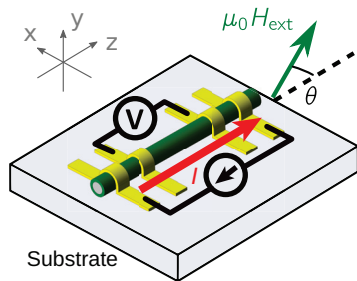


Figure 4.2 – With the vector magnets a field up to 100 mT can be rotated in the substrate plane.

and the step resolution better than 0.1 mT. The applied field is calibrated or actively monitored via a 2D hall probe. For the experiments presented in this thesis, the setups were equipped with electronics for low signal voltage and resistance measurements (cf. Sec. 4.1.2) and Electrically Detected Spin Wave Spectroscopy (EDSWS) (cf. Sec. 4.1.5). The data acquisition was automatized with custom software. In addition to the low frequency contacts, the room temperature setups include rf-probes attached to microposition stages. With these microwaves can be injected into co-planar wave guides (cf. Sec. 4.1.5). More detailed technical information can be found in Refs. [Hub13, Men14, Bra14].

**4.1.2 Electrical characterization & magnetotransport**

The electrical resistance  $R$  is determined by applying a known probe current  $I_p$  between two electrical contacts and measuring the voltage drop  $V$  between two contacts which are located between the other two. In this four point geometry, the influence of cable and contact resistances is excluded. In magnetotransport experiments the change of  $R$  as a function of the applied external field  $\mu_0 H_{ext}$  is determined. Typically, the measurement is initialized by a high magnetic field in order to saturate the sample and obtain a defined magnetic state. Subsequently, the field is lowered in steps. After each change of the field setpoint, the system is allowed to settle to the new field. In case of the resistive magnets the settling is almost instantaneous, but can take up to 2 mins for the superconducting coils, depending on the step size.

**Anisotropic magnetoresistance (AMR)**

Throughout the thesis the AMR effect, discovered by Lord Kelvin over 150 years ago [Tho57], plays a crucial role for the study of the magnetic structure in individual ferromagnetic nanotubes. It connects the electrical transport to the

magnetization orientation. Its fundamental origin is the spin-orbit coupling, which gives rise to spin-flip scattering. The spin-orbit coupling allows the scattering of majority spins into the vacant minority spin states at the Fermi energy and thus increases the resistivity  $\rho$ . The spin mixing is anisotropic because the orbital distribution is affected by the orientation of  $\mathbf{M}$  [Smi51, CFJ70]. In most materials, such as the 3d-ferromagnets, the density of vacant states is larger in direction of the magnetization and thus a higher resistance is observed for a current density  $\mathbf{J} \parallel \mathbf{M}$ . Defining the resistivity parallel and perpendicular to  $\mathbf{J}$  as  $\rho_{\parallel}$  and  $\rho_{\perp}$ , *Ohm's law* reads

$$\mathbf{E} = \rho_{\perp} \mathbf{J} + \frac{\rho_{\parallel} - \rho_{\perp}}{M_s^2} (\mathbf{J} \cdot \mathbf{M}) \mathbf{M}. \quad (4.1)$$

Alternatively, the resistivity  $\rho = \mathbf{E} \cdot \mathbf{J} / J^2$  can be written as function of the angle  $\vartheta_J$  between current flow and magnetization:

$$\rho(\vartheta) = \rho_{\perp} + (\rho_{\parallel} - \rho_{\perp}) \cos^2(\vartheta_J). \quad (4.2)$$

When comparing materials, usually the AMR ratio

$$\text{AMR} = \frac{\rho_{\parallel} - \rho_{\perp}}{\rho_{\perp}} \quad (4.3)$$

is considered.

**Instrumentation** Throughout the thesis, the injected current  $I_p$  is controlled by a current source, which has been either a *Keithley 2401* or *6221*. The voltage is detected via a *Keithley 2182* nanovoltmeter. In order to avoid excessive heating and irreversible damage of the nanotube, the applied current is usually kept around 100 nV to a few  $\mu\text{V}$ . The signal-to-noise (S/N) ratio is maximized and thermovoltages excluded by a 3 step current reversal technique [DGA05]. The current source and the nanovoltmeter are tightly linked with trigger lines. The sign of the applied current is switched after each voltage acquisition, resulting in a square-wave-like current signal with a frequency of about 25 Hz. Three voltage point  $V_1$ ,  $V_2$  and  $V_3$  are acquired and the signal calculated by

$$V = \frac{1}{2} [V_1 - 2V_2 + V_3] \cdot (-1)^n. \quad (4.4)$$

The resulting signal is filtered from low frequency noise and excludes any voltages not originating from the applied current, as e.g. thermovoltages.  $n$  is the sign of the current during the first voltage point  $V_1$ . The signal quality can be further improved by employing a moving average on the acquired points. For samples with low resistances or reactances, such current reversal techniques yield better results than traditional lock-in amplifiers [DGA05, R 09]. Additionally, the large dynamic range of sub-nV resolution at an input range of 10 mV allows for measurements with strongly varying signal strength. Furthermore, the detection of small deviation from a large constant background becomes feasible.

## 4.1.3 Cantilever Magnetometry

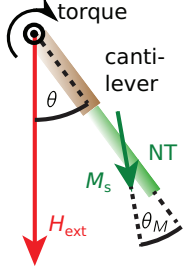


Figure 4.3 – Schematic of the cantilever magnetometry experiment.

In order to measure the saturation magnetization  $M_s$  and estimate the anisotropy of individual ferromagnetic nanotubes, an experiment was devised in collaboration with Arne Buchter, Prof. Martino Poggio and Dennis Weber from University Basel, Switzerland. They designed the setup and conducted all experimental work.

In such an experiment, a single nanotube is attached to the tip of an ultrasoft Si cantilever, whose motion is detected by the deflection of a laser by an integrated paddle. In an external field  $H_{\text{ext}}$  the magnetization  $\mathbf{M}$  generates a torque on the cantilever which in turn modifies its resonance frequency. For large enough fields,  $\mathbf{M}$  is almost saturated and one can apply a macro spin model. In such a model the relevant magnetic energies (cf. Sec. 3.2.2) can be expressed by the Zeeman energy  $E_z = M_s H_{\text{ext}} V \cos(\theta - \theta_M)$  and an uniaxial anisotropy term  $E_{\text{uni}} = KV \sin^2(\theta_M)$ . Here,  $\theta$  is the angle between tube axis and field and  $\theta_M$  the one between  $\mathbf{M}$  and tube axis [Fig. 4.3]. All possible uniaxial anisotropies are collected in  $E_{\text{uni}}$  using a single phenomenological anisotropy constant  $K$ . Following the idea developed in Sec. 3.4, the macro spin will orient itself such that the energy is minimized. Using this model the frequency shift is

$$\Delta f_0 = K_{\text{cant}} \left( \frac{2H_{\text{ext}}KV}{H_{\text{ext}} + \frac{2K}{M_s}} \right) \quad (4.5)$$

for  $H_{\text{ext}} > -2K/M_s$ . The constant  $K_{\text{cant}}$  is only a function of cantilever parameters such as length and the original resonance frequency. With Eq. 4.5 one can determine  $K$  and  $M_s$  by fitting. More details on the experiment and the full model including derivation can be found in Pub. B-I (cf. App. D) and the corresponding supplementary information [WRB<sup>+</sup> 12].

**Instrumentation** The nanotubes were glued to the Si cantilevers with less than 100 fL of epoxy (*Gatan GI*). The cantilever and the nanotube were actuated under an optical microscope with precision micromanipulators (*Narishige MMO-202ND*). The cantilevers have a typical resonance frequency of 2 to 3 kHz, quality factors in the order of  $3 \times 10^4$  and spring constants around 60  $\mu\text{N/m}$ . The cantilever dimensions are  $18\mu\text{m} \times 4\mu\text{m} \times 100\text{nm}$ . Additionally it incorporates the 12  $\mu\text{m}$  wide paddle and a 18  $\mu\text{m}$  long and 1  $\mu\text{m}$  thick mass. The light of a laser diode operating at 1550 nm is reflected from the paddle and fed into an optical fiber interferometer. A piezoelectric element is linked to the deflection signal in order to maintain the desired amplitude at self-oscillation. This way the resonance frequency can be determined very accurately.

#### 4.1.4 Local probing of magnetization orientation by anomalous Nernst effect

The small dimensions and the curvature of ferromagnetic nanotubes inhibit conventional Magneto-Optical Kerr-Effect (MOKE) experiments. Thus magnetothermal imaging via the Anomalous Nernst Effect (ANE) (cf. Sec. 7.1) was employed in cooperation with the group of Prof. Grundler in Munich. In such an experiment a temperature gradient  $\nabla T$  is induced locally by the laser spot. According to the ANE [Ner87], a temperature gradient in a magnetic body generates an electric field normal to  $\nabla T$  and  $\mathbf{M}$ :

$$\mathbf{E}_{\text{ANE}} = -N_{\text{ANE}}\mu_0\mathbf{M} \times \nabla T \quad (4.6)$$

Here, the Nernst coefficient  $N_{\text{ANE}}$  is a material specific constant. The ANE's microscopic origin is the spin-orbit interaction which leads to a broken time-reversal symmetry, similar to the anomalous Hall effect. The origin can be either *intrinsic*, caused by Berry phase effects, or *extrinsic* by disorder scattering via the *side jump* or *skew scattering* mechanism. An exhaustive review of the physics can be found in Ref. [NSO<sup>+</sup>10]. In planar samples the ANE based imaging was recently employed to study the magnetization reversal [WAC<sup>+</sup>12, vBBGA13].

The voltage drop is measured along the tube axis (the  $z$ -axis in Fig. 4.2). It follows from Eq. 4.6 that the ANE signal is sensitive to the component of the magnetization which is parallel to the substrate surface and normal to the tube axis (the  $x$ -axis in Fig. 4.2).

**Instrumentation** The ANE measurements were performed in a room temperature vector magnet setup with laser stage (cf. Sec. 4.1.1). The laser (*Toptica iBeam Smart 405 HP*) is operating at a wavelength of 407 nm and provides a laser spot size  $w_{1s}$  of about 1  $\mu\text{m}$ . The position reproducibility is in the order of 100 nm. For long term spot stability, its position can be automatically stabilized using the *TFPDAS4-Micro* software [Sch10]. During the moment of actual data acquisition, the position adjustment is deactivated. The drift during the data acquisition is negligible. More details can be found in the doctoral thesis of Florian Brandl (TUM) [Bra14], who devised the laser stage, in Ref. [BG14] or in the master thesis of Johannes Mendil [Men14], who conducted the actual measurements. For the electrical measurements the same combination of *Keithley 2182 Nanovoltmeter* and the *Keithley 2401* or *6221* current source (see above) were employed, albeit in standard DC four point mode.

## 4.1.5 Electrically detected spin wave spectroscopy

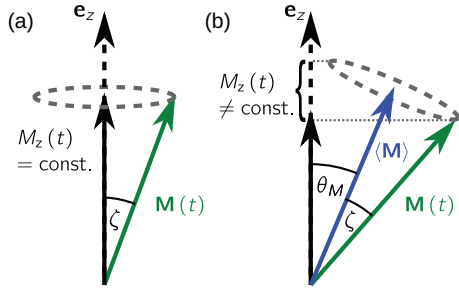


Figure 4.4 – Schematic describing the angle dependence of spin-rectification

Five decades ago, Juretschke and co-workers predicted [Jur60] and measured [EJ63] the existence of a microwave *photoconductivity* or a *photovoltage* in a Ferromagnetic Resonance (FMR) condition. It was shown a bit later that the same holds true in case of spin wave resonances [MJ70]. The photoconductivity is caused by a combination of bolometric effects [GHMH05, GSB<sup>+</sup>07, MGH07] and magnetoresistive effects such as the AMR [GMW<sup>+</sup>07, GMH07, GMZ<sup>+</sup>07a, MGH07, HCG<sup>+</sup>11, GY13] (cf. Sec. 4.1.2). The AMR based effect gener-

ates even without applied current a photovoltage by interacting with the induced microwave current. For this reason, the effect is usually called spin-rectification. It can be understood when considering the vectorial depiction of *Ohm's* law including AMR and the anomalous Hall effect (AHE) with  $R_H$  as the anomalous Hall constant [Jur60]:

$$\mathbf{E} = \rho_{\perp} \mathbf{J} + \frac{\Delta\rho}{M_s^2} (\mathbf{J} \cdot \mathbf{M}) \mathbf{M} - R_H \mathbf{J} \times \mathbf{M}. \quad (4.7)$$

Assuming that the microwave field induces current parallel to the axis of the tube,  $\mathbf{J} = J \cos(\omega t + \varphi) \mathbf{e}_z$ , the electric field along the axis reads

$$E_z(t) = \rho J \cos(\omega t + \varphi) + \frac{\Delta\rho}{M_s^2} M_z^2(t) J \cos(\omega t + \varphi). \quad (4.8)$$

The dc voltage drop between two contacts with distant  $L_p$  will then be

$$V_{DC} = \langle E_z \rangle L_p = \frac{\Delta\rho J L_p}{M_s^2} \langle M_z^2(t) \cos(\omega t + \varphi) \rangle. \quad (4.9)$$

If  $\mathbf{M}$  is perfectly parallel to the tube axis [Fig. 4.4 (a)],  $M_z(t)$  is constant and thus no DC voltage is expected. In case  $\mathbf{M}$  is tilted by an angle  $\theta_M$  to the axis and performs circular precession with a cone angle  $\zeta$ , Eq. 4.9 can be solved. From Fig. 4.4 (b) one finds that  $M_z(t) = -M_s \cos(\omega t) \sin(\zeta) \sin(\theta_M) + M_s \cos(\theta_M) \cos(\zeta)$ . It follows that

$$V_{DC} = -\frac{\Delta\rho J L_p}{4} \sin(2\zeta) \sin(2\theta_M) \cos(\varphi).$$

The strength of the spin-rectification thus depends on the phase shift  $\varphi$ . It is maximal for a tilt angle  $\theta_M = 45^\circ$ .

In practice the oscillation will not be circular but elliptic. In complex structures the trajectory of the motion can also be a function of the spatial coordinates. Furthermore, if a more complex

current distribution is considered, the AHE can further modify the signal. A comprehensive overview of spin-rectification in planar samples can be found in Ref. [MGH07] and in the thesis of Nikolai Mecking [Mec08]. It was found by Harder *et al.* [HCG<sup>+</sup>11], that in such planar samples the line shape and the symmetry of the spin-rectification signals depends on the orientation of the exciting rf-field. Excitation out-of-plane (in-plane) results in a  $\pi$ - ( $2\pi$ -) periodicity and Lorentzian (dispersive) line shape.

**Instrumentation** The experiments were conducted in close collaboration with the group of Prof. Grundler in Munich. For high frequency measurements the room temperature vector magnets (cf. Sec. 4.1.1) have been used. Microwaves in the range between 100 kHz and 20 GHz are fed from an *Agilent N5183A* microwave generator (with the UNT option for AM modulation) into asymmetric waveguides via microwave probes (*Picroprobe*) at maximal power (15 dBm). The stripline of the rf wave guide is located in vicinity and parallel to the nanotube [Fig. 5.5 (b)]. The stripline has a width of 2  $\mu\text{m}$  and is separated by a 1.2  $\mu\text{m}$  gap from the 35  $\mu\text{m}$  wide ground line. The nanotube has a distance of typically 500 to 800 nm from the stripline. The DC voltage is detected by a *Keithley 2182* nanovoltmeter which is triggered by *Keithley 2401* or *6221* current source (cf. Sec. 4.1.2). The output current is translated into a voltage, which in turn is used to control the AM modulation. As a result the rf-generator's output is switched on-off in sync with the nanovoltmeter. At zero and maximal output the voltage is sampled. Before each sample, a short settling period (5 ms) is included. On these samples, the 3-step delta technique (cf. Sec. 4.1.2) is employed in order to maximize the S/N-ratio. Because the signal is switched on-off rather than being reversed, the calculated voltage is half the real physical value.



### 4.2 Micromagnetic simulations

In order to gain more insight into the magnetic states and the magnetization dynamics, micromagnetic simulations have been performed using the open source simulation toolkit *Nmag*, which is provided free of charge by the University of Southampton<sup>1</sup> [FFBF07]. The simulation implements the LLG equation [cf. Eq. 3.32] in a Finite Element Method (FEM) approach. A tetrahedral mesh resembling the structure under investigation is generated. The tetrahedral mesh is more suited for the approximation of circular shapes than the rectangular mesh in the Finite Difference (FD) method. The *Nmag* package was chosen because it implements a hybrid FEM/BEM method in combination with hierarchical matrices. It is furthermore optimized for parallel computing and can be easily scripted due to its Python interface. The advantages and implications of these points are briefly reviewed in the following. A comprehensive overview of the numerical details behind *Nmag* can be found in the thesis of Knittel [Kni11].

#### 4.2.1 Hybrid-FEM/BEM

In micromagnetic simulations the computation of the magnetic scalar potential  $\phi$  [cf. Eq. 3.17] is numerically challenging. The open boundary condition described by Eq. 3.19 implies that conventional FEM, which assumes finite-domains, cannot be used for micromagnetic computations. A number of techniques were devised in order to overcome the problem of open boundaries [CK97]. The most simple approach is the truncation of the vacuum domain at a certain distance. If the point of truncation is sufficiently far away,  $\phi$  is approximately zero and thus the open boundary condition can be approximated with a finite boundary. Today, most state-of-the-art FEM solvers implement an approach which combines traditional FEM with an Boundary Element Matrix (BEM) approach [FK90, FSD<sup>+</sup>03, GCR06]. Here, the magnetic scalar potential  $\phi$  is divided into two contributions  $\phi_1 + \phi_2$  such that the problem is split into a Poisson equation in the magnetic body for  $\phi_1$  and a Laplace equation in the vacuum region ( $\phi_2$ ). It can be shown that  $\phi_2$  can be computed using the simple vector relation [FK90, GCR06]

$$\phi_2^j = B_{ij} \cdot f(\mathbf{M}, \phi_1^i). \quad (4.10)$$

The Boundary Element Matrix (BEM)  $\hat{B}$  describes thus the influence of the magnetic charge at node  $i$  onto node  $j$ . Interestingly,  $\hat{B}$  does only depend on the geometry of the simulation. For this reason it is sufficient to calculate it once in the initialization phase. Unfortunately,  $\hat{B}$  is a dense and non-symmetric matrix. It scales quadratically with the number of surface nodes and thus the BEM approach becomes numerically challenging for geometries with a large number of surface nodes.

---

<sup>1</sup><http://nmag.soton.ac.uk/nmag/>



### 4.2.2 Hierarchical matrices

The large size of  $\hat{B}$  is a general problem when simulating realistically sized problems while keeping the mesh size in the the order of the exchange length. This is especially problematic for a hollow tube with high aspect ratio, which comprises a large number of surface nodes. It is thus advantageous to compress  $\hat{B}$ . *Nmag* uses for this purpose the *HLib* library which implements hierarchical matrices, or  $\mathcal{H}$ -matrices [Hac99, HK00]. The underlying theory is very complex. In a simple picture the BEM is divided into a number of sub-matrice, organized in a hierarchical tree with only few matrix elements. For a complete introduction, the interested reader is referred to the lecture notes of Börm, Grasedyck and Hackbusch [BGH06]. In practice, the method allows for a data-sparse approximation of a non-sparse matrix and thus a high degree of compression of the effective data. Instead of the quadratic scaling ( $\sim N^2$ ) with the number of surface elements  $N$ , a much more favorable  $\sim N \log(N)$  scaling is found for the data compression and the speed of the matrix-vector product.

### 4.2.3 Quasi-periodic boundary conditions

Due to computational limitations, the aspect ratios which can be readily simulated are very limited. One option, common in numerical computations, is to apply periodic boundary conditions. This is problematic in micromagnetic simulations, as the behavior is highly shape-sensitive due to the influence of the long-range dipolar interaction. To circumvent the problem, a new approach was devised by Fangohr *et al.* [FBF<sup>+</sup>09] and implemented in *Nmag*. The quasi-periodic boundary condition approach takes advantage of the fact that the BEM depends only on the geometry. This means the matrix has to be calculated only once and can then be reused during the following computation. The problem is split into a number of similar unit cells. The full LLG computation is only performed on one copy. The dipolar interaction, however, is calculated using the full matrix, describing correctly the demagnetizing field. This approach correctly includes the shape, but neglects the influence of potentially varying  $\mathbf{M}(\mathbf{r})$  at the outer unit cells. One should be aware, that this method is limited to certain scenarios.

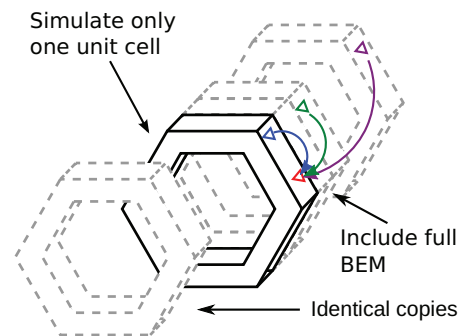


Figure 4.5 – Illustration of the quasi-periodic boundary conditions

### 4.2.4 Methodology

In this thesis the meshes have been generated either using *netgen*<sup>2</sup> in the case of nanotubes with cylindrical cross-section or *gmsh*<sup>3</sup> for hexagonal nanotubes. In all simulations the average

<sup>2</sup><http://sourceforge.net/projects/netgen-mesher/>

<sup>3</sup><http://geuz.org/gmsh/>

cell size was chosen to be in the order of  $\lambda_{\text{ex}}$ . The magnetization vector should barely vary from cell to cell in order to fulfill the assumptions of the micromagnetic equations. *Nmag* gives the user the possibility to verify the maximal angle that occurred between neighboring cells during simulation. The maximal angle should be smaller than  $30^\circ$  in order to have a solution which is most likely reliable<sup>4</sup>. Furthermore, if possible, a simulation should be performed with smaller cell size to verify that no modification of any output parameter is linked to the meshsize. The simulation takes the exchange coupling constant  $A$  and the saturation magnetization  $M_s$  as material parameters. Furthermore, for dynamic simulations, the Gilbert damping parameter  $\alpha$  has to be correctly defined. The values that were employed for this thesis are listed in Tab. 4.1.

**Hysteresis curves** To determine the equilibrium configuration, the system is relaxed by following the time evolution of the system until it converges. For the determination of the global ground state, the magnetization would have to be initialized randomly and the relaxation process repeated numerous times. In this thesis, the micromagnetic simulations were employed to determine the hysteresis curves of a system. For this purpose, the simulation was commenced at  $H_{\text{ext}} > M_s$ . At such high fields,  $\mathbf{M}$  is known to be almost perfectly aligned with the external field.  $\mathbf{M}$  can thus be initialized parallel to  $\mathbf{H}_{\text{ext}}$ . The magnetic field was then gradually reduced. At each field step the magnetization has been relaxed until the convergence criterion is reached, i.e.  $d\mathbf{M}/dt$  is smaller than  $d|\mathbf{m}|/dt < 3^\circ/\text{ns}$ . To save computation time, the influence of the damping term was neglected in all simulations. In the simulation presented in publication B-II (cf. App. D) the complete nanotube was simulated in order to correctly describe the behavior of  $\mathbf{M}$  at the ends. In the simulations of Sec. 7.2 only very long nanotubes in transverse fields were considered. Here, in order to save computational time and be able to simulate rather large diameter tubes, quasi-periodic boundary conditions (cf. Sec. 4.2.3) were employed. This means that any deviations of  $\mathbf{M}$  along the axis were neglected.

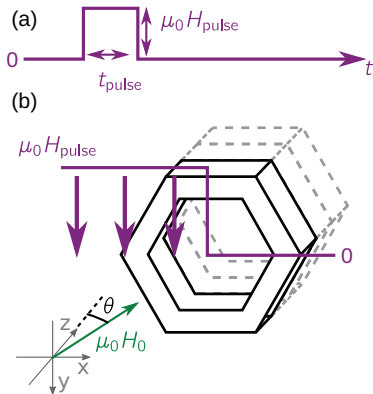


Figure 4.6 – Depiction of the pulse shape (a) and the field geometry for the dynamic simulations with asymmetric excitation (b).

**Dynamic simulations** To simulate the response of  $\mathbf{M}$  in a ferromagnetic nanotube, the equilibrium state at the desired  $\mathbf{H}_{\text{ext}}$  had been determined as mentioned in the previous paragraph. The long nanotubes were approximated by the quasi-periodic boundary conditions (cf. Sec. 4.2.3). The damping term was included and a realistic value for the damping parameter chosen (cf. Tab. 4.1). After having found the equilibrium state, a short field pulse  $\mathbf{H}_{\text{pulse}}(\mathbf{x}, t)$  was added to  $\mathbf{H}_{\text{ext}}$ . The pulse shape in the presented simulations was of rectangular shape in the time domain with a pulse width  $t_{\text{pulse}}$  [Fig. 4.6 (a)].

<sup>4</sup>from <http://nmag.soton.ac.uk/nmag/0.2/manual/html/tutorial/doc.html>

## 4.2. Micromagnetic simulations

	$M_s$ [kA/m]	$A$ [pJ/m]	$\alpha$	precession	$L_{\text{cell}}$ [nm]	$\langle x_{\text{cs}} \rangle$ [nm]
Ni	406	7	1	off	-	6.9
CoFeB	1430	28	1	off	50	6.4
Py	400	13	0.008	on	20	5.8

Table 4.1 – Simulation parameters

In order to reproduce the experimental conditions,  $H_{\text{ext}}$  was applied in the  $x$ - $z$  plane and  $\mathbf{H}_{\text{pulse}} = H_{\text{pulse}} \mathbf{e}_y$  normal to it. The excitation profile was chosen to be either uniform over the entire volume, or to vary as [Fig. 4.6 (a)]:

$$H_{\text{pulse}}(\mathbf{x}) = \begin{cases} H_{\text{pulse}} & \forall x < 0 \\ 0 & \forall x \geq 0 \end{cases} \quad (4.11)$$

While the first profile excites symmetric modes, the latter gives an excitation of modes with asymmetric amplitude distribution.

The time evolution of  $\mathbf{M}(t)$  was followed and stored in time steps of  $\Delta t$  for a total simulated time period  $t_{\text{evo}}$ . The frequency spectrum of the response was then extracted by Fast Fourier Transform (FFT) of the dynamic magnetization  $\mathbf{m}(\mathbf{x}, t) = \mathbf{M}(\mathbf{x}, t) - \mathbf{M}(\mathbf{x}, t = 0)$ . The frequency resolution is  $\Delta f = 1/t_{\text{evo}}$  and the Nyquist-Frequency, the maximum reachable frequency,  $f_N = 1/2\Delta t$ . In geometries resembling a standard coordinate system, e.g. planar or cylindrical object, the FFT is usually computed of a single component (e.g. out-of-plane) of  $\mathbf{m}(t)$ . Peaks in the modulus of the complex FFT spectrum are then attributed to resonances. When investigating arbitrary geometries, such as an hexagonal nanotube (cf. Sec. 8), no orthonormal coordinate system is natural to the system. Thus, the two-dimensional FFT vector  $\mathbf{F}(\mathbf{m}_{\perp})$  was considered in the analysis. Here,  $\mathbf{m}_{\perp}$  are the two components orthogonal to  $\mathbf{M}(\mathbf{x}, t = 0)$ , i.e.  $\mathbf{m}_{\perp} = m_x \mathbf{e}_x + m_y \mathbf{e}_y$  in case of  $H_{\text{ext}} \parallel \mathbf{e}_z$ . One obtains a two-dimensional, complex spectral map  $\mathbf{F}(\mathbf{m}_{\perp}) = \text{FFT}(m_x) \mathbf{e}_x + \text{FFT}(m_y) \mathbf{e}_y$ . Considering that the components of  $\mathbf{F}(\mathbf{m}_{\perp})$  are complex numbers, the power spectrum was calculated using the magnitude of  $\mathbf{F}(\mathbf{m}_{\perp})$  as <sup>5</sup>

$$\|\mathbf{F}(\mathbf{m}_{\perp})\| = \sqrt{\|\text{FFT}(m_x)\|^2 + \|\text{FFT}(m_y)\|^2}. \quad (4.12)$$

**Simulation Parameters** Table 4.1 gives the parameters which were utilized for the simulations. The table also indicates whether the precession term was included and the length of the cell for the quasi-periodic boundary conditions  $L_{\text{cell}}$ . The average cell size, as determined by the *nmeshpp* of the *nmag* distribution, is given as  $\langle x_{\text{cs}} \rangle$ . The value for Ni nanotubes with  $L < 2 \mu\text{m}$  ([Fig. 4 in Pub. B-II, App. D]) is given in the first row, the CoFeB tubes with periodic boundaries of Sec. 7.2 in the second. In the last row, the value for the dynamic simulations on Py tubes of Pub. A-III Sec. 8 are listed.

<sup>5</sup>Note that  $\|z\| = z^* \cdot z$  denotes the modulus of a complex number or vector.



# 5 Sample fabrication

One goal of this thesis was to develop new fabrication methods for ferromagnetic nanotubes from magnetically isotropic materials. In this chapter the reader is introduced to fabrication methods based on nanowire templates (cf. Sec. 5.1.1). Furthermore, the process to contact individual magnetic nanotubes is outlined (cf. Sec. 5.2). In this context the newly developed scheme to automatize the location of microstructures and the lithography layout design will be described.

## 5.1 Ferromagnetic tube fabrication based on nanowire templates

Ususally, to fabricate magnetic nanotubes, the walls of a porous template, often porous anodized alumina, are coated with a thin film of a magnetic material (cf. Sec. 2.1). An inverse approach was followed in order to produce magnetically hollow tubes: comparable to the fabrication of epitaxial core/ferromagnetic-shell nanowire systems [ZLH<sup>+</sup>04, HTH<sup>+</sup>09, RSK<sup>+</sup>09], arrays of self assembled semiconductor nanowires have been coated with a thin shell of the desired material. In contrast to previous works, the materials Nickel (Ni), Permalloy (Py) and an alloy Cobalt, Iron and Boron (CoFeB) were chosen for this thesis in order to obtain polycrystalline or amorphous materials. The reason is that these materials are known to be magnetically isotropic.

### 5.1.1 Nanowire growth

The nanowires used for this thesis were grown using the Vapor-Liquid-Solid (VLS) growth mechanism [WE64]. In a Molecular-Beam-Epitaxy system, Gallium (Ga) droplets serve as catalysts and nucleation points for subsequent nanowire growth along the preferred (111)B orientation [FiMCA<sup>+</sup>08, CSF<sup>+</sup>08]. An incoming Ga flux will give rise to diffusion of Ga adatoms on the oxide surface. These form and feed the Ga droplets which will act as seed for the later nanowire growth. A flux of Arsenic (As) is directed onto the surface. The As, otherwise subject to desorption, dissolves in the liquid Ga. Once supersaturation is reached, GaAs

precipitates and forms the mono-crystalline GaAs in epitaxial relation to the underlying substrate. Throughout the thesis Si(111) substrates were utilized [JGRM08, PNYS09]. The substrate is typically heated to a temperature between 590 and 650 °. In an As pressure of about  $3 \times 10^{-6}$  mbar, a Ga flux equivalent to 0.3 to 1.1 Å/s planar growth is applied. Because this thesis is not concerned with the complex details of nanowire growth, the reader is referred to Refs. [CSF<sup>+</sup>08, PNYS09, PDL<sup>+</sup>10, KJJ<sup>+</sup>13, RHG<sup>+</sup>13] for more detailed information regarding the growth process.

### 5.1.2 Deposition of ferromagnetic shell material

After the nanowire growth, the ferromagnetic shells were deposited conformally around the nanowires. Depending on the desired material, the chosen process varied. The Ni shells were fabricated using Atomic Layer Deposition (ALD), the CoFeB one with via magnetron sputtering and Py with thermal evaporation. For this the as-grown nanowires were shipped to the group of Prof. Grundler in Munich for deposition. ALD processes were performed by Rupert Huber and Thomas Schwarze. Florian Heimbach performed both, the thermal evaporation and the sputtering.

**Atomic Layer Deposition** Atomic Layer Deposition (ALD), first called Atomic Layer Epitaxy [Sun89], was originally developed in the 1970s [SA77] for the deposition of epitaxial semiconductor films on large area substrates. ALD is more commonly known for the highly isotropic and homogeneous growth of polycrystalline or amorphous materials without shadowing effect [Sun92, Geo10]. It has been successfully employed to fabricate ferromagnetic Ni [DKGN07], Co [DKGN07] and Fe<sub>3</sub>O<sub>4</sub> [BJK<sup>+</sup>07, EBJ<sup>+</sup>08, BEP<sup>+</sup>09, AZP<sup>+</sup>10] nanotubes in porous membranes

In principle ALD can be understood as a special case of chemical vapor deposition (CVD). It differs from conventional CVD in that the reactants are supplied in sequence without mixing. This way the process is dominated by the surface chemistry. The process is a cyclic repetition of multiple steps. The choice of precursor in each step is such that the chemi- or physisorption at the surface is self-terminated. In between these reaction steps, the reactor is purged from any reaction products and residuals of the precursor. Figure 5.1 depicts schematically the ALD process for Al<sub>2</sub>O<sub>3</sub>, which is one of the most common processes. More comprehensive reviews can be found in literature, e.g. [Sun92, Geo10, Hub13].

Although having made significant advances [DKGN07, BJK<sup>+</sup>07, LKP<sup>+</sup>09, CGM<sup>+</sup>10], ALD of ferromagnetic transition metals, and in particular of their alloys, is still in its infancy [Les11]. One challenge is that using Nickelocene (Ni(C<sub>5</sub>H<sub>5</sub>)<sub>2</sub> or NiCp<sub>2</sub>) and O<sub>3</sub> as precursors results in an oxidic process. This means a large amount of NiO is generated. Thus an additional ex-situ reduction step is required. Although the fabrication of metallic films using ex-situ reduction were reported in literature [DKGN07, BJK<sup>+</sup>07], the method can give rise to non-homogeneous films [Hub13] due to Ostwald ripening [Ost00, Wag61]. Ostwald ripening describes the process

## 5.1. Ferromagnetic tube fabrication based on nanowire templates

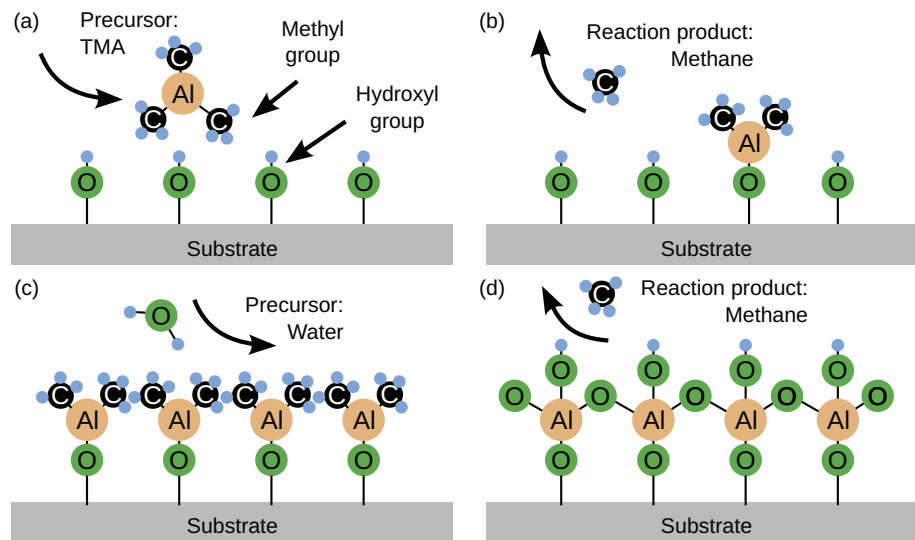


Figure 5.1 – Schematic depiction of the Al<sub>2</sub>O<sub>3</sub> ALD process. Tri-methyl aluminum Al(CH<sub>3</sub>)<sub>3</sub> (TMA) is injected as precursor (a) and reacts with Hydroxyl (OH) terminated surface of the substrate under production of Methane CH<sub>4</sub> (b). The reaction stops once the surface is saturated. Then, after purging, water is inserted as precursor (c). The reaction will form a single layer of Al<sub>2</sub>O<sub>3</sub>, which again offers OH groups (d) for a cyclic repetition and layer by layer growth.

that smaller grain shrink and larger grains grow under elevated temperatures, which are necessary for the reduction step, resulting into movement of material.

To improve the material quality and diminish problems of homogeneity, an additional step with Hydrogen (H<sub>2</sub>) was introduced after each ozone pulse. The process flow for the fabrication of Ni thin films via in-situ reduction can be summarized as [Hub13]:

$$N_C \times (t_1|t_2 + t_3|t_4 + t_5|t_6) =$$

$$N_C \times (0.8\text{s}|4\text{s} + 10\text{s}|10\text{s} + 16\text{s}|20\text{s})$$

Here  $N_C$  denotes the number of cycles, which is directly proportional to the film thickness. The times  $t_1, t_3$  and  $t_5$  give the pulse duration for NiCp<sub>2</sub>, O<sub>3</sub> and H<sub>2</sub>,  $t_2, t_4$  and  $t_6$  the corresponding purge times. It has been found that a sub-sequent ex-situ reduction step further improves the material properties. For this the Ni nanotubes were held in hydrogen atmosphere at 350 °C for four hours. A more detailed description of the ALD technique can be found in the dissertation of Rupert Huber [Hub13], who developed and optimized the process at the Technical University of Munich, Germany in the group of Prof. Dirk Grundler.

**Physical thin film deposition** The limitation in the material choice made it necessary to develop a different process in order to obtain magnetic nanotubes which are suitable for spin

dynamics. Py and CoFeB are interesting materials in that they do not show magnetocrystalline anisotropy and very little damping of spin excitation [YWL<sup>+</sup>06, YHS<sup>+</sup>12]. In this thesis magnetron sputtering [KA00] and thermal evaporation were utilized to fabricate high-aspect ratio magnetic nanotubes made of CoFeB and Py, respectively. In both cases, the Si(111) substrate with vertical GaAs nanowires was installed on a rotating sample holder. The rotational axis was tilted by 35° with respect to the direction of the incoming flux. In order to minimize shadowing effects it is necessary to optimize the nanowire growth process for a high yield of vertical wires and comparatively low densities [RAHM<sup>+</sup>12]. Due to the rotation and the deposition angle the deposition rate can not be directly determined by reference films. For this reason, the shell thicknesses have been calibrated and verified using Transmission Electron Microscopy analysis (TEM), performed by Reza R. Zamani and Jordi Arbiol at ICMA-B-CSIC and ICREA at Barcelona, Spain. The custom-build vacuum systems achieve base pressures below  $3 \times 10^{-7}$  mbar. The CoFeB has been sputtered using a  $\text{Co}_{20}\text{Fe}_{60}\text{B}_{20}$  target in a Xenon atmosphere of  $3.5 \times 10^{-3}$  mbar at a thin film deposition rate of 9.6 Å/s. The Py growth rate on a planar substrate equals 1.5 Å/s. It was found that the deposition on the side facets is smaller by a factor of  $2.6 \pm 0.1$ .

## 5.2 Fabrication of samples for electrical measurements

The previous section outlined how the ferromagnetic nanotubes themselves are fabricated. In the following, the process steps which are needed to fabricate the final samples are described.

### 5.2.1 Novel method for automatized localization of microstructures

The as-grown nanowires are distributed in a random fashion and normal to the substrate surface. For the fabrication of contacts, they have been transferred to another substrate. In the context of this thesis a novel method was developed to locate and contact these nanotubes or other microstructures in a highly automatized manner<sup>1</sup>. The pattern for the individual nanotubes is designed by a software tool with minimal interaction of the user. The user can easily create new layout templates. Using image recognition tools, the positional accuracy of the layout is better than the resolution limit imposed by the optical microscope, typically in the range of 100 nm. The following steps are involved and described in the following:

1. Definition of alignment markers on the target substrate
2. Nanotube transfer
3. Nanotube localization
4. Pattern design and Elecheretron Beam Lithography (EBL)

---

<sup>1</sup>The technological achievement was honored with the NCCR QSIT qstarter Tech Transfer Award 2013 <http://www.qstarter.ch/qstarter-awards-2013>



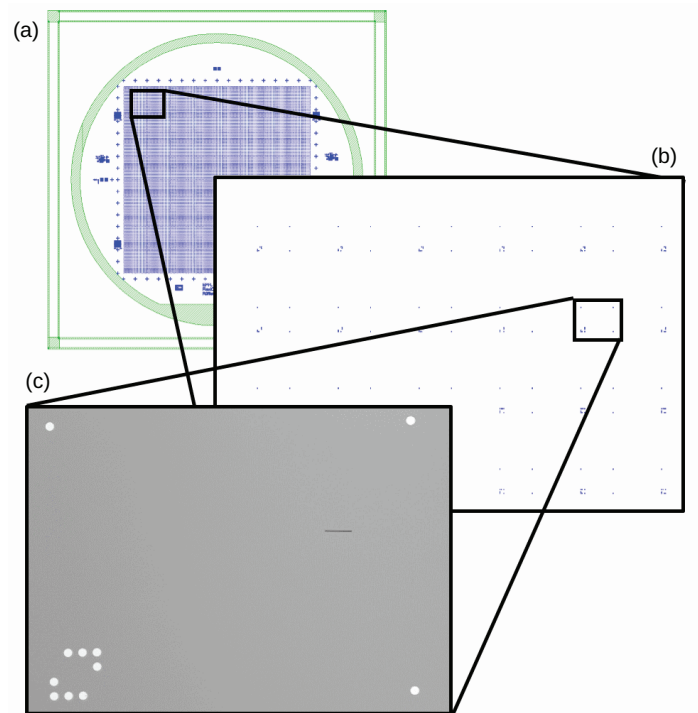


Figure 5.2 – (a) Depiction of the pattern layout for location of nanotubes and other microstructures. (b) Numerous circles are spread over the surface defining cells. (c) In the optical microscopy image a typical cell is shown. The absolute position on the wafer is encoded in the “barcode”-like pattern in the lower left and a local coordinate system defined by the framing circles.

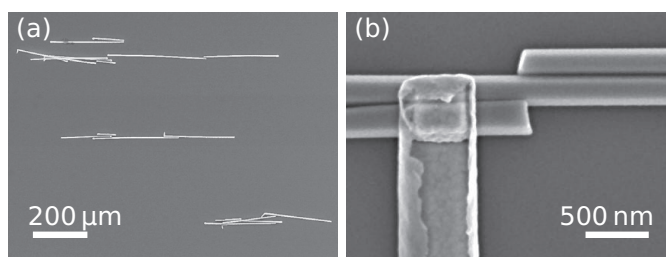


Figure 5.3 – Examples of nanotube (a) bundling and (b) pairing

**1. Alignment markers** A photo-lithography mask was developed for patterning of adequate markers for nanotube localization. As shown in Fig. 5.2, markers are spread over the surface of a 4-inch substrate. The marker geometry has to be chosen such, that the detection of the objects becomes as reliable as possible. Here, we employ circular shapes. The center position of a circle is independent of its diameter. This makes the pattern tolerant against over or underexposure in photo lithography. The absence of sharp edges, as e.g. in rectangles, further facilitates lift-off processes. Moreover, the detection of a circle is comparatively easy using image recognition algorithms. In addition to the circular markers for nanotube localization, the mask comprises square markers for the *Vistec EBPG 5000* electron beam lithography (EBL) tool. More details on the mask layout can be found in App. C.1.

The absolute accuracy of the circle position relative to the EBL markers has to be in the order of or better than the desired precision. During the initial stage of the project it was found that the *Heidelberg DWL-200 Laser Writer* available at CMi, EPFL exhibited a stitching mismatch of up to 1 μm between subsequent stripes. Because this number is far outside the required position accuracy, a process to write photo lithography mask using the *Vistec EBPG 5000* EBL tool has been devised. The process flow is given in App. C.1. Using this mask, the pattern can be transferred to the target substrate by standard photo lithography. Depending on the substrate and the desired future use, the markers can be generated using a lift-off process, leading to positive markers, or by etching, giving rise to negative markers. For both types it is essential that the resulting markers show enough contrast in optical microscopy.

**2. Nanotube transfer** The as-grown ferromagnetic nanotubes are first stripped of the substrate and placed on the target substrate for further processing. For that, the original growth substrate is placed in isopropanol. The nanotubes are released by sonication of the solution, which then can be transferred to the target wafer by, e.g., a pipette. The nanotubes perform Brownian motion within the deposited solution. Upon contact with the surface, the nanotubes attach to the surface at random positions and orientations. In this step, the correct nanotube density in the solution is of importance. Clearly, too low density gives an insufficient amount of tubes for contacting. On the other hand, too high density complicates the design of the surrounding pattern. The presence of too many tubes might render short-free pattern design impossible.

## 5.2. Fabrication of samples for electrical measurements

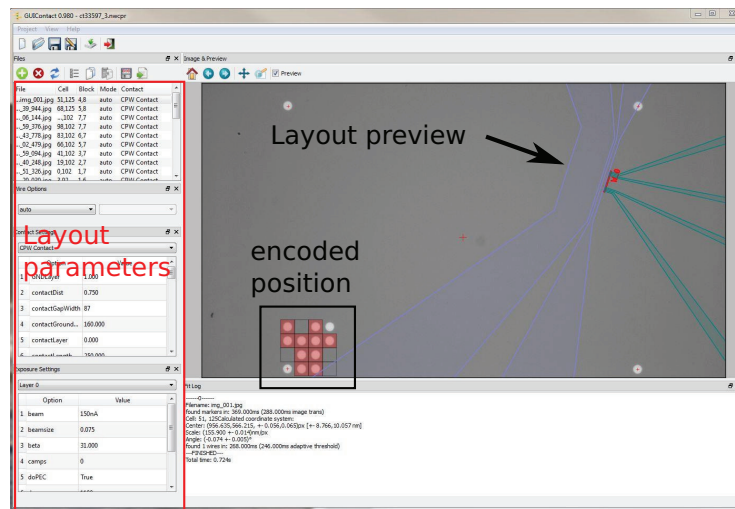


Figure 5.4 – Gaphical User Interface (GUI) of the software tool for automatized nanotube detection and pattern generation

At this point it should be noted that ferromagnetic nanotubes tend to bundle due to their magnetic interaction [Fig. 5.3 (a)]. Another manifestation of the same is the paring of tubes [Fig. 5.3 (b)]. This problem can be mitigated by deploying the solution directly after sonication and by using very low density solution. Furthermore it is advisable to not use solution that has been stored for more than a few weeks.

**3. Nanotube localization** Standard optical microscopes can be used to localize the nanotubes on the target substrate. Currently, the image acquisition step is performed manually, but it could easily be automated in the future. The user scans the wafer surface for nanotubes. A simple image of the nanotube and the surrounding cell is sufficient [Fig. 5.2 (c)]. The developed software tool<sup>2</sup> [Fig. 5.4], locates the nanotubes in the images and determines their position. The framing circles define a coordinate system and the “barcode” like pattern on the lower left encodes the position of this coordinate system relative to the coordinates of the entire wafer. For the detection of the circles, as well as of the nanotubes, algorithms of the open source computer vision (opencv) toolkit<sup>3</sup> are used.

Because the contrast of the circles is usually rather high, the image can be binarized using a simple median threshold. Contours are detected in the binary image with the *findContours* algorithm devised by Suzuki *et al.* [Sb85]. Subsequently, ellipses are fitted to the contour points and circles discriminated by various conditions: first of all, the contour is approximated by a polygon using the Ramer-Douglas-Peucker algorithm [Ram72, DP73]. Rectangular, pentagonal and hexagonal objects are then excluded by the low number of vertices. Also, only a small difference between the principal axes is permitted. Furthermore, the area encircled by the

<sup>2</sup>Developed using the Python, numpy, matplotlib, python-gdsii and PyQt packages.

<sup>3</sup><http://opencv.org/>

contour is compared to the area calculated from the fitted circle radius.

For the nanotube detection, the binarization is performed by an adaptive threshold method. This is necessary to overcome the inevitable brightness gradients in the optical microscopy images. In addition, the tubes exhibit lower contrast than the markers. As before, contours are detected and the minimal area rectangles determined by the *minAreaRect* function which implements Toussaint's rotating calipers algorithm [Tou83]. For discrimination a minimal length and aspect ratio are chosen.

The circles with extremal  $x$ - and  $y$ -coordinates define the cell's coordinate system. Assuming an undistorted image, a set of two markers would be sufficient. In this design, the number was set to four. By averaging over the three independent vectors, the calculation of the coordinate system becomes more accurate by a factor of  $\sqrt{3}$  and more tolerant to fabrication problems. From the standard deviation of the scale and the center position an estimate of the fit quality and thus the expected sample quality can be given. If microscopes with sufficient image quality are utilized, the number could be reduced<sup>4</sup>. This would further improve design flexibility and give more choices of framing during image acquisition.

**4. Pattern design and EBL** The pattern is automatically designed using the two extremal points of the fitted nanotube, relative to the established coordinate system. Multiple different templates can be chosen for the pattern layout. The GUI allows simple modification of important design parameters, such as width etc., and of the EBL tool parameters, such as beam current and dose. Further templates can be easily integrated via a Python plugin file. The software outputs all the files necessary to run an automated EBL run<sup>5</sup>. The layout is stored in the GDS-II data format. All files are compressed and scripts provided to automate pattern fractioning and batch job creation. Currently the software is optimized for use with the *CATS* or the *LayoutBeamer* fractioning software and the *Vistec cjob* job handling software at CMi, EPFL. Using *LayoutBeamer* it is possible to perform *Proximity Effect Correction* (PEC) by beam dose adaption.

### 5.2.2 Fabrication of contacts and rf waveguides

In the course of this thesis, different layouts for electrical experiments on magnetic nanotubes were devised. Scanning Electron Microscopy (SEM) images of typical patterns can be found in Fig. 5.5. All structures were defined by EBL and the detailed process flows are listed in App. C.2.

Typically four or five electrical contacts were fabricated [Fig. 5.5 (a)] for the magnetotransport experiments. The pattern is written into a spin-coated double layer resist. The double layer ensures good lift-off by providing an undercut. The thin films are then deposited by DC

---

<sup>4</sup>Please note that the optical distortion can be calibrated using an array of circles at the edges of the wafer. From a single calibration image a look-up table could be constructed. The feasibility was shown but not yet implemented in the software.

<sup>5</sup>In theory, the same method could be used to use laser writing technology.

## 5.2. Fabrication of samples for electrical measurements

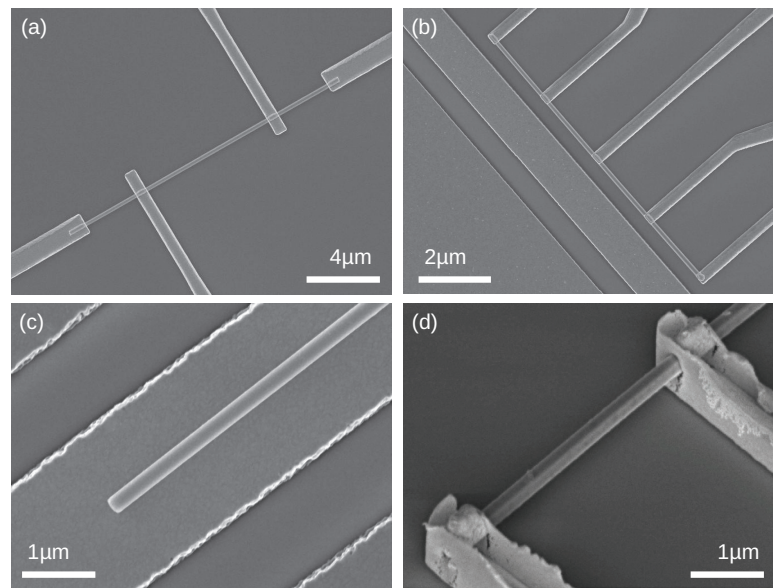


Figure 5.5 – Pattern layouts for electrical contacting of ferromagnetic nanotubes: simple four point contact (a), contacted nanotube with asymmetric co-planar waveguide (CPW) (b) and CPW fabricated below a nanotube (c). The nanotubes can be lifted from the substrate to avoid contact with the substrate (d).

magnetron sputtering with in-situ, pre-deposition rf-etch. Finally, ultra-sound assisted lift-off is performed in acetone. It was found that sputtering yields more reliable contacts with less film thicknesses. In thermal or electron beam evaporation normal to the surface, usually employed for lift-off, shadowing at the nanotube itself can lead to very thin material bridges or even gaps [Fig. 5.6 (a)]. The improved contact of sputtered contacts comes at the cost of significant side walls at the edges [Fig. 5.6 (b)]. In the case of spin wave resonance experiments (cf. Sec. 4.1.5), the electrical contacts were complemented by an asymmetric co-planar wave guide (CPW) [Fig. 5.5 (b)]. In order to avoid the side walls and proximity effects, the wave guide is defined in a secondary EBL step, in which the film for lift-off is deposited via e-beam evaporation.

Two additional designs were realized but did not yet lead to experimental results. The first is a contact-less design for inductive detection of spin wave excitation [ZOI<sup>+</sup>97, KVS<sup>+</sup>04, GPKG05]. As depicted in Fig. 5.5 (c), a symmetric CPW is fabricated below an individual nanotube. For this purpose, the entire wafer is metallized and coated with a thin isolating oxide layer. Following this, negative markers (cf. Sec. 5.2.1) are defined by Ion Beam Etching (IBE). The subsequently deposited nanotubes are located and the CPW layout is designed. Using a negative resist, the entire metallic layer is etched by IBE except for the area defining the CPW.

The second new design features nanotubes lifted from the substrate by the electrical contacts [Fig. 5.5 (d)]. A layer of ebeam resist was spin-coated before the actual nanotube deposition. After coating the usual MMA/PMMA double layer resist on top of this lifting layer, the nanotubes

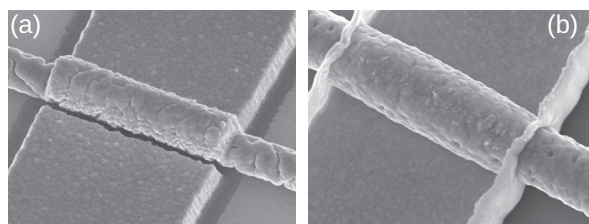


Figure 5.6 – SEM images of Ni tubes contacted by electron beam evaporation (a) and magnetron DC sputtering. Sputtering gives more reliable contacts at the cost of side walls at the edge of the structure.

are completely embedded. The usual ebeam process defines the structure and the contacts are sputter-deposited with appropriate film thickness. After resist stripping, the nanotubes are held by the contacts in a position floating above the substrate.

## **Results & Discussion Part II**





## 6 Characterization of ferromagnetic nanotubes

The chapter is devoted to the characterization of Ni, CoFeB and Py nanotubes prepared in cooperation with partners in Munich. The first two sections have been published in peer-reviewed journals and are reproduced with permission. Section 6.1 presents a magnetotransport study of an individual Ni nanotube at liquid helium temperature. The study is extended to CoFeB tubes and a temperature range from 2 K to room temperature in Sec. 6.2. In Sec. 6.3 magnetotransport experiments on Py tubes are discussed. Sec. 6.4 reports the values of the saturation magnetization which were measured in a collaboration with the Poggio group in Basel. Finally, the results of a study on the magnetization reversal of an individual Ni nanotube in axial field is presented in Sec. 6.5.

### 6.1 Pub. A-I: Magnetic states of an individual Ni nanotube probed by anisotropic magnetoresistance

D. Ruffer, R. Huber, P. Berberich, S. Albert, E. Russo-Averchi, M. Heiss, J. Arbiol, A. Fontcuberta i Morral and D. Grundler

*Nanoscale*, 2012, 4, 4989-4995  
doi: 10.1039/C2NR31086D

*Reproduced by permission of the Royal Society of Chemistry. The paper was reformatted for uniformity and the references integrated into the thesis' bibliography, but otherwise the content remains unchanged.*

I designed the experiment, conducted largely the sample preparation (cf. Sec. 5), coordinated the data acquisition and analyzed the data. I wrote the draft version of the manuscript.

### 6.1.1 Abstract

Defined magnetization states in magnetic nanotubes could be the basic building blocks for future memory elements. Till today, it has been extremely challenging to measure the states at the single-nanotube level. We investigate the magnetization states of an individual Ni nanotube by measuring the anisotropic magnetoresistance effect at cryogenic temperature. Depending on the magnitude and direction of the magnetic field, we program the nanotube to be in a vortex- or onion-like state near remanence.

### 6.1.2 Introduction

Ferromagnetic top-down and bottom-up nanostructures constitute the basic building blocks for future high-density memory elements. They are an alternative to the current planar technology which is expected to face fundamental physical limits in the next few years [TP06]. Three-dimensional architectures based on ferromagnetic nanowires have been proposed to overcome the limits [PHT08]. Especially interesting is the application of nanoscale ferromagnetic materials in magnonic devices [NG09, KDG10]. There, the control and manipulation of spin waves at the nanoscale are expected to offer novel perspectives for data transmission [ITR09] and data processing [KBW10]. At the same time, magnetic nanoparticles and disks are powerful for biological applications, drug delivery, targeted magnetic resonance imaging and magnetothermal treatment of tissue [PCJD03, SRH<sup>+</sup>05, AZM<sup>+</sup>09, KRU<sup>+</sup>10]. Low-dimensional ferromagnetic nanostructures are particularly interesting due to unique magnetic configurations [RKLD<sup>+</sup>01, CnRF<sup>+</sup>03, PGB<sup>+</sup>05, WKN<sup>+</sup>02, TPHG08, VVAE10]. In contrast to nanowires or dots, hollow nanotubes possess three independent geometrical parameters for the control of the magnetic properties via shape anisotropy, i.e., the length  $L$ , the inner radius  $r_i$  and the outer radius  $r_o$ . It has been predicted that the magnetization reversal via vortex wall formation and propagation might be more controlled in nanotubes compared to solid nanowires since in nanotubes the Bloch point structure is avoided [HK04]. Numerous theoretical predictions exist concerning remanent states of an individual ferromagnetic nanotube [EDL<sup>+</sup>07, ELA<sup>+</sup>07, LGSE09, LSCV09, LAE<sup>+</sup>07, LNn10]. So far, however, only large ensembles of nanotubes have been studied experimentally which were fabricated from a ferromagnetic metal [BJK<sup>+</sup>07, DKG07, BEP<sup>+</sup>09, RSK<sup>+</sup>09, CGM<sup>+</sup>10, AZA<sup>+</sup>11, EBJ<sup>+</sup>08, BEH<sup>+</sup>09]. Not only the nanotubes exhibited different diameters, but also a different orientation with respect to the magnetic field  $\mathbf{H}$ . All this led to magnetic hysteresis curves that were difficult to interpret. Recently an individual nanotube of GaMnAs was studied [BRG<sup>+</sup>11]. There, magnetocrystalline anisotropy of the ferromagnetic semiconductor dominated over the shape anisotropy. This does not allow one to address the peculiar magnetic states of a nanotube. In this paper we report an experimental study performed on individual nanotubes that have been fabricated from a metallic ferromagnet. The nanotubes consist of 40 nm thick Ni deposited by Atomic Layer Deposition (ALD) on GaAs nanowires as nano-templates. In particular the nickel film is polycrystalline and does not exhibit magnetocrystalline anisotropy. The use of ALD on self-assembled nanowires enables one to reach unprecedented aspect ratios and thereby

tailor shape anisotropy in magnetic systems. In this study, the nanotubes have a diameter of 150 nm and length of 20  $\mu\text{m}$ . The nanotubes are straight and mechanically robust as they are supported by the insulating GaAs nanowire core. This is an ideal configuration for the integration of electrical contacts and the measurement of the anisotropic magnetoresistance (AMR) effect. The AMR effect is a powerful tool to study the magnetization states of individual nanomagnets as demonstrated on planar nanostripes [HG95] and solid nanowires [WKF<sup>+</sup>99]. Following the theory of AMR in thin metallic films [RCdJdJ95] we discuss a classification of relevant nanotube magnetization states in terms of the relative AMR effect for the first time. This allows us to analyze the magnetization reversal under the two orthogonal orientations of  $H$  parallel and perpendicular to the nanotube axis. For both orientations, segments of the nanowires are found to align their remanent magnetization in azimuthal direction. The magnetoresistance traces for perpendicular field orientation suggest the transition from an onion-like state to a vortex configuration in opposing field.

### 6.1.3 Sample fabrication and thin-film properties

The magnetic nanotubes were fabricated using a two step process. In a first step, GaAs nanowires were grown on a 2" Si(111) substrate using the self-catalyzed growth mode. The growth was performed in a DCA P600 molecular beam epitaxy (MBE) system. Si wafers were used without removing the native oxide before starting the growth. After the axial growth, the mode was switched to planar growth in order to deposit an epitaxial shell of GaAs and thus increase the diameter in a controlled manner. Further details on the nanowire growth can be found elsewhere [UAM<sup>+</sup> 11, RAHM<sup>+</sup> 12]. Finally, the nanowires were coated with roughly 2 nm of aluminum to protect the wires from decomposition at the elevated temperatures needed for the following atomic layer deposition (ALD) of nickel oxide in the second step. For this, the samples were transferred to an ALD vacuum chamber PicoSun Sunale P, where first a 25 nm thick layer of  $\text{Al}_2\text{O}_3$  was deposited [KNN07] using trimethylaluminium and water. This layer of  $\text{Al}_2\text{O}_3$  was conformally grown around the nanowires to isolate the core and prevent arsenic from diffusing into the nickel nanotube. Second, the nanowires were exposed to successive pulses of nickelocene  $\text{NiCp}_2$ , ozone ( $\text{O}_3$ ) and hydrogen ( $\text{H}_2$ ). The substrate was held at 300 ° [HSB<sup>+</sup> 11]. We used 800 cycles to form a 40 nm thick nickeloxide layer which was partially reduced by the hydrogen pulses. To further improve the reduction of nickeloxide to metallic nickel the sample was held at 350 °C for four hours in an hydrogen atmosphere.

The ferromagnetic behavior was studied by ferromagnetic resonance (FMR) measurements at room temperature performed on planar reference films grown in the same ALD process. The FMR data showed a pronounced resonance line varying characteristically with the applied magnetic field [HSB<sup>+</sup> 11]. The FMR data did not depend on the orientation of the in-plane magnetic field. This behavior suggests vanishing magnetocrystalline anisotropy of the ALD-grown Ni. This is attributed to the polycrystalline nature (cf. Sec. 6.1.4) and in contrast to GaMnAs used in Ref. [BRG<sup>+</sup> 11].

AMR measurements on an ALD-grown planar Ni films of 10 nm thickness showed a relative MR effect

$$MR = (\rho_{\parallel} - \rho_{\perp}) / \rho_{\perp} \quad (6.1)$$

of about 0.7% at 4.2 K. Here  $\rho_{\parallel}$  ( $\rho_{\perp}$ ) is the specific resistivity for the device being saturated in the direction of (perpendicular to) the current  $\mathbf{I}$ . In this case,  $\rho_{\perp}$  was taken with  $\mathbf{H}$  being perpendicular to the plane. The shape anisotropy field of plain Ni films amounted to about 0.4 T in perpendicular field [Stu11].

### 6.1.4 Nanotube characterization

#### 6.1.4.1 Structure and composition

We proceed now with the presentation of the structure and composition of the magnetic nanotubes which were grown as a Ni shell on a core consisting of a 150 nm diameter semi-insulating GaAs nanowire. A Scanning Electron Microscopy (SEM) image of a core-shell device is shown in Fig. 6.1 (a). The morphology and conformal nature of the Ni layer is extracted from Fig. 6.1 (b), where a Scanning Transmission Electron Microscopy (STEM) High Angle Annular Dark Field (HAADF) image is shown. We find nickel of average thickness of about 40 nm along the up to 20  $\mu\text{m}$  long GaAs nanowires and around the Ga nanodroplets used to grow the semiconductor cores. The nickel shell is polycrystalline and exhibits some remaining nanotroughs. By SEM investigations we observed that the roughness depended on the diameter of the GaAs nanowires forming the templates for the ALD growth process. The roughness is due to the Ni deposition, as the GaAs nanowires themselves exhibit planar facets with a roughness on the atomic scale [SAG<sup>+</sup>09]. We attribute the formation of nanotroughs to surface tension effects in the hydrogen-based reduction process after the ALD growth. As a consequence, also the roughness of nanotubes and planar reference films are found to differ.

Randomly oriented grain boundaries are expected to exist in the Ni shell. Profiles obtained on the HAADF STEM images provide the expected hexagonal cross-section of the GaAs core [FiMSA<sup>+</sup>08], and a quasi spherical shell. Electron Energy Loss Spectroscopy (EELS) data shown in Fig. 6.1 (e-h) confirm the presence of the Ni at the extremal shell of the nanotube on the GaAs core. Due to the high electron scattering on the Ni shell, it was very difficult to obtain appropriate EELS maps. As seen above, the Ni shell can be clearly mapped by EELS, however Ga and As signals are noisy. In order to assure the core composition, we utilized an individual nanotrough where the shell was locally discontinuous [Fig. fig:SEM (i)]. In this case, one can appreciate on the EELS maps the Ga and As increasing signals on the uncovered area. The EELS profile shown in Fig. 6.1 (j) has been obtained along the red arrow direction.

## 6.1. Pub. A-I: Magnetic states of an individual Ni nanotube probed by AMR

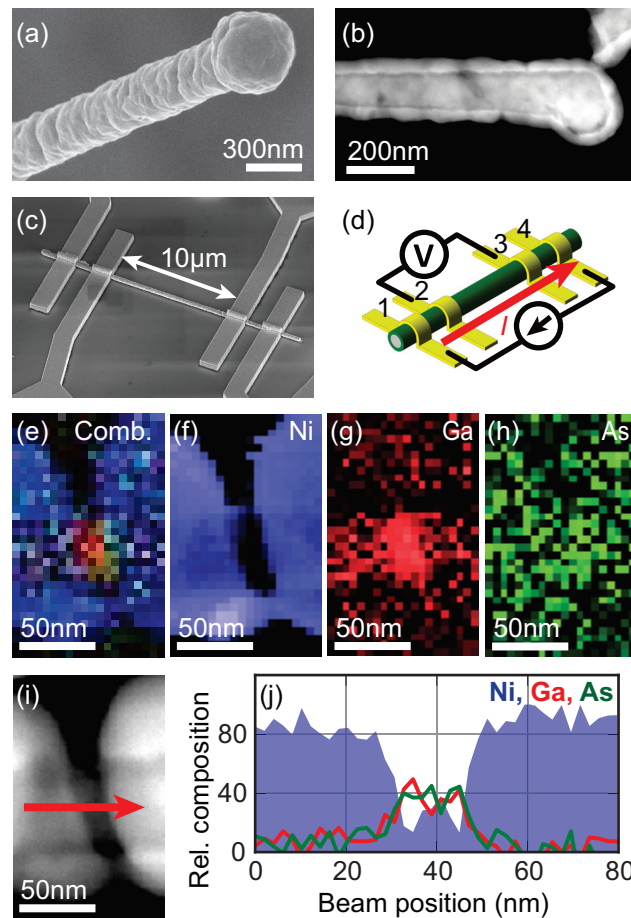


Figure 6.1 – (a) SEM and (b) HAADF STEM images of a magnetic nanotube. We find the nickel to conformally overgrow both the GaAs nanowire and the nanodroplet used for epitaxial growth of the core. (c-d) A Ni nanotube of a length of about  $20\ \mu\text{m}$  contacted by Au leads in a four-point configuration. (e-h) EELS data for the area around a nanotrough (i). The EELS profile (j) was obtained along the red arrow direction.

### 6.1.4.2 Electrical measurements

For the following magnetotransport studies we transferred nanotubes to a silicon wafer covered with 500 nm thick silicon oxide for electrical isolation. Single nanotubes were contacted with four Cr/Au probes using an electron beam lithography based process [Fig. fig:SEM (c)]. To obtain an interface resistance being as low as a few Ohms we cleaned the nickel surface through in situ ion milling before evaporation of the adhesion layer (5 nm thick Cr) and metal film (300 nm thick Au) and lift-off processing. We performed four-point probe measurements of the nanotube resistance by applying the current  $I$  at contacts 1 and 4 and measuring the voltage  $V$  at contacts 2 and 3 [Fig. fig:SEM (d)]. In order to improve the signal-to-noise ratio, we used either a nanovoltmeter and a current source operating in current-reversal mode or a lock-in amplifier to modulate  $I$  and detect phase-sensitively the voltage  $V$ . The current amplitude amounted to  $4\ \mu\text{A}$ . Assuming a shell thickness of 40 nm, this value corresponded to

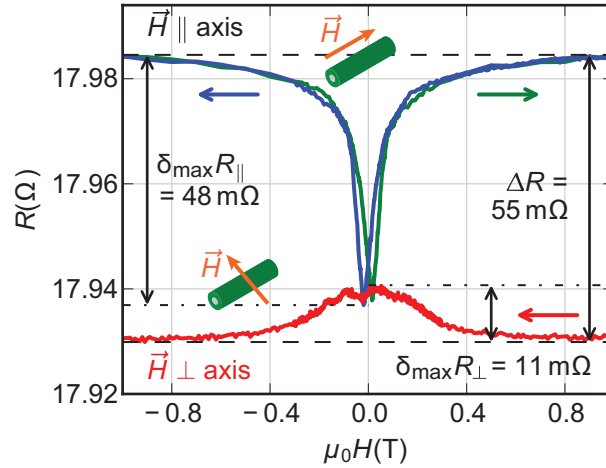


Figure 6.2 – Resistance of a 10  $\mu\text{m}$  long Ni nanotube segment for magnetic field sweeps in positive (green) and negative (blue) direction when  $\mathbf{H}$  is parallel to the long axis (upper curves). The magnetoresistance is hysteretic and positive at large fields. We extract a coercive field of  $\mu_0 H_c \approx 17 \text{ mT}$  from the data. The absolute variation is  $\delta_{\text{max}} R_{\parallel} = 48 \text{ m}\Omega$ . For  $\mathbf{H}$  perpendicular to the long nanotube axis the magnetoresistance is negative to large fields with  $\delta_{\text{max}} R_{\perp} = 11 \text{ m}\Omega$ . Overall the relative AMR effect amounts to  $\Delta R / R_{\perp, \text{min}} = 0.3\%$  in the given Ni nanotube.

a current density of about  $10^4 \text{ A cm}^{-2}$ .

All data presented in the following is taken on one individual tube. Data taken on a further nanowire is presented at the end of section 6.1.5.2. The electrical properties were studied by resistance measurements from room temperature down to 1.6 K. At room temperature the specific resistivity  $\rho$  was about  $(25 \pm 10) \mu\Omega\text{cm}$ . At 1.6 K we obtained  $\rho = (5 \pm 2) \mu\Omega\text{cm}$ . This value is smaller than for the planar Ni nanowires reported by Hong and Giordano [HG95] and substantiates the good quality of the ALD-grown Ni shell.

### 6.1.4.3 Magnetotransport measurements

The magnetic properties were investigated by magnetotransport studies for field orientations parallel and perpendicular to the tube axis. The sample was cooled down to a temperature  $T = 1.6 \text{ K}$  in a cryostat with a superconducting magnet providing an axial field  $\mu_0 H$  of up to 9 Tesla. The sample holder allows us to vary the orientation of the nanotube with respect to  $\mathbf{H}$  at low temperatures. In the course of a sweep, the resistance occasionally increased by an individual jump of 10-15 m $\Omega$ , which neither depended on the magnetic field nor was hysteretic. Such jumps were attributed to resistance changes in nanotroughs through electromigration. The resistance curves were corrected for such occasional effects. The large magnetic field  $\mathbf{H}$  allowed us to saturate the nanotube magnetization  $\mathbf{M}$  under different field orientations. This is a prerequisite to quantify the AMR effect. At the same time the low temperature enables us to be close to the condition  $T = 0$  used for the theoretical predictions.



## 6.1. Pub. A-I: Magnetic states of an individual Ni nanotube probed by AMR

We start by presenting the magnetoresistance and AMR effect for  $\mathbf{H}$  applied parallel to the long nanotube axis. Before applying a magnetic field for the first time, the resistance was measured to be 17.936 m $\Omega$ . Then the magnetic state was saturated in the longitudinal direction by a magnetic field of  $\mu_0 H = -1$  T. Figure 6.2 shows the typical field-dependent behavior  $R(H) = V(H)/I$  vs  $H$  for  $\mu_0 |H| \leq 1$  T. Towards larger fields, the nanotube exhibits a positive magnetoresistance. The resistance does not saturate up to 9 T. The increase of the resistance for  $\mu_0 H > 1$  T is attributed to the well-known Lorentz magnetoresistance [SS68]. To analyze the AMR effect we thus focus on data taken for  $\mu_0 |H| \leq 1$  T. At 1 T, the resistance is  $R_{\parallel, \max} = 17.985 \Omega$ . When decreasing  $\mu_0 H$  from 1 T,  $R$  deviates from  $R_{\parallel, \max}$  over a broad field regime ranging from about  $-0.2$  to  $+0.2$  T. This means that microscopic magnetic moments tilt away from the longitudinal direction, thereby reducing the spin-dependent scattering following: [MP75]

$$\rho(\theta) = \rho_{\perp} + (\rho_{\parallel} - \rho_{\perp}) \cos^2(\theta). \quad (6.2)$$

Here,  $\theta$  is the angle between the direction of current  $\mathbf{I}$  and magnetization  $\mathbf{M}$ . At small field, the magnetoresistance is found to be hysteretic. This means that the magnetization at  $H = 0$  depends on the magnetic history [HG95, RCdJdJ95, WKF<sup>+</sup>99]. We attribute the minima  $R_{\parallel, \min}$  in  $R_{\parallel}(H)$  to the coercive field amounting to  $\mu_0 |H_c| \approx 17$  mT. The maximum resistance change is found to be  $\delta_{\max} R_{\parallel} = R_{\parallel, \max} - R_{\parallel, \min} = (48 \pm 2)$  m $\Omega$  in Fig. 6.2. In minor loop measurements (not shown) the resistance is found to remain constant and non-hysteretic, if we stay with  $H$  in the regime  $\mu_0 |H| \lesssim 15$  mT. Increasing the reversal field beyond 15 mT we regain hysteretic behavior in  $R(H)$ . The hysteretic behavior and the minor loop measurements suggest an incoherent reversal mode of the nanotube.

Before we analyze the data in the parallel field configuration in more detail it is instructive to discuss the magnetoresistive behavior in perpendicular field. For this, we turn the direction of the sample in the cryostat at low temperatures and zero field after saturation at -1 T. The typical magnetoresistive behavior is shown in Fig. 6.2 (bottom curve). Starting from  $H = 0$ ,  $R(H)$  is found to decrease by  $\delta_{\max} R_{\perp} = (11 \pm 2)$  m $\Omega$  up to  $\mu_0 H = 1$  T. The magnetoresistance is thus negative. It exhibits a relatively steep slope  $R$  vs  $H$  for  $\mu_0 |H| \leq 0.4$  T. We attribute the field value of 0.4 T to the shape anisotropy field  $H_{\text{ani}}$ . For  $|H| > H_{\text{ani}}$ , the magnetization  $\mathbf{M}$  of the device becomes aligned with  $\mathbf{H}$  so that  $\mathbf{M}$  is perpendicular to the applied current  $\mathbf{I}$ . As a consequence,  $R_{\perp}$  takes a minimum of  $R_{\perp, \min} = 17.930 \Omega$  at 1 T. The overall resistance change  $\delta_{\max} R_{\perp} = (11 \pm 2)$  m $\Omega$  is significantly smaller than  $\delta_{\max} R_{\parallel} = (48 \pm 2)$  m $\Omega$  observed for parallel fields. Considering the resistance data from Fig. 6.2 we calculate the maximum relative AMR effect to be

$$\Delta R / R_{\perp, \min} = \frac{R_{\parallel, \max} - R_{\perp, \min}}{R_{\perp, \min}} = 0.3\%. \quad (6.3)$$

This is a reasonable value compared to the AMR effect observed on the ALD-grown planar Ni films. It is a factor of about two smaller. We attribute this discrepancy to the nanotroughs observed in Fig. 6.1. They locally reduce the cross section of the nanotube. In contrast to the thin film, the current might not be able to percolate around the nanotroughs. The series

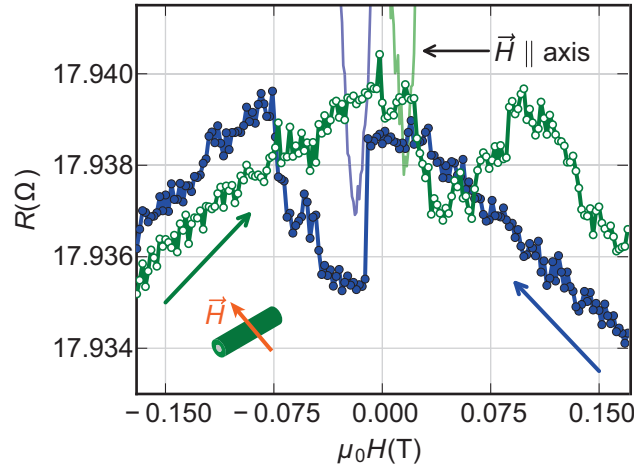


Figure 6.3 – Magnetoresistance data (symbols) for field sweeps between  $-0.17$  and  $+0.17$  T when  $H$  is perpendicular to the nanotube: Blue filled (green open) symbols show a sweep of  $H$  in negative (positive) direction. For clarity symbols are interconnected by lines. The nanotube exhibits an overall decrease of  $R$  for increasing fields and characteristic local minima at small opposing fields in the range of  $0.010\text{ T} \lesssim |\mu_0 H| \lesssim 0.075\text{ T}$ . For comparison, the lines show the major loop data presented in Fig. 6.2 for  $H \parallel$  axis. Large arrows indicate sweep directions of  $H$ .

of nanotroughs increases the specific resistivity which enters the denominator of Eq. 6.3 via  $R_{\perp, \min}$  and thereby reduces the overall MR value.

Interestingly,  $R$  is hysteretic in perpendicular fields as well. Figure 6.3 shows field-dependent data (symbols) taken in minor loops between  $-0.17$  and  $+0.17$  T where  $H$  was varied in small increments of 1 mT. For both sweep directions, field regions are found where  $R$  takes a local minimum. Coming from, e.g.,  $+0.17$  T and going to negative fields the resistance is found to drop abruptly by almost 3 m $\Omega$  at  $-0.010$  T. It remains small until  $-0.075$  T where  $R$  regains a large value within a range of a few mT. Note that the absolute value of the local minimum is larger than  $R_{\perp, \min}$  at  $\mu_0 H = 1$  T. For further decreasing field,  $R$  follows the negative magnetoresistance already seen in Fig. 6.2. The drop and local minimum in  $R$  for small opposing fields are reproducible features for successive field sweeps. Depending on the exact reversal field the relevant field region is found to vary slightly.

## 6.1.5 Discussion

### 6.1.5.1 AMR effect in nanotubes: development of a classification scheme

We start by introducing the well-known characteristics of the AMR effect in planar thin films and discuss what should be expected in a nanotube configuration. For the AMR effect, the angle  $\theta$  between the direction of current  $\mathbf{I}$  and magnetization  $\mathbf{M}$  is decisive. The specific resistivity  $\rho$  varies due to spin-dependent scattering provoked by spin-orbit coupling. In a ferromagnetic bulk material the field-dependent resistivity follows Eq. 6.2.



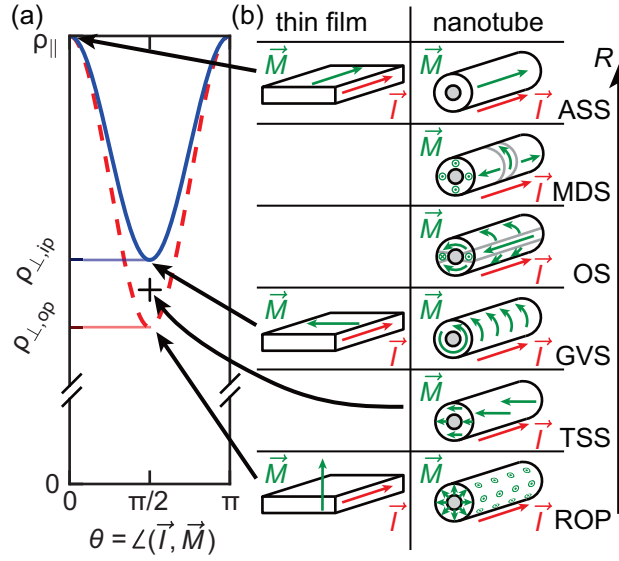


Figure 6.4 – (a) Theoretical variation of the specific resistivity  $\rho$  of a thin film as a function of the angle between  $\mathbf{I}$  and  $\mathbf{M}$  for rotation of  $\mathbf{M}$  in plane (blue, solid) and out-of-plane (red, dashed) [after Rijks *et al.* [RCdJdJ95]]. (b) Relevant magnetic states in the thin film (left) compared to configurations in a nanotube (right) as discussed in the text. Configurations are ordered such that the resistance increases from bottom to top. Arrows indicate the orientations of magnetic moments and current. The semiconductor core is gray.

Because  $\rho_{\parallel} > \rho_{\perp}$  in Ni,  $\rho$  is expected to be at maximum when  $\mathbf{I}$  and  $\mathbf{M}$  are collinear. It is at a minimum when the magnetization is perpendicular to the current. Rijks *et al.* [RCdJdJ95] showed that the relative magnetoresistance (MR) effect is modified by boundary scattering in a planar thin film. As a function of  $\theta$  they find a different behavior for  $\mathbf{M}$  staying in the film plane or pointing perpendicular to the film boundary. The qualitative behavior  $R(\theta)$  is sketched in Fig. 6.4 (a) as extracted from Ref. [RCdJdJ95]. In Fig. 6.4 (b) we illustrate the magnetic states of the thin film (left) at characteristic points of the  $R(\theta)$  dependencies. We will show that they allow us to classify the magnetic states of the nanotube (right). For the thin film, the largest resistance occurs when the magnetization is collinear with the current, resulting in  $\rho = \max(\rho) = \rho_{\parallel}$ . Now, if we compare the resistivity in the case where  $\mathbf{M}$  is in-plane ( $\rho = \rho_{\perp,ip}$ ) or out-of-plane ( $\rho = \rho_{\perp,op}$ ), the smallest resistance is achieved for an out-of-plane magnetization, due to the modified boundary scattering. Such a discrepancy does not occur in Eq. 6.2 for bulk materials where boundary scattering is not relevant. According to Rijks *et al.* [RCdJdJ95], a measurable difference between in-plane and out-of-plane AMR ratios is present for film thicknesses below a critical value  $t_c$  of approximately 100 nm.

We now turn to the discussion of the nanotube, for which we consider the current to be always parallel to the long nanotube axis. The shell thickness is about 40 nm and smaller than  $t_c$ . We thus attribute the MR behavior of the nanotube to the effect which was elaborated by Rijks *et al.* As in the thin film case, the maximum resistance is achieved when the magnetization is parallel to the current. We call this the axially-saturated state (ASS). Figure 6.4 would suggest the same

resistivity for the nanotube and the thin film. Interestingly, the minimum resistivity  $\rho_{\perp,op}$  obtained for the thin film would correspond to a state of the nanotube where the magnetic moments obey a radially aligned out-of-plane configuration (ROP). Such a state [bottom-most graph in Fig. 6.4 (b)] might be created by a tailored magnetocrystalline or interfacial anisotropy. For a nanotube prepared from an isotropic ferromagnet as considered here, the minimum resistivity state of Fig. 6.4 (a) can not be achieved. For such a nanotube, the lowest resistivity is obtained in a transversally-saturated state (TSS), where all magnetic moments are aligned along a direction perpendicular to the long nanotube axis. Such a configuration is attained at large magnetic fields. Here, it is interesting to note that due to the curved surface, only a small portion of the moments point perpendicularly to the nanotube surface. The relevant resistivity falls between  $\rho_{\perp,ip}$  and  $\rho_{\perp,op}$  and is marked with a cross in Fig. 6.4 (a). We now consider the intermediate magnetization states between ASS and TSS. Slightly above the resistivity of the TSS, we find the global vortex state (GVS), in which the moments follow the circumference of the nanotube and are aligned in azimuthal direction. Such a state has been predicted to occur in equilibrium for nanotubes above a certain diameter [LSCV09]. The resistivity of the global vortex state coincides with the resistivity  $\rho_{\perp,ip}$  of the thin film.

In close analogy to the onion-state (OS) in ferromagnetic ring structures [RKLD<sup>+</sup>01, CnRF<sup>+</sup>03, PGB<sup>+</sup>05], we propose the existence of a comparable state in magnetic nanotubes. Here, the two halves of the nanotube exhibit parallel magnetic moments being aligned in azimuthal direction. The two halves are separated by domain walls. To minimize the stray field energy the moments in the domain walls are expected to align with the long axis and in opposite direction for both domains. With this, the overall resistivity will increase according to Eq. 6.2. The resistivity of OS is thus expected to be larger compared to GVS [Fig. 6.4 (b)]. For the vortex state in an individual permalloy ring, a higher resistance compared to the onion state was observed [PGB<sup>+</sup>05]. This was due to the orientation of the current which was in the plane of the magnetic moments. In contrast, the current is perpendicular to the moments in our nanotube, leading to the opposite behavior in  $R(H)$ .

At an even higher resistivity but still below the ASS, we classify the multi-domain state (MDS) formed by a series of domains in the ASS configuration of opposite directions separated domain walls. Domain walls might be in a TSS- or GVS-like configuration [LAE<sup>+</sup>07].

### 6.1.5.2 Magnetic states assigned to measured resistance values

We turn now to the discussion of magnetic states observed with the magnetic field applied in a direction parallel or perpendicular to the long nanotube axis. We use the classification developed in Fig. 6.4 to attribute magnetic states to the measured resistance values as sketched in Fig. 6.5. Experimentally, we obtain the lowest resistance in the magnetic nanotube when we generate the transversely saturated state (TSS) by applying  $\mu_0 H = 1 \text{ T} > \mu_0 H_{ani}$  in a direction perpendicular to the long axis [Fig. 6.2]. When reducing the magnetic field, the TSS is found to be unstable. The demagnetization field is largest where the surface normal is parallel to the external magnetic field. At these points, the magnetic moments tilt away from the field

## 6.1. Pub. A-I: Magnetic states of an individual Ni nanotube probed by AMR

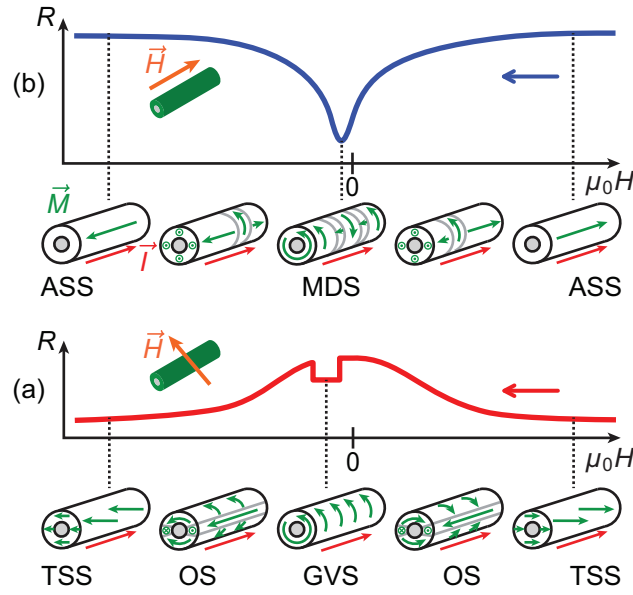


Figure 6.5 – Magnetic states schematically attributed to characteristic resistance values in (a) a perpendicular and (b) a parallel magnetic field.

direction if  $H < H_{\text{ani}}$  and form head-to-head or tail-to-tail domain walls. To minimize the stray-field energy, moments will most likely turn into an axial direction, provoke a domain wall and form the OS [Fig. 6.5 (a)]. The domain walls exhibit  $\rho_{\parallel} > \rho_{\perp, \text{ip}}$ . By this, we explain the gradual increase in  $R$  when reducing  $H$  in the perpendicular field direction. As a stable configuration at  $H = 0$ , we propose the OS. The increased value of  $R$  at  $H = 0$  depends on the total width of segments with  $\rho_{\parallel} > \rho_{\perp, \text{ip}}$ . The overall specific resistivity is certainly larger than  $\rho = \rho_{\perp, \text{ip}}$ . In an opposing magnetic field, large parts of the nanotube are expected to switch irreversibly and form a GVS. In the vortex state, the small specific resistivity  $\rho_{\perp, \text{ip}}$  is realized around the nanotube. Following this argument, we attribute the abrupt jump of reduced  $R$  in Fig. 6.3 to the creation of the GVS [Fig. 6.5 (a)]. This state is stable for a small field region and has a resistance which is between the one of TSS and OS at  $H = 0$ . At a field of  $\mu_0 |H| \approx 0.075$  T, the energy attributed to the misalignment of the spins in the external field will be higher than the energy gain due to the flux-closure configuration. At this field, the configuration changes abruptly back to the OS with nanotube halves being aligned in the negative field direction.

It is now interesting to address the reversal in a field  $H$  applied parallel to the long axis. In Fig. 6.2 and 6.3 we observe that  $R(H_C)$  is almost as small as the resistance of the vortex-like state discussed above. Comparing  $\delta_{\text{max}} R_{\parallel} = 48$  m $\Omega$  from Fig. 6.2 with the maximum absolute change  $\Delta R = 59$  m $\Omega$ , we calculate the relative amount of magnetic moments being perpendicular to  $\mathbf{I}$  during reversal to be 87 % of the total magnetization. In Ref. [LAE<sup>+</sup>07] the reversal mechanism was investigated theoretically assuming an ideal nanotube without surface roughness. For the geometrical parameters realized by our nanotubes, the authors predicted an *abrupt* reversal to occur via a single vortex wall. In the real nanotube, we find the resistance to change *gradually* with  $H$  in a wide field region. At this point we can not decide whether the reversal occurs

via a global vortex state or segments of vortex-like domain walls (vortex walls) separated by ASS domains. The scenario of vortex walls sketched in Fig. 6.5 (b) seems to be more likely considering the surface roughness of our nanotubes. Vortex walls might enter the nanotube in a sequential manner and thereby explain the wide field region where  $R$  deviates from  $R_{\parallel, \max}$ . The gradual change of  $R$  implies the creation, movement and pinning of a large number of vortex walls where locally  $\mathbf{M}$  is perpendicular to  $\mathbf{I}$ . The minimum resistance  $R_{\parallel, \min}$  is achieved at  $H = H_c$  when the maximum number of domain walls reside between the voltage probes.

In the scenarios discussed above, the *absolute* resistance changes  $\Delta R$  between ASS and TSS as well as  $\delta_{\max} R_{\perp}$  between VS and TSS should depend little on the exact number of nanotroughs. In contrast, we expect  $\delta_{\max} R_{\parallel}$  to depend on the number of nanotroughs serving as pinning sites. Magnetotransport experiments performed on a further nanotube with similar geometrical parameters provided the following data at 4 K:  $\Delta R = 51 \text{ m}\Omega$ ,  $\delta_{\max} R_{\perp} = 12 \text{ m}\Omega$ , and  $\delta_{\max} R_{\parallel} = 22 \text{ m}\Omega$ . The number of nanotroughs and their microscopic shape were different compared to the device of Fig. 6.2. However, only the value  $\delta_{\max} R_{\parallel}$  deviated substantially (by a factor of 2) from values obtained on the nanotube presented above. This is consistent with the argument that we expect nanotroughs to change mainly  $\delta_{\max} R_{\parallel}$ .

### 6.1.6 Conclusion

We have discussed magnetotransport experiments performed on individual ferromagnetic nanotubes. For parallel field orientation, the vortex wall reversal mode predicted by theoretical studies seems to be consistent with the anisotropic magnetoresistance data. The reversal occurs in segments in a sequential manner. For a magnetic field applied perpendicular to the long axis we suggest onion and vortex states to form in the reversal. This field geometry has not been considered theoretically before. In this work, we have developed a classification scheme for magnetic states of nanotubes which is derived from the AMR effect known for planar films. This scheme allows one to relate resistance changes to different magnetic states. For memory applications, it would be extremely important to control all the different magnetization configurations depending on the magnitude and orientation of the magnetic field applied. Interestingly, both, the ROP and GVS lead to zero magnetization but significantly different stray field. In the GVS the stray field is zero, avoiding magnetostatic interaction between memory elements.

**Acknowledgement** The authors kindly thank Kornelius Nielsch, Julien Bachmann and Tobias Stückler for discussions and experimental support. The research leading to these results has received funding from the European Community's Seventh Framework Programme (FP7/2007-2013) under Grant Agreement No. 228673 MAGNONICS. DR, MH, ER and AFM acknowledge financial support from the NCCR QSIT, ERC 'Upcon' and the School of Basic Sciences at Ecole Polytechnique Federale de Lausanne. This work was supported by the Spanish MICINN Projects MAT2010-15138 and CSD2009-00013. J. A. also acknowledge Generalitat de Catalunya 2009-SGR-770 and XarMAE.

## 6.2 Pub. A-II: Anisotropic magnetoresistance of individual CoFeB and Ni nanotubes with values of up to 1.4% at room temperature

D. Ruffer, M. Slot, R. Huber, T. Schwarze, F. Heimbach, G. Tütüncüoğlu, F. Matteini, E. Russo-Averchi, A. Kovács, R. Dunin-Borkowski, R. R. Zamani, J. R. Morante, J. Arbiol, A. Fontcuberta i Morral, and D. Grundler

*APL Materials* 2, 076112 (2014)

doi: 10.1063/1.4891276

*Reproduced with permission from APL Materials 2, 076112 (2014). Copyright 2014, AIP Publishing LLC. The paper was reformatted for uniformity and the references integrated into the thesis' bibliography, but otherwise the content remains unchanged.*

I designed the experiment, conducted largely the sample preparation (cf. Sec. 5), coordinated the data acquisition and analyzed the data. The magnetotransport measurements were performed by the Master student Marlou Slot, supervised by myself. I wrote the draft version of the manuscript.

### 6.2.1 Abstract

Magnetic nanotubes (NTs) are interesting for magnetic memory and magnonic applications. We report magnetotransport experiments on individual 10 to 20  $\mu\text{m}$  long Ni and CoFeB NTs with outer diameters ranging from 160 to 390 nm and film thicknesses of 20 to 40 nm. The anisotropic magnetoresistance (AMR) effect studied from 2 K to room temperature (RT) amounted to 1.4 and 0.1% for Ni and CoFeB NTs, respectively, at RT. We evaluated magnetometric demagnetization factors of about 0.7 for Ni and CoFeB NTs having considerably different saturation magnetization. The relatively large AMR value of the Ni nanotubes is promising for RT spintronic applications. The large saturation magnetization of CoFeB is useful in different fields such as magnonics and scanning probe microscopy using nanotubes as magnetic tips.

### 6.2.2 Main

Ferromagnetic nanostructures with tubular shape are fascinating objects for fundamental research as well as for applications. Due to their hollow structure, theory predicts the existence of Bloch-point free vortex states and domain walls [ELA<sup>+</sup>07, LAE<sup>+</sup>07, LGSE09]. The motion of vortex domain walls in nanotubes is expected to occur at very high velocities [LNn10, YAK<sup>+</sup>11], possibly fast enough to generate a Cherenkov-type spin wave exci-

tation [YKAH13]. Such magnetic properties and high velocities could be beneficial in future low-power and high-speed memory applications [PHT08]. For this, polycrystalline or even better amorphous materials, being soft-magnetic and magnetically isotropic, represent a very promising basis. While soft-magnetic behavior allows for mobile domain-walls, isotropic magnetic properties are key for the formation of the characteristic magnetic states predicted for tubes. Molecular beam epitaxy and epitaxial growth as reported for GaMnAs, MnAs and Fe<sub>3</sub>Si nanotubes recently [HTH<sup>+</sup>09, RSK<sup>+</sup>09, YWP<sup>+</sup>13] introduce however magnetocrystalline anisotropy. Magnetron sputtering as a technologically relevant deposition technique has not been reported for the fabrication of magnetic nanotubes yet. Instead ferromagnetic nanotubes were first fabricated by electrodeposition into nanoporous membranes [TPLL00, BTX<sup>+</sup>01]. Various other methods were developed such as hydrogen reduction of porous alumina templates preloaded with metallic salts [SSSS04] or decomposition of polymers containing a metallo-organic precursor wetting such templates [NCRK05]. Different deposition techniques including atomic layer deposition (ALD) were employed to fabricate tubes in nanopores [DKGN07, BJK<sup>+</sup>07] or as shells onto semiconductor nanowires [DKGN07, HTH<sup>+</sup>09, DLC<sup>+</sup>10, HHJ<sup>+</sup>13]. Early magnetic characterization was restricted to large ensembles of nanotubes. In the last years, the investigation of individual nanotubes became technologically feasible [ZLH<sup>+</sup>04, LWP<sup>+</sup>12, RHB<sup>+</sup>12, WRB<sup>+</sup>12, BNR<sup>+</sup>13, BRR<sup>+</sup>13]. The role of both magnetocrystalline [LWP<sup>+</sup>12, BRR<sup>+</sup>13] and shape anisotropy [HHJ<sup>+</sup>13] has been discussed but the relevant magnetometric demagnetization factor for individual nanotubes has not yet been addressed. For Ni nanotubes anisotropic magnetoresistance (AMR) data presented recently revealed a technologically unfavourable relative AMR effect of only 0.3% at 4 K [RHB<sup>+</sup>12]. Here we report on the structural characterization of polycrystalline Ni and amorphous CoFeB nanotubes. Studying their AMR over a broad temperature range we obtain a large relative effect of up to 1.4% for the Ni nanotubes at room temperature. For both types of nanotubes we evaluate a consistent magnetometric demagnetization factor  $N_{\perp}$  of about 0.7. Thereby we account for the different fields  $H_d$  needed to saturate the Ni and CoFeB nanotubes in transverse ( $\perp$ ) direction. Correspondingly the magnetic anisotropy is argued to be dominated by the shape. Large room-temperature AMR values are interesting if one thinks about e.g. sensor applications or transport studies on magnetic configurations predicted for nanotubes [ELA<sup>+</sup>07, LAE<sup>+</sup>07, LGSE09]. The nanotubes from CoFeB are expected to advance both nanomagnonics and magnetic sensing. Their large saturation magnetization favors fast spin dynamics [YHS<sup>+</sup>12] and provides one with large stray fields from nanoscopic tips, respectively, helping to improve magnetic microscopy [NBX<sup>+</sup>13].

Magnetic nanotubes were fabricated from either Ni or CoFeB by depositing the ferromagnetic shells around bottom-up grown GaAs nanowires [UAM<sup>+</sup>11, RAHM<sup>+</sup>12]. The nanowires, which were grown using Ga droplets as catalysts, had lengths between about 10 and 20  $\mu\text{m}$ . Their diameters ranged from 100 to 150 nm [UAM<sup>+</sup>11, RAHM<sup>+</sup>12]. A list of relevant geometrical parameters is given in the table in the supplementary information (cf. Suppl. Inf., Sec. A.1). The Ni was deposited by ALD [RHB<sup>+</sup>12, BNR<sup>+</sup>13], while the CoFeB was obtained by magnetron sputtering using Xenon gas at room temperature [YHS<sup>+</sup>12]. In the ALD process we



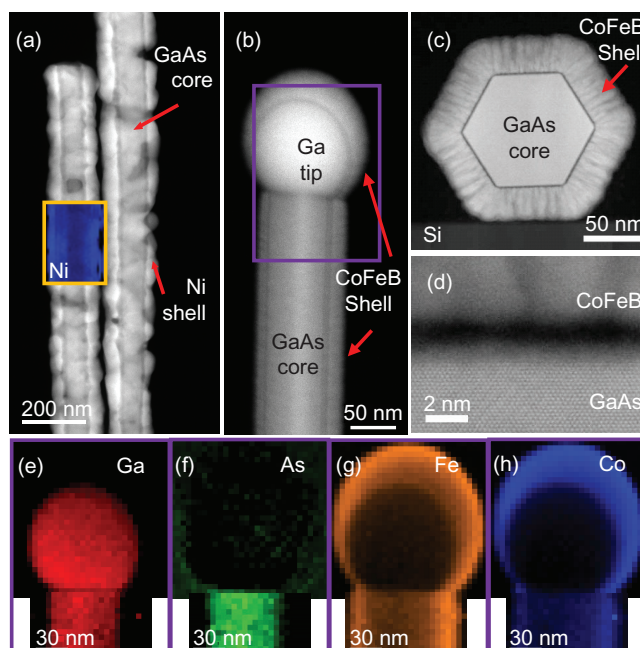


Figure 6.6 – (a) Low-magnification ADF STEM image of Ni nanotubes, the inset shows an EELS Ni map obtained on the same region of the tube. (b) ADF STEM image of one of the CoFeB nanotubes covering the GaAs nanowire template as well as the Ga tip used for bottom-up growth. (c) Cross-section ADF STEM view showing the hexagonal prismatic morphology of the GaAs core template and the CoFeB nanotube shell. (d) Atomic resolution ADF STEM image showing the crystallinity of the GaAs and the amorphous CoFeB shell. The CoFeB shows a columnar morphology. The inner ADF detector semi-angle used was 78 mrad. (e)-(h) EELS chemical maps corresponding to Ga, As, Fe and Co, respectively, obtained on the squared region in (b).

intentionally produced an intermediate  $\text{Al}_2\text{O}_3$  layer in order to vary the inner diameter of the supporting core before depositing the ferromagnetic shell. For magnetron sputtering of CoFeB we mounted the Si (111) substrate containing the GaAs nanowires on a rotatable sample holder facing a  $\text{Co}_{20}\text{Fe}_{60}\text{B}_{20}$  (CoFeB) target that was positioned under an angle of  $35^\circ$  with respect to the substrate normal. Intentionally choosing ensembles of nanowires with rather large nanowire-to-nanowire separation, the substrate rotation allowed us to obtain nanotubes showing homogeneously thick CoFeB shells.

Annular Dark Field (ADF) Scanning Transmission Electron Microscopy (STEM) images were obtained in order to determine the morphology and thicknesses of the Ni [Fig. 6.6 (a)] and CoFeB shells [Fig. 6.6 (b-c)]. The Ni shells were found to exhibit a surface roughness with peak-to-peak values of about 10 nm [RHB<sup>+</sup> 12, BNR<sup>+</sup> 13]. The magnetron-sputtered CoFeB shells were much smoother. Atomic-resolution ADF STEM analyses as those presented in Fig. 6.6 (d) evidenced a zinc-blende structure of the GaAs core that grew along one of the [111]B directions as demonstrated recently [UAM<sup>+</sup> 11, dIMMG<sup>+</sup> 12]. Cross sections of the core/shell systems were prepared by means of Focused Ion Beam showing that the hexagonal cross-section of

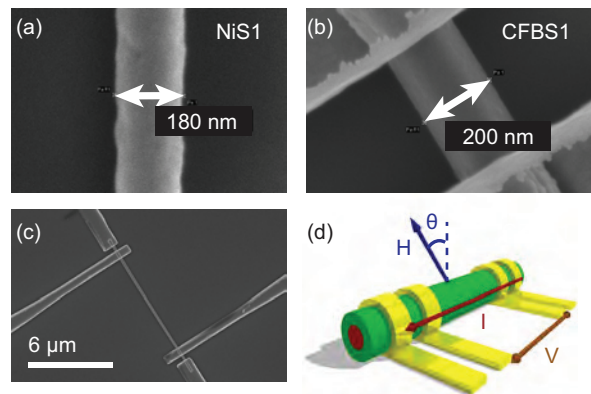


Figure 6.7 – Scanning electron microscopy images of a small segment of sample (a) NiSi and (b) CFBS1. (c) Overview of sample CFBS1 with electrical contacts. (d) Measurement configuration.

the core was transferred to the CoFeB shell [Fig. 6.6 (c)]. This was not observed for the Ni shells due to the larger surface roughness [RHB<sup>+</sup> 12, BNR<sup>+</sup> 13] [Fig. 6.6 (a)]. The Ni consisted of grains being ellipsoids with a long (short) axis of roughly 30 nm (10 nm). The conformal CoFeB shell appeared instead amorphous. The amorphous structure is provoked by adding B to the CoFe alloy [HKM<sup>+</sup> 08]. The columnar structure seen in Fig. 6.6 (d) is attributed to local variations in the density of the material. These might be caused by directional deposition on the rotating nanowires. This peculiar feature is under further investigation. Electron Energy Loss Spectroscopy (EELS) spectrum images were obtained in STEM mode in order to study the composition. The nanowire cores are composed of GaAs. Shells are shown to be Ni rich in the inset of Fig. 6.6 (a) and Fe and Co rich in Fig. 6.6 (g) and (h), respectively. EELS analyses performed on the CoFeB shell provided a relative composition of Fe 77% (at. %), Co 20%, and Xe 3%. Note that the content of B could not be obtained as the energy range of the B in the EELS spectra falls far from the Fe and Co signal. The upper bound for the oxygen content in the shell is determined to be 2%. The values are consistent with energy dispersive x-ray analysis performed on planar films [YHS<sup>+</sup> 12]. Remarkably, the catalyst seed for nanowire growth is composed of pure Ga covered with a slight thin shell containing As. The CoFeB layer coats the seed as well. In contrast to Refs. [DLC<sup>+</sup> 10, LWP<sup>+</sup> 12, HHJ<sup>+</sup> 13] we do not find an epitaxial relationship between the magnetic shells and the semiconductor cores. For polycrystalline Ni and amorphous CoFeB [YHS<sup>+</sup> 12, SG13] prepared on planar substrates a magnetocrystalline anisotropy was not observed.

The core/shell systems were released in isopropanol using sonication and transferred to Si wafers covered with 200 nm thick silicon oxide. The absolute position of nanotubes was determined using prepatterned gold alignment markers, optical microscopy and an in-house developed software for image recognition<sup>1</sup>. In-situ plasma etching was performed before sputtering electrical contacts from 5 nm thick titanium and 150 nm thick gold [Fig. 6.7 (b)]. The

<sup>1</sup><http://www.qstarter.ch/projects/automated-contacting-of-random-microstructures>



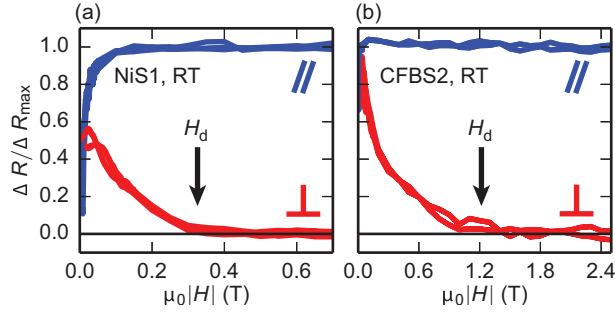


Figure 6.8 – Normalized resistance change  $\Delta R(H)/\Delta R_{\max}$  as a function of  $|H|$  for sample (a) NiS1 and (b) CFBS2 at room temperature. Magnetic field sweeps in both directions and field polarities are shown for field parallel (top) and perpendicular (bottom) to the long axis. We define  $H_d$  as the field at which most of the magnetization saturates and  $\Delta R(H)/\Delta R_{\max}$  is smaller than the noise level. For CFBS2, the saturation occurs at very small fields for the parallel field configuration.

separation between voltage probes  $L_{\text{contact}}$  [Fig. 6.7 (c)] was varied between 6.5 and 13.2  $\mu\text{m}$  depending on the investigated nanotube. The Ni nanotubes have a thickness of 40 nm (NiL1, NiL2) and 20 nm (NiM). By inserting an  $\text{Al}_2\text{O}_3$  layer between the ferromagnetic shell and the GaAs core, we achieved different outer diameters of about 350 nm (large, 'L') and 220 nm (middle, 'M'). The CoFeB nanotubes considered here have thicknesses of 30 nm (CFBM1, CFBM2) and 20 nm (CFBS1, CFBS2) where 'S' (small) indicates an outer diameter of about 180 nm. The CoFeB nanotubes stick to the substrate with one of their side facets.

Magnetotransport experiments were performed on wire-bonded samples mounted on a rotatable stage in a bath cryostat with a superconducting magnet providing a magnetic field  $\mu_0 H$  of up to 9 T. The resistance  $R(H, \theta)$  as a function of the magnetic field and the rotation angle  $\theta$  was measured in a four-point-probe configuration [Fig. 6.7 (d)] using a nanovoltmeter in combination with a programmable current source and a three-step current operated at 25 Hz to compensate for thermovoltages. The data from the bath cryostat were corrected for thermal drifts and the field dependent characteristics of the temperature sensor. To compare different nanotubes when rotating a fixed field  $H$ , we consider the relative resistance change  $\Delta R(\theta) = (R(\theta) - \min(R)) / \min(R)$  where  $\min(R)$  is the minimum resistance value. The AMR ratio is defined as  $\text{AMR} = \frac{R_{\parallel} - R_{\perp}}{R_{\perp}}$  where  $R_{\parallel}$  and  $R_{\perp}$  are the absolute maximum ( $\max(R)$ ) and minimum ( $\min(R)$ ) resistance values for a magnetic field  $H$  being parallel and perpendicular, respectively, to the current  $I$  and being larger than the field  $H_d$  at which most parts of the magnetization saturate [APK00]. Furthermore we utilize the normalized resistance  $\Delta R(H)/\Delta R_{\max} = (R(H) - \min(R)) / (\max(R) - \min(R))$ .

Before discussing the electrical properties and magnetoresistance of the nanotubes in detail we determine  $H_d$  [APK00]. Magnetic field sweeps can be found in Fig. 6.8 for sample NiS1 (a) and CFBS1 (b) with  $H$  being parallel (top) and perpendicular (bottom) to the long axis (see supplementary information for further experimental data (cf. Suppl. Inf., Sec. A.1). In

the parallel configuration only small fields were needed to saturate the nanotubes. CoFeB was in particular soft magnetic. In the perpendicular configuration we extracted  $\mu_0 H_d$  (black arrow) to be  $0.35 \pm 0.05$  T for the Ni nanotube. This value was much smaller compared to the CoFeB nanotube for which we found  $1.2 \pm 0.2$  T. We attribute this observation to different demagnetization fields. If we consider  $M_s \approx 375$  kA/m for Ni [WRB<sup>+</sup>12], we estimate the magnetometric demagnetization factor [APK00] to be  $N_{\perp}(\text{Ni}) = |H_d(\text{Ni})/M_s(\text{Ni})| \approx 0.7^2$ . If we assume  $N_{\perp}(\text{CoFeB}) = N_{\perp}(\text{Ni})$  and take the saturation magnetization of 1430 kA/m measured for our CoFeB when magnetron-sputtered on a planar substrate [SG13], we calculate  $\mu_0 H_d = \mu_0 N_{\perp}(\text{CoFeB}) \times M_s(\text{CoFeB}) \approx 1.3$  T. This value is consistent with the experimental value of  $\mu_0 H_d = 1.2 \pm 0.2$  T observed for the CoFeB nanotube in Fig. 6.8 (b). We do not expect the hexagonal shape of the smooth CoFeB nanotubes to vary significantly the effective component of the demagnetization factor compared to the rougher and thereby more circular Ni nanotubes. The different values  $H_d$  thus reflect the different saturation magnetization values of Ni and CoFeB. Note that a large and thin film is expected to exhibit  $N_{\perp}$  of 1.0 whereas an infinitely long (full) cylinder acquires  $N_{\perp} = 0.5$ . The extracted effective demagnetization factor of 0.7 for the nanotubes being hollow cylinders is in between these values and seems reasonable to us. The specific shape of the nanotubes reduces the overall demagnetization effect compared to a film, but still provides a larger effective demagnetization effect compared to a full cylinder. The nanobar-magnet behavior reported in Ref. [HHJ<sup>+</sup>13] is consistent with the shape anisotropy provided by the relatively large  $N_{\perp} \approx 0.7$  extracted here.

We now present the electrical properties and magnetoresistance of the nanotubes. Figure 6.9 (a) shows the temperature dependent resistance  $R(T)$  of a Ni nanotube (NiL1) at zero magnetic field.  $R$  decreases from 40.9  $\Omega$  at room temperature down to 15.8  $\Omega$  at 2 K. The behavior is expected for a polycrystalline metallic material. Using the geometrical parameters (cf. Suppl. Inf., Sec. A.1), we calculate a specific resistivity  $\rho = R \cdot A / L_{\text{contact}}$  of 18  $\mu\Omega\text{cm}$  and 7  $\mu\Omega\text{cm}$  for room and low temperature, respectively ( $A$  is the cross-section of Ni). Our values of  $\rho$  are in relatively good agreement with values measured on nanostripes fabricated from thermally evaporated Ni [RCGG11, JCZ97] indicating a good electrical quality of the ALD-grown metal. The temperature dependent  $R(T)$  for two CoFeB samples is shown in Fig. 6.9 (b). Here, we obtain specific resistivities of  $\rho = 1 - 2 \times 10^3 \mu\Omega\text{cm}$  at room temperature. As a function of  $T$  we do not observe the typical metallic behavior. For sample CFBS1 the resistance decreases from room temperature down to 140 K and then increases. In case of CFBM1 the resistance increases monotonously with decreasing temperature. The measured resistances range from 7.63 to 7.79 k $\Omega$  and 7.35 to 7.79 k $\Omega$  for CFBS1 and CFBM1, respectively. The semi-logarithmic plot suggests  $R(T)$  to exhibit a logarithmic dependence on  $1/T$  for  $T < T_{\text{min}} \approx 130$  K (190 K) for CFBS1 (CFBM1) [ET03], albeit a small deviation can be found for CFBM1 at

Figure 6.9 (c) shows the resistance change of Ni tubes as a function of the rotation angle  $\theta$

<sup>2</sup>Nanotubes are non-ellipsoidal magnetic elements for which an inhomogeneous internal field is expected when  $H$  is perpendicular to the long axis. This would make position-dependent demagnetization factors necessary when describing the micromagnetic behavior in detail. This is why we define the so-called magnetometric demagnetization factor.

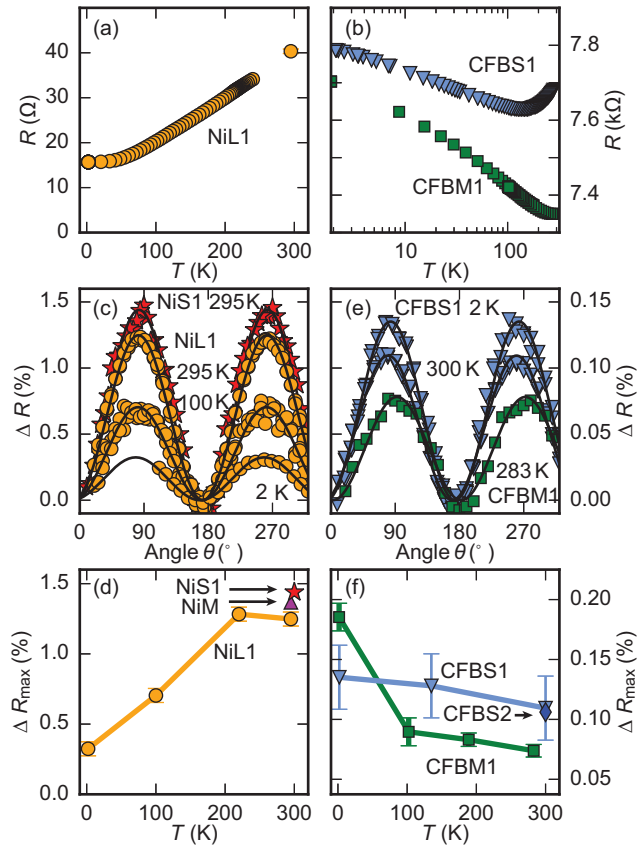


Figure 6.9 – Resistance  $R$  as a function of the temperature  $T$  for (a) the Ni nanotube NiL1 (circles) and (b) the two different CoFeB nanotubes CFBM1 (squares) and CFBS1 (triangles). For CoFeB,  $R$  is more than two orders of magnitude larger and shows a different temperature dependence (note the different axes) compared to the metallic Ni. (c) Resistance variation as a function of the angle  $\theta$  displayed as  $\Delta R(\theta)$  for NiL1 (circles) and NiS1 (stars) at 3 T and 2 T, respectively. The field values  $H$  were chosen such that  $H > H_{\text{sat}}$  and magnetic saturation was achieved for all angles  $\theta$ . (d) AMR ratios as a function of temperature for NiL1 (circles). For NiS1 (star) and NiM (triangle) room-temperature AMR ratios are given. (e)  $R(\theta)$  of CFBS1 at 5 T at two temperatures (triangles) and CFBM1 at 2 T and 283 K. The data for CFS1 were taken in two-point configuration. (f) AMR ratios of samples CFBM1 (squares), CFBS1 (triangles), and CFBS2 (diamond) at room temperature. The AMR effect of CFBM1 was extracted from magnetic field sweeps performed at different  $\theta$  (cf. Suppl. Inf., Sec. A.1). Solid lines in (c) and (e) indicate a  $\cos^2(\theta)$  relationship. The maximum AMR ratio is one order of magnitude smaller for CoFeB compared to Ni.

at different temperatures. We rotated a field  $H > H_d$  to saturate the tubes at all angles.  $R(\theta)$  follows a  $\cos^2(\theta)$  dependence remodelled by solid lines in Fig. 6.9 (c). This is expected for ferromagnetic conductors displaying the AMR. Relative AMR values are shown in Fig. 6.9 (d) as a function of  $T$ . Between 3 and 220 K the AMR is found to increase linearly with  $T$  from about 0.35 to 1.2%. Then, up to 295 K the AMR stays almost constant for sample NiL1. The low-temperature value is consistent with data obtained previously on different Ni nanotubes [RHB<sup>+</sup>12]. At room temperature we now find a much larger value of up to 1.4% for NiS1 and NiM [Fig. 6.9 (d)]. In Refs. [RCGG11, JCZ97] stripes from thermally evaporated Ni were studied and the authors provided values of 1.6% and 1.8%, respectively. We attribute the slightly smaller AMR effect of our nanotubes compared to the planar stripes mainly to the influence of the nanotube roughness. We assume the roughness-induced scattering of electrons to enhance the resistivity and thereby to reduce the overall AMR effect (compare considerations on boundary scattering in Ref. [RCdJdJ95]).

$R(\theta)$  of CoFeB nanotubes CFBS1 (triangles) and CFBM1 (squares) shown in Fig. 6.9 (e) also follows a  $\cos^2(\theta)$  dependence consistent with the AMR effect. The AMR effect is found to diminish with increasing  $T$  [Fig. 6.9 (f)]. This is different from the Ni nanotubes. For CFBM1 we get AMR = 0.18% at 2 K and 0.08% at room temperature being more than an order of magnitude smaller than Ni. We attribute this to the amorphous structure of our unannealed CoFeB leading to a short electron mean free path and reducing the MR ratio [TJIK97]. The measured CoFeB resistivity of  $1\text{--}2 \times 10^3 \mu\Omega\text{cm}$  is one order of magnitude larger compared to the best values given in literature for CoFeB alloy films with a comparable thickness [CX12, JYC<sup>+</sup>06]. For  $R(T)$  we do not find a  $T^{3/2}$  dependence in the accessible temperature range and rule out magnetic contributions to  $R(T)$  [KKR86]. The characteristic minima in  $R(T)$  [Fig. 6.9 (b)] have been reported for many amorphous and granular alloys with intermediate resistivities [TKM<sup>+</sup>08, KKR87] including CoFeB [FMIO94, SPS<sup>+</sup>13]. The following dependencies have been discussed for the low-temperature  $R$  when considering Coulomb interaction in disordered systems:  $\exp(\sqrt{T_0/T})$  [ES75], a power law  $1/T^\alpha$  or  $\ln(T_0/T)$  [ET03] ( $T_0$  is a characteristic temperature and  $0 < \alpha \ll 1$ ). The first (latter) occurs for systems with high (intermediate) resistivity [CDLM81, SDVV<sup>+</sup>87, FMIO94, ET03]. Following Ref. [ET03], we attribute the logarithmic behavior of  $R(T)$  in Fig. 6.9 (b) for  $T < T_{\min}$  to electron-electron interaction in the disordered and amorphous material. The role of the columnar structure is not yet fully clear and under further investigation. Despite the complex  $R(T)$  dependence the AMR value of up to 0.18% that we observe for CoFeB nanotubes at small  $T$  is slightly larger than the value of 0.12% obtained by DFT simulations [SFZ<sup>+</sup>11].

The large room-temperature AMR ratios of up to 1.4% for Ni are encouraging for possible applications of nanotubes and, in general, magnetic devices on curved surfaces [PHT08] prepared by ALD. Still there is room for improvement as the AMR ratio of bulk Ni is known to be 2% [MP75]. We expect an improved AMR ratio after reducing the surface roughness of the nickel. The smooth side facets of the CoFeB nanotubes make the integration of magnetic tunnel junctions [IMY<sup>+</sup>10] feasible, thereby enhancing the perspectives of nanotube-based sensing and local detection of domain walls.

In conclusion, we prepared nanotubes from Ni and CoFeB on non-magnetic nanotemplates using two different technologically relevant deposition techniques, i.e., atomic layer deposition and magnetron sputtering, respectively. Structural analysis of the CoFeB proved the shell to be amorphous. For polycrystalline Ni and amorphous CoFeB the magnetic anisotropy was argued to be dominated by the shape. Both the relatively small resistivity and large AMR ratio of 1.4% obtained for Ni indicated a good electrical performance of the ALD-grown metal at room temperature. Magnetron-sputtered CoFeB nanotubes exhibited a much smoother surface but a smaller AMR effect attributed to the amorphous structure and thereby enhanced electron scattering. The materials are highly eligible for magnetotransport studies on individual domain walls in nanotubes and nanotube-based sensing or logic applications. For room temperature spintronic applications the relatively large AMR of Ni is promising. The larger saturation magnetization makes the CoFeB nanotubes favorable as magnetic tips in scanning probe microscopy.

### 6.2.3 Acknowledgments

The work has been supported by the DFG via GR1640/5-1 in SPP1538 "Spin caloric transport". Funding through the Swiss National Science Foundation NCCR QSIT and FP7 ITN Nanoembrace are greatly acknowledged. We acknowledge financial support from the European Union under a contract for an integrated Infrastructure Initiative 312483 - ESTEEM2 project that facilitates the use of advanced electron microscopes at ER-C JÄ¼lich. The authors would like to thank D. Meertens for the preparation of FIB lamellas. J.A. acknowledges the funding from the Spanish MICINN project MAT2010-15138 (COPEON), and Generalitat de Catalunya 2009 SGR 770. R.R.Z. acknowledges the former. The authors would also like to thank the TEM facilities in CCiT from Universitat de Barcelona.

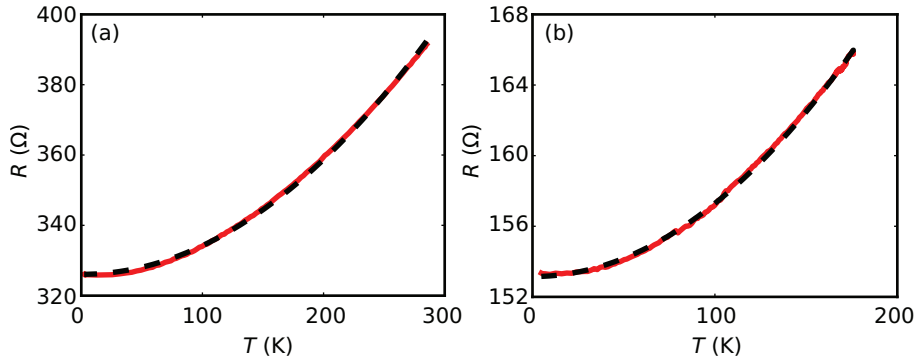


Figure 6.10 – Resistance  $R$  as function of the temperature  $T$  for samples (a) Py1 and (b) Py2. The measured data (red solid line) can be fitted by a  $T^2$ -function (black dashed line). Sample Py1 follows  $R(T) = 326\Omega + 0.8 \cdot 10^{-3} \Omega/K^2 \times T^2$  and sample two (b)  $R(T) = 153\Omega + 0.4 \cdot 10^{-3} \Omega/K^2 \times T^2$  after an irreversible resistance drop (cf. text for details)

### 6.3 Resistivity and AMR of Permalloy nanotubes

Two Py tubes, Py1 and Py2, similar to the ones used in Pub. A-III (cf. Sec. 8), have been characterized electrically and the AMR ratios have been determined. The data extends upon the work of Pub. A-I and Pub. A-II. For the experiment, the methodology described in Chap. 4 and Pub. A-I & A-II was followed.

#### 6.3.1 Electrical Characterization

**Sample Py1** Figure 6.10 (a) gives the resistance  $R$  as function of the sample temperature  $T$  of a tube with a total length of  $12.3 \mu\text{m}$ , film thickness  $t = 30 \text{ nm}$  and outer diameter  $2r_o$  between 190 and 205 nm. The resistance drops from about  $390 \Omega$  to  $325 \Omega$  when cooling the sample from room temperature to 2 K [cf. red solid line in Fig. 6.10 (a)]. The  $T$ -dependence is fitted by a  $T^2$ -function [cf. black dashed line in Fig. 7.7 (a)]. Using the length between the voltage contacts  $L_p = 4.4 \mu\text{m}$ , the resistivity  $\rho$  is determined to be  $140 \pm 10 \mu\Omega\text{cm}$  at room temperature and  $115 \pm 5 \mu\Omega\text{cm}$  at 2 K. At room temperature the AMR of this sample was determined to be  $0.45 \pm 0.05\%$ .

**Sample Py2** The tube has similar thickness  $t = 30 \text{ nm}$ , outer diameter  $2r_o = 180$  to  $215 \text{ nm}$ , contact length  $L_p = 6.4 \mu\text{m}$  and a total length of  $14.2 \mu\text{m}$ . The sample exhibited a resistance of about  $530 \Omega$ , i.e.  $\rho = 130 \pm 20 \mu\Omega\text{cm}$ , and an AMR ratio of  $0.45 \pm 0.05\%$  at room temperature in Fig. 6.11a. The resistance dropped approximately linearly to  $490 \Omega$  at 210 K. After being kept at 190 K for a day, the resistance had dropped irreversibly to around  $170 \Omega$  at 190 K. The decrease in resistance correlated with an increase in AMR to  $0.63 \pm 0.05\%$ . After that,  $R$  followed  $T^2$  with decreasing  $T$  [Fig. 7.7 (b)], until it saturated at a value of  $153 \Omega$  below  $\lesssim 30 \text{ K}$ . At the same time the AMR increased to  $0.74 \pm 0.05\%$ . The resistance related to  $41 \pm 4 \mu\Omega\text{cm}$  at 190 K and  $38 \pm 3 \mu\Omega\text{cm}$  at 2 K.



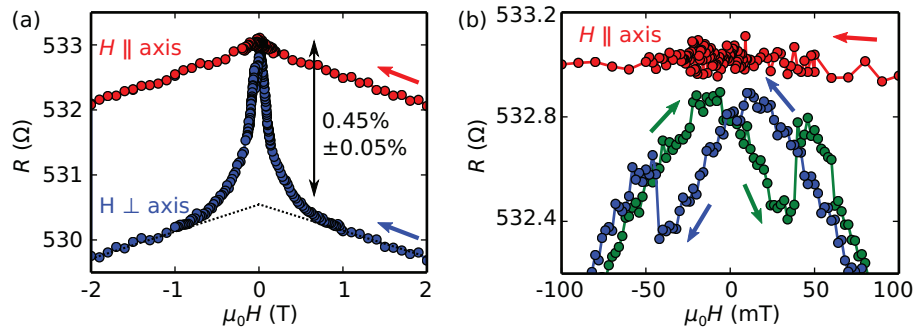


Figure 6.11 – Resistance  $R$  as function of the magnetic field  $\mu_0 H$  of nanotube Py2 at room temperature. The low field regime of (a) is shown in (b). Arrows indicate the sweep direction.

### 6.3.2 Hysteresis curves

The high field data for sample Py2 is plotted in Fig. 6.11 (a). Here, the resistance  $R$  is shown as function of the applied field  $\mu_0 H$  for field parallel (red circles) and perpendicular to the axis (blue circles). The field was initialized at 2 T and then gradually decreased to -2 T. For both field orientations a linear negative magnetoresistance can be found. Figure 6.11 (b) shows a magnification of the small field regime. Here, an additional trace for perpendicular field is given with inverted sweep direction (green circles). The maximum  $R$  obtained near  $H = 0$  is almost similar for fields parallel and normal to the tube axis. Both traces for perpendicular fields exhibit a jump to higher resistance at  $|\mu_0 H| \approx 40$  mT after decreasing gradually in inverse field. This feature is well reproducible. In parallel field direction, no significant deviation of the linear  $R$  can be found before inversion of the field direction (Fig. 6.12 and Fig. A.4, p. 133). A dip can be found at  $7 \pm 3$  mT with an amplitude which is about a tenth of the maximal resistance change. The available data suggests, that the dip is not always present but occurs statistically.

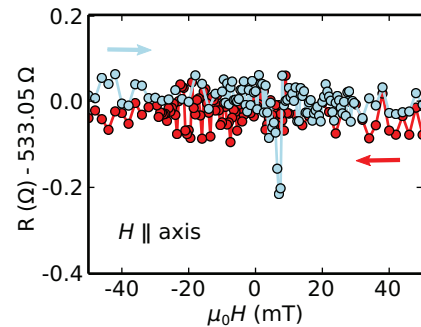


Figure 6.12 – Resistance  $R$  for  $\mathbf{H} \parallel$  axis and both sweep directions for Py2 at room temperature. Some sweeps exhibit a dip at an opposing field of around 7 mT.

### 6.3.3 Discussion

The resistivity of sample Py1 and Py2 before the sudden decrease is a factor of about five higher than values reported in literature [MJG74, CDK<sup>+</sup>06, BA09]. Because of increased influence of surface scattering and considering the large surface to volume ration in the tubes, this value seems reasonable. The significant decrease in resistance after a certain time could be explained by an annealing effect of the measurement current, either via electromigration or localized heating. It is known that  $\rho$  can be decreased significantly by annealing of the

sample [KGD73], but whether and how this can be held responsible for the observed decrease cannot be answered without further experimental data.

The  $T^2$ -dependence, found in both samples, was also reported in Py films by Council *et al.* [CDK<sup>+</sup>06]. The same behavior was calculated by Richter *et al.* [RWG79] and discussed by Kaul *et al.* [KKR86] two decades before. They make coherent electron-magnon scattering responsible for the  $T^2$ -dependence. For amorphous materials additionally a  $T^{3/2}$  term related to incoherent electron-magnon scattering is expected. In crystalline samples the  $T^{3/2}$  term is zero and only the square dependence remains.

The reason for decreased AMR in Py samples was not clear until redirection of this thesis. It is known that the grain size influences the AMR because of changed grain boundary scattering. The grain size is dependent on the substrate and the conditions of the deposition process [LTT<sup>+</sup>00]. A possible route to further improve could be annealing [FOKS94].

The hysteresis curves correspond to a uni-axial anisotropy. No significant deviation of the resistance during the reversal in parallel fields occur before inversion of the field orientation. Furthermore, only statistically a dip, corresponding to a certain azimuthal component, can be found. The statistical behavior and the small magnitude of the dip are in agreement with a reversal via a vortex domain wall. The wall would then stick to pinning sites, giving rise to the statistical observation. Another possible explanation is the expansion of end-vortices as discussed in Sec. 7.1.

By comparison of the resistance at the dip minimum with the maximal change of resistance we can estimate that about 9% of the probed length is aligned azimuthally. This equals to a length of approximately 550 nm with azimuthal orientation. Using the geometrical dimensions of Py2, the expected domain wall width can be estimated to be around 85 nm from Eq. 3.53. This would mean that in total 6 to 7 domain walls participate in the reversal. On the other hand, if end-vortices are made responsible for the measured dip, the azimuthal part has to extend into the probe part of the tube. Because of the position of the electrical probes, this implies that the end-vortices extend for more than 4  $\mu\text{m}$  from the end. To get a better understanding of the reversal process data from complementary experiments, such as e.g. spatially resolved ANE mapping (cf. Sec. 7.1), are desirable. The jump towards higher resistance relates to an increased axial component of  $\mathbf{M}$ , following the discussion Sec. 6.1 [Fig. 6.4 p. 65]. Further investigations are needed to understand the origin of this jump in detail.

### 6.4 Saturation magnetization

Ni, CoFeB and Py are materials with very different saturation magnetization  $M_s$ . Because of the small involved volume measuring  $M_s$  can be challenging with conventional techniques which are designed for bulk samples. For this reason, cantilever magnetometry on individual nanotubes was performed in collaboration with the group of Prof. Martino Poggio at Basel (cf. Sec. 4.1.3). The results have been published (cf. Pub. B-I in App. D) and are summarized in the



## 6.5. Magnetization reversal in Ni nanotubes under axial field

	$A$ (J/m)	$M_s$ (kA/m)	$\lambda_{\text{ex}}$ (nm)
Ni	$7 \cdot 10^{-12}$ [Boa05]	375	9
CoFeB	$2.8 \cdot 10^{-11}$ [BDK <sup>+</sup> 06]	800	8
Py	$1.3 \cdot 10^{-11}$ [Boa05]	400	11

Table 6.1 – Calculated exchange length  $\lambda_{\text{ex}}$

following paragraph.

Cantilever magnetometry experiments were performed on Ni nanotubes attached in three different geometries to the cantilever. This way, the anisotropy due to the shape for the different field orientations could be evaluated. For the determination of the saturation magnetization  $M_s$  the chosen orientation is irrelevant as long as the applied magnetic fields are strong enough to saturate the entire tube homogeneously. In the experiment the change of the cantilever's resonance frequency  $\Delta f_0$  was measured and fitted to Eq. 4.5 at fields above saturation. The fit yielded a value of  $M_s = 375 \pm 70$  kA/m, which is in good agreement with the reported values of 406 kA/m for bulk crystalline Ni at low temperature [KM05] and 450 kA/m for ultra fine Ni particles [GLZC91].

Cantilever magnetometry was recently performed for the CoFeB tubes [Web14]. Here, the fits gave  $M_s = 870 \pm 30$  kA/m. The value is significantly below the values of 1430 kA/m obtained on planar CoFeB films deposited in the same vacuum chamber [SG13, YDH<sup>+</sup>13a]. Whether this decrease is related to the growth under an angle and rotation is not clear at the moment. It is possible that the columnar structure observed in TEM [cf. Fig. 6.6 (c)] is linked to the findings. Further studies comparing planar films grown under similar angle and rotation are under way.

No magnetometry data is yet available for Py tubes. However, the spin wave spectrum which was measured in such tubes (cf. Sec. 8), is well reproduced by simulations when using  $M_s = 400$  kA/m. An effective magnetization of 620 kA/m was measured in Py films deposited on planar substrates with the same evaporation system [Hei].<sup>3</sup>

## 6.5 Magnetization reversal in Ni nanotubes under axial field

Considering the determined  $M_s$  of the investigated nanotubes and literature values for the exchange coupling parameter  $A$ , we find comparable exchange lengths  $\lambda_{\text{ex}} = \sqrt{2A/(\mu_0 M_s^2)}$  between 8 and 11 nm for all three materials (cf. Tab. 6.1). In terms of  $\lambda_{\text{ex}}$ , the length of the studied nanotubes ranged from 1000 to 2000  $\lambda_{\text{ex}}$  and the outer radii from about 7 to 15  $\lambda_{\text{ex}}$ . The parameter  $\beta$  is 0.6–0.8. According to the phasediagram in Fig. 3.4, developed by Landeros *et al.* [LSCV09], all tubes were well within the mixed state phase. Coming from a uniform axial alignment in high parallel fields, the end-vortices should nucleate below a certain critical field [WLL<sup>+</sup>05, LSS<sup>+</sup>07, LSCV09]. The collected data suggest, however, that the ground state

<sup>3</sup>Note that the effective magnetization takes the surface anisotropy into account and can thus be smaller than the saturation magnetization.

## Chapter 6. Characterization of ferromagnetic nanotubes

---

differs significantly between the Ni tubes and the tubes with CoFeB or Py. In the following we will briefly summarize the findings on Ni nanotubes which have been published in Pub. A-I, A-II and B-II. A detailed analysis of the reversal in CoFeB tubes is given in Chap. 7.

The magnetoresistance traces recorded on Ni nanotubes in axial field show without exception a smaller resistance  $R$  at remanence than at saturation [cf. Fig. 6.2 p. 62, Fig. 6.8 (a) p. 73 and Fig. A.2 p. 132]. Following the theory of the AMR effect, a smaller  $R$  is related to an azimuthal or transverse component of the magnetization  $\mathbf{M}$ . To further elucidate the magnetization reversal, cantilever experiments were performed on an individual Ni nanotube in collaboration with the group of Prof. Martino Poggio at Basel. For this particular experiment, a nanoSQUID<sup>4</sup> magnetic flux sensor was added in vicinity of the tube tip by the group of Prof. Dieter Kölle. While the cantilever signal is an integral measure of the projection of  $\mathbf{M}$  onto the field direction, the nanoSQUID senses the generated stray field close to the nanotube apex. The experimental results were compared to micromagnetic simulations of circular tubes with lengths up to 2  $\mu\text{m}$  (cf. Sec. 4.2). We used a value of 406 kA/m for  $M_s$  and an exchange coupling constant of 7 pJ/m. More experimental details can be found in the Pub. B-II, which is reproduced with permission in App. D.

The cantilever magnetometry data revealed a significant decrease of the axial component of  $\mathbf{M}$  at  $H = 0$  [cf. Fig. 3 (c) in Pub. B-II]. In contrast, the hysteresis curve measured by the nanoSQUID exhibits a square shape [cf. Fig. 2 (a) in Pub. B-II]. The superposition of simulated curves of nanotubes with lengths between 250 nm and 1  $\mu\text{m}$  reproduced the observed cantilever data closely. In the simulation, anti-chiral end-vortices, i.e. end-vortices having opposite senses of rotations, nucleate and expand until they touch, only separated by a Néel-type domain wall [cf. Fig. 4 (c) in Pub. B-II]. Such a finding is consistent with other numerical results for short tube in literature [WLL<sup>+</sup>05, LSS<sup>+</sup>07, CUBG07]. At a switching field of approximately  $25 \pm 10$  mT, the magnetization in the domain wall switches spontaneously and the end-vortices retract. The good qualitative and quantitative agreement of simulation and measurement suggests switching of multiple independent segments during reversal. This argument is supported by the nanoSQUID data deviating strongly from both, the cantilever data and the simulation. The nanoSQUID probes locally the tip of the nanotube and thus does not see the full integral measure of the magnetization, as the cantilever does. This discrepancy is also consistent with multiple segments that switch individually, if the end segment happens to switch last.

---

<sup>4</sup>Superconducting quantum interference devices (SQUIDs) are superconducting loops including one or two Josephson-contacts. Based on the Josephson-effect [Jos62], they act as highly sensitive sensor for the magnetic flux. Because the technology and performance of SQUIDs is beyond the scope of this thesis, the interested reader is referred to Ref. [CB06].

# 7 Magnetization reversal in CoFeB tubes

This chapter treats the microscopic nature of magnetization reversal in CoFeB tubes. In Sec. 7.1, the microscopic details of the magnetization reversal in axial fields are studied by a combination of magnetotransport and magnetothermal mapping. Then, in Sec. 7.2, the influence of the inhomogeneous internal field in nanotubes under a perpendicular field is investigated.

To understand whether CoFeB nanotubes exhibit non-uniform configurations, e.g. the mixed state, locally probed magnetotransport and magnetothermal mapping experiments were conducted. The findings of this chapter were obtained in close collaboration with the group of Prof. Dirk Grundler at Technical University Munich (cf. Sec. 1.3). I measured the high field data. The low field and ANE measurements were conducted by the Master student Johannes Mendil whom I co-supervised. The laser stage was designed and setup by the PhD student Florian Brandl and the experimental rig was adapted to the ANE measurement by Johannes Mendil. The detailed analysis of the behavior in perpendicular fields in Sec. 7.2 was achieved by micromagnetic simulations that I performed and interpreted.

## 7.1 Magnetization reversal of an individual ferromagnetic nanotube probed via anisotropic magnetoresistance and anomalous Nernst effect

### 7.1.1 Anisotropic magnetoresistance

We first present AMR data obtained on two different segments, the end and center segment, as sketched in Fig. 7.1. For the center segment, we are able to perform a 4-point resistance measurement. Due to the sample layout, we have to resort to a 3-point measurement for the end segment, utilizing the same contact for current supply and voltage sense. The nanotubes employed in the AMR experiments have  $L = 10 - 16 \mu\text{m}$ ,  $r_1 = 65$  to  $105$  nm and thickness  $t = r_0 - r_1$  of 20 or 30 nm. Note that for parallel field orientation the resistive magnet coils deliver

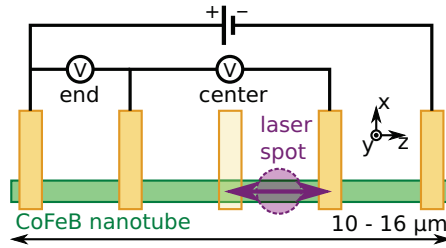


Figure 7.1 – Schematic of the measurement details. For the AMR measurements, the resistance is either determined in the center via 4-point configuration or at the end segment using only 3 points. For the ANE experiments, the voltage is always measured between the center contacts. Here, the position of the laser spot is changed. The nanotube explored in perpendicular field orientation had only four contacts.

sufficient field amplitude (cf. Sec. 4.1.1). To fully saturate the tube in transverse direction, higher fields are needed. For this orientation, the data was acquired in a superconducting magnet at 180 K on a different sample. In this case, the sample had a wall thickness  $t = 20$  nm and four leads [Fig. 7.1]. Its dimensions and relevant contact spacings were comparable. The applied measurement current was  $1 \mu\text{A}$  in all cases.

The results of the 3-point (4-point) AMR data at the end (center) segment are shown in Fig. 7.2 in blue and green (red and black) for parallel field orientation. Starting from high negative fields  $H$ , the resistance remains at its highest level for a wide field range, indicating saturation along this direction. The resistance for the end (center) segment starts to significantly decrease at  $-5$  mT ( $+2$  mT) until magnetization reversal takes place and the resistance increases in a step-like manner back to the saturated value at  $+4$  mT ( $+5$  mT). Note the two-step nature of the resistance increase for the center segment. The curve contains a plateau-like resistance state around  $+5$  mT which we will call intermediate state throughout the following analysis. Note that this intermediate state is a common feature of all 8 investigated CoFeB nanotubes with  $H$  applied along the long axis. The AMR trace behaves correspondingly for the sweep in opposite direction.

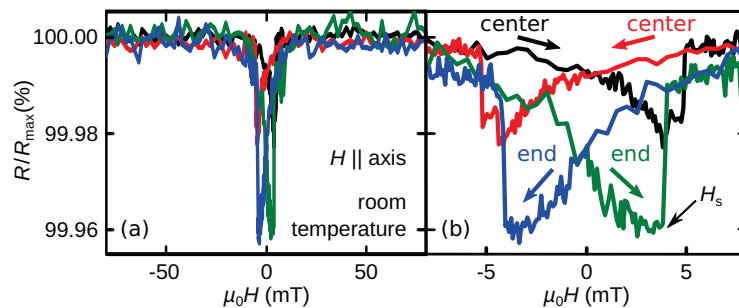


Figure 7.2 – Normalized resistance  $R/R_{\text{max}}$  as a function of the axially aligned magnetic field (a) for the full field range and in (b) the field regime of the switching. The jump which is interpreted as switching field  $H_s$  is indicated in (b).

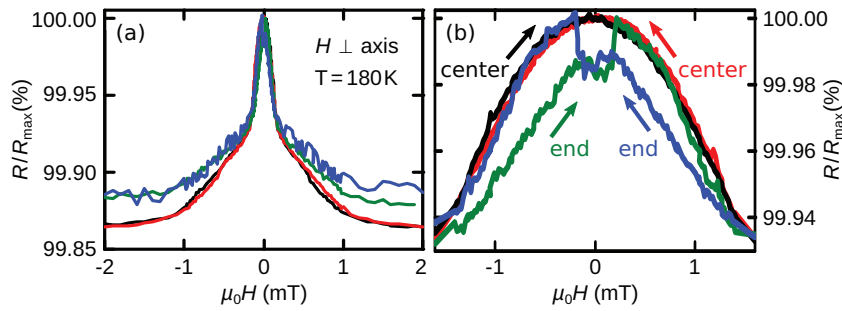


Figure 7.3 – Normalized resistance  $R/R_{\max}$  as a function of the magnetic field perpendicular to the tube axis (a) for the full field range and in (b) the field regime of the switching.

Resistance traces that have been acquired for perpendicular field orientation are given in Fig. 7.3. When the field was decreased from 2 T, the resistance increases already at comparably large fields. This indicates a deviation from the fully perpendicular alignment of the magnetization  $\mathbf{M}$ . For the center segment [cf. red line in Fig. 7.3 (b)], reducing the field to zero shows a monotonically increasing resistance<sup>1</sup>. Decreasing the field further to the negative regime, a continuous trace with a maximum in  $R$  close to zero field is observed. As discussed in Sec. 6.1, this maximum can be attributed to a parallel magnetization alignment. However, the trace is different for the end segment [cf. blue line in Fig. 7.3 (b)]. In particular, it shows a smaller resistance when approaching zero field and finally a step-like change of resistance shortly after reversing the field to negative values at about -5 mT. Both, the behavior of the end and center segment are symmetrically reproduced for the opposite field sweep direction (cf. black/green lines in Fig. 7.3 (b)).

Note a common feature of AMR data taken in both parallel and perpendicular  $H$ : the AMR traces of the end segments show a significantly smaller relative resistance compared to the center segment when approaching zero field from saturation. This observation indicates a different alignment of magnetization for the end than for the center segment. Further insight is gained in the following where we report ANE experiments.

### 7.1.2 Anomalous Nernst effect

In the ANE experiments, a laser spot was placed onto a 30 nm-thick nanotube as sketched in Fig. 7.1 (cf. Sec. 4.1.4). The remaining experimental configuration is exactly the same as employed for the magnetotransport experiments. Again, we perform a field sweep from negative to positive fields along the axis of the tube and back. Figure 7.4 (b) shows the voltage in a similar field regime as for Fig. 7.2 (b). To keep comparable experimental conditions, a biasing current of 1  $\mu\text{A}$  was applied.

For the sweep in negative direction, we observe a sharp transition from about 6.52 to 6.5 mV,

<sup>1</sup>The change in resistance can be divided into a field dependent change with three different slopes. This behavior is investigated in combination with demagnetization field simulations in Sec. 7.2.

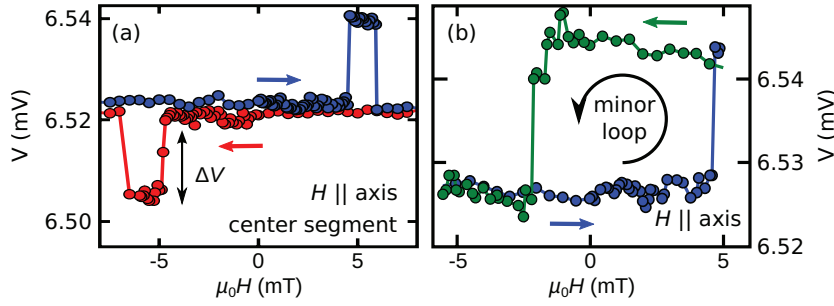


Figure 7.4 – (a) Voltage  $V$  across a segment of a CoFeB NT that was locally heated with a focused laser spot while sweeping the magnetic field  $\mu_0 H$  and applying a bias current of  $1 \mu\text{A}$ . We attribute the voltage spikes to the anomalous Nernst effect (ANE). (b) Data obtained in a minor loop with a reversal field of 5 mT. The zero-field magnetic state is persistent when the laser is found to be switched on and off.

i.e. a difference  $\Delta V \approx -20 \mu\text{V}$  at fields around -5 mT. Sweeping in positive direction, a positive peak of  $\Delta V \approx 20 \mu\text{V}$  is observed at similar field strength. The signal  $\Delta V$  only occurs for sweeps with the laser turned on and placed onto the nanotube. The sign change of  $\Delta V$  with the sweep direction of  $H$  distinguishes the signal clearly from the AMR. Furthermore, minor-loops were performed. An example is plotted in Fig. 7.4 (c). Starting from negative fields, the sweep direction is reversed at +5 mT where the voltage plateau is reached. Sweeping the field back to zero,  $V$  stays at the elevated level and finally falls back to the original value at -2 mT when continuing the sweep in negative field direction.

To study the spatial dependence of the signal, the laser-spot is placed onto different segments of a comparable nanotube of the same batch. The spike-like features of before are reproduced at a similar position [Fig. 7.5 (e)]. The detailed trace  $V(H)$  however depends on the laser position along the long axis of the nanotube [Fig. 7.5 (.)] The traces are reproducible, when repeating the measurements at the same position, even after varying the position and returning to the corresponding spot. At pos. 1 [Fig. 7.5 (b)], no pronounced peak but a step-like jump of about  $5 \mu\text{V}$  can be observed. Heating at pos. 2 results in a similar trace but with a step amplitude of about  $2 \mu\text{V}$  [Fig. 7.5 (c)]. When heating at pos. 3, a reversed spike-like feature occurs with an amplitude of about  $30 \mu\text{V}$  [Fig. 7.5 (d)]. At pos. 4 the polarity is spontaneously inverted [Fig. 7.5 (e)]. For a positive sweep we find now a positive signal and not, as before, a negative one. Interestingly, this does not hold true for pos. 5, where the polarity changes again [Fig. 7.5 (f)]. Also, the voltage signal does not show spike-like but rather gradual change. Note that the signals have an offset voltage at large  $H$  and with  $I = 0$  which increases from pos. 1 to pos. 5. A similar behavior can be found without magnetic field and is thus attributed to the conventional Seebeck effect. More details and measurements can be found in Ref. [Men14].

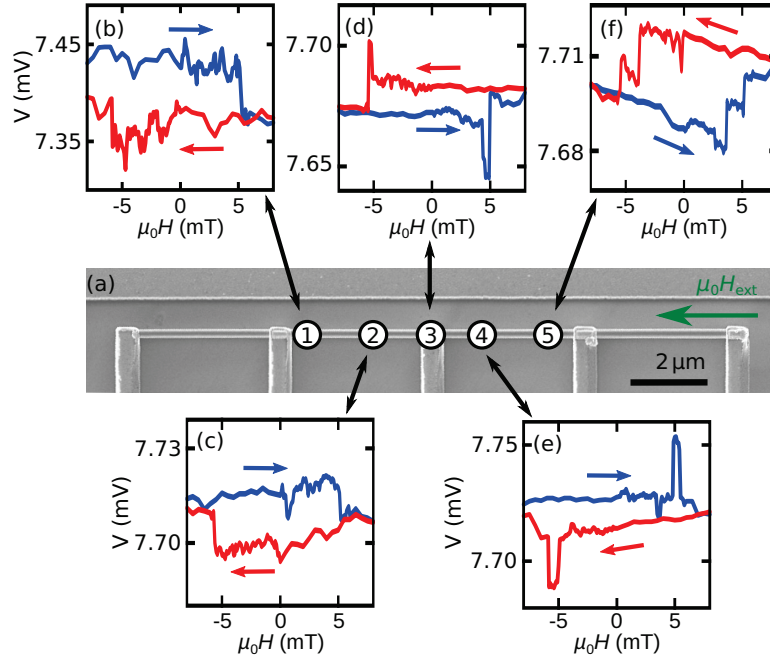


Figure 7.5 – While the laser is positioned on different spots as indicated in (a), voltage sweeps  $V(H)$  are recorded (b-f).

### 7.1.3 Discussion

**Switching field** Before discussing the spatially resolved data, the determined switching fields are compared to theory [EDL<sup>+</sup>07] (cf. Sec. 3.4.3). The switching field  $H_s$  is extracted from  $V(H)$  in inverted axial fields. For this, the field values of the first jump in the AMR data after reversing  $H$  are used [Fig. 7.2 (b)]. The measured values of  $H_s$  are plotted as function of the outer radius  $r_o$  in Fig. 7.6 (symbols). The solid lines depict the theoretical prediction for the vortex nucleation field  $H_n^{\text{cur}}$  as given by Eq. 3.61. The exchange constant is assumed as  $A = 28 \cdot 10^{-12}$  J/m [BDK<sup>+</sup>06] and the effective saturation magnetization  $M_s = 870$  kA/m [Web14].  $H_s$  and  $H_n^{\text{cur}}$  have similar dependence on the external radius: both decrease for increasing  $r_o$ . Because of the good qualitative agreement, one can assume that reversal occurs via nucleation of vortex domain walls. Interestingly, we observe a smaller measured  $H_s$  than the theoretical nucleation field. This finding is agreement with calculations of Landeros *et al.* [LSCV09] (cf. Sec. 3.4.3) and suggests nucleation from the end-vortices.

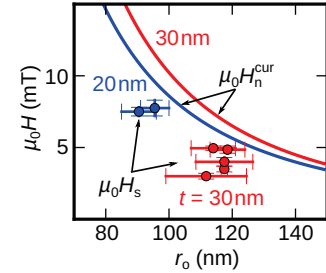


Figure 7.6 – Experimentally determined switching fields  $\mu_0 H_s$  (symbols) and calculated vortex nucleation fields  $H_n^{\text{cur}}$  (lines) as a function of external radius  $r_o$  for  $t = 20$  (blue) and  $30$  nm (red). The error bars give the tapering in  $r_o$  as determined by scanning electron microscopy images.



**ANE signal** Due to our measurement configuration, the voltage detection direction is set along the long axis of the nanotube ( $z$ -axis) and the heat gradient is induced normal to the substrate surface ( $y$ -axis). Therefore, following Eq. 4.6, the experiment is only sensitive to variations of  $\mathbf{M}$  along the  $x$ -axis. The onion, transverse and the vortex configuration fulfill this condition [Fig. 6.4 (b)]. Using the ANE based detection of transverse magnetization components, an experimental distinction between the three states is very challenging and cannot be undertaken with the available data. Because of the involved stray field energies, only the vortex configuration is expected to be formed in tubes with the given dimensions under parallel or negligible field (cf. Sec. 3.4). Furthermore, the switching field analysis above suggest similarly a reversal via vortex domain walls. Thus only the vortex configuration is considered in the following. Please note, that for the vortex a net voltage is only possible if the heat gradient is different for the top facet and the bottom facet. The environments of both facets are very different. While the top facet is mainly surrounded by air, the bottom facet is in direct contact with the silicon surface, which acts as a heat sink. We therefore assume different temperature gradients  $\nabla T$  for the top and bottom facet in the following.

**Spatial mapping** Let us now consider the spatial dependence found in the AMR as well as the ANE experiments. Following Ref. [LSCV09], the typical geometrical dimensions of nanotubes employed in this study fall into the mixed state phase [Fig. 3.4]. The length of the end-vortices, which terminate the tube [Fig. 2.3], depends on the sign and amplitude of  $H$  [CUBG07, LSCV09, CGG10, BNR<sup>+</sup>13]. The relative chirality depends sensitively on geometrical parameters [CGG10, BNR<sup>+</sup>13]. For decreasing field the end-vortices are expected to expand until they either, in short enough tubes, touch [CUBG07] or a vortex wall is nucleated [LSCV09]. Such an expansion correspond to a decrease in resistance [RHB<sup>+</sup>12] and an increase in the magnitude of the ANE signal at the ends of the nanotube. The existence and expansion of such end-vortices can thus explain the discrepancy in AMR data for the end and the center segment in Fig. 7.2 and Fig. 7.3. Furthermore the vortex expansion is consistent with the gradual change of  $V_{\text{ANE}}$  at pos. 5 in Fig. 7.5 (f).

Two evidences support the picture in which at least one vortex DW is nucleated from an expanded end-vortex after a certain expansion length: first, no gradual increase of  $V_{\text{ANE}}$  is observed at pos. 3 and 4. Additionally, the change in  $R$  is much less pronounced for the central segment in Fig. 7.2. Second, the ANE signal, which had gradually build up at pos. 5 in Fig. 7.5 (f) releases before the peaks are detected in the more central pos. 3 and 4 [Fig. 7.5 (c-d)]. Similarly, the intermediate state in Fig. 7.2 (b) is only present in the center segment. We thus assume that the nucleation of vortex DWs is responsible for the observed  $H_s$ .

Two scenarios can now explain the existence of the intermediate state: first, the nucleated DWs could be pinned. The pinning strength would thus determine the field which is necessary for complete reversal [Fig. 7.2 (b)]. In the second scenario the DWs would have opposite chirality, generating an additional energy barrier for annihilation. The minor loop favors the first scenario, as no energy barrier is expected to separate anti-chiral DWs. One would thus expect



## 7.1. Magnetization reversal [...] probed via AMR and ANE

---

no stable state in negative field if blocked anti-chiral DWs cause the switchin field[Fig. 7.4 (b)]. Because there is the possibility of the DWs being pinned while moving apart, it cannot be decided which scenario holds true.

The AMR data alone does not allow the distinction between the chiralities. According to Eq. 4.6, the polarity of the voltage signal in the ANE curves allows us to determine the chirality of the underlying vortex state. A decrease (increase) of the voltage has to be linked to an increase of azimuthal magnetization component in negative (positive)  $x$ -direction. The voltage sweeps of Fig. 7.5 are translated to a sense of rotation in Tab. 7.1. Note, a position-dependent comparison of the chirality is only possible, if the nucleating DWs for magnetization reversal follow a very similar evolution in time, no matter which position is heated. We consider this to be fulfilled, due to the high reproducibility for each position. The observation of two transitions (clockwise to counter-clock-wise from position 3 to 4 and back from position 4 to 5) would thus support the nucleation of DWs at multiple sites. Please note, that recent calculations predict a chirality switching of DWs traveling withing a certain field range [OLLVL12]. This effect cannot conclusively be ruled out at the current stage.

position	1	2	3	4	5
clockwise	✓	✓	✓		✓
counter-clockwise				✓	

Table 7.1 – Position-dependent chirality of the azimuthal magnetization orientation.

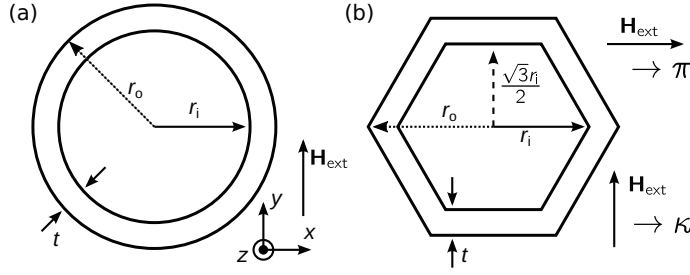


Figure 7.7 – Cross-sectional schematic of a (a) cylindrical and (b) hexagonal nanotube with film thickness  $t$ , inner and outer Radius,  $r_i$  and  $r_o$ . The hexagonal geometry comprises two principal field orientations, named  $\kappa$  for field normal and  $\pi$  for field parallel to two facets.

## 7.2 Influence of the inhomogeneous demagnetization field on the hysteresis curves in transverse fields

Non-elliptic magnetic objects experience an inhomogeneous internal field. The following section presents and discusses results of micromagnetic simulations on the reversal of CoFeB nanotubes in a perpendicular field  $H_{\text{ext}}$ . In particular, the influence of the internal field on the shape of the hysteresis curve and its dependence on geometrical parameters are discussed. Circular tubes as well as hexagonal tubes along their two symmetry axes are considered. The results are compared to experimental data acquired by magnetotransport measurements.

### 7.2.1 Simulation results

For the simulation of the magnetization reversal in nanotubes, quasi-periodic boundary conditions along the long axis and compressed  $\mathcal{H}$ -matrices are employed (cf. Sec. 4.2). The saturation magnetization was set to  $M_s = 1430$  kA/m [SG13] and the exchange coupling to  $A = 28$  pJ/m [BDK<sup>+</sup>06]. Figure 7.7 depicts the three different geometries: apart from cylindrical tubes [Fig. 7.7 (a)], hexagonal tubes were simulated with the external field being parallel ( $\pi$  configuration) and normal ( $\kappa$  configuration) to the facets [Fig. 7.7 (b)]

In this paragraph, we compare the simulation results at saturation with the analytic solution of Prat-Camp *et al.* [PCNCS12]. They calculated the demagnetization field  $H_d$  in an infinitely long cylindrical tube in saturation. In Fig. 7.8 we show simulation results of tubes with internal radius  $r_i = 75$  nm and thickness  $t = 20$  and  $21$  nm for cylindrical and hexagonal shape, respectively. We apply an external field of  $H_{\text{ext}} = 1.2 M_s$  along the  $y$ -axis in cylindrical and along the  $x$ -axis in  $\pi$  configuration. In Fig. 7.8 (a) we plot the simulation result for the normalized demagnetization field  $h_d = -H_d/H_{\text{ext}}$  as a function of the azimuthal coordinate  $\vartheta$  along the tube circumference. A  $\cos(2\vartheta)$  behavior similar to the results of Prat-Camp *et al.* (not shown) is obtained [PCNCS12]. Also we find that  $h_d$  has a stronger dependence on  $\vartheta$  at the inner surface, i.e. at smaller radial distance  $r$  from the center. A two-dimensional plot of  $h_d$  is given in Fig. 7.8 (b). For comparison, maps for both hexagonal orientations are provided in Fig. 7.8 (c) and (d). While the field distribution is comparable in the cylindrical and the

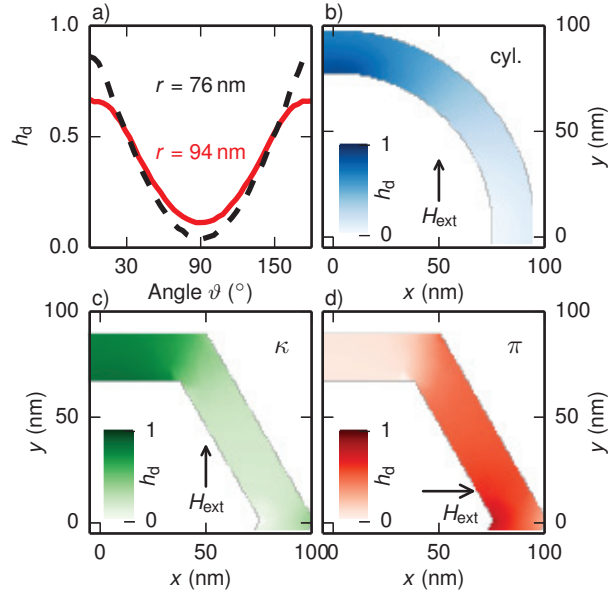


Figure 7.8 – (a) Normalized demagnetization field  $h_d = -H_d/H_{\text{ext}}$  in field direction in a cylinder as a function of the azimuthal coordinate  $\vartheta$  at a radial position  $r = 76$  nm (dashed line) and  $94$  nm (full line). Cross-sections of  $h_d$  for (b) a cylinder, (c) hexagon in normal orientation and (d) in parallel orientation. Parameters employed:  $r_i = 75$  nm,  $t = 20$  and  $21$  nm for cylinder and hexagon, respectively. In all cases, an external field of  $H_{\text{ext}} = 1.2 M_s$  was applied.

scenario  $\kappa$ , it differs strongly for  $\pi$ .

We now investigate simulated hysteresis curves and extract the influence of the demagnetization field. In Fig. 7.9 (a) the projection of the averaged and normalized magnetization on the field direction,  $\langle m_H \rangle = \langle \mathbf{M} \cdot \mathbf{H}_{\text{ext}} / M_s / H_{\text{ext}} \rangle$ , is given for the  $\kappa$  configuration. The axial component  $\langle m_z \rangle = \langle M_z / M_s \rangle$  is given in Fig. 7.9 (b). We find two characteristic changes in the slope of  $\langle m_H \rangle$  and  $\langle m_z \rangle$  as a function of  $H_{\text{ext}}$ . We denote the field positions where the slope  $\langle m \rangle (H_{\text{ext}})$  changes with A and B. Both curves saturate for large fields. The variations in the slope can be detected by maxima in the second derivative of  $\langle m_z \rangle$  [Fig. 7.9 (c)]. In Fig. 7.9 (d-f) similar curves can be found for the  $\pi$  configuration of a nanotube with the same dimensions. Here, the kink A in  $\langle m_z \rangle$  is less pronounced and a third maxima in  $\langle m_z \rangle''$ , which we label with C, is observed. We define the field values of such maxima A, B and C as

$$\eta_j = H(\max(\langle m_z \rangle'')) / M_s \text{ with } j = A, B, C. \quad (7.1)$$

In Fig. 7.10 evaluated parameters<sup>2</sup>  $\eta_j$  are summarized for a wide variety of  $r_i = 12.5, 25, \dots, 150$  nm and  $t = 15, 20, \dots, 50$  nm and plotted as a function of the ratio between inner and outer radius  $\beta = r_i/r_o$ .

<sup>2</sup>The maxima were calculated automatically by a script. First,  $\langle m_z \rangle''$  was calculated and the signal smoothed with a 10 point hanning window. Only local maxima above a threshold of  $0.04 \times \max(\langle m_z \rangle'')$  were considered.

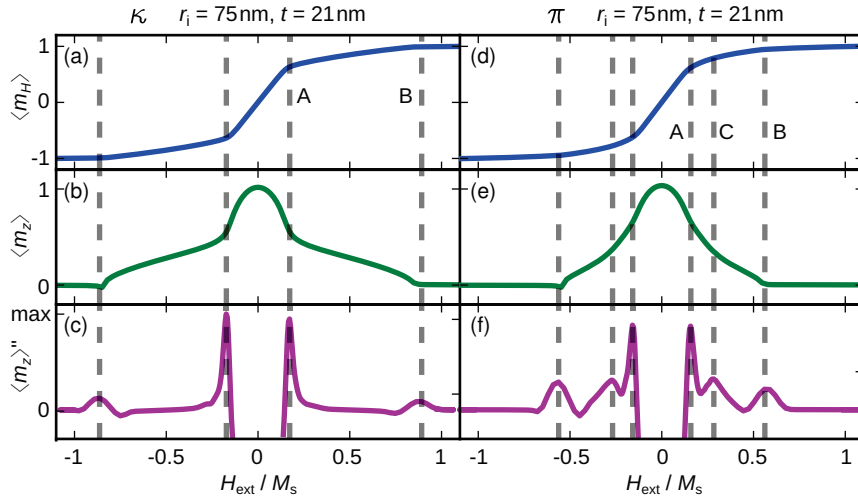


Figure 7.9 – Projection of the averaged magnetization (a)  $\langle m_H \rangle$ , parallel to the external field, and (b)  $\langle m_z \rangle$ , parallel to the axis in an hexagonal tube with  $r_i = 75$  nm and  $t = 21$  nm in  $\kappa$  orientation. The curves exhibit two characteristic changes, denoted A and B in the slope of the hysteresis curve: The field positions A and B can be extracted via maxima in the second derivative of  $m_z$ , depicted in (c). Similar curves for the  $\pi$  orientation are shown in (d-f). Here, the kink A is less pronounced in  $\langle m_z \rangle$  and a third maxima in  $\langle m_z \rangle''$  is observed and denoted with C.

For cylinders (circles) and the  $\kappa$  configuration (squares), we find two consistent branches  $\eta(\beta)$ . They almost meet at a value of about 0.5 for small  $\beta$ . In the limit  $\beta \rightarrow 1$ ,  $\eta$  reaches values of 0 and 1 for A and B, respectively. For  $\beta < 0.7$ , the difference between  $\eta$  for cylinder and  $\pi$  configuration is negligible. The A branch shows only minimal deviation between the two cases. In contrast, we find that  $\eta$  of the  $\pi$  configuration never exceeds  $\sim 0.6$  and stays almost constant for all simulated dimensions ( $B_\pi$  in Fig. 7.10). Furthermore, we find a third branch of  $\eta$  (C in Fig. 7.10), which tends towards zero for  $\beta \rightarrow 1$ .

## 7.2.2 Measurements

Before we discuss the microscopic understanding, we turn to the experimental findings. Figure 7.11 shows magnetotransport data for an individual CoFeB nanotube with a total length  $L = 16.7 \mu\text{m}$ , contact spacing of  $L_p = 7.8 \mu\text{m}$  and  $t = 20$  nm. A slight tapering leads to a variation of the outer diameter  $2 \times (r_i + 2/\sqrt{3} \cdot t)$  from 185 to 225 nm along the full length. We plot  $R$  as a function of  $\mu_0 H_{\text{ext}}$  for field sweeps from positive to negative fields (solid line) and back (dashed line). The curves on the top were acquired with  $\mathbf{H}_{\text{ext}} \parallel \mathbf{e}_z$ , the bottom curves with perpendicular field. The linear and negative magnetoresistance found for  $\mathbf{H}_{\text{ext}} \parallel \mathbf{e}_z$  is attributed to the suppression of magnon-scattering. This slope is also found at large fields in the bottom curve. We thus believe that  $\mathbf{M}$  saturates at about 1 T in perpendicular fields. We find

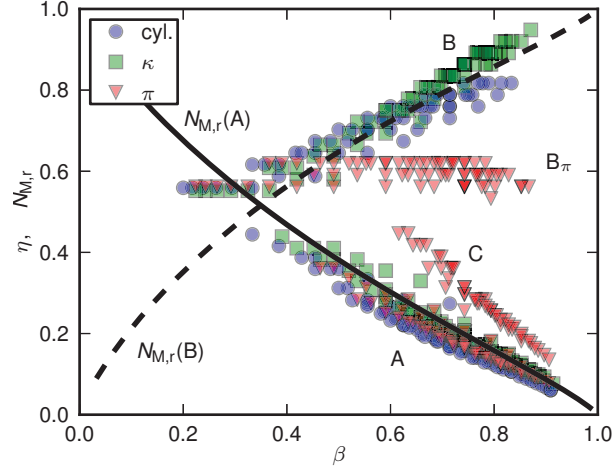


Figure 7.10 – Simulated parameters  $\eta_j$  as a function of the ratio of inner and outer radii  $\beta = r_i/r_o$  for cylinders (circles), as well as hexagons with  $\kappa$  (squares) and  $\pi$  (triangles) configuration. For comparison, the analytic solutions  $N_{M,r}$  for a rectangular prism with side ratios  $p_r$  (A) =  $[2r_i \cos(30^\circ)]/t$  (solid line) and  $p_r$  (B) =  $t/2r_i$  (dashed line) are given [Aha98].

two kinks A and B where the slope of  $R(H_{\text{ext}})$  changes<sup>3</sup> for  $H_{\text{ext}} \perp \mathbf{e}_z$ . The observed  $R(H_{\text{ext}})$  is consistent with the simulations of  $\langle m_z \rangle(H_{\text{ext}})$  considering that the AMR effect depends on the relative orientation between  $\mathbf{M}$  and the axially applied current [cf. Eq. 4.2]. The kink position A is determined manually to be  $\mu_0 H_{\text{ext}}(A) = 0.17 \pm 0.03$  T (magenta shaded region).

### 7.2.3 Discussion

We now turn to discuss the physical origins of the characteristic signatures found in simulation and experiment. We know from the calculations of Prat-Camps *et al.* and the data presented in Fig. 7.7 that  $H_d$  is inhomogeneous. This is to be expected, considering the non-elliptical form of a hollow tube. Aharoni *et al.* [APK00] argued that the magnitude of the field at which most of the magnetization saturates equals  $N_M \times M_s$  in isotropic materials.  $N_M$  is the magnetometric demagnetization factor (cf. Sec. 3.2.2.3). Following this argumentation, one can interpret the determined  $\eta$  of Eq. 7.1 as an effective demagnetization factor for a certain segment of the tube cross-section. In a first approximation, we approximate such segments by rectangular prisms as sketched in Fig. 7.12. The magnetometric demagnetization factors  $N_{M,r}$  for such prisms are to be calculated by Eq. 3.27.

In the cylindrical and  $\kappa$  case, the two kinks in the hysteresis curve suggest that the tube can be modeled as a conjunction of elongated prisms aligned parallel [Fig. 7.12 (a)] and perpendicular to the field [Fig. 7.12 (b)]. Because of their relative orientation to the field, each prism is expected to experience a different average demagnetization factor  $N_{M,r}$ , which we label

<sup>3</sup>Note that due to the limited S/N-ratio, the calculation of a second derivative is not feasible. The kink positions are determined by eye.

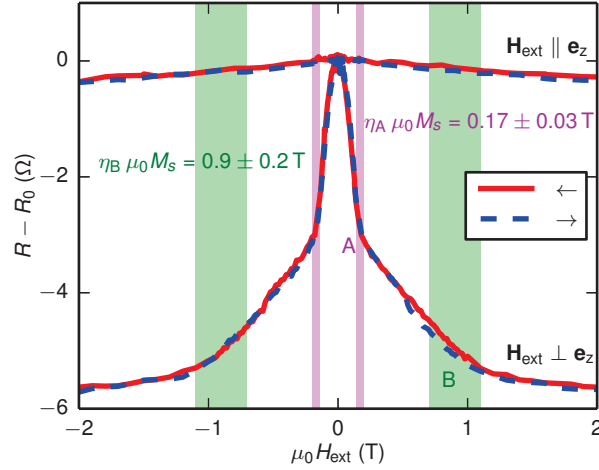


Figure 7.11 – Resistance  $R - R_0 = R - 4.166 \text{ k}\Omega$  as a function of the external field  $\mu_0 H_{\text{ext}}$  for field parallel (top) and perpendicular (bottom) to the axis at 180 K. The field was swept from high to low fields (solid lines) and back (dashed lines). We determine the point of kink A  $\mu H_{\text{ext}}(A) = \eta_A \mu_0 M_s$  to  $0.17 \pm 0.03 \text{ T}$  (magenta colored region). Using the simulation results (see text) this allows us to estimate  $M_s = 800 \pm 170 \text{ kA/m}$ . The magenta colored region depicts the position of kink B as calculated from  $M_s$  and the simulated  $\eta_B$  (see text).

$N_{M,r}(A)$  and  $N_{M,r}(B)$  in the following. If one dimension is much larger than the other two, the demagnetization factor can be expressed as a function of  $p_r = l_{\parallel} / l_{\perp}$ , which is the ratio of the length of the prism's sides parallel and perpendicular to the field [Fig. 3.1]. In a first approximation, the short axis is chosen equal to the wall thickness  $t$  of the tube. For the long axis, the projection of the hexagonal tube onto the cartesian axis is chosen, as can be seen in Fig. 7.12. The prism with  $H_{\text{ext}}$  pointing normal to its surface [Fig. 7.12 (b)] experiences a strong demagnetizing effect leading to high values of  $N_{M,r}$ . In case of the field being parallel to the surface [Fig. 7.12 (a)], the smaller amount of surface charges will cause less opposing field. Therefore we expect small  $N_{M,r}$  in these segments.

In Fig. 7.10 we plot the analytic solution  $N_{M,r}(A)$  for a rectangular prism with infinite extension in the  $z$ -axis and  $p_r(A) = [2r_i \cos(30^\circ)] / t$  (solid line) as well as  $N_{M,r}(B)$  with  $p_r(B) = t / [1 + 2 \times \cos(60^\circ)] r_i = t / 2r_i$  (dashed line). We find a close agreement between the simulated  $\eta$  and  $N_{M,r}$  from the model consideration. The peculiar behavior of the  $\pi$  orientation is discussed in the same framework: here, however, the tube is considered to comprise three pairs of prisms: one with the long axis aligned parallel to the field, one under an angle of  $30^\circ$  and finally the edge where two facets touch. This region is expected to behave as an almost square rod. While the first two prisms lead to very similar  $\eta < 0.5$ , the other, due to its rod-like cross-section, is expected to have  $\eta$  close to 0.5 and independent of  $r_i / r_o$ .  $B_\pi$  in Fig. 7.10 exhibits such a behavior.

In Pub. A-II (cf. Sec. 6.2), the saturation field of a Ni and a CoFeB tube, i.e. field positions B, were compared assuming comparable  $N_M$ . On the one hand, the results of the presented

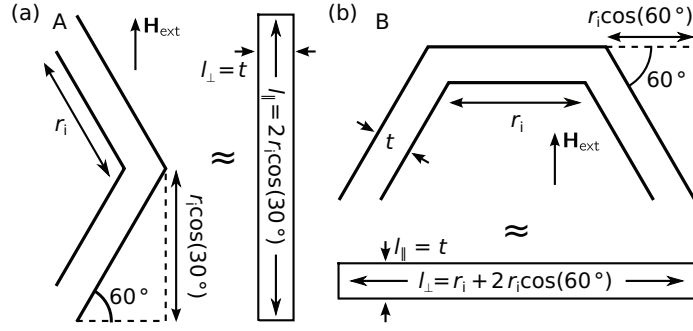


Figure 7.12 – Model for approximation of a hexagonal tube in  $\kappa$  configuration by two rectangular prisms for the two branches (a) A and (b) B. For the shorter axis,  $t$  is chosen. The longer axis is the appropriate projection of the tube along the field direction.

simulations support comparable  $N_M$  in that the deviation between  $\eta$  for a cylinder and for a hexagon is comparatively small and negligible for  $r_i/r_o \lesssim 0.7$ , if the field is oriented normal to two facets ( $\kappa$  orientation). This was the case in Pub. A-II (cf. Sec. 6.2). On the other hand, due to the relatively small change of slope at B, the field position defining  $N_M$  (B) inherits a larger error compared to  $N_M$  (A). It is advantageous to use  $N_M$  (A) because the stronger curvature reduces the uncertainty in the determination of the relevant field position A.

Assuming that the resistance traces  $R(H_{\text{ext}})$  for a perpendicular field (bottom curves in Fig. 7.11) are related to  $\langle m_z \rangle^2$ , we use the simulation result of  $\eta_A$  to estimate  $M_s$ <sup>4</sup>. The median radius of the tube corresponds to the curve presented in Fig. 7.9 (a). Our simulations assume constant  $r_i$  and thus neglect the tapering of the nanowire. To give an estimate of an error using our simulations, we take the difference of values  $\eta_A$  and  $\eta_B$  calculated for the extremal values of  $r_i$  to the one at  $\langle r_i \rangle$  as the uncertainty (curves not shown). By this, we yield  $\eta_A = 0.17 \pm 0.02$  and  $\eta_B = 0.87 \pm 0.03$ . Setting the measured kink position of A,  $\mu_0 H_{\text{ext}}(A) = 0.17 \pm 0.03$  T, equal to the simulated saturation field  $\eta_A \mu_0 M_s$  of the corresponding segment, we derive  $M_s = 800 \pm 160$  kA/m. As a cross-check we calculate the predicted saturation field of the remaining segment, which corresponds to position B, via  $\mu_0 H_{\text{ext}}(B) = \eta_B \mu_0 M_s$  to  $0.9 \pm 0.2$  T (green shaded region). The field region corresponds well with the experimental data, further supporting the interpretation. The simulations support the approach in Pub. A-II, where high-field kinks in  $R(H_{\text{ext}})$  were suggested to provide the magnetometric demagnetization factor.

So far we assumed  $\eta$  to be a solely geometric parameter, similar to the magnetometric demagnetization factors  $N_M$ . As long as the magnetization is not homogeneous over the whole sample, this assumption is not completely correct. The domain boundary linking the two segments adds additional energies and varies the exact position of the kinks as a function of  $M_s$ . For more accurate results, a number of simulations with an iterative adaptation of  $M_s$  would be necessary. Because the tapering was ignored and the determination of the kink

<sup>4</sup>The relation neglects the influence of Ohm's law in combination with locally varying angle between current flow and magnetic moments. As we use the field values at which the slope of  $\langle m_z \rangle$  changes, it is negligible.

## Chapter 7. Magnetization reversal in CoFeB tubes

---

position in the measured data introduces an additional uncertainty, we think the influence of this error not to be relevant for the evaluation. Note that the derived  $M_s$  is equal to the value of  $870 \pm 30$  kA/m, determined via cantilever magnetometry (cf. Sec. 6.4) by our collaborators in Basel [Web14], within the accuracy.



## 8 Pub. A-III: Quantized exchange spin waves in ferromagnetic nanotubes

The following chapter focuses on the study of spin dynamics in individual ferromagnetic nanotubes. Here a draft version of a manuscript is reproduced.

D. Ruffer, J. Mendil, S. Wang, T. Stückler, R. Huber, T. Schwarze, F. Heimbach, G. Tütüncüoğlu, F. Matteini, E. Russo-Averchi, R. R. Zamani, J. R. Morante, J. Arbiol, A. Fontcuberta i Morral, and D. Grundler

I designed the experiment and the relevant parts of the measurement when visiting the group Prof Dirk Grundler in Munich. I coordinated and conducted largely the sample preparation and pushed the data analysis and interpretation. The simulations were conducted and analyzed by myself.

### Introduction

Recent advances in magnonics [KDG10, DUD10, LUGM11, YDH<sup>+</sup>13a, VFP<sup>+</sup>14] fostered new ideas for information processing concepts without charge transport, based on the propagation of spin waves with a characteristic wavelength of few nanometer. This sets new grounds for new and much smaller logic elements. The potential of these new building blocks will materialize only when the underlying spin wave dynamics is understood. In this paper we demonstrate ferromagnetic nanotubes as tubular cavities for dipole-exchange spin waves and evidence their functionality for spin wave-based electronics by electrical detection of magnonic resonance modes via the spin-rectification effect [MGH07, HCG<sup>+</sup>11, GY13]. The GHz near-field of an adjacent microwave antenna excites the modes in individual nanotubes created from the three different materials, i.e., Ni [RHB<sup>+</sup>12], CoFeB [RSH<sup>+</sup>14] and Ni<sub>80</sub>Fe<sub>20</sub> (permalloy Py). Here, we focus on Py that has already turned out to be of utmost relevance in magnetoelectronics, spintronics and magnonics. The symmetry and microscopic nature of the modes is modeled by micromagnetic simulation. The modeling substantiates the exchange

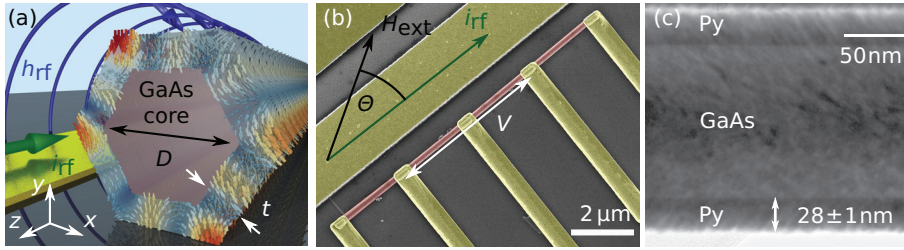


Figure 8.1 – (a) Depiction of the simulated dynamic spin configuration of mode  $\mu_6$ . A SEM image of the nanotube with voltage probes is given in (b). (c) TEM image of a Py tube, indicating a shell thickness of  $28 \pm 1$  nm.

character of the modes and is the basis for creating more advanced devices.

## Main

To the best of our knowledge, experiments addressing the spin dynamics in an individual nanotube with a radius below 100 nm have not yet been reported. The previous experimental studies on spin wave resonances of ferromagnetic tubular structures have been limited to large ensembles formed in porous alumina [WLZ<sup>+</sup>06] or rolled-up ferromagnetic layers (RUFLs) on semiconductor membranes with micrometric radii [MPT<sup>+</sup>08, BMK<sup>+</sup>10, BJH<sup>+</sup>12, BNM13, BBJ<sup>+</sup>13]. Addressing individual RUFLs the authors translated spin wave physics from the planar to the tubular form [KS86]. The model is not valid for radii below 100 nm due to increased relevance of the short-range exchange interaction. Dispersion relations have also been calculated using models for cylindrical systems with thin tube walls [LV04, GLNn10, DC11]. These models are not directly applicable to our system because of the non-negligible thickness and the hexagonal cross-section of the tubes.

Figure 8.1 (a) shows a schematic drawing of the device. A coplanar microwave waveguide (CPW) positioned next to a ferromagnetic nanotube induces a dynamic magnetization. The latter induces a voltage across the nanotube, which is detected by the contacts. An image of the device is shown in Fig. 8.1 (b). A nanotube with 5 electrical contacts is positioned parallel and 720 nm away from the CPW. The ferromagnetic nanotube consists of a 28 nm thick permalloy (Py) layer wrapped-around a non-ferromagnetic GaAs nanowire, obtained by sputtering as explained in Refs. [RHB<sup>+</sup>12, RSH<sup>+</sup>14]. Py constitutes an ideal candidate thanks to its low damping and the sufficiently large anisotropic magneto resistance (AMR) [MP75]. A transmission electron micrograph of the material is shown in Fig. 8.1 (c). In the lateral view image we can observe a 28 nm thick permalloy (Py) layer covering the GaAs NW core. Notice that the permalloy is forming columnar-like structure which present a  $55^\circ$  angle versus the lateral GaAs surface.

Following the Biot-Savart law, the rf-current  $i_{rf}$  travelling through the CPW generates a dynamic magnetic field  $h_{rf}$  around it, which in turn couples to the adjacent ferromagnetic nano-

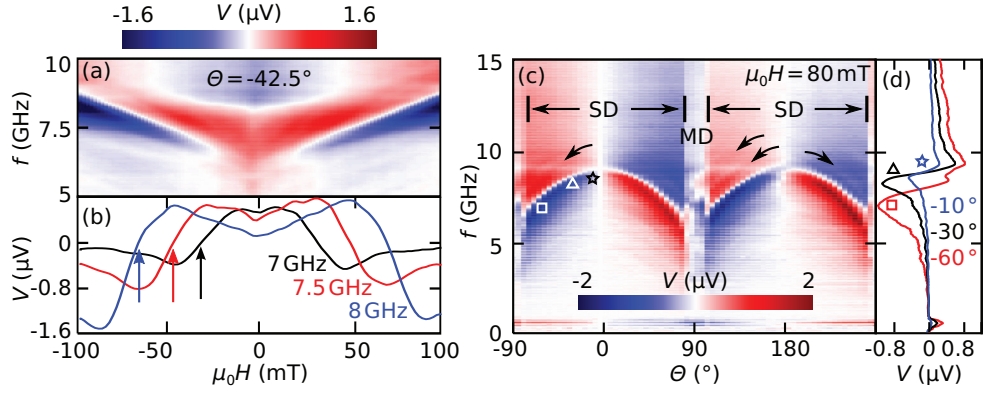


Figure 8.2 – (a) Generated voltage  $V$  as function of the external field  $\mu_0 H$  at an angle  $\theta = -42.5^\circ$  to the tube axis. A feature with Lorentzian line shape, ranging from 6 GHz at zero field to 8.8 GHz at 100 mT, can be discerned. Cuts at fixed  $f$  are given in (b). (c) The frequency of the mode decreases from 8.9 GHz at  $H \parallel$  axis to about 6 GHz at  $|\theta| \approx 70 - 80^\circ$ , at which point a sharp change in the signal indicates the transition from the single domain (SD) to a multi domain (MD) configuration. The signal is found to be antisymmetric around 0 and it shows a  $180^\circ$  periodicity. (d) Traces at  $\theta = -10^\circ$  (blue),  $-30^\circ$  (black) and  $-60^\circ$  (red).

tube and induces a dynamic magnetization  $\mathbf{M}$  [Fig. 8.1 (a)]. Thanks to the spin-rectification effect, the induced spin-dynamics are translated into a resistance modulation at the same frequency  $f$ . Adding this to the current generated inductively by the CPW, there will be a frequency-dependent voltage drop across the ferromagnetic nanotube directly related to the spin-dynamics [GMZ<sup>+</sup>07b, MGH07, HCG<sup>+</sup>11, GY13]. As a consequence, the interaction between the CPW and the ferromagnetic nanotube generates a dc voltage in the form:  $V = \langle R(t) \cdot I(t) \rangle \propto \langle \Delta R \cos(\omega t + \phi) \cdot \cos(\omega t) \rangle \propto \Delta R \cdot \cos(\phi)$ . Following this expression,  $V$  does not only depend on the change of resistance due to precession,  $\Delta R$ , but also on the phase difference  $\phi$  between the induced current and resistance oscillation. In order to explore the role of the overall magnetization configuration of the nanotube with the spin wave dynamics, we have also applied an external magnetic field,  $H$ , and rotated it an angle  $\theta$  with respect to the nanotube axis.

The data presented in Fig. 8.2 were acquired on the device shown in Fig. 8.1 (b). The signal was measured between contacts 2 and 4, defining a roughly  $4 \mu\text{m}$  long segment. The inner nanowire exhibits a tapering of 7%, resulting in a slight gradual variation of the inner and outer diameter of the nanotube. The inner diameter is  $D = 130 \pm 15 \text{ nm}$ . Figure 8.2a depicts the generated  $V$  as a function of  $f$  and the amplitude of the external field  $\mu_0 H$ , for an angle  $\theta$  between  $\mathbf{H}$  and axis of  $-42.5^\circ$ . The most pronounced resonance (main mode) is detected by a peak in the generated voltage. The resonance frequency depends on the magnitude of the magnetic field applied. Traces of the generated voltage at a fixed frequency are shown in Fig. 8.2 (b). The curves are symmetric with respect to  $H = 0$ . In Fig. 8.2 (c), we show the evolution of the generated voltage as function of the angle of the magnetic field with the nanotube axis. The mode frequency exhibits a  $180^\circ$  periodicity. The maximum frequency is

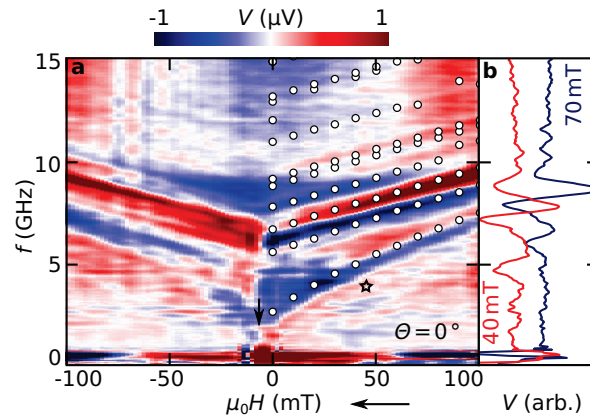


Figure 8.3 – (a)  $V(f, \mu_0 H, \theta = 0)$ , showing a dominant feature in the range of 6.5 to 10 GHz and multiple higher modes. The field was swept from positive to negative fields. For low frequencies, we find another non-linear mode, which extends into negative fields until the magnetization reverses, marked by an arrow. The circles give the position of resonant modes as determined by simulation. (b) Voltage traces at  $\mu_0 H = 40$  and 70 mT.

found when the field is aligned with the easy axis, i.e., the long axis of the nanotube, meaning  $\theta = 0$  and  $180^\circ$ . At the same time the voltage signal is zero as a sign change of the detected voltage occurs at zero degree and multiples of  $90^\circ$ . We observe the maximum signal strength at about  $\theta = 60^\circ$  (Fig. 8.2 (d)). Here further modes of significantly smaller intensity (arrows in Fig. 8.2 (a)) are resolved. For slightly larger angles, around  $80^\circ$ , we see an abrupt change in the voltage signal that we attribute to the magnetization reversal of the nanotube (AMR traces proving this can be found in the supplementary information, App. A.2).

We turn now to the study of the spin-dynamics of the nanotube when we apply  $H$  along the long axis ( $\theta = 0$ ), i.e., the easy axis. Outside the hysteretic region around  $H = 0$  the magnetization is expected to be parallel to the applied field allowing for a detailed mode analysis. In Fig. 8.3 we show the voltage signal detected for a broad regime of frequencies and applied fields. The main mode (varying from about 6.5 GHz at zero field to 9 GHz at  $\pm 100$  mT) is weak for this angle  $\theta$  as described above and the signal strength is not perfectly symmetric around zero magnetic field. This feature is attributed to the zero crossing of the signal at  $\theta = 0$ . Besides this mode, we resolve a number of further resonances that depend on the applied field  $H$ . Up to four modes can be discerned for frequencies between 10 to 15 GHz that seem to depend almost linearly on  $H$ . For  $H < 0$  and  $f$  slightly below the main mode, we find a fine structure suggesting a few new resonant peaks. A further mode exhibits a resonance frequency of  $f \approx 2$  GHz at zero field and reaches about 6.5 GHz at 100 mT [star in Fig. 8.3 (a)]. This mode obeys an approximately square-root dependence on  $H$  different from the earlier discussed modes. When decreasing  $H$  from large positive fields we observe that several of the mode branches are continuous at  $H = 0$  and can be followed down to about -7 mT [arrow in Fig. 8.3 (a)]. This indicates that the uniaxial anisotropy of the long nanotube supports a single-domain configuration at zero field and in a small opposing field. Similarly rich mode spectra were found in Ni and CoFeB tubes (cf. supplementary information App. A.2).

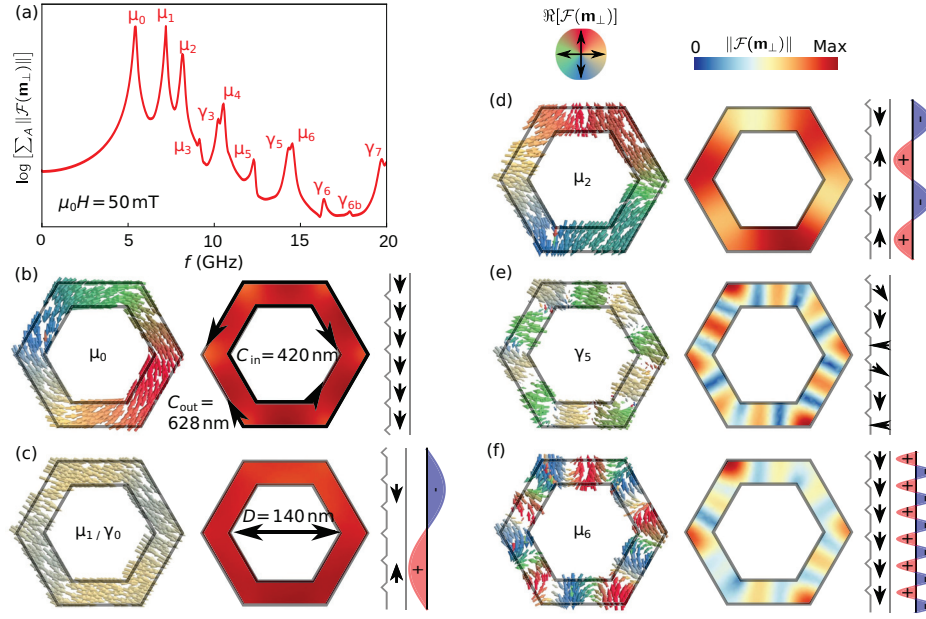


Figure 8.4 – (a) Simulated mode spectrum for an applied field  $\mu_0 H = 50$  mT along the axis. We identify thin-film-like modes ( $\mu$ ) and 2D-modes ( $\gamma$ ) from the vectorial representation of the modes [(b-f), left column]. The thin film modes can be understood as standing spin waves, quantized along the circumference, and can be illustrated in a picture of an unrolled film (right column). The spatial distribution of the magnitude of precession,  $\|\mathcal{F}(\mathbf{m}_\perp)\|$ , is depicted in the center column of (b-f). The 3D-modes split off from existing thin-film-like modes above 10 GHz and show segments with correlated phase in the global coordinates. Adjacent segments have roughly  $\pi$  phase shift. As an example, we show the modes  $\gamma_5$  and  $\mu_6$  in (e) and (f).

Consistent with the smaller (larger) saturation magnetization compared to Py, the modes of the Ni (CoFeB) nanotubes were shifted to smaller (larger) frequencies. In their case, the single domain state was not present at zero field.

In order to understand the rich spectra of the Py nanotube of Fig. 8.3 in detail we performed dynamic micromagnetic simulations. Circles in Fig. 8.3 (a) represent eigenfrequencies of spin wave resonances extracted from the simulations (Methods section). An exemplary spectra,  $\sum_A \|\mathcal{F}(\mathbf{m}_\perp)\|$ , at  $\mu_0 H = 50$  mT and  $\theta = 0$  is depicted in Fig. 8.4 (a). Taking into account phase profiles such as those shown in the right column of Fig. 8.4 (b-f), we distinguish between thin-film-like modes following the tubular geometry ( $\mu_x$ ,  $\mu=0,1,\dots$ ) and 3D-like modes ( $\gamma_x$ ,  $\gamma = 0, 1, \dots$ ) where the phase-evolution does not fulfill the interference condition along the perimeter. This complex spin-precessional motion occurs when azimuthal spin waves hybridize with perpendicular standing spin waves. Such a hybridization could occur in a segment-wise manner as the thickness of the ferromagnetic material varies between the planar facets and the corners. The  $\mu$ -modes represent azimuthal spin waves fulfilling the interference condition along the perimeter of the nanotube. The condition for interference reads  $\mu \times \lambda = C$ , i.e.,  $k = 2\pi\mu/C$  with  $\mu = 0, 1, 2, \dots$  and a circumference  $C = 3 \times D$ . This condition becomes evident if we unroll the simulated spin-precessional motion extracted at a specific point of



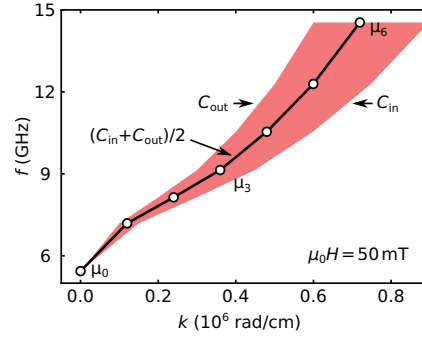


Figure 8.5 – Dispersionrelation  $f(k)$  calculated with the standing spin-wave condition  $k = \mu \cdot 2\pi/C$ . While the black line shows the results for median circumference,  $\langle C \rangle = (C_{in} + C_{out})/2$ , the red area gives the range for inner,  $C_{in}$ , and outer,  $C_{out}$ , circumference.

time [cf. third column of Fig. 8.4 (b-f)] and follow the phase evolution (right). For the lowest frequency mode  $\mu_0$ , the dynamic magnetization component rotates exactly once through  $360^\circ$  along the circumference. Projected on a plane, the spin-precessional motion agrees to the uniform precession in a plain film, i.e., a thin-film spin wave with infinite wavelength, i.e.,  $\mu = 0$ . For the next higher-frequency mode, the dynamic magnetization component is found to be parallel over the full cross-section. This compares to the ferromagnetic resonance, i.e., uniform precession, in a bulk material ( $\gamma_0$ ). However, if projected on a plane, the spin-precessional motion is also consistent with a standing wave exhibiting a wavelength that equals the perimeter, i.e.,  $\mu = 1$ . In total, we identify modes with  $\mu = 0, \dots, 7$ . 3D-modes have parameters  $\gamma = 0, 3, 5, 6, 7$  for  $0 < f < 20$  GHz.

Using the interference condition for the  $\mu$ -modes, we extract a dispersion relation  $f(k)$  as shown in Fig. 8.5. For the open circles we assume the perimeter to be relevant. The shaded area takes into account that spin waves move closer to the inner (outer) surface, thereby experiencing a smaller (larger) circumference  $C_{in}$  ( $C_{out}$ ). The relevant wave vectors  $k$  of the mode frequencies observed in the experiment are as large as  $0.8 \cdot 10^6$  rad/cm. The group velocities  $v_g = 2\pi df/dk$  range from 500 to 1200 m/s. For  $\mu > 1$   $f(k)$  follows roughly a  $k^2$  dependence. This dependence is consistent with exchange-dominated spin waves [LV04, GLNn10, DC11]. Going beyond the rolled-up thin films reported in Refs. [MPT<sup>+</sup>08, BMK<sup>+</sup>10, BJH<sup>+</sup>12, BNM13, BBJ<sup>+</sup>13] the nanotubes presented here are thus true tubular spin wave resonators and provoke azimuthal interference for both dipolar- and exchange-dominated spin waves. Our results obtained on nanotubes prepared from Ni, Py and CoFeB (cf. supplementary information, App.A.2) show that the relevant frequency band for the spin waves is determined by the specific ferromagnetic material. Figure 8.5 indicates that within a given band the exact resonance frequencies are then tailored by the diameter of the semiconductor core, i.e., the circumference  $C$ . The nanotubes presented here thus allow one to optimize and fine-tune the operational frequency if exploited in nanomagnonic devices.

In summary, we measured azimuthally confined spin wave modes in nanoscale ferromagnetic nanotubes using the spin-rectification method. The rich spectra of observed modes

---

was analyzed using micromagnetic simulations and attributed to the interference of both dipolar- and exchange-dominated azimuthal spin waves. Magnonics aims at transmitting and processing information with spin waves on the nanoscale. Here exchange-dominated spin waves are key as propagation velocities are proportional to  $df/dk \propto k$  and become large for large  $k$ , i.e., short wavelengths. The spin-rectification effect explored here paves the way for the integration of nanotube-based magnonics with spintronics.

## Methods

The ferromagnetic nanotubes are fabricated by thermal evaporation of  $\text{Ni}_{80}\text{Fe}_{20}$  under an angle of  $35^\circ$  onto the facets of vertical GaAs nanowires grown catalyst-free in a molecular beam epitaxy chamber [UAM<sup>+</sup> 11, RAHM<sup>+</sup> 12]. The homogeneity of the shell was verified on nanotubes fabricated in the same batch by means of bright field (BF) transmission electron microscopy (TEM) in a Tecnai F20 operated at 200 keV with a lattice resolution of 0.14 nm. The relative composition of the shell determined by electron energy loss spectroscopy (EELS) to  $79.6 \pm 0.4\%$  ( $20.4 \pm 0.4\%$ ) for Ni (Fe). The tubes are released by sonication in isopropyl alcohol and transferred to a 4" Si(100) wafer with 200 nm of oxide. The wafer comprises pre-patterned gold alignment markers for the precise location of the randomly positioned nanotubes by optical lithography via a custom developed software. In a first electron beam lithography (EBL) step, the five contacts to the nanotubes are defined in a Vistec EPBG500ES system. In an Alliance Concept DP650 system, a 1 min in-situ RF-etch at  $5 \cdot 10^{-2}$  mbar Ar atmosphere and 100 W is followed by sputter deposition of 5 nm Ti and 150 nm Au. After ultra-sound assisted lift-off, a second EBL defines the waveguide, which are sub-sequentially deposited by thermal evaporation of 5 nm Ti and 120 nm Au utilizing a LAB600H system and released by lift-off. The waveguides' dimensions are chosen such as to avoid insertion loss due to impedance mismatch. The stripline, having a width of  $2.0 \pm 0.1 \mu\text{m}$  is separated by a gap of  $1.3 \pm 0.1 \mu\text{m}$  to the  $35 \mu\text{m}$  wide ground line.

The contacts to the nanotubes are wire-bonded and the samples mounted into a custom designed two-vector magnet generating fields up to 100 mT under arbitrary in-plane angle. The microwaves are guided from a Agilent N5183A 100 kHz to 20 GHz signal generator via coaxial cable to Picroprobe rf wafer probe tips contacting the waveguides. The voltage signal, measured between contacts 2 and 4 [Fig. 8.1b (,)] is detected using a Keithley 2182 nanovoltmeter. To improve the S/N ratio and suppress spurious signals we employ a three-step delta method: the rf output is modulated by a rectangular signal synchronized with the nanovoltmeter and the signal is calculated as the difference of samples at zero and maximal power.

A slowly varying background signal is removed from the acquired raw data by subtracting the frequency trace for  $\theta = -2.5^\circ$  [Fig. 8.2] or taking the difference at each frequency with the average value over  $H$  [Fig. 8.3]. Noise was removed using a 4<sup>th</sup> order 2D Savitzky-Golay filter with a window size of 11 samples on the  $102 \times 299$  matrix of  $(H \times f)$ -data in Fig. 8.3.

Mecking et al. [MGH07] found the largest spin-rectification signal when the magnetization

vector of a saturated ferromagnetic stripe was tilted by  $45^\circ$  with respect to the antenna. For our nanotube we apply a field below the saturation field and achieve the largest signal only for  $\theta = 60^\circ > 45^\circ$  due to the demagnetization effect.

For the micromagnetic simulations, the open source finite element method (FEM) simulation toolkit Nmag [FFBF07] was utilized. Using a quasi-periodic approach [FBF<sup>+</sup>09], the tube was approximated by 250 copies on either side of a hexagonal 20 nm nanotube slice with 30 nm film thickness, inner diameter  $D = 140$  nm and an average mesh size of 5 nm. Values of  $1.3 \cdot 10^{-11}$  J/m and 400 kA/m were chosen for the exchange coupling parameter and the saturation magnetization, respectively. Having  $\mathbf{M}$  relaxed for given  $\mu_0 H$  and  $\theta$ , a 10 ps and 100 mT pulse in  $y$ -direction was added to the static field, which was oriented along the  $z$ -axis. To achieve an asymmetric excitation, the pulse was only applied for  $x < 0$ . Using a damping parameter of 0.008, the time evolution was calculated and stored every 10 ps for 20 ns and transformed into the frequency domain using Fast Fourier Transform (FFT). The pulse strength was chosen to minimize numerical noise and artifacts and it was verified that at smaller pulse amplitudes the mode position does not vary significantly. Using the saturation magnetization value of  $M_s = 400$  kA/m, we obtained the best agreement between data and simulation.

The spin-precession amplitude, second column in Fig. 8.4 (b-f), is almost perfectly homogeneous over the entire nanotube cross-section for  $\mu = 0$  and  $\mu = 1$ . The condition for a standing spin wave agrees with an integer number of phase cycles around the nanotube. The distribution of the spin-precession amplitude however can be more involved at shorter wavelengths in azimuthal direction due to the complex geometry. This can be seen for e.g.  $\mu_2$  showing maximal amplitudes in three locations [Fig. 8.4 (d)].

## Acknowledgments

The work has been supported by the DFG via GR1640/5-1 in SPP1538 "Spin caloric transport". Funding through the Swiss National Science Foundation NCCR QSIT and FP7 ITN Nanoembrace are greatly acknowledged. The authors D. Ruffer and D. Grundler would like to thank P. Landeros and J. Otálora for fruitful discussion.



## 9 Summary

The results of this thesis are summarized in this final chapter. For the reader's convenience, the cumulative summary is organized topically. First, the advances in fabrication and the results of the material characterization are summarized in Sec. 9.1. Here, the structure, the electrical characteristics, the AMR and the saturation magnetization of all three materials are compared. Section 9.2 continues with the quasi-static magnetic properties of the tube and the reversal of the magnetization. Finally, the spin wave resonance experiments are summarized in Sec. 9.3.

### 9.1 Ferromagnetic nanotubes

In the present thesis, the fabrication of ferromagnetic nanotubes composed of Ni, Py or CoFeB were successfully demonstrated. While previous works mainly considered deposition on side-walls of porous membranes or epitaxial growth of crystalline shells, a new approach was applied. Here, a ferromagnetic shell was deposited onto bottom-up grown semiconductor nanowires using ALD, thermal evaporation or magnetron sputtering for the fabrication of Ni, Py and CoFeB shells, respectively. The resulting shells were either polycrystalline or amorphous and in turn magnetically isotropic. Anisotropic magnetic the material is of importance, if the influence of the peculiar tubular shape on the magnetic properties is to be investigated

The structural quality of the tubes has been investigated by TEM microscopy. All methods yielded conformal shell thickness along the tube. The ALD-deposited Ni is polycrystalline and consists of ellipsoidal grains with dimensions of 10 nm×30 nm. The high roughness of the film surface led to the formation of nanothroughs. The process resulted in a circular outer shape of the Ni nanotubes. The thermally evaporated Py showed, in contrast, very little surface roughness. The film was homogeneous and polycrystalline. The sputtered CoFeB resulted in an amorphous material for the shell. Although the shell exhibited little surface roughness, a peculiar columnar structure can be found in cross-section TEM images. The origins of this feature are not understood at this point. The deposition with rotation under an angle could be responsible for the columnar structure. It should be noted at this point that both, the Py and

CoFeB shells, perfectly reproduce the faceting of the nanowire. The obtained nanotubes were found to have a hexagonal cross-section.

The resistivity  $\rho$  of individually contacted Ni nanotubes was measured as a function of the sample temperature  $T$ . It was found that  $\rho$  was a linear function of  $T$  for  $T \gtrsim 20\text{K}$ , which is typical for polycrystalline metals with dominant electron-phonon scattering. Enhanced electron scattering at the surfaces might motivate the low residual resistance ratio of about 2.6. The values of  $\rho$ , which are in the order of 20 to 30  $\mu\Omega\text{cm}$ , coincide well with numbers reported in nanostripes fabricated from thermally evaporated Ni. No typical metallic  $\rho(T)$  was observed for CoFeB tubes. Instead, the resistivity went through a minimum at around 100 to 200 K. For lower  $T$ ,  $\rho(T) \propto \log(1/T)$ . This particular behavior was attributed to electron-electron interaction in disordered and amorphous materials. The observed  $\rho \approx 1 - 2 \times 10^3 \mu\Omega\text{cm}$  were by one order of magnitude larger than literature values for CoFeB thin films. Due to the limited number of measured samples, no final conclusive results was given for Py. The existing data suggested that  $\rho$  scaled with  $T^2$ . Such a square dependence is usually understood as a sign for coherent electron-magnon scattering and had also been reported for Py planar thin films. As fabricated, the samples exhibited resistivities in the range of 100 to 150  $\mu\Omega\text{cm}$ , which is approximately a factor of 5 larger than in plain films. Interestingly, one sample showed a drastically decreased  $\rho$  after a certain measurement time, potentially due to annealing effects. The drop was accompanied by an increased AMR.

For all materials the AMR ratio was determined at low and room temperature. The values for Py and Ni are slightly smaller than values reported in literature for microstructured thin films. The values found in CoFeB correspond well to the few values reported in literature. The reason for a decreased AMR in Ni can be related to the structural surface roughness. The reason for decreased AMR in Py samples was not clear at the time of writing.

Cantilever magnetometry has been performed in collaboration with the group of Martino Poggio at Basel. By modeling the magnetic tube in a macrospin model, the saturation magnetization  $M_s$  was extracted from the measured change of the cantilever's resonance frequency.  $M_s$  was determined to be  $M_s = 375 \pm 70 \text{ kA/m}$  for nanotubes with Ni and  $M_s = 870 \pm 30 \text{ kA/m}$  for CoFeB nanotubes. While the Ni value is in good agreement with literature, the CoFeB value is significantly smaller. Whether this decrease was related to the observed columnar structure and the growth on the side facets, is not clear at the moment. No magnetometry data is available for Py tubes yet. However, the spin wave spectrum which was measured in Py tubes was well reproduced by simulations when using  $M_s = 400 \text{ kA/m}$ . This value is about 30% smaller than the effective magnetization measured on planar substrates, deposited with the same system.

## 9.2 Magnetic states and reversal

The magnetoresistance curves recorded on Ni nanotubes show without exception a smaller resistance  $R$  at remanence than close to saturation in parallel fields. A smaller  $R$  is related to an

azimuthal or transverse component of the magnetization  $\mathbf{M}$ . In collaboration with the group of Prof. Martino Poggio and Prof. Dieter Kölle, hysteresis curves for axial field were recorded by cantilever and nanoSQUID magnetometry. The cantilever data revealed a significant decrease of the axial component of  $\mathbf{M}$  at  $H = 0$ . The nanoSQUID, which was positioned at the tip, measured hysteresis curves with almost perfect squareness. The data were compared to micromagnetic simulations and close agreement was obtained for the cantilever curve and the simulations of tubes with lengths between 250 nm and 1  $\mu\text{m}$ . It was thus concluded that the Ni nanotube reversed by switching of multiple individual segments.

For the reversal of Ni nanotubes in perpendicular field, the maximum of  $R$  was found at or close to zero field. In inverted fields,  $R$  jumps to a lower value, forming a plateau which was stable for a significant field range. Then  $R$  returned to a higher value. The signal was attributed to vortex formation. The resistance of the plateau was higher than the minimal value observed in saturation. It was discussed that a difference in the AMR ratio for in- and out-of-plane rotation, caused by modified boundary scattering, could result in an increased  $R$  for the vortex. It is also possible that only segments exhibited the vortex configuration. At zero field the onion state was proposed to exist.

The recorded AMR traces were different for CoFeB and Py nanotubes. In the reversal process in axially applied magnetic field, only little deviation due to the AMR was observed. This was attributed to a uniform axial configuration of the magnetization  $M$  in the probed central segment. In collaboration with the group of Prof. Dirk Grundler, the AMR measurements were complemented by ANE based magnetothermal mapping of CoFeB tubes. It was found that the magnetization in the end-segments obtained a non-axial component at smaller field than the center segment. This was interpreted as an evidence for the existence and expansion of end-vortices. In the center segment voltage spikes were observed and attributed to vortex domain walls. Whether these are pinned by pinning sites or blocked by having opposite chirality could not be determined. Also, no concluding evidence could be found yet for the nucleation sites of the domain walls.

The reversal of CoFeB nanotubes in perpendicular field has been investigated by magnetotransport experiments, in combination with micromagnetic simulations. Two to three characteristic changes in the slope of the hysteresis curve could be found. Using micromagnetic simulations, it could be shown that this peculiar form is a direct result of the inhomogeneity of the internal field. The observed behavior could be modeled for a large range of geometrical dimensions by approximating the hexagonal tube by rectangular prisms. To describe the segments with high and low demagnetization field, the relative orientation of the prisms was chosen to be perpendicular. Comparing the simulated curve and measured data, the saturation magnetization was estimated to  $800 \pm 160 \text{ kA/m}$ , which falls within the error of the value determined by cantilever magnetometry.

### 9.3 Spin wave resonances

Spin wave resonances have been excited in individual ferromagnetic nanotubes by coupling to an asymmetric co-planar waveguide. The waveguide was fabricated lithographically in close vicinity of the tube. For the detection of a resonance condition the spin rectification effect has been used. Here, the resonant excitation generated dc-voltages that were detected in electrical leads contacting the tube. Similar to data reported on planar stripes, the measured signal strength was maximal when the external field comprised an angle with the tube axis.

A number of additional, weak modes were observed and were measured in axially aligned field. The characteristic frequency spacing and field dependence could not be explained by models reported in literature. The spectra could be closely matched by dynamic micro-magnetic simulations. The analysis of the spatial distribution of magnitude and phase of the simulated eigenmodes revealed two types of modes: a set of azimuthally quantized excitations which resemble thin-film modes with periodic boundary conditions and more complex 3D modes, which split from higher order modes. The dispersion relation, extracted from the thin film modes, exhibited wave vectors with values up to  $0.8 \cdot 10^6$  rad/cm. The square dependence of the eigenfrequencies on the wave vector is a strong indication of exchange dominated nature of the modes.

# Bibliography

- [AEA<sup>+</sup>08] S. Allende, J. Escrig, D. Altbir, E. Salcedo, and M. Bahiana. *Angular dependence of the transverse and vortex modes in magnetic nanotubes*. Eur. Phys. J. B, **66** (1), 37–40, (2008). doi : 10.1140/epjb/e2008-00385-4.
- [Aha96] A. Aharoni. *Introduction to the Theory of Ferromagnetism*, (1996).
- [Aha97] A. Aharoni. *Angular dependence of nucleation by curling in a prolate spheroid*. J. Appl. Phys., **82** (3), 1281–1287, (1997). doi : 10.1063/1.365899.
- [Aha98] A. Aharoni. *Demagnetizing factors for rectangular ferromagnetic prisms*. J. Appl. Phys., **83** (6), 3432–3434, (1998). doi : 10.1063/1.367113.
- [AM01] R. Arias and D. L. Mills. *Theory of spin excitations and the microwave response of cylindrical ferromagnetic nanowires*. Phys. Rev. B, **63**, 134439, (2001). doi : 10.1103/PhysRevB.63.134439.
- [APK00] A. Aharoni, L. Pust, and M. Kief. *Comparing theoretical demagnetizing factors with the observed saturation process in rectangular shields*. J. Appl. Phys., **87** (9), 6564–6566, (2000). doi : 10.1063/1.372771.
- [AS58] A. Aharoni and S. Shtrikman. *Magnetization Curve of the Infinite Cylinder*. Phys. Rev., **109**, 1522–1528, (1958). doi : 10.1103/PhysRev.109.1522.
- [AZA<sup>+</sup>11] O. Albrecht, R. Zierold, S. Allende, J. Escrig, C. Patzig, B. Rauschenbach, K. Nielsch, and D. Görlitz. *Experimental evidence for an angular dependent transition of magnetization reversal modes in magnetic nanotubes*. J. Appl. Phys., **109** (9), 093910, (2011). doi : 10.1063/1.3583666.
- [AZM<sup>+</sup>09] E. Amstad, S. Zurcher, A. Mashaghi, J. Y. Wong, M. Textor, and E. Reimhult. *Surface Functionalization of Single Superparamagnetic Iron Oxide Nanoparticles for Targeted Magnetic Resonance Imaging*. Small, **5** (11), 1334–1342, (2009). doi : 10.1002/smll.200801328.
- [AZP<sup>+</sup>10] O. Albrecht, R. Zierold, C. Patzig, J. Bachmann, C. Sturm, B. Rheinländer, M. Grundmann, D. Görlitz, B. Rauschenbach, and K. Nielsch. *Tubular magnetic nanostructures based on glancing angle deposited templates and atomic layer deposition*. Phys. Status Solidi (b), **247** (6), 1365–1371, (2010). doi : 10.1002/pssb.200945560.
- [BA09] L. K. Bogart and D. Atkinson. *Domain wall anisotropic magnetoresistance in planar nanowires*. Appl. Phys. Lett., **94** (4), 042511, (2009). doi : 10.1063/1.

- 3077174.
- [BBJ<sup>+</sup>13] F. Balhorn, C. Bausch, S. Jeni, W. Hansen, D. Heitmann, and S. Mendach. *Azimuthal spin-wave modes in rolled-up permalloy microtubes: Tuneable mode frequency, mode patterns, and mode splitting*. Phys. Rev. B, **88**, 054402, (2013). doi:10.1103/PhysRevB.88.054402.
- [BDK<sup>+</sup>06] C. Bilzer, T. Devolder, J.-V. Kim, G. Counil, C. Chappert, S. Cardoso, and P. P. Freitas. *Study of the dynamic magnetic properties of soft CoFeB films*. J. Appl. Phys., **100** (5), 053903, (2006). doi:10.1063/1.2337165.
- [BEH<sup>+</sup>09] S. Barth, S. Estrade, F. Hernandez-Ramirez, F. Peiro, J. Arbiol, A. Romano-Rodriguez, J. R. Morante, and S. Mathur. *Studies on Surface Facets and Chemical Composition of Vapor Grown One-Dimensional Magnetite Nanostructures*. Cryst. Growth Des., **9** (2), 1077–1081, (2009). doi:10.1021/cg8009095.
- [BEP<sup>+</sup>09] J. Bachmann, J. Escrig, K. Pitzschel, J. M. M. Moreno, J. Jing, D. Görlitz, D. Altbir, and K. Nielsch. *Size effects in ordered arrays of magnetic nanotubes: Pick your reversal mode*. J. Appl. Phys., **105** (7), 07B521, (2009). doi:10.1063/1.3074109.
- [BG14] F. Brandl and D. Grundler. *Fabrication and local laser heating of freestanding Ni<sub>8</sub>OFe<sub>2</sub>O bridges with Pt contacts displaying anisotropic magnetoresistance and anomalous Nernst effect*. Appl. Phys. Lett., **104** (17), 172401, (2014). doi:10.1063/1.4874302.
- [BGH06] S. Börm, L. Grasedyck, and W. Hackbusch. *Lecture Notes: Hierarchical Matrices*. online, (2006). URL: <http://www.mis.mpg.de/publications/other-series/ln/lecturenote-2103.html>.
- [BJH<sup>+</sup>12] F. Balhorn, S. Jeni, W. Hansen, D. Heitmann, and S. Mendach. *Axial and azimuthal spin-wave eigenmodes in rolled-up permalloy stripes*. Appl. Phys. Lett., **100** (22), 222402, (2012). doi:10.1063/1.3700809.
- [BJK<sup>+</sup>07] J. Bachmann, Jing, M. Knez, S. Barth, H. Shen, S. Mathur, U. Gösele, and K. Nielsch. *Ordered Iron Oxide Nanotube Arrays of Controlled Geometry and Tunable Magnetism by Atomic Layer Deposition*. J. Am. Chem. Soc., **129** (31), 9554–9555, (2007). doi:10.1021/ja072465w.
- [BMK<sup>+</sup>10] F. Balhorn, S. Mansfeld, A. Krohn, J. Topp, W. Hansen, D. Heitmann, and S. Mendach. *Spin-Wave Interference in Three-Dimensional Rolled-Up Ferromagnetic Microtubes*. Phys. Rev. Lett., **104** (3), 037205, (2010). doi:10.1103/PhysRevLett.104.037205.
- [BNM13] F. Balhorn, L. Nagrodzki, and S. Mendach. *Spin-wave interference in microscopic permalloy tubes*. Appl. Phys. Lett., **102** (22), 3432, (2013). doi:10.1063/1.4801472.
- [BNR<sup>+</sup>13] A. Buchter, J. Nagel, D. Ruffer, F. Xue, D. P. Weber, O. F. Kieler, T. Weimann, J. Kohlmann, A. B. Zorin, E. Russo-Averchi, R. Huber, P. Berberich, A. Fontcuberta i Morral, M. Kemmler, R. Kleiner, D. Koelle, D. Grundler, and M. Poggio.

- Reversal Mechanism of an Individual Ni Nanotube Simultaneously Studied by Torque and SQUID Magnetometry.* Phys. Rev. Lett., **111** (6), 067202, (2013). doi:10.1103/PhysRevLett.111.067202.
- [Boa05] R. Boardman. *Computer simulation studies of magnetic nanostructures*. PhD thesis, University of Southampton, (2005).
- [Bra14] F. Brandl. PhD thesis, Technical University Munich, (2014).
- [BRG<sup>+</sup>11] C. H. Butschkow, E. Reiger, S. Geißler, A. Rudolph, M. Soda, D. Schuh, G. Woltersdorf, W. Wegscheider, and D. Weiss. *Magneto-resistance of individual ferromagnetic GaAs/(Ga,Mn)As core-shell nanowires*. ArXiv e-prints, October (2011). arXiv:1110.5507.
- [BRH93] D. V. Berkov, K. Ramstöck, and A. Hubert. *Solving Micromagnetic Problems. Towards an Optimal Numerical Method*. Phys. Status Solidi (a), **137** (1), 207–225, (1993). doi:10.1002/pssa.2211370118.
- [Bro40] W. F. Brown. *Theory of the Approach to Magnetic Saturation*. Phys. Rev., **58**, 736–743, (1940). doi:10.1103/PhysRev.58.736.
- [Bro63] W. F. Brown. *Thermal Fluctuations of a Single-Domain Particle*. Phys. Rev., **130**, 1677–1686, (1963). doi:10.1103/PhysRev.130.1677.
- [Bro78] W. Brown. *Micromagnetics*. Krieger, (1978).
- [BRR<sup>+</sup>13] C. Butschkow, E. Reiger, A. Rudolph, S. Geißler, D. Neumaier, M. Soda, D. Schuh, G. Woltersdorf, W. Wegscheider, and D. Weiss. *Origin of negative magnetoresistance of GaAs/(Ga,Mn)As core-shell nanowires*. Phys. Rev. B, **87** (24), 245303, (2013). doi:10.1103/PhysRevB.87.245303.
- [BTX<sup>+</sup>01] J. Bao, C. Tie, Z. Xu, Q. Zhou, D. Shen, and Q. Ma. *Template Synthesis of an Array of Nickel Nanotubules and Its Magnetic Behavior*. Adv. Mater., **13** (21), 1631–1633, (2001). doi:10.1002/1521-4095(200111)13:21%3C1631::AID-ADMA1631%3E3.O.CO;2-R.
- [CB06] J. Clarke and A. I. Braginski. *The SQUID Handbook: Fundamentals and Technology of SQUIDS and SQUID Systems, Volume I*. Wiley-VCH Verlag, (2006). ISBN: 978-3-527-60458-6.
- [CDK<sup>+</sup>06] G. Counil, T. Devolder, J.-V. Kim, P. Crozat, C. Chappert, S. Zoll, and R. Fournel. *Temperature Dependences of the Resistivity and the Ferromagnetic Resonance Linewidth in Permalloy Thin Films*. IEEE Trans. Magn., **42** (10), 3323–3325, (2006). doi:10.1109/TMAG.2006.879718.
- [CDLM81] T. Chui, G. Deutscher, P. Lindenfeld, and W. L. McLean. *Conduction in granular aluminum near the metal-insulator transition*. Phys. Rev. B, **23** (11), 6172–6175, (1981). doi:10.1103/PhysRevB.23.6172.
- [CDM<sup>+</sup>05] T. A. Crowley, B. Daly, M. A. Morris, D. Erts, O. Kazakova, J. J. Boland, B. Wu, and J. D. Holmes. *Probing the magnetic properties of cobalt-germanium nanocable arrays*. J. Mater. Chem., **15**, 2408–2413, (2005). doi:10.1039/B502155C.
- [CFJ70] I. A. Campbell, A. Fert, and O. Jaoul. *The spontaneous resistivity anisotropy in*



## Bibliography

---

- Ni-based alloys*. J. Phys. C: Solid State Phys., **3** (1S), S95, (1970). doi:10.1088/0022-3719/3/1S/310.
- [CGG10] A. P. Chen, K. Y. Guslienko, and J. Gonzalez. *Magnetization configurations and reversal of thin magnetic nanotubes with uniaxial anisotropy*. J. Appl. Phys., **108** (8), 083920, (2010). doi:10.1063/1.3488630.
- [CGG11] A.-P. Chen, J. M. Gonzalez, and K. Y. Guslienko. *Magnetization configurations and reversal of magnetic nanotubes with opposite chiralities of the end domains*. J. Appl. Phys., **109** (7), 073923, (2011). doi:10.1063/1.3562190.
- [CGM<sup>+</sup>10] Y. T. Chong, D. Görlitz, S. Martens, M. Y. E. Yau, S. Allende, J. Bachmann, and K. Nielsch. *Multilayered Core/Shell Nanowires Displaying Two Distinct Magnetic Switching Events*. Adv. Mater., **22** (22), 2435–2439, (2010). doi:10.1002/adma.200904321.
- [CK97] Q. Chen and A. Konrad. *A review of finite element open boundary techniques for static and quasi-static electromagnetic field problems*. IEEE Trans. Magn., **33** (1), 663–676, (1997). doi:10.1109/20.560095.
- [CLY94] C.-R. Chang, C. M. Lee, and J.-S. Yang. *Magnetization curling reversal for an infinite hollow cylinder*. Phys. Rev. B, **50**, 6461–6464, (1994). doi:10.1103/PhysRevB.50.6461.
- [CnRF<sup>+</sup>03] F. J. Castaño, C. A. Ross, C. Frandsen, A. Eilez, D. Gil, H. I. Smith, M. Redjda, and F. B. Humphrey. *Metastable states in magnetic nanorings*. Phys. Rev. B, **67**, 184425, (2003). doi:10.1103/PhysRevB.67.184425.
- [CSA<sup>+</sup>13] J. Y. Chen, D. W. Shi, N. Ahmad, D. P. Liu, W. P. Zhou, and X. F. Han. *Fabrication and magnetic properties of La-X (X = Co, Ni, and Fe) nanotube arrays prepared by electrodeposition methods*. J. Appl. Phys., **114** (5), 054303, (2013). doi:10.1063/1.4817284.
- [CSF<sup>+</sup>08] C. Colombo, D. Spirkoska, M. Frimmer, G. Abstreiter, and A. Fontcuberta i Morral. *Ga-assisted catalyst-free growth mechanism of GaAs nanowires by molecular beam epitaxy*. Phys. Rev. B, **77**, 155326, (2008). doi:10.1103/PhysRevB.77.155326.
- [CST<sup>+</sup>07] J. Curiale, R. D. Sánchez, H. E. Troiani, C. A. Ramos, H. Pastoriza, A. G. Leyva, and P. Levy. *Magnetism of manganite nanotubes constituted by assembled nanoparticles*. Phys. Rev. B, **75**, 224410, (2007). doi:10.1103/PhysRevB.75.224410.
- [CUBG07] A. P. Chen, N. A. Usov, J. M. Blanco, and J. Gonzalez. *Equilibrium magnetization states in magnetic nanotubes and their evolution in external magnetic field*. J. Magn. Magn. Mater., **316** (2), e317–e319, (2007). doi:10.1016/j.jmmm.2007.02.132.
- [CX12] Y.-T. Chen and S. M. Xie. *Magnetic and Electric Properties of Amorphous Co<sub>40</sub>Fe<sub>40</sub>B<sub>20</sub> Thin Films*. Journal of Nanomaterials, **2012**, 486284, (2012). doi:10.1155/2012/486284.



- [DC07] T. K. Das and M. G. Cottam. *Magnetostatic modes in nanometer sized ferromagnetic and antiferromagnetic tubes*. Surf. Rev. Lett., **14** (03), 471–480, (2007). doi : 10.1142/S0218625X07009505.
- [DC11] T. K. Das and M. G. Cottam. *Theory of dipole-exchange spin waves in metallic ferromagnetic nanotubes of large aspect ratio*. J. Appl. Phys., **109** (7), 07D323, (2011). doi : 10.1063/1.3554208.
- [DCJR<sup>+</sup>14] S. Da Col, S. Jamet, N. Rougemaille, A. Locatelli, T. O. Mentès, B. S. Burgos, R. Afid, M. Darques, L. Cagnon, J. C. Toussaint, and O. Fruchart. *Observation of Bloch-point domain walls in cylindrical magnetic nanowires*. Phys. Rev. B, **89**, 180405, (2014). doi : 10.1103/PhysRevB.89.180405.
- [DE61] R. W. Damon and J. R. Eshbach. *Magnetostatic modes of a ferromagnet slab*. J. Phys. Chem. Solids, **19** (3–4), 308–320, (1961). doi : 10.1016/0022-3697(61)90041-5.
- [DGA05] A. Daire, W. Goeke, and T. M. Anne. *New Instruments Can Lock Out Lock-ins*. Whitepaper, Keithley Instruments, Inc., (2005).
- [DHS01] S. O. Demokritov, B. Hillebrands, and A. N. Slavin. *Brillouin light scattering studies of confined spin waves: linear and nonlinear confinement*. Physics Reports, **348** (6), 441–489, (2001). doi : 10.1016/S0370-1573(00)00116-2.
- [DKGN07] M. Daub, M. Knez, U. Goesele, and K. Nielsch. *Ferromagnetic nanotubes by atomic layer deposition in anodic alumina membranes*. J. Appl. Phys., **101** (9), 09J111, (2007). doi : 10.1063/1.2712057.
- [DLC<sup>+</sup>10] N. S. Dellas, J. Liang, B. J. Cooley, N. Samarth, and S. E. Mohnéy. *Electron microscopy of GaAs/MnAs core/shell nanowires*. Appl. Phys. Lett., **97** (7), 072505, (2010). doi : 10.1063/1.3481066.
- [dIMMG<sup>+</sup>12] M. de la Mata, C. Magen, J. Gazquez, M. I. B. Utama, M. Heiss, S. Lopatin, F. Furtmayr, C. J. Fernández-Rojas, B. Peng, J. R. Morante, R. Rurali, M. Eickhoff, A. Fontcuberta i Morral, Q. Xiong, and J. Arbiol. *Polarity Assignment in ZnTe, GaAs, ZnO, and GaN-AlN Nanowires from Direct Dumbbell Analysis*. Nano Lett., **12** (5), 2579–2586, (2012). doi : 10.1021/nl300840q.
- [DP73] D. H. Douglas and T. K. Peucker. *Algorithms for the reduction of the number of points required to represent a digitized line or its caricature*. Cartographica: The International Journal for Geographic Information and Geovisualization, **10** (2), 112–122, (1973). doi : 10.3138/FM57-6770-U75U-7727.
- [DUD10] V. E. Demidov, S. Urazhdin, and S. O. Demokritov. *Direct observation and mapping of spin waves emitted by spin-torque nano-oscillators*. Nature materials, **9** (12), 984–988, (2010). doi : 10.1038/nmat2882.
- [EBJ<sup>+</sup>08] J. Escrig, J. Bachmann, J. Jing, M. Daub, D. Altbir, and K. Nielsch. *Crossover between two different magnetization reversal modes in arrays of iron oxide nanotubes*. Phys. Rev. B, **77** (21), 214421, (2008). doi : 10.1103/PhysRevB.77.214421.

## Bibliography

---

- [EDL<sup>+</sup>07] J. Escrig, M. Daub, P. Landeros, K. Nielsch, and D. Altbir. *Angular dependence of coercivity in magnetic nanotubes*. *Nanotechnology*, **18** (44), 445706, (2007). doi:10.1088/0957-4484/18/44/445706.
- [EJ63] W. G. Egan and H. J. Juretschke. *DC Detection of Ferromagnetic Resonance in Thin Nickel Films*. *J. Appl. Phys.*, **34** (5), 1477–1484, (1963). doi:10.1063/1.1729604.
- [ELA<sup>+</sup>07] J. Escrig, P. Landeros, D. Altbir, E. Vogel, and P. Vargas. *Phase diagrams of magnetic nanotubes*. *J. Magn. Magn. Mater.*, **308** (2), 233–237, (2007). doi:10.1016/j.jmmm.2006.05.019.
- [ES75] A. L. Efros and B. I. Shklovskii. *Coulomb gap and low temperature conductivity of disordered systems*. *J. Phys. C: Solid State Phys.*, **8** (4), L49, (1975). doi:10.1088/0022-3719/8/4/003.
- [ET03] K. B. Efetov and A. Tschersich. *Coulomb effects in granular materials at not very low temperatures*. *Phys. Rev. B*, **67** (17), 174205, (2003). doi:10.1103/PhysRevB.67.174205.
- [FBF<sup>+</sup>09] H. Fangohr, G. Bordignon, M. Franchin, A. Knittel, P. A. J. de Groot, and T. Fischbacher. *A new approach to (quasi) periodic boundary conditions in micromagnetics: The macrogeometry*. *J. Appl. Phys.*, **105** (7), 07D529, (2009). doi:10.1063/1.3068637.
- [FFBF07] T. Fischbacher, M. Franchin, G. Bordignon, and H. Fangohr. *A Systematic Approach to Multiphysics Extensions of Finite-Element-Based Micromagnetic Simulations: Nmag*. *IEEE Trans. Magn.*, **43** (6), 2896–2898, (2007). doi:10.1109/TMAG.2007.893843.
- [FiMCA<sup>+</sup>08] A. Fontcuberta i Morral, C. Colombo, G. Abstreiter, J. Arbiol, and J. R. Morante. *Nucleation mechanism of gallium-assisted molecular beam epitaxy growth of gallium arsenide nanowires*. *Appl. Phys. Lett.*, **92** (6), 063112, (2008). doi:10.1063/1.2837191.
- [FiMSA<sup>+</sup>08] A. Fontcuberta i Morral, D. Spirkoska, J. Arbiol, M. Heigoldt, J. R. Morante, and G. Abstreiter. *Prismatic Quantum Heterostructures Synthesized on Molecular-Beam Epitaxy GaAs Nanowires*. *Small*, **4** (7), 899–903, (2008). doi:10.1002/smll.200701091.
- [FK90] D. Fredkin and T. R. Koehler. *Hybrid method for computing demagnetizing fields*. *IEEE Trans. Magn.*, **26** (2), 415–417, (1990). doi:10.1109/20.106342.
- [FMIO94] H. Fujimori, S. Mitani, T. Ikeda, and S. Ohnuma. *High electrical resistivity and permeability of soft magnetic granular alloys*. *IEEE Trans. Magn.*, **30** (6), 4779–4781, (1994). doi:10.1109/20.334219.
- [FOKS94] H. Funaki, S. Okamoto, O. Kitakami, and Y. Shimada. *Improvement in Magnetoresistance of Very Thin Permalloy Films by Post-Annealing*. *Jpn. J. Appl. Phys.*, **33** (9B), L1304, (1994). doi:10.1063/1.372908.
- [FSD<sup>+</sup>03] H. Forster, T. Schrefl, R. Dittrich, W. Scholz, and J. Fidler. *Fast boundary methods*

- for magnetostatic interactions in micromagnetics. *IEEE Trans. Magn.*, **39** (5), 2513–2515, (2003). doi:10.1109/TMAG.2003.816458.
- [FST57] E. H. Frei, S. Shtrikman, and D. Treves. *Critical Size and Nucleation Field of Ideal Ferromagnetic Particles*. *Phys. Rev.*, **106**, 446–455, (1957). doi:10.1103/PhysRev.106.446.
- [GAB74] J. I. Gittleman, B. Abeles, and S. Bozowski. *Superparamagnetism and relaxation effects in granular Ni-SiO<sub>2</sub> and Ni-Al<sub>2</sub>O<sub>3</sub> films*. *Phys. Rev. B*, **9**, 3891–3897, May (1974). doi:10.1103/PhysRevB.9.3891.
- [GCR06] C. Garcia-Cervera and A. Roma. *Adaptive mesh refinement for micromagnetics simulations*. *IEEE Trans. Magn.*, **42** (6), 1648–1654, (2006). doi:10.1109/TMAG.2006.872199.
- [Geo10] S. M. George. *Atomic Layer Deposition: An Overview*. *Chemical Reviews*, **110** (1), 111–131, (2010). PMID: 19947596. doi:10.1021/cr900056b.
- [GHMH05] Y. S. Gui, S. Holland, N. Mecking, and C. M. Hu. *Resonances in Ferromagnetic Gratings Detected by Microwave Photoconductivity*. *Phys. Rev. Lett.*, **95** (5), 056807, (2005). doi:10.1103/PhysRevLett.95.056807.
- [Gil04] T. Gilbert. *A phenomenological theory of damping in ferromagnetic materials*. *IEEE Trans. Magn.*, **40** (6), 3443–3449, (2004). doi:10.1109/TMAG.2004.836740.
- [GLNn10] A. González, P. Landeros, and A. S. Núñez. *Spin wave spectrum of magnetic nanotubes*. *J. Magn. Magn. Mater.*, **322** (5), 530–535, (2010). doi:10.1016/j.jmmm.2009.10.010.
- [GLZC91] W. Gong, H. Li, Z. Zhao, and J. Chen. *Ultrafine particles of Fe, Co, and Ni ferromagnetic metals*. *J. Appl. Phys.*, **69** (8), 5119–5121, (1991). doi:10.1063/1.348144.
- [GMH07] Y. S. Gui, N. Mecking, and C. M. Hu. *Quantized Spin Excitations in a Ferromagnetic Microstrip from Microwave Photovoltage Measurements*. *Phys. Rev. Lett.*, **98** (21), 217603, (2007). doi:10.1103/PhysRevLett.98.217603.
- [GMW<sup>+</sup>07] Y. S. Gui, N. Mecking, A. Wirthmann, L. H. Bai, and C.-M. Hu. *Electrical detection of the ferromagnetic resonance: Spin-rectification versus bolometric effect*. *Appl. Phys. Lett.*, **91** (8), 082503, (2007). doi:10.1063/1.2772764.
- [GMZ<sup>+</sup>07a] Y. S. Gui, N. Mecking, X. Zhou, G. Williams, and C.-M. Hu. *Realization of a Room-Temperature Spin Dynamo: The Spin Rectification Effect*. *Phys. Rev. Lett.*, **98** (10), 107602, (2007). doi:10.1103/PhysRevLett.98.107602.
- [GMZ<sup>+</sup>07b] Y. S. Gui, N. Mecking, X. Zhou, G. Williams, and C.-M. Hu. *Realization of a Room-Temperature Spin Dynamo: The Spin Rectification Effect*. *Phys. Rev. Lett.*, **98**, 107602, (2007). doi:10.1103/PhysRevLett.98.107602.
- [GPKG05] F. Giesen, J. Podbielski, T. Korn, and D. Grundler. *Multiple ferromagnetic resonance in mesoscopic permalloy rings*. *J. Appl. Phys.*, **97** (10), 10A712, (2005). doi:10.1063/1.1851932.

## Bibliography

---

- [GSB<sup>+</sup>07] S. T. B. Goennenwein, S. W. Schink, A. Brandlmaier, A. Boger, M. Opel, R. Gross, R. S. Keizer, T. M. Klapwijk, A. Gupta, H. Huebl, C. Bihler, and M. S. Brandt. *Electrically detected ferromagnetic resonance*. Appl. Phys. Lett., **90** (16), 162507, (2007). doi:10.1063/1.2722027.
- [GY13] H. C. Gui YongSheng, Bai LiHui. *The physics of spin rectification and its application*. Science China Physics, Mechanics & Astronomy, **56** (1), 124, (2013). doi:10.1007/s11433-012-4956-6.
- [Hac99] W. Hackbusch. *A Sparse Matrix Arithmetic Based on H-Matrices. Part I: Introduction to H-Matrices*. Computing, **62** (2), 89–108, (1999). doi:10.1007/s006070050015.
- [HCG<sup>+</sup>11] M. Harder, Z. X. Cao, Y. S. Gui, X. L. Fan, and C.-M. Hu. *Analysis of the line shape of electrically detected ferromagnetic resonance*. Phys. Rev. B, **84** (5), 054423, (2011). doi:10.1103/PhysRevB.84.054423.
- [Hei] F Heimbach.
- [HG95] K. Hong and N. Giordano. *Approach to mesoscopic magnetic measurements*. Phys. Rev. B, **51** (15), 9855–9862, (1995). doi:10.1103/PhysRevB.51.9855.
- [HHJ<sup>+</sup>13] M. Hilse, J. Herfort, B. Jenichen, A. Trampert, M. Hanke, P. Schaaf, L. Geelhaar, and H. Riechert. *GaAs-Fe<sub>3</sub>Si Core-Shell Nanowires: Nanobar Magnets*. Nano Lett., **13** (12), 6203–6209, (2013). doi:10.1021/nl4035994.
- [HK51] C. Herring and C. Kittel. *On the Theory of Spin Waves in Ferromagnetic Media*. Phys. Rev., **81**, 869–880, (1951). doi:10.1103/PhysRev.81.869.
- [HK00] W. Hackbusch and B. N. Khoromskij. *A Sparse H-Matrix Arithmetic. Part II: Application to Multi-Dimensional Problems*. Computing, **64** (1), 21–47, (2000). doi:10.1007/PL00021408.
- [HK04] R. Hertel and J. Kirschner. *Magnetic drops in a soft-magnetic cylinder*. J. Magn. Mater., **278** (3), L291–L297, (2004). doi:10.1016/j.jmmm.2004.02.032.
- [HKM<sup>+</sup>08] A. T. Hindmarch, C. J. Kinane, M. MacKenzie, J. N. Chapman, M. Henini, D. Taylor, D. A. Arena, J. Dvorak, B. J. Hickey, and C. H. Marrows. *Interface Induced Uniaxial Magnetic Anisotropy in Amorphous CoFeB Films on AlGaAs(001)*. Phys. Rev. Lett., **100**, 117201, (2008). doi:10.1103/PhysRevLett.100.117201.
- [HKS<sup>+</sup>12] Y.-C. Huang, C.-Y. Kuo, J.-H. Shyu, C.-M. Lee, L. Horng, and J.-C. Wu. *Fabrication and magnetic properties of 100-nm-scaled permalloy nanotube arrays*. J. Vac. Sci. Technol. B, **30** (6), 06FF07, (2012). doi:10.1116/1.4762843.
- [HPMGLLJ11] L. Hai-Peng, H. Man-Gui, C. Li, and D. Long-Jiang. *Fabrication and electromagnetic wave absorption properties of amorphous Ni—P nanotubes*. Chinese Phys. B, **20** (6), 060701, (2011). doi:10.1088/1674-1056/20/6/060701.
- [HRSJY<sup>+</sup>09] L. Hai-Rui, S. Shamaila, C. Jun-Yang, R. Sharif, L. Qing-Feng, and H. Xiu-Feng. *Magnetization Reversal Mechanism for CoFeB Ferromagnetic Nanotube Arrays*. Chinese Phys. Lett., **26** (7), 077503, (2009). doi:10.1088/0256-307X/26/7/

- 077503.
- [HRSM11] C. M. Hangarter, Y. Rheem, T. Stahovich, and N. V. Myung. *Synthesis and magneto-transport properties of single PEDOT/Ni and PEDOT/Ni<sub>30</sub>Fe<sub>70</sub> core/shell nanowires*. *Electrochim. Acta*, **56** (16), 5561 – 5565, (2011). doi: 10.1016/j.electacta.2011.03.115.
- [HSB<sup>+</sup>11] R. Huber, T. Schwarze, P. Berberich, T. Rapp, and D. Grundler. *Atomic layer deposition for the fabrication of magnonic metamaterials*. In *Metamaterials '2011: The Fifth International Congress on Advanced Electromagnetic Materials in Microwaves and Optics, Metamorphose-VI*, page 588, Barcelona, (2011).
- [HSS<sup>+</sup>09] X.-F. Han, S. Shamaila, R. Sharif, J.-Y. Chen, H.-R. Liu, and D.-P. Liu. *Structural and Magnetic Properties of Various Ferromagnetic Nanotubes*. *Adv. Mater.*, **21** (45), 4619–4624, (2009). doi:10.1002/adma.200901065.
- [HTH<sup>+</sup>09] M. Hilse, Y. Takagaki, J. Herfort, M. Ramsteiner, C. Herrmann, S. Breuer, L. Geelhaar, and H. Riechert. *Ferromagnet-semiconductor nanowire coaxial heterostructures grown by molecular-beam epitaxy*. *Appl. Phys. Lett.*, **95** (13), 133126, (2009). doi:10.1063/1.3240405.
- [Hub13] R. Huber. *Control of Spin Waves on the Nanoscale in One-Dimensional Magnonic Crystals and Atomic Layer Deposition of Metallic Ferromagnets for Second Generation of Nanomaterials*. PhD thesis, Technische Universität München, (2013). URL: <http://mediatum.ub.tum.de/node?id=1174959>.
- [HZLW03] G. C. Han, B. Y. Zong, P. Luo, and Y. H. Wu. *Angular dependence of the coercivity and remanence of ferromagnetic nanowire arrays*. *J. Appl. Phys.*, **93** (11), 9202–9207, (2003). doi:10.1063/1.1572197.
- [IMY<sup>+</sup>10] S. Ikeda, K. Miura, H. Yamamoto, K. Mizunuma, H. D. Gan, M. Endo, S. Kanai, J. Hayakawa, F. Matsukura, and H. Ohno. *A perpendicular-anisotropy CoFeB–MgO magnetic tunnel junction*. *Nat. Mater.*, **9** (9), 721–724, (2010). doi:10.1038/nmat2804.
- [ITR09] *International Technology Roadmap for Semiconductors (ITRS)*, (2009).
- [JCZ97] Y. Q. Jia, S. Y. Chou, and J.-G. Zhu. *Effect of bar width on magnetoresistance of nanoscale nickel and cobalt bars*. *J. Appl. Phys.*, **81** (8), 5461–5463, (1997). doi:10.1063/1.364947.
- [JGRM08] F. Jabeen, V. Grillo, S. Rubini, and F. Martelli. *Self-catalyzed growth of GaAs nanowires on cleaved Si by molecular beam epitaxy*. *Nanotechnology*, **19** (27), 275711, (2008). doi:10.1088/0957-4484/19/27/275711.
- [Jos62] B. Josephson. *Possible new effects in superconductive tunnelling*. *Phys. Lett.*, **1** (7), 251 – 253, (1962). doi:10.1016/0031-9163(62)91369-0.
- [JSY<sup>+</sup>05] C.-J. Jia, L.-D. Sun, Z.-G. Yan, L.-P. You, F. Luo, X.-D. Han, Y.-C. Pang, Z. Zhang, and C.-H. Yan. *Single-Crystalline Iron Oxide Nanotubes*. *Angew. Chem. Int. Ed.*, **44** (28), 4328–4333, (2005). doi:10.1002/anie.200463038.
- [Jur60] H. J. Juretschke. *Electromagnetic Theory of dc Effects in Ferromagnetic Reso-*



## Bibliography

---

- nance. *J. Appl. Phys.*, **31** (8), 1401–1406, (1960). doi:10.1063/1.1735851.
- [JYC<sup>+</sup>06] S. U. Jen, Y. D. Yao, Y. T. Chen, J. M. Wu, C. C. Lee, T. L. Tsai, and Y. C. Chang. *Magnetic and electrical properties of amorphous CoFeB films*. *J. Appl. Phys.*, **99** (5), 053701, (2006). doi:doi:10.1063/1.2174113.
- [KA00] P. Kelly and R. Arnell. *Magnetron sputtering: a review of recent developments and applications*. *Vacuum*, **56** (3), 159 – 172, (2000). doi:10.1016/S0042-207X(99)00189-X.
- [KBW10] A. Khitun, M. Bao, and K. L. Wang. *Magnonic logic circuits*. *J. Phys. D: Appl. Phys.*, **43** (26), 264005, (2010). doi:10.1088/0022-3727/43/26/264005.
- [KDG10] V. V. Kruglyak, S. O. Demokritov, and D. Grundler. *Magnonics*. *J. Phys. D: Appl. Phys.*, **43** (26), 264001, (2010). doi:10.1088/0022-3727/43/26/264001.
- [KGD73] S. Krongelb, A. Gangulee, and G. Das. *Annealing of thin magnetoresistive permalloy films*. *IEEE Trans. Magn.*, **9** (3), 568–570, (1973). doi:10.1109/TMAG.1973.1067608.
- [Kit48] C. Kittel. *On the Theory of Ferromagnetic Resonance Absorption*. *Phys. Rev.*, **73** (2), 155–161, (1948). doi:10.1103/PhysRev.73.155.
- [KJJ<sup>+</sup>13] P. Krogstrup, H. I. Jørgensen, E. Johnson, M. H. Madsen, C. B. Sørensen, A. F. i Morral, M. Aagesen, J. Nygård, and F. Glas. *Advances in the theory of III–V nanowire growth dynamics*. *J. Phys. D: Appl. Phys.*, **46** (31), 313001, (2013). doi:10.1088/0022-3727/46/31/313001.
- [KKLT02] S. Khizroev, M. H. Kryder, D. Litvinov, and D. A. Thompson. *Direct observation of magnetization switching in focused-ion-beam-fabricated magnetic nanotubes*. *Appl. Phys. Lett.*, **81** (12), 2256–2257, (2002). doi:10.1063/1.1508164.
- [KKM<sup>+</sup>11] J. Kimling, F. Kronast, S. Martens, T. Böhnert, M. Martens, J. Herrero-Albillos, L. Tati-Bismaths, U. Merkt, K. Nielsch, and G. Meier. *Photoemission electron microscopy of three-dimensional magnetization configurations in core-shell nanostructures*. *Phys. Rev. B*, **84**, 174406, (2011). doi:10.1103/PhysRevB.84.174406.
- [KKR86] S. N. Kaul, W. Kettler, and M. Rosenberg. *Evidence for a magnetic contribution to the electrical resistivity in amorphous Fe<sub>80</sub>B<sub>20</sub>-xCx alloys*. *Phys. Rev. B*, **33** (7), 4987–4997, (1986). doi:10.1103/PhysRevB.33.4987.
- [KKR87] S. N. Kaul, W. Kettler, and M. Rosenberg. *Electrical resistivity of amorphous Fe<sub>82</sub>B<sub>18</sub>-xGex alloys: Coherent electron-magnon scattering contribution*. *Phys. Rev. B*, **35**, 7153–7156, (1987). doi:10.1103/PhysRevB.35.7153.
- [KM05] C. Kittel and P. McEuen. *Introduction to solid state physics*, volume 8th ed. Wiley New York, (2005).
- [Kni11] A. Knittel. *Micromagnetic simulations of three dimensional core-shell nanostructures*. Thesis, (2011). URL: <http://eprints.soton.ac.uk/333186/>.
- [KNN07] M. Knez, K. Nielsch, and L. Niinistö. *Synthesis and Surface Engineering of Complex Nanostructures by Atomic Layer Deposition*. *Adv. Mater.*, **19** (21),

- 3425–3438, (2007). doi : 10.1002/adma.200700079.
- [KRU<sup>+</sup>10] D.-H. Kim, E. A. Rozhkova, I. V. Ulasov, S. D. Bader, T. Rajh, M. S. Lesniak, and V. Novosad. *Biofunctionalized magnetic-vortex microdiscs for targeted cancer-cell destruction*. *Nat. Mater.*, **9** (2), 165–171, (2010). doi : 10.1038/nmat2591.
- [KS86] B. A. Kalinikos and A. N. Slavin. *Theory of dipole-exchange spin wave spectrum for ferromagnetic films with mixed exchange boundary conditions*. *J. Phys. C: Solid State Phys.*, **19** (35), 7013, (1986). doi : 10.1088/0022-3719/19/35/014.
- [KVS<sup>+</sup>04] M. Kerekes, A. D. C. Viegas, D. Stanescu, U. Ebels, P. Xavier, and G. Suran. *Frequency domain studies of CoZr continuous thin films and FeNi wires using coplanar transmission lines*. *J. Appl. Phys.*, **95** (11), 6616–6618, (2004). doi : 10.1063/1.1669340.
- [LAE<sup>+</sup>07] P. Landeros, S. Allende, J. Escrig, E. Salcedo, D. Altbir, and E. E. Vogel. *Reversal modes in magnetic nanotubes*. *Appl. Phys. Lett.*, **90** (10), 102501, (2007). doi : 10.1063/1.2437655.
- [LC96] C.-M. Lee and C.-R. Chang. *Coercivity and nucleation field of hollow ferromagnetic particles*. *Mater. Chem. Phys.*, **43** (2), 183 – 186, (1996). doi : 10.1016/0254-0584(95)01622-2.
- [Les11] M. Leskelä. *Challenges in Atomic Layer Deposition*, pages 401–421. Wiley-VCH Verlag GmbH & Co. KGaA, (2011). doi : 10.1002/9783527639915.ch17.
- [LGSE09] P. Landeros, P. R. Guzmán, R. Soto-Garrido, and J. Escrig. *Magnetostatic fields in tubular nanostructures*. *J. Phys. D: Appl. Phys.*, **42** (22), 225002, (2009). doi : 10.1088/0022-3727/42/22/225002.
- [LKP<sup>+</sup>09] H.-B.-R. Lee, W.-H. Kim, Y. Park, S. Baik, and H. Kim. *Cobalt and nickel atomic layer depositions for contact applications*. In *Interconnect Technology Conference, 2009. IITC 2009. IEEE International*, pages 157–158, (2009). doi : 10.1109/IITC.2009.5090371.
- [LL35] L. D. Landau and E. Lifshitz. *On the theory of the dispersion of magnetic permeability in ferromagnetic bodies*. *Phys. Z. Sowjet.*, **8** (153), 101–114, (1935). URL: <http://ujp.bitp.kiev.ua/files/journals/53/si/53SI06p.pdf>.
- [LNn10] P. Landeros and A. S. Núñez. *Domain wall motion on magnetic nanotubes*. *J. Appl. Phys.*, **108** (3), 033917, (2010). doi : 10.1063/1.3466747.
- [LSCV09] P. Landeros, O. J. Suarez, A. Cuchillo, and P. Vargas. *Equilibrium states and vortex domain wall nucleation in ferromagnetic nanotubes*. *Phys. Rev. B*, **79** (2), 024404, (2009). doi : 10.1103/PhysRevB.79.024404.
- [LSS<sup>+</sup>07] J. Lee, D. Suess, T. Schrefl, K. H. Oh, and J. Fidler. *Magnetic characteristics of ferromagnetic nanotube*. *J. Magn. Magn. Mater.*, **310** (2, Part 3), 2445–2447, (2007). doi : 10.1016/j.jmmm.2006.10.1137.
- [LTBL08] D. Li, R. S. Thompson, G. Bergmann, and J. G. Lu. *Template-based Synthesis and Magnetic Properties of Cobalt Nanotube Arrays*. *Adv. Mater.*, **20** (23), 4575–4578, (2008). doi : 10.1002/adma.200801455.

## Bibliography

---

- [LTT<sup>+</sup>00] W.-Y. Lee, M. F. Toney, P. Tameerug, E. Allen, and D. Mauri. *High magnetoresistance permalloy films deposited on a thin NiFeCr or NiCr underlayer*. J. Appl. Phys., **87** (9), 6992–6994, (2000). doi:10.1063/1.372908.
- [LUGM11] B. Lenk, H. Ulrichs, F. Garbs, and M. Munzenberg. *The building blocks of magnonics*. Physics Reports, **507** (4), 107, (2011). doi:10.1016/j.physrep.2011.06.003.
- [LV04] H. Leblond and V. Veerakumar. *Magnetostatic spin solitons in ferromagnetic nanotubes*. Phys. Rev. B, **70**, 134413, (2004). doi:10.1103/PhysRevB.70.134413.
- [LWP<sup>+</sup>12] J. Liang, J. Wang, A. Paul, B. J. Cooley, D. W. Rench, N. S. Dellas, S. E. Mohny, R. Engel-Herbert, and N. Samarth. *Measurement and simulation of anisotropic magnetoresistance in single GaAs/MnAs core/shell nanowires*. Appl. Phys. Lett., **100** (18), 182402, (2012). doi:10.1063/1.4710524.
- [LXWS08] B. Lv, Y. Xu, D. Wu, and Y. Sun. *Preparation and properties of magnetic iron oxide nanotubes*. Particuology, **6** (5), 334 – 339, (2008). doi:10.1016/j.partic.2008.04.006.
- [LZH<sup>+</sup>05] Z. Liu, D. Zhang, S. Han, C. Li, B. Lei, W. Lu, J. Fang, and C. Zhou. *Single Crystalline Magnetite Nanotubes*. J. Am. Chem. Soc., **127** (1), 6–7, (2005). doi:10.1021/ja0445239.
- [M<sup>+</sup>65] G. E. Moore et al. *Cramming more components onto integrated circuits*, (1965).
- [MDT66] R. Moskowitz and E. Della Torre. *Theoretical aspects of demagnetization tensors*. IEEE Trans. Magn., **2** (4), 739–744, (1966). doi:10.1109/TMAG.1966.1065973.
- [Mec08] N. Mecking. *A comprehensive study of the AMR-induced microwave photovoltage, photocurrent and photoresistance in Permalloy microstrips*. PhD thesis, Universität Hamburg, (2008). URL: [http://www.physik.uni-hamburg.de/services/fachinfo/\\_\\_\\_Volltexte/Nikolai\\_\\_\\_Mecking/Nikolai\\_\\_\\_Mecking.pdf](http://www.physik.uni-hamburg.de/services/fachinfo/___Volltexte/Nikolai___Mecking/Nikolai___Mecking.pdf).
- [Men14] J. Mendil. *Spin-wave and magnetization states in ferromagnetic nanotubes*. Master's thesis, Technical University Munich, (2014).
- [MGH07] N. Mecking, Y. S. Gui, and C.-M. Hu. *Microwave photovoltage and photoresistance effects in ferromagnetic microstrips*. Phys. Rev. B, **76** (22), 224430, (2007). doi:10.1103/PhysRevB.76.224430.
- [MJ70] W. M. Moller and H. J. Juretschke. *Determination of Spin-Wave Boundary Conditions by dc Effects in Spin-Wave Resonance*. Phys. Rev. B, **2**, 2651–2660, (1970). doi:10.1103/PhysRevB.2.2651.
- [MJG74] A. F. Mayadas, J. F. Janak, and A. Gangulee. *Resistivity of Permalloy thin films*. J. Appl. Phys., **45** (6), 2780–2781, (1974). doi:10.1063/1.1663668.
- [MKP98] M. Mertig, R. Kirsch, and W. Pompe. *Biomolecular approach to nanotube fabrication*. Appl. Phys. A Mater. Sci. Process., **66** (1), S723–S727, (1998). doi:10.1007/s003390051230.
- [MP75] T. McGuire and R. Potter. *Anisotropic magnetoresistance in ferromagnetic 3d*



- alloys*. IEEE Trans. Magn., **11** (4), 1018–1038, (1975). doi:10.1109/TMAG.1975.1058782.
- [MPT<sup>+</sup>08] S. Mendach, J. Podbielski, J. Topp, W. Hansen, and D. Heitmann. *Spin-wave confinement in rolled-up ferromagnetic tubes*. Appl. Phys. Lett., **93** (26), 262501, (2008). doi:10.1063/1.3058764.
- [NBD<sup>+</sup>07] K. Nielsch, J. Bachmann, M. Daub, J. Jing, M. Knez, U. Gösele, S. Barth, S. Mathur, J. Escrig, and D. Altbir. *Ferromagnetic Nanostructures by Atomic Layer Deposition: From Thin Films Towards Core-Shell Nanotubes*. ECS Transactions, **11** (7), 139–148, (2007). doi:10.1149/1.2779078.
- [NBX<sup>+</sup>13] J. Nagel, A. Buchter, F. Xue, O. F. Kieler, T. Weimann, J. Kohlmann, A. B. Zorin, D. Ruffer, E. Russo-Averchi, R. Huber, P. Berberich, A. Fontcuberta i Morral, D. Grundler, R. Kleiner, D. Koelle, M. Poggio, and M. Kemmler. *Nanoscale multifunctional sensor formed by a Ni nanotube and a scanning Nb nanoSQUID*. Phys. Rev. B, **88**, 064425, (2013). doi:10.1103/PhysRevB.88.064425.
- [NC06] T. Nguyen and M. Cottam. *Spin-wave excitations in ferromagnetic nanotubes*. In *Surface Science*, volume 600, pages 4151 – 4154, (2006). Berlin, Germany: 4–9 September 2005 Proceedings of the 23th European Conference on Surface Science. doi:10.1016/j.susc.2006.01.138.
- [NCM<sup>+</sup>05] K. Nielsch, F. J. Castaño, S. Matthias, W. Lee, and C. A. Ross. *Synthesis of Cobalt/Polymer Multilayer Nanotubes*. Adv. Eng. Mater., **7** (4), 217–221, (2005). doi:10.1002/adem.200400192.
- [NCRK05] K. Nielsch, F. J. Castaño, C. A. Ross, and R. Krishnan. *Magnetic properties of template-synthesized cobalt/polymer composite nanotubes*. J. Appl. Phys., **98** (3), 034318, (2005). doi:10.1063/1.2005384.
- [Ner87] W. Nernst. *Ueber die electromotorischen Kräfte, welche durch den Magnetismus in von einem Wärmestrome durchflossenen Metallplatten geweckt werden*. Ann. Phys. (Berlin), **267** (8), 760–789, (1887). doi:10.1002/andp.18872670815.
- [NG09] S. Neusser and D. Grundler. *Magnonics: Spin Waves on the Nanoscale*. Adv. Mater., **21** (28), 2927–2932, (2009). doi:10.1002/adma.200900809.
- [nis] NIST referenc on Constants, Units and Uncertainty. URL: <http://physics.nist.gov/cgi-bin/cuu/Value?gammaebar>.
- [NSO<sup>+</sup>10] N. Nagaosa, J. Sinova, S. Onoda, A. H. MacDonald, and N. P. Ong. *Anomalous Hall effect*. Rev. Mod. Phys., **82**, 1539–1592, (2010). doi:10.1103/RevModPhys.82.1539.
- [OLLNnL12] J. A. Otálora, J. A. López-López, A. S. Núñez, and P. Landeros. *Domain wall manipulation in magnetic nanotubes induced by electric current pulses*. J. Phys.: Condens. Matter, **24** (43), 436007, (2012). doi:10.1088/0953-8984/24/43/436007.
- [OLLVL12] J. A. Otálora, J. A. López-López, P. Vargas, and P. Landeros. *Chirality switching and propagation control of a vortex domain wall in ferromagnetic nanotubes*.

## Bibliography

---

- Appl. Phys. Lett., **100** (7), 072407, (2012). doi:10.1063/1.3687154.
- [Ost00] W. Ostwald. *Über die vermeintliche Isomerie des roten und gelben Quecksilberoxyds und die Oberflächenspannung fester Körper*. Z. Phys. Chem., **34**, 495–503, (1900).
- [PCJD03] Q. A. Pankhurst, J. Connolly, S. K. Jones, and J. Dobson. *Applications of magnetic nanoparticles in biomedicine*. J. Phys. D: Appl. Phys., **36**, R167–R181, (2003). doi:10.1088/0022-3727/36/13/201.
- [PCNCS12] J. Prat-Camps, C. Navau, D.-X. Chen, and A. Sanchez. *Exact Analytical Demagnetizing Factors for Long Hollow Cylinders in Transverse Field*. Magnetics Letters, IEEE, **3**, 500104, (2012). doi:10.1109/LMAG.2012.2198617.
- [PDL<sup>+</sup>10] S. Plissard, K. A. Dick, G. Larrieu, S. Godey, A. Addad, X. Wallart, and P. Caroff. *Gold-free growth of GaAs nanowires on silicon: arrays and polytypism*. Nanotechnology, **21** (38), 385602, (2010). doi:10.1088/0957-4484/21/38/385602.
- [PGB<sup>+</sup>05] J. Podbielski, F. Giesen, M. Berginski, N. Hoyer, and D. Grundler. *Spin configurations in nanostructured magnetic rings: From DC transport to GHz spectroscopy*. Superlattices and Microstructures - Spintronics: Spin Injection, Transport, and Manipulation, **37** (5), 341 – 348, (2005). doi:10.1016/j.spmi.2004.12.006.
- [PHT08] S. S. P. Parkin, M. Hayashi, and L. Thomas. *Magnetic Domain-Wall Race-track Memory*. Science, **320** (5873), 190–194, (2008). doi:10.1126/science.1145799.
- [PNYS09] J. H. Paek, T. Nishiwaki, M. Yamaguchi, and N. Sawaki. *Catalyst free MBE-VLS growth of GaAs nanowires on (111)Si substrate*. Phys. Status Solidi (c), **6** (6), 1436–1440, (2009). doi:10.1002/pssc.200881520.
- [RAHM<sup>+</sup>12] E. Russo-Averchi, M. Heiss, L. Michelet, P. Krogstrup, J. Nygard, C. Magen, J. R. Morante, E. Uccelli, J. Arbiol, and A. Fontcuberta i Morral. *Suppression of three dimensional twinning for a 100 % yield of vertical GaAs nanowires on silicon*. Nanoscale, **4**, 1486–1490, (2012). doi:10.1039/C2NR11799A.
- [Ram72] U. Ramer. *An iterative procedure for the polygonal approximation of plane curves*. Comput. Graph. Image Process., **1** (3), 244 – 256, (1972). doi:10.1016/S0146-664X(72)80017-0.
- [RCdJdJ95] T. G. S. M. Rijks, R. Coehoorn, M. J. M. de Jong, and W. J. M. de Jonge. *Semiclassical calculations of the anisotropic magnetoresistance of NiFe-based thin films, wires, and multilayers*. Phys. Rev. B, **51**, 283–291, (1995). doi:10.1103/PhysRevB.51.283.
- [RCGG11] D. Ruffer, F. D. Czeschka, R. Gross, and S. T. B. Goennenwein. *Experimental observation of an enhanced anisotropic magnetoresistance in non-local configuration*. Appl. Phys. Lett., **99** (14), 142112, (2011). doi:10.1063/1.3640487.
- [RHB<sup>+</sup>12] D. Ruffer, R. Huber, P. Berberich, S. Albert, E. Russo-Averchi, M. Heiss, J. Arbiol, A. Fontcuberta i Morral, and D. Grundler. *Magnetic states of an individual Ni*

- nanotube probed by anisotropic magnetoresistance*. *Nanoscale*, **4**, 4989–4995, (2012). doi : 10.1039/C2NR31086D.
- [RHG<sup>+</sup>13] M. R. Ramdani, J. C. Harmand, F. Glas, G. Patriarche, and L. Travers. *Arsenic Pathways in Self-Catalyzed Growth of GaAs Nanowires*. *Cryst. Growth Des.*, **13** (1), 91–96, (2013). doi : 10.1021/cg301167g.
- [RKLD<sup>+</sup>01] J. Rothman, M. Kläui, L. Lopez-Diaz, C. A. F. Vaz, A. Bleloch, J. A. C. Bland, Z. Cui, and R. Speaks. *Observation of a Bi-Domain State and Nucleation Free Switching in Mesoscopic Ring Magnets*. *Phys. Rev. Lett.*, **86**, 1098–1101, (2001). doi : 10.1103/PhysRevLett.86.1098.
- [RSH<sup>+</sup>14] D. Ruffer, M. Slot, R. Huber, T. Schwarze, F. Heimbach, G. Tütüncüoğlu, F. Matteini, E. Russo-Averchi, A. Kovács, R. Dunin-Borkowski, R. R. Zamani, J. R. Morante, J. Arbiol, A. Fontcuberta i Morral, and D. Grundler. *Anisotropic magnetoresistance of individual CoFeB and Ni nanotubes with values of up to 1.4% at room temperature*. *APL Mat.*, **2**, 076112, (2014). doi : 10.1063/1.4891276.
- [RSK<sup>+</sup>09] A. Rudolph, M. Soda, M. Kiessling, T. Wojtowicz, D. Schuh, W. Wegscheider, J. Zweck, C. Back, and E. Reiger. *Ferromagnetic GaAs/GaMnAs Core-Shell Nanowires Grown by Molecular Beam Epitaxy*. *Nano Lett.*, **9** (11), 3860–3866, (2009). doi : 10.1021/nl9020717.
- [RWG79] R. Richter, M. Wolf, and F. Goedsche. *On the spin-disorder resistivity of amorphous ferromagnets*. *physica status solidi (b)*, **95** (2), 473–482, (1979). doi : 10.1002/pssb.2220950217.
- [Rü09] D. Ruffer. *Nonlocal Phenomena in Metallic Nanostructures – On the Search for the Spin Hall Effect*. Master’s thesis, Technical University Munich, (2009). URL: [http://www.wmi.badw.de/publications/theses/Rueffer\\_Diplomarbeit\\_2009.pdf](http://www.wmi.badw.de/publications/theses/Rueffer_Diplomarbeit_2009.pdf).
- [SA77] T. Suntola and J. Antson. *Method for producing compound thin films*, November 15 (1977). US Patent 4,058,430.
- [SAG<sup>+</sup>09] D. Spirkoska, J. Arbiol, A. Gustafsson, S. Conesa-Boj, F. Glas, I. Zardo, M. Heigoldt, M. H. Gass, A. L. Bleloch, S. Estrade, M. Kaniber, J. Rossler, F. Peiro, J. R. Morante, G. Abstreiter, L. Samuelson, and A. Fontcuberta i Morral. *Structural and optical properties of high quality zinc-blende/wurtzite GaAs nanowire heterostructures*. *Phys. Rev. B*, **80**, 245325, (2009). doi : 10.1103/PhysRevB.80.245325.
- [Sb85] S. Suzuki and K. be. *Topological structural analysis of digitized binary images by border following*. *Comput. Vis. Graph. Image Process.*, **30** (1), 32–46, (1985). doi : 10.1016/0734-189X(85)90016-7.
- [Sch10] H. Schultheiß. *Kohärenz und Dämpfungsverhalten von Spinwellen in magnetischen Mikrostrukturen*. PhD thesis, Technische Universität Kaiserslautern, (2010). URL: [https://www.physik.uni-kl.de/fileadmin/hillebrands/Diplom-\\_und\\_Doktorarbeiten/Phd\\_Schultheiss.pdf](https://www.physik.uni-kl.de/fileadmin/hillebrands/Diplom-_und_Doktorarbeiten/Phd_Schultheiss.pdf).

## Bibliography

---

- [SDVV<sup>+</sup>87] R. W. Simon, B. J. Dalrymple, D. Van Vechten, W. W. Fuller, and S. A. Wolf. *Transport measurements in granular niobium nitride cermet films*. Phys. Rev. B, **36** (4), 1962–1968, (1987). doi:10.1103/PhysRevB.36.1962.
- [SDY<sup>+</sup>99] W. Shenton, T. Douglas, M. Young, G. Stubbs, and S. Mann. *Inorganic–Organic Nanotube Composites from Template Mineralization of Tobacco Mosaic Virus*. Adv. Mater., **11** (3), 253–256, (1999). doi:10.1002/(SICI)1521-4095(199903)11:3<253::AID-ADMA253>3.E3.CO;2-Z.
- [SE01] O. G. Schmidt and K. Eberl. *Nanotechnology: Thin solid films roll up into nanotubes*. Nature, **410** (6825), 168–168, (2001). doi:10.1038/35065525.
- [SFZ<sup>+</sup>11] K. M. Seemann, F. Freimuth, H. Zhang, S. Blügel, Y. Mokrousov, D. E. Bürgler, and C. M. Schneider. *Origin of the Planar Hall Effect in Nanocrystalline  $\text{Co}_{60}\text{Fe}_{20}\text{B}_{20}$* . Phys. Rev. Lett., **107** (8), 086603, (2011). doi:10.1103/PhysRevLett.107.086603.
- [SG13] T. Schwarze and D. Grundler. *Magnonic crystal wave guide with large spin-wave propagation velocity in  $\text{CoFeB}$* . Appl. Phys. Lett., **102** (22), 222412, (2013). doi:10.1063/1.4809757.
- [SHK<sup>+</sup>14] R. Streubel, L. Han, F. Kronast, A. A. Ünal, O. G. Schmidt, and D. Makarov. *Imaging of Buried 3D Magnetic Rolled-up Nanomembranes*. Nano Lett., (2014). doi:10.1021/nl501333h.
- [SLE<sup>+</sup>12] J. Schumann, K. G. Lisunov, W. Escoffier, B. Raquet, J. M. Broto, E. Arushanov, I. Mönch, D. Makarov, C. Deneke, and O. G. Schmidt. *Magnetoresistance of rolled-up  $\text{Fe}_3\text{Si}$  nanomembranes*. Nanotechnology, **23** (25), 255701, (2012). doi:10.1088/0957-4484/23/25/255701.
- [SLS<sup>+</sup>09] S. Shamaila, D. P. Liu, R. Sharif, J. Y. Chen, H. R. Liu, and X. F. Han. *Electrochemical fabrication and magnetization properties of  $\text{CoCrPt}$  nanowires and nanotubes*. Appl. Phys. Lett., **94** (20), 203101, (2009). doi:10.1063/1.3139059.
- [Smi51] J. Smit. *Magnetoresistance of ferromagnetic metals and alloys at low temperatures*. Physica, **17** (6), 612 – 627, (1951). doi:10.1016/0031-8914(51)90117-6.
- [SPS<sup>+</sup>13] G. V. Swamy, H. Pandey, A. K. Srivastava, M. K. Dalai, K. K. Maurya, Rashmi, and R. K. Rakshit. *Effect of thermal annealing on Boron diffusion, micro-structural, electrical and magnetic properties of laser ablated  $\text{CoFeB}$  thin films*. AIP Adv., **3** (7), 072129, (2013). doi:10.1063/1.4816811.
- [SRH<sup>+</sup>05] S. J. Son, J. Reichel, B. He, M. Schuchman, and S. B. Lee. *Magnetic Nanotubes for Magnetic-Field-Assisted Bioseparation, Biointeraction, and Drug Delivery*. J. Am. Chem. Soc., **127** (20), 7316–7317, (2005). doi:10.1021/ja0517365.
- [SS68] F. C. Schwerer and J. Silcox. *Electrical Resistivity of Nickel at Low Temperatures*. Phys. Rev. Lett., **20**, 101–103, (1968). doi:10.1103/PhysRevLett.20.101.
- [SSM<sup>+</sup>08] R. Sharif, S. Shamaila, M. Ma, L. D. Yao, R. C. Yu, X. F. Han, and M. Khaleeq-ur Rahman. *Magnetic switching of ferromagnetic nanotubes*. Appl. Phys. Lett., **92**

- (3), 032505, (2008). doi:10.1063/1.2836272.
- [SSS<sup>+</sup>13] R. Sharif, S. Shamaila, F. Shaheen, J. Y. Chen, M. Khaleeq-ur Rahman, and K. Hussain. *Bloch law for ferromagnetic nanotubes*. Appl. Phys. Lett., **102** (1), 013114, (2013). doi:10.1063/1.4774081.
- [SSSS04] Y. C. Sui, R. Skomski, K. D. Sorge, and D. J. Sellmyer. *Nanotube magnetism*. Appl. Phys. Lett., **84** (9), 1525–1527, (2004). doi:10.1063/1.1655692.
- [Stu11] T. Stueckler. *Magnetowiderstand von ferromagnetischen Filmen auf 3D beschichteten Substraten*. bachelor thesis, TUM E10, (2011).
- [Sun89] T. Suntola. *Atomic layer epitaxy*. Materials Science Reports, **4** (5), 261–312, (1989). doi:10.1016/S0920-2307(89)80006-4.
- [Sun92] T. Suntola. *Atomic layer epitaxy*. In *Thin Solid Films*, volume 216, pages 84 – 89, (1992). International Workshop on Science and Technology of Thin Films for the 21st Century, Evanston,IL, USA, July 28-August 2, 1991. doi:10.1016/0040-6090(92)90874-B.
- [SW48] E. C. Stoner and E. P. Wohlfarth. *A Mechanism of Magnetic Hysteresis in Heterogeneous Alloys*. Phil. Trans. R. Soc. A, **240** (826), 599–642, (1948).
- [SW74] N. L. Schryer and L. R. Walker. *The motion of 180° domain walls in uniform dc magnetic fields*. J. Appl. Phys., **45** (12), 5406–5421, (1974). doi:10.1063/1.1663252.
- [SYL<sup>+</sup>05] Z. Sun, H. Yuan, Z. Liu, B. Han, and X. Zhang. *A Highly Efficient Chemical Sensor Material for H<sub>2</sub>S:  $\alpha$ -Fe<sub>2</sub>O<sub>3</sub> Nanotubes Fabricated Using Carbon Nanotube Templates*. Adv. Mater., **17** (24), 2993–2997, (2005). doi:10.1002/adma.200501562.
- [TGJ<sup>+</sup>06] F. Tao, M. Guan, Y. Jiang, J. Zhu, Z. Xu, and Z. Xue. *An Easy Way to Construct an Ordered Array of Nickel Nanotubes: The Triblock-Copolymer-Assisted Hard-Template Method*. Adv. Mater., **18** (16), 2161–2164, (2006). doi:10.1002/adma.200600275.
- [Tho57] W. Thomson. *On the Electro-Dynamic Qualities of Metals: Effects of Magnetization on the Electric Conductivity of Nickel and of Iron*. Proc. Royal Soc. London, (8), 546–550, (1856-1857).
- [TJIK97] S. Tsunashima, M. Jimbo, Y. Imada, and K. Komiyama. *Spin valves using amorphous magnetic layers*. J. Magn. Magn. Mater., **165** (1–3), 111 – 114, (1997). Symposium E: Magnetic Ultrathin Films, Multilayers and Surfaces. doi:10.1016/S0304-8853(96)00483-0.
- [TKM<sup>+</sup>08] O. Touraghe, M. Khatami, A. Menny, H. Lassri, and K. Nouneh. *Temperature dependence of the electrical resistivity of amorphous Co<sub>80-x</sub>Er<sub>x</sub>B<sub>20</sub> alloys*. Physica B: Condensed Matter, **403** (12), 2093 – 2096, (2008). doi:10.1016/j.physb.2007.11.018.
- [Tou83] G. T. Toussaint. *Solving geometric problems with the rotating calipers*. In *Proc. IEEE Melecon*, volume 83, page A10, (1983).



## Bibliography

---

- [TP06] S. E. Thompson and S. Parthasarathy. *Moore's law: the future of Si microelectronics*. *Materials Today*, **9** (6), 20–25, (2006). doi : 10 . 1016/S1369-7021(06)71539-5.
- [TPHG08] J. Topp, J. Podbielski, D. Heitmann, and D. Grundler. *Internal spin-wave confinement in magnetic nanowires due to zig-zag shaped magnetization*. *Phys. Rev. B*, **78**, 024431, (2008). doi : 10 . 1103/PhysRevB.78.024431.
- [TPLL00] G. Tourillon, L. Pontonnier, J. P. Levy, and V. Langlais. *Electrochemically Synthesized Co and Fe Nanowires and Nanotubes*. *Electrochem. Solid-State Lett.*, **3** (1), 20–23, (2000). doi : 10 . 1149/1.1390946.
- [UAM<sup>+</sup>11] E. Uccelli, J. Arbiol, C. Magen, P. Krogstrup, E. Russo-Averchi, M. Heiss, G. Mugny, F. Morier-Genoud, J. Nygard, J. R. Morante, and A. Fontcuberta i Morral. *Three-Dimensional Multiple-Order Twinning of Self-Catalyzed GaAs Nanowires on Si Substrates*. *Nano Lett.*, **11** (9), 3827–3832, (2011). doi : 10 . 1021/nl201902w.
- [UMC<sup>+</sup>09] E. B. Ureña, Y. Mei, E. Coric, D. Makarov, M. Albrecht, and O. G. Schmidt. *Fabrication of ferromagnetic rolled-up microtubes for magnetic sensors on fluids*. *J. Phys. D: Appl. Phys.*, **42** (5), 055001, (2009).
- [vBBGA13] A. von Bieren, F. Brandl, D. Grundler, and J.-P. Ansermet. *Space- and time-resolved Seebeck and Nernst voltages in laser-heated permalloy/gold microstructures*. *Appl. Phys. Lett.*, **102** (5), 052408, (2013). doi : 10 . 1063/1.4789974.
- [VFP<sup>+</sup>14] K. Vogt, F. Fradin, J. Pearson, T. Sebastian, S. Bader, B. Hillebrands, A. Hoffmann, and H. Schultheiss. *Realization of a spin-wave multiplexer*. *Nat. Commun.*, **5**, 3727, (2014). doi : 10 . 1038/ncomms4727.
- [VVAE10] E. Vogel, P. Vargas, D. Altbir, and J. Escrig. *Nanotubes and Nanowires*, volume 4 of *Handbook of Nanophysics*, chapter 14: Magnetic Nanotubes. CRC Press, (2010).
- [WAC<sup>+</sup>12] M. Weiler, M. Althammer, F. D. Czeschka, H. Huebl, M. S. Wagner, M. Opel, I.-M. Imort, G. Reiss, A. Thomas, R. Gross, and S. T. B. Goennenwein. *Local Charge and Spin Currents in Magnetothermal Landscapes*. *Phys. Rev. Lett.*, **108**, 106602, (2012). doi : 10 . 1103/PhysRevLett.108.106602.
- [Wag61] C. Wagner. *Theorie der Alterung von Niederschlägen durch Umlösen (Ostwald-Reifung)*. *Z. Elektrochem., Ber. Bunsenges. Phys. Chem.*, **65** (7-8), 581–591, (1961). doi : 10 . 1002/bbpc.19610650704.
- [WE64] R. S. Wagner and W. C. Ellis. *Vapor - liquid - solid mechanism of single crystal growth*. *Appl. Phys. Lett.*, **4** (5), 89–90, (1964).
- [Web14] D. Weber. *Cantilever Magnetometry of Individual Ferromagnetic Nanotubes*. PhD thesis, University Basel, (2014).
- [WGW<sup>+</sup>10] Q. Wang, B. Geng, S. Wang, Y. Ye, and B. Tao. *Modified Kirkendall effect for fabrication of magnetic nanotubes*. *Chem. Commun.*, **46**, 1899–1901, (2010). doi : 10 . 1039/B922134D.

- [WKF<sup>+</sup>99] J.-E. Wegrowe, D. Kelly, A. Franck, S. E. Gilbert, and J.-P. Ansermet. *Magnetoresistance of Ferromagnetic Nanowires*. Phys. Rev. Lett., **82**, 3681–3684, (1999). doi:10.1103/PhysRevLett.82.3681.
- [WKN<sup>+</sup>02] Z. K. Wang, M. H. Kuok, S. C. Ng, D. J. Lockwood, M. G. Cottam, K. Nielsch, R. B. Wehrspohn, and U. Gösele. *Spin-Wave Quantization in Ferromagnetic Nickel Nanowires*. Phys. Rev. Lett., **89**, 027201, (2002). doi:10.1103/PhysRevLett.89.027201.
- [WLL<sup>+</sup>05] Z. K. Wang, H. S. Lim, H. Y. Liu, S. C. Ng, M. H. Kuok, L. L. Tay, D. J. Lockwood, M. G. Cottam, K. L. Hobbs, P. R. Larson, J. C. Keay, G. D. Lian, and M. B. Johnson. *Spin Waves in Nickel Nanorings of Large Aspect Ratio*. Phys. Rev. Lett., **94**, 137208, (2005). doi:10.1103/PhysRevLett.94.137208.
- [WLZ<sup>+</sup>06] Z. K. Wang, H. S. Lim, V. L. Zhang, J. L. Goh, S. C. Ng, M. H. Kuok, H. L. Su, and S. L. Tang. *Collective Spin Waves in High-Density Two-Dimensional Arrays of FeCo Nanowires*. Nano Lett., **6** (6), 1083–1086, (2006). doi:10.1021/nl060026+.
- [WRB<sup>+</sup>12] D. P. Weber, D. Ruffer, A. Buchter, F. Xue, E. Russo-Averchi, R. Huber, P. Berberich, J. Arbiol, A. Fontcuberta i Morral, D. Grundler, and M. Poggio. *Cantilever Magnetometry of Individual Ni Nanotubes*. Nano Lett., **12** (12), 6139–6144, (2012). doi:10.1021/nl302950u.
- [WWL<sup>+</sup>06] T. Wang, Y. Wang, F. Li, C. Xu, and D. Zhou. *Morphology and magnetic behaviour of an Fe<sub>3</sub>O<sub>4</sub> nanotube array*. J. Phys.: Condens. Matter, **18** (47), 10545, (2006).
- [YAK<sup>+</sup>11] M. Yan, C. Andreas, A. Kákay, F. García-Sánchez, and R. Hertel. *Fast domain wall dynamics in magnetic nanotubes: Suppression of Walker breakdown and Cherenkov-like spin wave emission*. Appl. Phys. Lett., **99** (12), 122505, (2011). doi:10.1063/1.3643037.
- [YAK<sup>+</sup>12] M. Yan, C. Andreas, A. Kákay, F. García-Sánchez, and R. Hertel. *Chiral symmetry breaking and pair-creation mediated Walker breakdown in magnetic nanotubes*. Appl. Phys. Lett., **100** (25), 252401, (2012). doi:10.1063/1.4727909.
- [YC11] A. Yourdkhani and G. Caruntu. *Highly ordered transition metal ferrite nanotube arrays synthesized by template-assisted liquid phase deposition*. J. Mater. Chem., **21**, 7145–7153, (2011). doi:10.1039/C0JM04441E.
- [YDH<sup>+</sup>13a] H. Yu, G. Duerr, R. Huber, M. Bahr, T. Schwarze, F. Brandl, and D. Grundler. *Omnidirectional spin-wave nanograting coupler*. Nat. Commun., **4**, 2702, (2013). doi:10.1038/ncomms3702.
- [YDH<sup>+</sup>13b] X. Yu, J. P. DeGrave, Y. Hara, T. Hara, S. Jin, and Y. Tokura. *Observation of the Magnetic Skyrmion Lattice in a MnSi Nanowire by Lorentz TEM*. Nano Lett., **13** (8), 3755–3759, (2013). doi:10.1021/nl401687d.
- [YHS<sup>+</sup>12] H. Yu, R. Huber, T. Schwarze, F. Brandl, T. Rapp, P. Berberich, G. Duerr, and D. Grundler. *High propagating velocity of spin waves and temperature dependent damping in a CoFeB thin film*. Appl. Phys. Lett., **100** (26), 262412, (2012).

## Bibliography

---

doi:10.1063/1.4731273.

- [YKAH13] M. Yan, A. Kákay, C. Andreas, and R. Hertel. *Spin-Cherenkov effect and magnonic Mach cones*. Phys. Rev. B, **88** (22), 220412, (2013). doi:10.1103/PhysRevB.88.220412.
- [YWL<sup>+</sup>06] L. F. Yin, D. H. Wei, N. Lei, L. H. Zhou, C. S. Tian, G. S. Dong, X. F. Jin, L. P. Guo, Q. J. Jia, and R. Q. Wu. *Magnetocrystalline Anisotropy in Permalloy Revisited*. Phys. Rev. Lett., **97**, 067203, (2006). doi:10.1103/PhysRevLett.97.067203.
- [YWP<sup>+</sup>13] X. Yu, H. Wang, D. Pan, J. Zhao, J. Misuraca, S. von Molnár, and P. Xiong. *All Zinc-Blende GaAs/(Ga,Mn)As Core-Shell Nanowires with Ferromagnetic Ordering*. Nano Lett., **13** (4), 1572–1577, (2013). doi:10.1021/nl304740k.
- [ZCWL07] D. Zhou, L.-h. Cai, F.-s. Wen, and F.-s. Li. *Template Synthesis and Magnetic Behavior of FeNi Alloy Nanotube Arrays*. Chin. J. Chem. Phys., **20** (6), 821–825, (2007). doi:10.1088/1674-0068/20/06/821-825.
- [ZLH<sup>+</sup>04] D. Zhang, Z. Liu, S. Han, C. Li, B. Lei, M. P. Stewart, J. M. Tour, and C. Zhou. *Magnetite (Fe<sub>3</sub>O<sub>4</sub>) Core-Shell Nanowires: Synthesis and Magnetoresistance*. Nano Lett., **4** (11), 2151–2155, (2004). doi:10.1021/nl048758u.
- [ZOI<sup>+</sup>97] S. Zhang, S. A. Oliver, N. E. Israeloff, A. Widom, and C. Vittoria. *Ferromagnetic resonance of micrometer-sized samples*. J. Appl. Phys., **81** (8), 4307–4309, (1997). doi:10.1063/1.364810.
- [ZWZ<sup>+</sup>11] D. Zhou, T. Wang, M. Zhu, Z. Guo, W. Li, and F. Li. *Magnetic Interaction in FeCo Alloy Nanotube Array*. Journal of Magnetism, **16** (4), 413–416, (2011). doi:10.4283/JMAG.2011.16.4.413.
- [ZZW<sup>+</sup>13] X. Zhang, H. Zhang, T. Wu, Z. Li, Z. Zhang, and H. Sun. *Comparative study in fabrication and magnetic properties of FeNi alloy nanowires and nanotubes*. J. Magn. Magn. Mater., **331** (0), 162 – 167, (2013). doi:10.1016/j.jmmm.2012.11.033.



# Appendix Part



# A Supplementary Information

## A.1 Pub. A-II: Supplementary Information

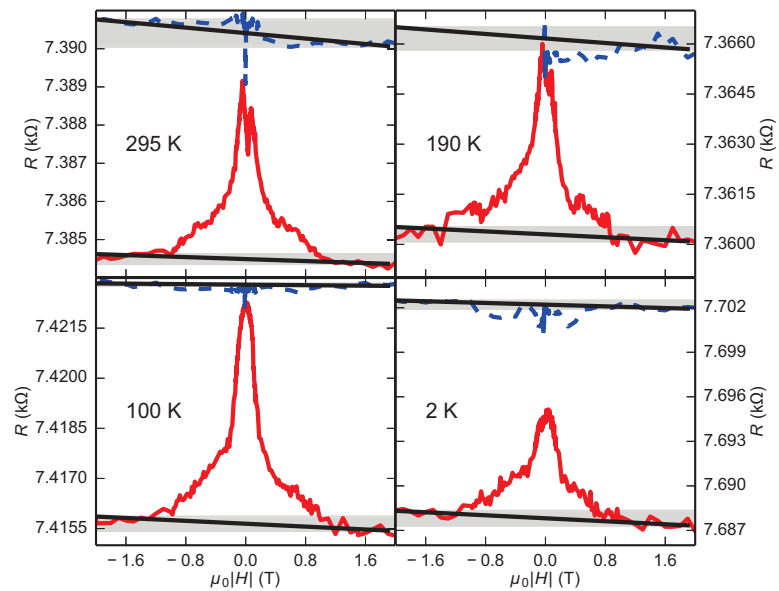


Figure A.1 – Data used for the calculation of the AMR ratio for CFBM1: the black lines show the linear fits to  $R(B > 1$  T). The shaded span gives the area considered for the estimation of the accuracy of the fit.

## Appendix A. Supplementary Information

Sample	$T$	Material	$D_{\text{total}}$	$L_{\text{contact}}$	$t_{\text{nominal}}$	$R(M_{\text{sat}})$	$\rho$ (RT)	AMR	$\mu_0 H_{\text{sat},\perp}$
NiS1	300 K	Ni	180-190 nm	13.2 $\mu\text{m}$	20 nm	54.3 $\Omega$	4 m $\Omega\text{cm}$	1.4%	$0.35 \pm 0.05$ T
NiS2	300 K	Ni	170-180 nm	11.0 $\mu\text{m}$	20 nm	284.7 $\Omega$	25 m $\Omega\text{cm}$	1.0%	-
NiM	295 K	Ni	220-230 nm	8.4 $\mu\text{m}$	20 nm	110.3 $\Omega$	17 m $\Omega\text{cm}$	1.4%	-
NiL1	300 K	Ni	330-350 nm	8.4 $\mu\text{m}$	40 nm	40.9 $\Omega$	18 m $\Omega\text{cm}$	1.2%	-
NiL2	300 K	Ni	330-390 nm	11.5 $\mu\text{m}$	40 nm	94.7 $\Omega$	33 m $\Omega\text{cm}$	-	-
CFBS1	300 K	CoFeB	160-180 nm	8.1 $\mu\text{m}$	20 nm	7.8 k $\Omega$	$1 \cdot 10^3$ m $\Omega\text{cm}$	0.1%	$1.2 \pm 0.2$ T
CFBS2	300 K	CoFeB	180-200 nm	8.1 $\mu\text{m}$	20 nm	8.3 k $\Omega$	$1 \cdot 10^3$ m $\Omega\text{cm}$	0.1%	$1.2 \pm 0.2$ T
CFBS3	300 K	CoFeB	160-185 nm	6.5 $\mu\text{m}$	20 nm	5.6 k $\Omega$	$1 \cdot 10^3$ m $\Omega\text{cm}$	-	-
CFBM1	280 K	CoFeB	220-250 nm	8.1 $\mu\text{m}$	30 nm	7.4 k $\Omega$	$2 \cdot 10^3$ m $\Omega\text{cm}$	0.1%	$1.2 \pm 0.2$ T
CFBM2	300 K	CoFeB	205-250 nm	8.1 $\mu\text{m}$	30 nm	7.8 k $\Omega$	$2 \cdot 10^3$ m $\Omega\text{cm}$	0.1%	$1.1 \pm 0.2$ T
CFBM3	300 K	CoFeB	220-250 nm	8.0 $\mu\text{m}$	30 nm	7.7 k $\Omega$	$2 \cdot 10^3$ m $\Omega\text{cm}$	-	-
NiL1	2 K	Ni	330-350 nm	8.4 $\mu\text{m}$	40 nm	15.8 $\Omega$	7 m $\Omega\text{cm}$	0.3%	$0.30 \pm 0.05$ T
CFBS1	2 K	CoFeB	160-180 nm	8.1 $\mu\text{m}$	20 nm	8.0 k $\Omega$	$1 \cdot 10^3$ m $\Omega\text{cm}$	0.1%	-
CFBM1	2 K	CoFeB	220-250 nm	8.1 $\mu\text{m}$	30 nm	7.7 k $\Omega$	$2 \cdot 10^3$ m $\Omega\text{cm}$	0.2%	$1.1 \pm 0.1$ T
CFBM2	2 K	CoFeB	205-250 nm	8.1 $\mu\text{m}$	30 nm	8.3 k $\Omega$	$2 \cdot 10^3$ m $\Omega\text{cm}$	0.1%	$1.1 \pm 0.1$ T

Table A.1 – Overview of samples, geometrical dimensions and measured values. The diameter  $D_{\text{total}}$  provides the values measured by a scanning electron microscopy at the head and tail of the nanotubes. The values differ most likely due to the conical shape of the nanowire core.

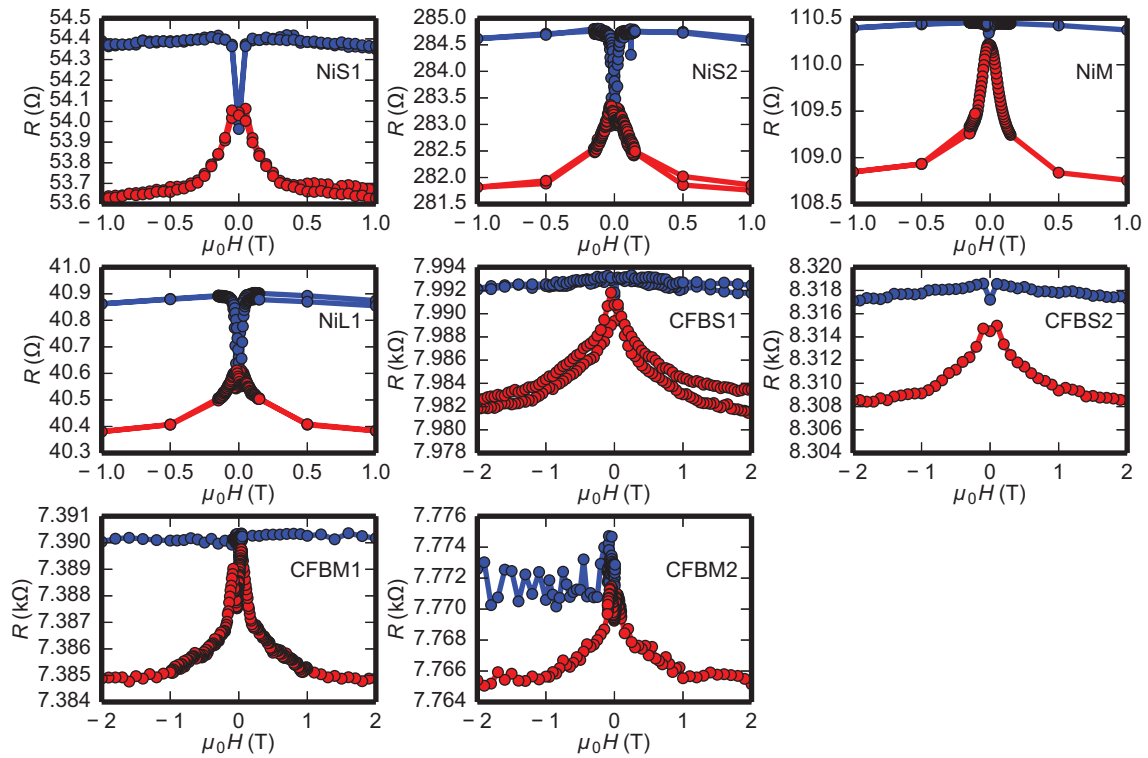


Figure A.2 – Field sweep raw data at room temperature for samples given in Tab. A.1.

## A.2 Pub. A-III: Supplementary Information

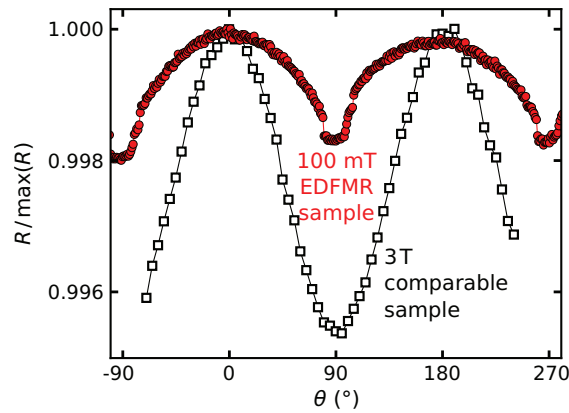


Figure A.3 – Normalized resistance  $R/\max(R)$  for the sample presented in the main paper (red circles) as function of the angle  $\theta$  between the axis and the external field  $\mu_0 H = 100$  mT. For comparison we plot the same curve for a comparable sample, measured in a setup with superconducting solenoid magnets at 3 T.

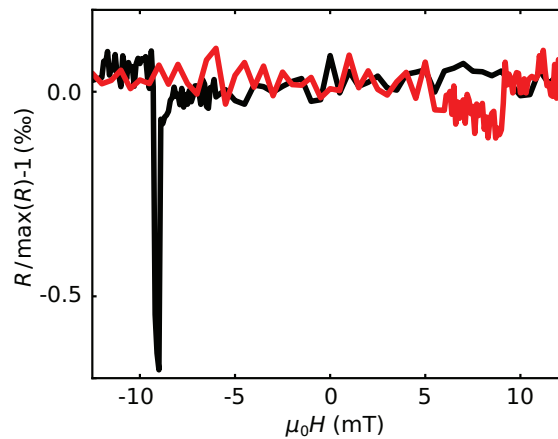


Figure A.4 – Normalized resistance  $R/\max(R) - 1$  for the sample presented in the main paper as function of the external field  $\mu_0 H$  for parallel alignment.

## Appendix A. Supplementary Information

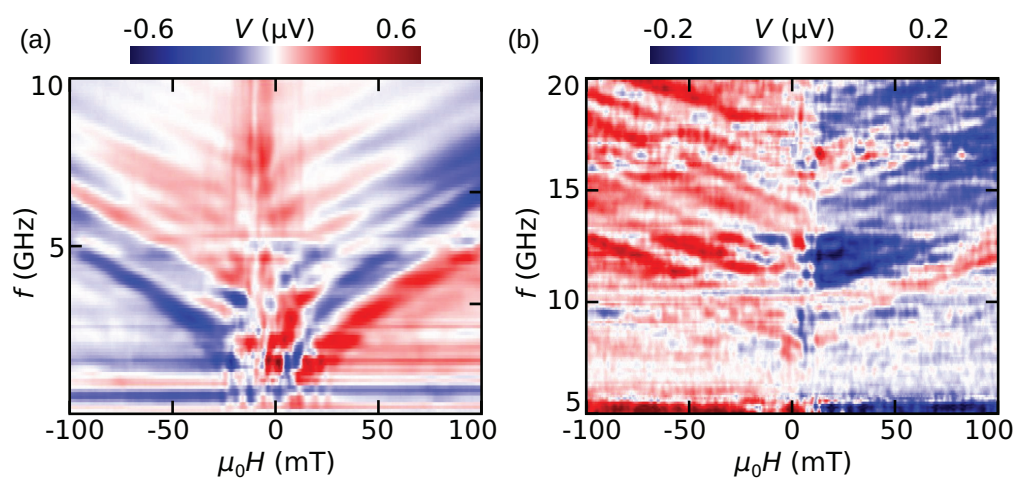


Figure A.5 – **a**  $V(f, H)$  for a 12.0  $\mu\text{m}$  Nickel tube with film thickness of 40 nm and  $D = 310 - 390$  nm, as well as for **b** a 16.5  $\mu\text{m}$  CoFeB tube with a 30 nm film and total diameter of between 210 and 250 nm.

## B Additional data

### B.1 Ni tubes

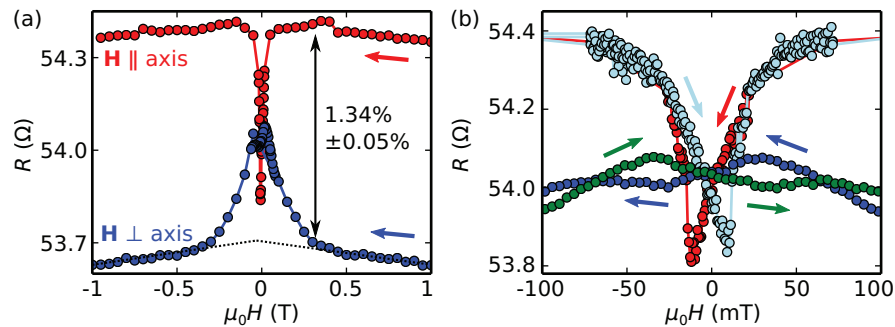


Figure B.1 – Hysteresis curves for Ni sample NiS1 with  $L = 16.4 \mu\text{m}$ ,  $L_{\text{contact}} = 13.2 \mu\text{m}$ ,  $r_o = 90 - 95 \text{ nm}$  and  $t = 20 \text{ nm}$  at room temperature for (a) a large field range and (b) zoom around zero field.

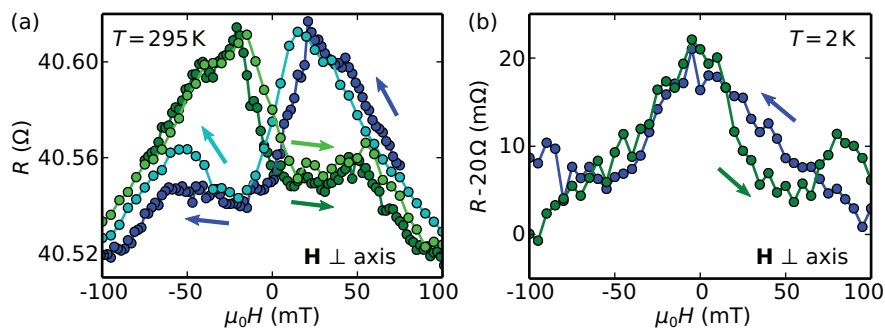


Figure B.2 – Hysteresis curves for Ni sample NiL1 with  $L = 14.5 \mu\text{m}$ ,  $L_{\text{contact}} = 8.4 \mu\text{m}$ ,  $r_o = 165 - 175 \text{ nm}$  and  $t = 40 \text{ nm}$  at (a) room temperature and (b) 2 K.

The exact form of the hysteresis curve in Ni samples differs from sample to sample and from measurement to measurement. Local minima can almost always be found. The transition

## Appendix B. Additional data

has not always been non-continuous as shown in Pub. A-I (cf. Fig. 6.3 p. 64 in Sec. 6.1). At the current point, the collected data allows not for a clear understanding of the reason. Examples are given in Fig. B.1 and B.2. The measurements were performed collaboratively by Marlou Slot and me.

### B.2 CoFeB tube

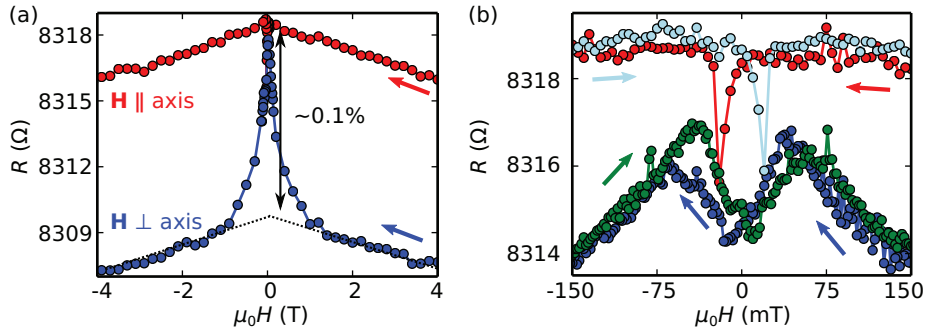


Figure B.3 – Hysteresis curves for CoFeB sample CFBS2 with  $L = 11.2 \mu\text{m}$ ,  $L_{\text{contact}} = 8.1 \mu\text{m}$ ,  $r_o = 80 - 90 \text{ nm}$  and  $t = 20 \text{ nm}$  at room temperature for (a) a large field range and a (b) zoom around zero field.

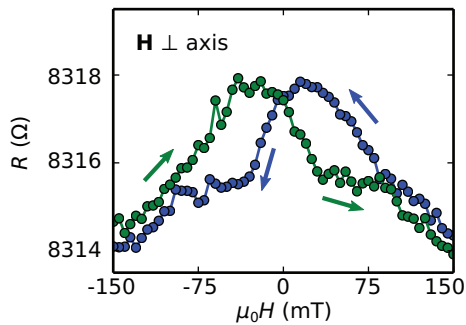


Figure B.4 – Another hysteresis curve recorded before the curves of Fig. B.3 (b). The field was applied with a misalignment of  $5^\circ$  relative to the normal.

Although the characteristic hysteresis curve with a change of slope (cf. Sec. 7.2) can be found in all CoFeB samples, some showed additionally a fine structure close to zero field. Field sweeps of sample CFBS2 in Pub. A-II can be found in Fig. B.3. Before acquiring the data of Fig. B.3 (b), another sweep at  $5^\circ$  misalignment from the normal was performed. The curves, showing different behavior, can be found in Fig. B.4. Because of the limited data available, the origin of the difference cannot be determined. It is not clear whether the angle, statistics or an aging of the sample can be made responsible for the discrepancy.

The measurements were performed collaboratively by Marlou Slot and me.



# C Parameters & Values

## C.1 Lithography mask fabrication by e-beam lithography

Figure C.1 depicts the layout of the photolithography mask for automated localization of nanotubes and sub-sequent e-beam patterning. The mask comprises four Pre-Alignment Markers (PAMM), comprising 29x29 square markers. The square markers all have slightly varying distances. This way the *Vistec* EBL tool can determine its position with only three to four markers. The active area of the wafer is surrounded by crosses, which can serve as guides for dicing or cleaving. The area is divided into 8x8 blocks, which are again divided into 16x16 cells. All in all there are 128x128 cells. Each block is surrounded by 64 square markers for EBL stage alignment. They have a distance of 500  $\mu\text{m}$  to each other. The markers at corners between the blocks serve as wafer level alignment marker. The remaining markers are used in sets of four for a block-level alignment. Although redundancy is used, in case a marker is hidden below some deposited structure, not all markers are used.

Each cell comprises an area of 500  $\mu\text{m}$   $\times$  500  $\mu\text{m}$ . In its center is a 200  $\mu\text{m}$   $\times$  150  $\mu\text{m}$  frame defined by four 4  $\mu\text{m}$  circles. These circles are used by the software to scale the image. In bottom left corner, each cell integrates a simple “barcode”. The number is encoded using existence or non-existence of the circle: circle corresponds to a binary one and a void equals zero. To describe the 128x128 cells, two 7 bit numbers are employed.

## C.2 Process flows for the sample fabrication

### C.2.1 Mask writing via e-beam lithography

The *Vistec EBPB 5000* at CMi, EPFL is capable of writing masks for photolithography on 4”-wafers. Because writing of a mask was not a common task at CMi at this time, masks for laser writing were used. Here, the photo resist had to be stripped in piranha bath prior to usage<sup>1</sup>. In

---

<sup>1</sup>Note that additional cleaning in oxygen plasma is advisable but not always possible due to the chromium layer of the mask.

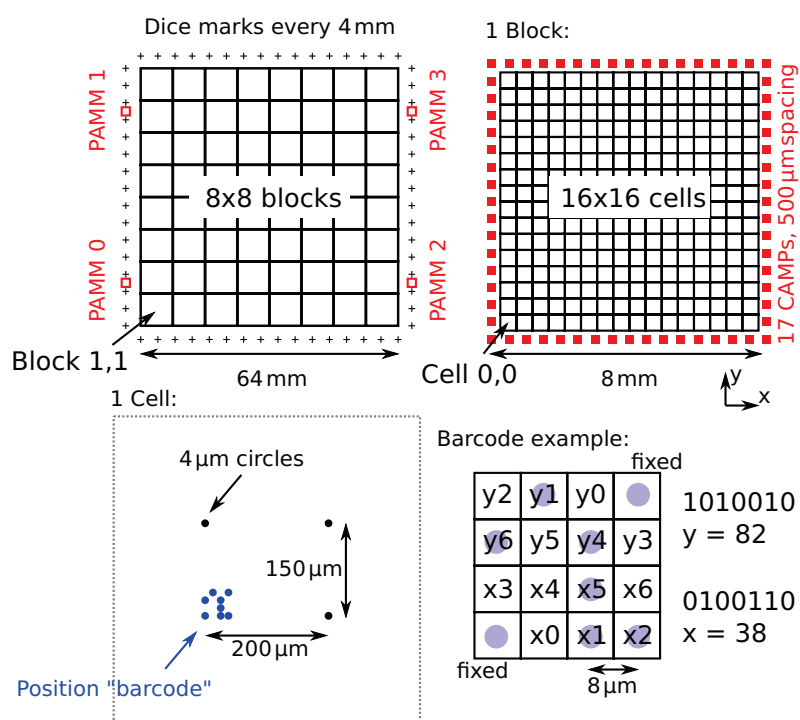


Figure C.1 – Detailed mask layout for automated nanotube detection and e-beam patterning

such cases the adhesion of the PMMA to the mask can be limited and defects in the etching step occur. It is thus highly recommended to use clean new glass, or better quartz, masks without pre-coated resist. The process is not fully optimized and further improvements of the recipe are most likely possible.

1. Surface activation: rinse the mask with MF CD26, then with DI water and finally let it dry<sup>2</sup>.
2. Spin-coating of 500 nm of PMMA 495K A4 at 4000 rpm. Cover the mask well with resist before spinning.
3. 8 min baking at 190 °C.
4. Leave the mask to cool for at least 30 min.
5. It is advisable to give the mask enough time to thermalize, e.g. perform loading before other jobs or, better, over night.
6. Development in MiBK:IPA 1:3 solution for 1 min. Ensure homogeneous contact with fresh solution over the surface for the complete process.
7. Etch Cr with CR-7 MOS ( $\text{HClO}_4 + \text{Ce}(\text{NH}_4)_2(\text{NO}_3)_6 + \text{H}_2\text{O}$ ). Etch time is feature size dependent and can be controlled visually. We experienced etch times around 70 s excluding transfer to QDR bath.
8. Stop etching by Quick Dump and Rinse (QDR), Ultra Clean (UC) bath and dry with  $\text{N}_2$ .
9. Rinse with Technistrip P1316.

<sup>2</sup>This step is meant to improve adhesion by activating the surface. It might not be necessary.

10. Immersion for 10 min in Technistrip P1316.
11. QDR, UC and dry with N<sub>2</sub>.

### C.2.2 Default alignment pattern

Compare Fig. 5.2 (c):

1. Substrate: 4"-Si Si(100) with 200 nm wet oxide (CMI Test wafer)
2. Surface treatment / dehydrate: 4 min oxygen plasma, 500 W 400 ml/min O<sub>2</sub> (TEPLA 300)
3. Spin coating of double layer positive lift-off resist, 1.2 μm MicroChem Corp. AZ© 1512 on 400 nm LOR, (EVG 150)
  - (a) 150 °C dehydration for 3 min and 30 s
  - (b) LOR coating at 6500 rpm
  - (c) Bake at 190 °C for 4 min CPW with unprotected tube
  - (d) Coat AZ1512 at 6000 rpm
  - (e) Softbake at 100 °C for 1 min and 30 s
4. UV exposure using Flexipattern mask, 1.7 s at 10 mW/cm<sup>2</sup> (Süss Microtec MA150)
5. Development, MIF CD 26 with 50 s total contact time and 1 min post-development bake at 100 °C (EVG 150)
6. Deposition of 5 nm Ti / 50 nm Au via e-beam evaporation with 4 Å/s at RT and 1.5 · 10<sup>-6</sup> mbar base pressure in the HRN configuration (Leybold Optics LAB 600H)
7. Lift-off in Remover 1165 at 70 °, approx. 1 min of ultrasound, left for multiple hours in bath

### C.2.3 Electrical contacts to nanotube

Compare Fig. 5.5 (a):

1. Prepare default alignment pattern (cf. C.2.2)
2. Deposit nanotubes from isopropanol solution
3. Clean wafer with acetone and isopropanol
4. Pattern definition by e-beam using positive double layer lift-off resist:
  - (a) Dehydrate: 10 min at 180 °C
  - (b) Spin-coat ~400 nm MMA EL9 at 2500 rpm (manual)
  - (c) Bake 5 min at 180 °C
  - (d) Spin-coat ~150 nm PMMA 495K A4 at 4000 rpm (manual)
  - (e) Bake 5 min at 180 °C
  - (f) E-beam exposure (Vistec EPBG 5000-ES), 150 nA beam (equiv. 75 nm spot size), 25 nm grid and a dose of 800 μC/mm<sup>2</sup>
  - (g) Development in MiBK:IPA 1:3 solution for 1 min
  - (h) Rinse with DI water

## Appendix C. Parameters & Values

---

5. DC magnetron sputter deposition of typically 5 nm Ti / 150 nm Au (Alliance Concept DP650)
  - (a) RF-etch in  $5 \cdot 10^{-2}$  mbar Ar, 100 W
  - (b) 12.2 s Ti at 4.1 Å/s,  $5 \cdot 10^{-3}$  mbar Ar, 250 W
  - (c) 120.97 s Au at 11.4 Å/s,  $5 \cdot 10^{-3}$  mbar Ar, 400 W
6. Lift-off in Acetone, 30 s of ultrasound, left for multiple hours in bath

### C.2.4 Lifted nano-tubes

Compare Fig. 5.5 (d):

1. Prepare default alignment pattern (cf. C.2.2)
2. ~300 nm sacrificial MMA EL9 layer at 3000 rpm (manual coater)
3. Deposit nanotubes from isopropanol solution
4. Clean wafer with isopropanol only
5. Default e-beam process (Step 4 C.2.3)
6. DC magnetron sputter deposition of 5 nm Ti / 500 nm Au (Alliance Concept DP650)
  - (a) RF-etch in  $5 \cdot 10^{-2}$  mbar Ar, 100 W
  - (b) 12.2 s Ti at 4.1 Å/s,  $5 \cdot 10^{-3}$  mbar Ar, 250 W
  - (c) 438.6 s Au at 11.4 Å/s,  $5 \cdot 10^{-3}$  mbar Ar, 400 W
7. Lift-off in Acetone, 30 s of ultrasound, left for multiple hours in bath

### C.2.5 Asymmetric waveguide with contacts

Compare Fig. 5.5 (b):

1. Deposit electrical contacts (cf. C.2.3), using separate layers in the software
2. Clean wafer with acetone and isopropanol
3. Second e-beam process for waveguide pattern (Step 4 C.2.3)
4. Deposition of 5 nm Ti / 120 nm Au via e-beam evaporation with 4 Å/s at RT and  $1.5 \cdot 10^{-6}$  mbar base pressure in the HRN configuration (Leybold Optics LAB 600H)
5. Lift-off in Acetone, 30 s of ultrasound, left for multiple hours in bath

### C.2.6 Co-planar waveguide underneath nanotube

Compare Fig. 5.5 (c). In this process Ion Beam Etching (IBE) is performed on negative nLOF resist. This leads to hardening of the resist and complicates its removal. It can either be left on top and mechanically removed before contacting of the waveguide, or an oxygen plasma step has to be used. The nanotube has to be protected during the oxygen plasma and thus additional steps for coating of the protective layer are introduced. These steps are marked with a star (\*). In future, the IBE process could be replaced by appropriate chemical etching and thus the problem of hardening avoided.

### C.2.6.1 Metallization of wafer and negative alignment markers

1. Substrate: 4"-Si Si(100) with 200 nm wet oxide (CMI Test wafer)
2. Deposition of 10 nm Ti / 100 nm Au via e-beam evaporation with 4 Å/s at RT and  $1.5 \cdot 10^{-6}$  mbar base pressure in the HRN configuration (Leybold Optics LAB 600H)
3. Deposition of 10 nm Al<sub>2</sub>O<sub>3</sub> in 75 cycles as isolation layer by ALD (Beneq TF200)<sup>3</sup>
4. Spin coating of 1.5 μm of MicroChem Corp. AZ© 1512 positive resist (EVG 150)
  - (a) Coat AZ© 1512 at 3000 rpm
  - (b) Bake at 112 °C for 1 min and 30 s
5. UV exposure using Flexipattern V11 mask, 1.7 s at 10 mW/cm<sup>2</sup> (Süss Microtec MA150)
6. Development, MIF CD 26 with 40 s total contact time and 90 s post-development bake at 112 °C (EVG 150)
7. Ion beam etching for 70 s at High, corresponding to 700 V acceleration voltage, and -5° fixture angle and rotation (Veeco Nexus IBE350)
8. 10 min oxygen plasma, 500 W 400 ml/min O<sub>2</sub> (TEPLA 300)

### C.2.6.2 CPW etch

Steps marked with \* can be left out, if the organic resist is to be removed mechanically before contacting.

1. Fabricate metallized wafer (cf. C.2.6.1)
2. Deposit nanotubes from isopropanol solution
3. \* Deposition of 10 nm Al<sub>2</sub>O<sub>3</sub> in 75 cycles to protect nanotubes (Beneq TF200)
4. Definition of rectangle around nanotube (first layer) by e-beam using negative resist in order to remove the isolation layer:
  - (a) Dehydration for 5 min at about 200 °C
  - (b) Spin-coating ~300 nm of nLOF:PGMEA 1:1 at 3000 rpm
  - (c) Bake 2 min at 115 °C
  - (d) E-beam exposure (Vistec EPBG 5000-ES), 20 nA beam (equiv. 15 nm spot size), 25 nm grid and a dose of 90 μC/mm<sup>2</sup>
5. Custom development process at CMI, developed by Laszlo Pethö (EVG150), it basically consists of:<sup>4</sup>
  - (a) 2 min post-exposure bake at 107 °C
  - (b) 30 s development with MIF726
6. 10 s buffered HF (BHF) dip
7. Stripping of nLOF in SVC-14 for about 2 × 5 min and sub-sequent DI rinsing

---

<sup>3</sup>This step could be replaced by, e.g., sputtering of a desired insulator.

<sup>4</sup>Please note, that the development steps is very sensitive and undeveloped nLOF prone to aging. It is thus recommended to have less than one hour delay between exposure and development. Furthermore, use of an automatized development procedure (as with the EVG150) is highly recommended for reproducible results.

## Appendix C. Parameters & Values

---

8. Definition of CPW by e-beam using negative resist (Step 4 with second layer). Dose correction with correction parameters of  $\eta = 0.5$  and  $\beta = 33.0$  in GenISys Layout BEAMER.
9. Development (Step 5)
10. Ion beam etching for 70 s at High, corresponding to 700 V acceleration voltage, and  $-5^\circ$  fixture angel and rotation (Veeco Nexus IBE350)
11. \* Removal of hardened resist: 10 min oxygen plasma, 500 W 400 ml/min O<sub>2</sub> (TEPLA 300)

## D Co-authored papers

### **Publication B-I: Cantilever Magnetometry of Individual Ni Nanotubes**

D. P. Weber, D. Ruffer, A. Buchter, F. Xue, E. Russo-Averchi, R. Huber, P. Berberich, J. Arbiol, A. Fontcuberta i Morral, D. Grundler, and M. Poggio

*Nano Letters*, 2012, 12 (12), 6139–6144  
doi: 10.1021/nl302950u

*Reprinted with permission from Nano Letters, 2012, 12 (12), 6139–6144.  
Copyright 2012 American Chemical Society.*

I participated actively in the discussion and interpretation. The experiment and the modeling were done by Arne Buchter, Martino Poggio and Dennis Weber, who wrote the majority of the manuscript.

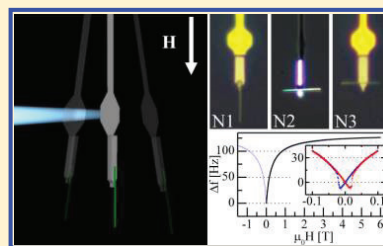
## Cantilever Magnetometry of Individual Ni Nanotubes

D. P. Weber,<sup>†</sup> D. Ruffer,<sup>‡</sup> A. Buchter,<sup>†</sup> F. Xue,<sup>†</sup> E. Russo-Averchi,<sup>‡</sup> R. Huber,<sup>§</sup> P. Berberich,<sup>§</sup> J. Arbiol,<sup>#</sup> A. Fontcuberta i Morral,<sup>‡</sup> D. Grundler,<sup>§,||</sup> and M. Poggio<sup>\*,†</sup><sup>†</sup>Departement Physik, Universität Basel, 4056 Basel, Switzerland<sup>‡</sup>Laboratoire des Matériaux Semiconducteurs, Institut des Matériaux, Ecole Polytechnique Fédérale de Lausanne, 1015 Lausanne, Switzerland<sup>§</sup>Lehrstuhl für Physik funktionaler Schichtsysteme, Physik Department E10, Technische Universität München, James-Frank-Str. 1, 85748 Garching, Germany<sup>||</sup>Faculté des Sciences et Techniques de l'Ingénieur STI, Ecole Polytechnique Fédérale de Lausanne, 1015 Lausanne, Switzerland<sup>#</sup>Institució Catalana de Recerca i Estudis Avançats and Institut de Ciència de Materials de Barcelona, 08193 Bellaterra, CAT, Spain

## Supporting Information

**ABSTRACT:** Recent experimental and theoretical work has focused on ferromagnetic nanotubes due to their potential applications as magnetic sensors or as elements in high-density magnetic memory. The possible presence of magnetic vortex states—states which produce no stray fields—makes these structures particularly promising as storage devices. Here we investigate the behavior of the magnetization states in individual Ni nanotubes by sensitive cantilever magnetometry. Magnetometry measurements are carried out in the three major orientations, revealing the presence of different stable magnetic states. The observed behavior is well-described by a model based on the presence of uniform states at high applied magnetic fields and a circumferential onion state at low applied fields.

**KEYWORDS:** Magnetic nanotubes, cantilever magnetometry, magnetic tubular architectures, nanomagnetic states



The synthesis and investigation of ferromagnetic nanostructures has been motivated both by a large number of potential applications and by fundamental questions about the physics of nanometer-scale magnetism. Magnetic nanoparticles have potential biological and biomedical applications,<sup>1–6</sup> applications in high-resolution magnetic imaging,<sup>7–9</sup> as magnetic sensors,<sup>10</sup> and as dense magnetic storage media.<sup>11</sup> At the same time, the low-dimensionality of these structures results in magnetic configurations not present in macroscopic magnets.<sup>12–15</sup> In particular, magnetic nanotubes distinguish themselves from magnetic nanowires in that they support core-free magnetic states. Such configurations avoid the magnetic point singularity along the axis of the structure,<sup>16</sup> thereby resulting in a fast and controllable reversal process.<sup>17</sup> In addition, previously unforeseen dynamic effects are possible in nanotubes. Domain walls moving in nanotubes are predicted to avoid a Walker breakdown and give rise to Cherenkov-like spin wave emission.<sup>18</sup> Both numerical simulations<sup>19</sup> and analytical calculations<sup>20,21</sup> show that the tubular geometry favors two main in-plane states: a uniform axial state (UAS) with the magnetic moments pointing along the tube axis and a global vortex state (GVS) with moments pointing circumferentially around the tube. Due to their flux-closure configuration, vortex states produce much lower stray fields than uniform states; as a result, magneto-static interactions between nanomagnets could be reduced resulting in densely packed magnetic memories. Further possibilities include a multidomain state (MDS)<sup>17</sup>

composed of a mixture of uniform and vortex domains, an onion state (OS)<sup>22,23</sup> consisting of two oppositely oriented circumferential domains, and uniform states in which all magnetic moments align along the applied field. For nanotubes with tailored magneto-crystalline or interfacial anisotropy a radial out-of-plane state (ROS), in which magnetic moments align along the tube radius, is also possible. Here we present experimental measurements of individual Ni nanotubes supporting the presence of various states including uniform states, the MDS, and the OS.

We use sensitive dynamic-mode cantilever magnetometry<sup>24</sup> to investigate the magnetic states of the nanotubes. Our approach allows us to measure the moment, anisotropy, and switching behavior of a single Ni nanotube as a function of applied magnetic field and orientation. Until recently, magnetization measurements had only been carried out on large ensembles of ferromagnetic nanotubes.<sup>25–31</sup> Due to the distribution in size and orientation, these measurements are difficult to interpret. In 2012, Ruffer et al. probed the magnetic states of a single Ni nanotube in transport measurements using the anisotropic magnetoresistance effect.<sup>23</sup> Here we use a different method to measure the magnetization and effective

Received: August 8, 2012

Revised: October 19, 2012

Published: November 6, 2012



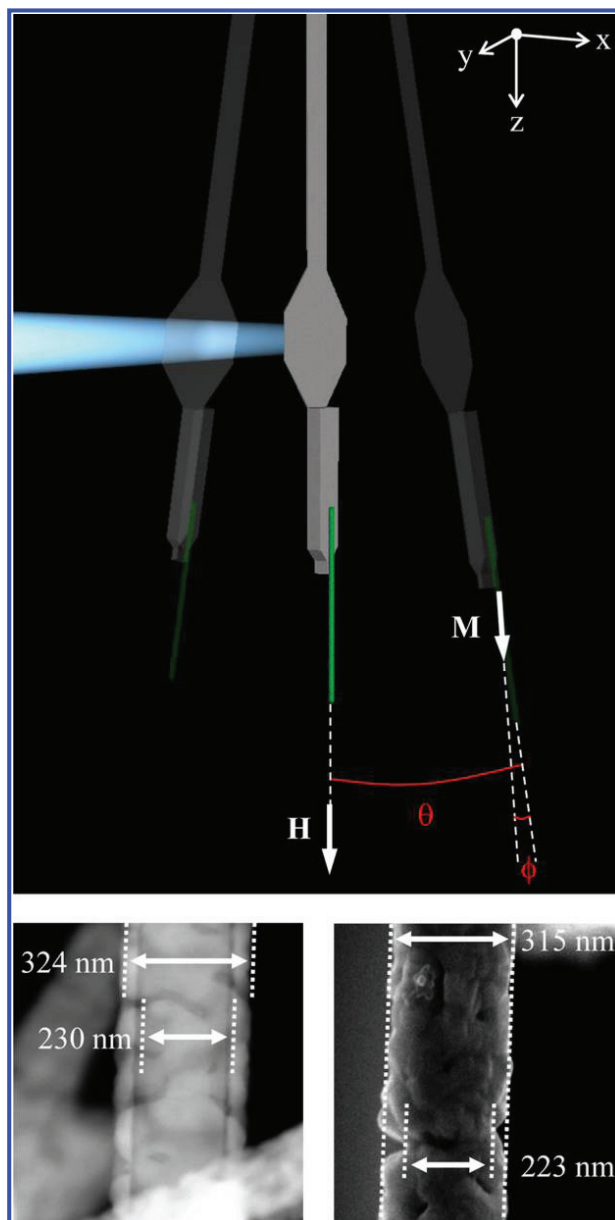


**Figure 1.** Top: Schematic diagram showing the oscillating cantilever (gray), laser light from the interferometer (white), the Ni nanotube (green), and the relative orientations of the cantilever axis, the applied magnetic field  $H$ , and the Ni nanotube magnetization  $M$ . Bottom: Transmission electron micrograph (TEM) (left), and scanning electron micrograph (SEM) (right) of a single Ni nanotube. Arrows indicate both the maximal inner and the outer diameter of the Ni shell.

magnetic anisotropy of individual Ni nanotubes, shedding further light on their magnetic states. Due to its high sensitivity, cantilever magnetometry is well-suited for the detection of the

weak magnetic response of a variety of nanometer-scale systems. We note recent measurements of the persistent currents in normal metal rings,<sup>32</sup> of the magnetization of

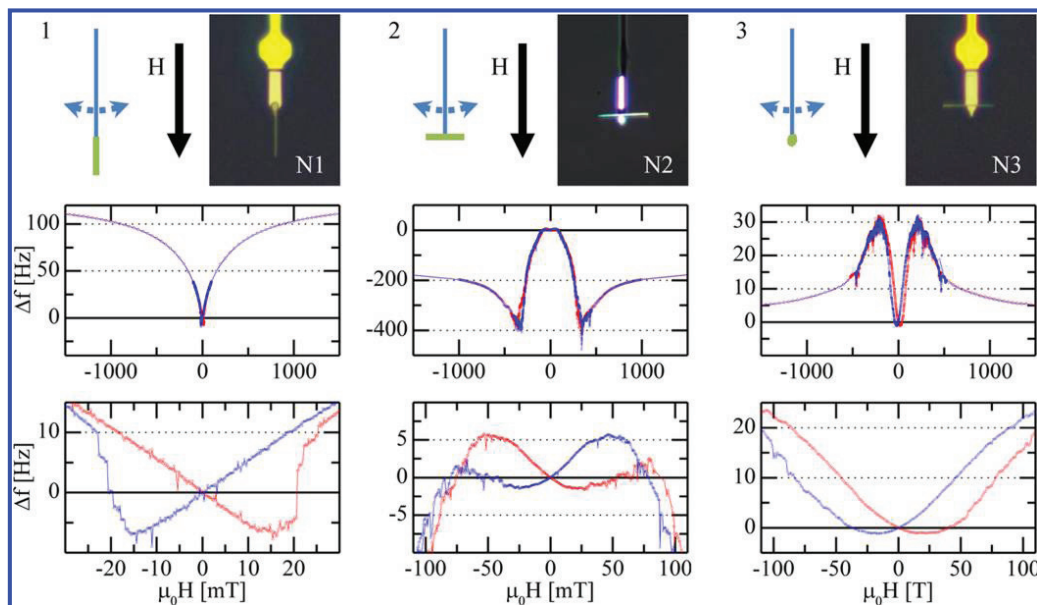


**Figure 2.** Cantilever magnetometry measurements in three major orientations. Each column shows measurements from one of the major orientations as indicated by the schematic diagrams at the top; from left to right we show configurations 1, 2, and 3, with optical micrographs of the nanotube samples N1, N2, and N3. The lower two rows show the corresponding measurements of  $\Delta f$  as a function of  $H$  in different field ranges for each configuration. Red (blue) points represent data taken while sweeping  $H$  in the positive (negative) direction.

superconducting nanostructures,<sup>33</sup> and of magnetization reversal in a single iron-filled carbon nanotube<sup>34</sup> and a single Ni nanorod.<sup>35</sup>

Cantilever magnetometry experiments are carried out in a vacuum chamber with a pressure below  $1 \times 10^{-6}$  mbar at the bottom of a  $^4\text{He}$  cryostat. A superconducting magnet allows the application of an external magnetic field  $\mu_0 H$  of up to 6 T along the cantilever axis  $\hat{z}$ . Each single Ni nanotube that we investigate is affixed to the tip of an ultrasoft cantilever (see Supporting Information, Figures S1 and S2) with less than 100 fL of epoxy (Gatan G1) applied under an optical microscope by means of precision micromanipulators (Narishige MMO-202ND). The nanomagnets are produced by atomic layer deposition (ALD) of Ni on a nanowire template made of GaAs<sup>23</sup> (see Figure 1). Since the GaAs nanowires have the shape of a slightly sloped truncated cone, the 20- $\mu\text{m}$ -long nanotubes have an outer diameter which narrows from around 360 nm at one end to 280 nm at the other. The thickness of the Ni shell is just over 40 nm (see Supporting Information, Table S1). The single-crystal Si cantilevers used here are 150  $\mu\text{m}$  long, 4  $\mu\text{m}$  wide, and 0.1  $\mu\text{m}$  thick and include a 18- $\mu\text{m}$ -long, 1- $\mu\text{m}$ -thick mass on their end.<sup>36</sup> The motion of the levers is detected using laser light focused onto a 12- $\mu\text{m}$ -wide paddle near the mass-loaded end and reflected back into an optical fiber interferometer.<sup>37</sup> 100 nW of light are incident on the paddle from a temperature-tuned 1550 nm distributed feedback laser diode. At  $T = 4.2$  K and  $\mu_0 H = 0$  T, the nanotube-loaded cantilevers have resonant frequencies  $f_0 = \omega_0/(2\pi)$  between 2 and 3 kHz and intrinsic quality factors around  $Q_0 = 3 \times 10^4$ . Their spring constants  $k_0$  are determined to be close to 60  $\mu\text{N}/\text{m}$  through measurements of thermal noise spectra at several

different temperatures (see Supporting Information, Table S1). The interferometric cantilever deflection signal is fed through a field programmable gate array (FPGA) circuit (National Instruments) back to a piezoelectric element which is mechanically coupled to the cantilever. In this way, we are able to self-oscillate the cantilever at its fundamental resonance frequency and at a desired amplitude. Self-oscillation allows for fast and accurate measurement of the cantilever resonance frequency.

We measure  $f_0$  as a function of  $H$  at  $T = 4.2$  K with a self-oscillation amplitude of  $x_{\text{rms}} = 40$  nm. For such small cantilever deflections  $x \ll l_c$ , where  $l_c = 105 \mu\text{m}$  is the effective cantilever length for the fundamental mode, the Ni nanotube tilts by an angle  $\theta = x/l_c$  with respect to  $\hat{z}$  as shown in Figure 1. The measured shift in resonance frequency  $\Delta f$  depends on the torque acting between the Ni nanotube and  $H$ . The experiments are carried out for identically grown Ni nanotubes mounted on the cantilever tip in the three major orientations. Configuration 1 corresponds to the nanotube's symmetry axis  $\hat{z}'$  aligned along  $\hat{z}$ . Configurations 2 and 3 correspond to  $\hat{z}'$  aligned along  $\hat{x}$  and  $\hat{y}$ , respectively, where  $\hat{x}$  corresponds to the direction of cantilever deflection. The orientations, samples, and  $\Delta f$  as a function of  $H$  are shown in Figure 2. Note that the three configurations are realized using three different nanotubes fabricated in the same growth and ALD process; we label the nanotubes N1, N2, and N3, respectively.

The dependence of  $\Delta f$  on  $H$  is fundamentally different for each configuration. In configuration 1,  $\Delta f$  is positive for large  $|H|$  and approaches a constant value. At low fields, the data show a clear hysteresis with switching occurring through a series of discrete steps in  $\Delta f$ . In the other configurations the

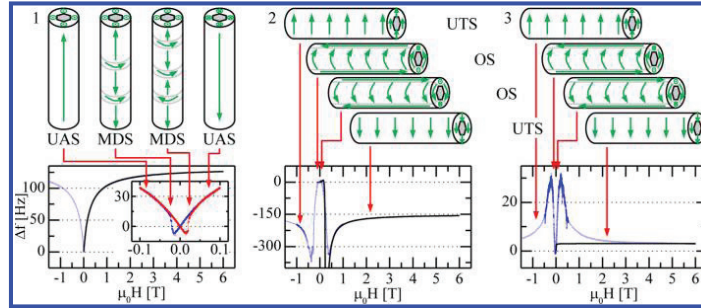


**Figure 3.** Magnetic state progression and model fits in three major orientations. In the top row we show schematic diagrams of the magnetization states described in the text. The lower row shows measurements of  $\Delta f$  (blue points), and the fit functions based on eq 2 (black lines) as a function of  $H$  for each configuration. Red arrows indicate magnetic fields corresponding to the specified state.

dependence is more complex: in configuration 2,  $\Delta f$  becomes negative, and for large  $|H|$  eventually approaches a constant negative value; minima in  $\Delta f$  are observed near +400 and -400 mT. In configuration 3,  $\Delta f$  is positive and goes through a maximum, and for large  $|H|$  approaches a small positive value. Both configurations 2 and 3 show hysteresis at low fields. For all orientations, we measure a negligible dependence of the mechanical dissipation on  $H$  beyond that intrinsic to the Si cantilevers.<sup>38</sup> The fluctuation–dissipation theorem implies that magnetic-field dependent dissipation is the result of magnetic moment fluctuations in the sample or the cantilever. The lack of additional magnetic fluctuations due to the Ni nanotubes is likely due to their large magnetic anisotropy.

To interpret our data we begin by making the simplifying assumption that our nanotube behaves as a single-domain magnetic particle, that is, its magnetization is uniform and rotates in unison. For high enough applied fields, the nanotube is magnetized to saturation, and thus this single-domain assumption is valid. We therefore describe the nanotube's magnetic state by the orientation of its total magnetization vector  $\mathbf{M}$ . More complex states deviating from this assumption will be addressed separately later. Since the Ni nanotube is polycrystalline and does not exhibit magneto-crystalline anisotropy, we assume the nanotube to exhibit only shape anisotropy. The total energy of the system can be written as the sum of the cantilever energy, the Zeeman energy, and an effective anisotropy energy:<sup>39</sup>

$$E = \frac{1}{2}k_0(l_c\theta)^2 - MVH \cos(\theta - \phi) + KV \sin^2 \phi \quad (1)$$

where  $V$  is the volume of the nanotube,  $K$  is its anisotropy in the plane of the cantilever oscillation, and  $\phi$  is the angle between  $\mathbf{M}$  and  $\hat{z}'$ . To calculate  $\phi$ , we minimize the energy of the system with respect to this angle. The solutions must satisfy both  $\partial E/\partial \phi = 0$  and  $\partial^2 E/\partial \phi^2 > 0$ . Although solutions for  $\phi$  are difficult to obtain exactly, since  $\theta \ll 1$ , we can expand  $\phi$  as a function of  $\theta$  to first order around  $\theta = 0$ . We then substitute the expansion for  $\phi(\theta)$  into the expression for the torque acting on the cantilever,  $\tau = -\partial E/\partial \theta = -k_0 l_c^2 \theta - HMV \sin(\theta - \phi)$ . Keeping only terms up to first order in  $\theta$  and approximating the cantilever as a simple harmonic oscillator, we solve for the cantilever's frequency shift  $\Delta f = f - f_0$ , where  $f$  is the measured resonance frequency and  $f_0$  is the resonance frequency at  $H = 0$ . The expected frequency shift as a function of  $H$  is (see Supporting Information for full derivation):

$$\Delta f = \begin{cases} \frac{\omega_0}{4\pi k_0 l_c^2} \left( \frac{2HKV}{H + \frac{2K}{M}} \right) & H > -\frac{2K}{M} \\ \frac{\omega_0}{4\pi k_0 l_c^2} \left( \frac{2HKV}{H - \frac{2K}{M}} \right) & H < \frac{2K}{M} \\ \frac{\omega_0}{4\pi k_0 l_c^2} \left[ \frac{H^2 M^2 V}{2K} \right. & K < 0 \text{ and } |H| \\ \left. \left( \frac{(2K/M)^2}{M} - H^2 \right) \right] & < \frac{2K}{M} \end{cases} \quad (2)$$

Singularities at  $H = \pm(2K/M)$  reflect the breakdown of the small angle approximation, and the solutions become invalid near this field. The first two solutions correspond to  $\mathbf{M}$  pointing along  $\pm \hat{z}$  respectively. The third solution, valid only for  $K < 0$ , corresponds to  $\mathbf{M}$  along an easy axis perpendicular to  $\hat{z}$  (the implication of a negative  $K$ ) and rotating toward  $\hat{z}$  with increasing  $H$ .

Using this model based on a single-domain magnetic particle, we can fit the data taken in configuration 1. The data and the fit function, given by eq 2, are plotted together in Figure 3.  $\omega_0$ ,  $k_0$ , and  $V$  are set to their measured values (see Supporting Information, Table S1), while  $M = M_s = 330 \pm 50$  kA/m and  $K = 44 \pm 6$  kJ/m<sup>3</sup> are extracted as fit parameters for sample N1. Here the effective anisotropy  $K$  represents the anisotropy of the easy axis oriented along the nanotube's axis of symmetry  $\hat{z}'$  in the plane of the cantilever oscillation.

While at high fields ( $\mu_0 H > 100$  mT), the measurements are consistent with a UAS, at low fields the step-like structures shown in Figure 2 (see also Supporting Information, Figure S3) cannot be described by the uniform magnetization model. These discrete magnetization steps indicate the presence of transition states between the two UASs. In addition, the number of steps, which occur at slightly different fields each time the field is swept, suggest the presence of three to five MDSs. According to calculations,<sup>17</sup> MDSs are possible and are configured as depicted in Figure 3; that is, they consist of uniform axially saturated domains separated by azimuthal, or vortex-like, domain walls.

A similar fit using eq 2 can be made for the data taken in configuration 2 as shown in Figure 3. Here  $K < 0$  since  $\mathbf{H}$  is directed along a hard axis of the nanotube, and the cantilever oscillates in a plane defined by this hard axis and its easy axis  $\hat{z}'$ . In this orientation and at sufficiently high field, the magnetic moments in the nanotube will align uniformly along the applied field, forming a uniform transverse state (UTS). The magnetometry measurement should therefore result in an  $M$  equal to that measured in configuration 1 and a  $K$  with an equal magnitude and the opposite sign. In fact, we extract  $M = M_S = 420 \pm 90$  kA/m and  $K = -52 \pm 11$  kJ/m<sup>3</sup> as fit parameters for sample N2. These values are equal to the values extracted in configuration 1 for N1 within the error of the measurement, which is dominated by the difficulty of determining each nanotube's exact volume. Although eq 2 describes the data for large  $|H|$ , the measurements deviate from the model at low fields. In particular, for  $|\mu_0 H| < 100$  mT the data show a clear hysteresis. According to eq 2, only one stable solution of  $\Delta f$  exists for  $K < 0$ , unlike in the case of  $K > 0$  where two exist for  $|H| < (2K/M)$ . With only one stable solution, hysteretic behavior cannot be reproduced; therefore we conclude that the description of a single uniform magnetization in the nanotube breaks down at low applied fields. Furthermore, the low-field hysteresis points to the presence of a magnetization state with positive effective anisotropy for small  $H$ .

One explanation for the differing behavior at high and low fields is that, while at high fields the Ni nanotube is uniformly magnetized, at low fields a more complex state emerges. One possible state, which has been predicted to be stable for such samples at low fields, is the OS.<sup>23</sup> This state is shown schematically in Figure 3 and consists of azimuthally oriented magnetization domains separated by axially oriented domain walls. The OS has a total magnetization  $M < (1/2\pi) \int_0^{2\pi} 2M_S \sin \theta' d\theta' = (2/\pi)M_S$  due to the azimuthal orientation of its domains and a positive effective anisotropy, related to the energy required to rotate the azimuthally oriented magnetization domains toward the nanotube axis. The presence of the OS at low fields could explain the hysteresis observed in configuration 2. Due to its lower magneto-static energy compared to saturated states, the OS is favored in low magnetic fields. For this reason we suppose the Ni nanotube to undergo a transition from the OS to the UTS as a function of increasing  $|H|$ . Given the region of deviation between the simple model and the data, this transition region is likely to be between  $|\mu_0 H| = 0$  and 2 T. Here we hypothesize the presence of a MDS with some segments of the nanotube in the OS and some in the UTS.

The aforementioned model is also consistent with the data measured in configuration 3 on sample N3. The high field behavior is well-described by a UTS with  $M = M_S = 375$  kA/m and a small positive magnetic anisotropy  $K = 0.90 \pm 0.25$  kJ/m<sup>3</sup>. Note that we choose  $M_S$  of N3 to be between the values extracted for N1 and N2, since the high field behavior of the fit in configuration 3 is highly insensitive to  $M$ .  $\mathbf{H}$  is directed along a hard axis of the nanotube, and the cantilever oscillates in a plane perpendicular to its axis of symmetry  $\hat{z}'$ . For an ideal nanotube in this orientation, no anisotropy should be present due to its circular symmetry; because of inevitable imperfections of real Ni nanotubes (see Figure 1), this symmetry is broken, and therefore we measure a small, in this case positive,  $K$ . For small  $|H|$  the data deviate from this small positive anisotropy behavior, showing the presence of an unsaturated low-field state as observed in configuration 2. Hysteresis again

appears for  $|\mu_0 H| < 100$  mT, and a transition region exists for  $|\mu_0 H| < 2$  T. In this case, the low-field magnetometry points to a state with a larger positive anisotropy in this plane than the UTS. Once again, this low-field behavior is consistent with the OS. In this plane the OS has a positive effective anisotropy, related to the energy required to move the axially oriented domain walls and thus rotate the magnetization around the nanotube axis. The total magnetization is  $M < (2/\pi)M_S$  due to the azimuthal orientation of its domains. Frequency measurements in both configurations 2 and 3 show pronounced and reproducible structures as a function of  $H$  for  $|\mu_0 H| < 1$  T. These changes in  $\Delta f$ , and thus in magnetic torque, likely result from the gradual transition of the low-field OS to the UTS throughout the volume of the nanotube.

A GVS, which has a total magnetization  $M = 0$ , should appear in our cantilever magnetometry measurements as a range in  $H$  for which  $\Delta f = 0$ . The ROS, which also has a total magnetization  $M = 0$  and would produce  $\Delta f = 0$ , cannot be achieved since the Ni nanotubes are composed of an isotropic ferromagnet without crystalline anisotropy. As long as the GVS is stable for a significant range, that is, a range greater than 10 mT, it would be observable in our experiment. In Figures 2.2 and 2.3 for  $|\mu_0 H| \approx 50$  mT,  $\Delta f = 0$  for a small field range. While this behavior is consistent with the GVS, we cannot exclude that  $\Delta f = 0$  might be produced by a MDS with  $M = 0$  or with the appropriate combination of magnetization  $M$  and anisotropy  $K$ . In minor hysteresis loops of the cantilever magnetometry (see Supporting Information, Figure S4), we can produce states with  $\Delta f = 0$  for field ranges of up to 50 mT. Again this evidence is consistent with the GVS but does not exclude the presence of other states. On the other hand, Rüffer et al. report evidence for a GVS in similar Ni nanotubes.<sup>23</sup> The discrepancy may be due to differences in the geometrical parameters of the nanotubes, indicating what is already known from numerical and analytical calculations: the GVS is supported only for nanotubes which meet specific geometric conditions.

In conclusion we have presented experimental evidence for an onion and a multidomain state (OS, MDS) in ALD-grown Ni nanotubes. Dynamic cantilever magnetometry measurements of single nanotubes in the three principal orientations highlight the stability of complex low-field magnetic configurations. The characteristics of these low-field states are compatible with both the OS and the MDS as predicted by various theoretical works. From the cantilever magnetometry data above, we cannot unambiguously identify the global vortex state; a specific MDS may account for the same behavior. From measurements on different nanotubes, the developed analytical model provides us with consistent values for the saturation magnetization  $M_S = 375 \pm 70$  kA/m and the anisotropy constant  $|K| = 48 \pm 9$  kJ/m<sup>3</sup> for the easy axis. The  $M_S$  measured in the Ni nanotubes is equal within the error to the value of 406 kA/m known for bulk crystalline Ni at low temperature.<sup>40</sup> Future high-resolution X-ray magnetic circular dichroism photoelectron emission microscopy (XMCD-PEEM)<sup>14,15</sup> or magnetic force microscopy (MFM)<sup>22,41</sup> experiments on such magnetic nanotubes could provide further evidence for the presence of an OS or a GVS.

## ■ ASSOCIATED CONTENT

### Supporting Information

Full derivation of the model, video of the fabrication of the Ni nanotubes, SEMs of the measured nanotubes, study of the step-

like structures of configuration 1, minor hysteresis loops, and a table of sample and cantilever specifications. This material is available free of charge via the Internet at <http://pubs.acs.org>.

### ■ AUTHOR INFORMATION

#### Corresponding Author

\*E-mail: [martino.poggio@unibas.ch](mailto:martino.poggio@unibas.ch).

#### Notes

The authors declare no competing financial interest.

### ■ ACKNOWLEDGMENTS

The authors thank Prof. J. Arbiol from ICREA/ICMAB for making TEM images and Sascha Martin of the Mechanical Workshop at the Physics Department of the University of Basel for important contributions to the measurement apparatus. We acknowledge support from the Canton Aargau, the Swiss National Science Foundation (SNF, Grant No. 200020-140478), the Swiss Nanoscience Institute, and the National Center of Competence in Research for Quantum Science and Technology. The research has also received funding from the European Community's Seventh Framework Programme (FP7/2007-2013) under Grant Agreement No. 228673, MAGNONICS.

### ■ REFERENCES

- Pankhurst, Q. A.; Connolly, J.; Jones, S. K.; Dobson, J. J. *Phys. D: Appl. Phys.* **2003**, *36*, R167.
- Son, S. J.; Reichel, J.; He, B.; Schuchman, M.; Lee, S. B. *J. Am. Chem. Soc.* **2005**, *127*, 7316.
- Leslie-Pelecky, D. L.; Labhasetwar, V. D.; Kraus, R. H., Jr. In *Advanced Magnetic Nanostructures*; Sellmyer, D., Skomski, R., Eds.; Springer: New York, 2006; pp 461–482.
- Lee, D.; Cohen, R. E.; Rubner, M. F. *Langmuir* **2007**, *23*, 123.
- Amstad, E.; Zurcher, S.; Wong, J. Y.; Textor, M.; Reimhult, E. *Small* **2009**, *5*, 1334.
- Kim, D.-H.; Rozhkova, E. A.; Ulasov, U. V.; Bader, S. D.; Rajh, T.; Lesniak, M. S.; Novosad, V. *Nat. Mater.* **2010**, *9*, 165.
- Khizroev, S.; Kryder, M. H.; Litvinov, D. *Appl. Phys. Lett.* **2002**, *81*, 2256.
- Poggio, M.; Degen, C. L. *Nanotechnology* **2010**, *21*, 342001.
- Campanella, H.; Jaafar, M.; Llobet, J.; Esteve, J.; Vázquez, M.; Asenjo, A.; del Real, R. P.; Plaza, J. A. *Nanotechnology* **2011**, *22*, 505301.
- Maqableh, M. M.; Huang, X.; Sung, S.-Y.; Reddy, K. S. M.; Norby, G.; Victoria, R. H.; Stadler, B. J. H. *Nano Lett.* **2012**, *12*, 4102–4109.
- Parkin, S. S. P.; Hayashi, M.; Thomas, L. *Science* **2008**, *320*, 190.
- Wang, Z. K.; Kuok, M. H.; Ng, S. C.; Lockwood, D. J.; Cottam, M. G.; Nielsch, K.; Wehrspohn, R. B.; Gösele, U. *Phys. Rev. Lett.* **2002**, *89*, 027201.
- Topp, J.; Podbielski, J.; Heitmann, D.; Grundler, D. *Phys. Rev. B* **2008**, *78*, 024431.
- Streubel, R.; Thurmer, J.; Makarov, D.; Kronast, F.; Kosub, T.; Kravchuk, V.; Sheka, D. D.; Gaididei, Y.; Schäfer, R.; Schmidt, O. G. *Nano Lett.* **2012**, *12*, 3961.
- Streubel, R.; Kravchuk, V. P.; Sheka, D. D.; Makarov, D.; Kronast, F.; Schmidt, O. G.; Gaididei, Y. *Appl. Phys. Lett.* **2012**, *101*, 132419.
- Hertel, R.; Kirschner, J. *J. Magn. Magn. Mater.* **2003**, *278*, L291.
- Landeros, P.; Suarez, O. J.; Cuchillo, A.; Vargas, P. *Phys. Rev. B* **2009**, *79*, 024404.
- Yan, M.; Andreas, C.; Kákay, A.; García-Sánchez, F.; Hertel, R. *Appl. Phys. Lett.* **2012**, *100*, 252401.
- Wang, Z. K.; Lim, H. S.; Liu, H. Y.; Ng, S. C.; Kuok, M. H. *Phys. Rev. Lett.* **2005**, *94*, 137208.
- Escrig, J.; Landeros, P.; Altbir, D.; Vogel, E. E.; Vargas, P. *J. Magn. Magn. Mater.* **2007**, *308*, 233.
- Escrig, J.; Landeros, P.; Altbir, D.; Vogel, E. E. *J. Magn. Magn. Mater.* **2007**, *310*, 2448q.
- Castañó, F. J.; Ross, C. A.; Frandsen, C.; Eilez, A.; Gil, D.; Smith, H. I.; Redjal, M.; Humphrey, F. B. *Phys. Rev. Lett.* **2003**, *67*, 184425.
- Rüffer, D.; Huber, R.; Berberich, P.; Russo-Averchi, E.; Heiss, M.; Arbiol, J.; Fontcuberta i Morral, A.; Grundler, D. *Nanoscale* **2012**, *4*, 4989.
- Stipe, B. C.; Mamin, H. J.; Stowe, T. D.; Kenny, T. W.; Rugar, D. *Phys. Rev. Lett.* **2001**, *86*, 2874.
- Bachmann, J.; Jing, J.; Knez, M.; Barth, S.; Shen, H.; Mathur, S.; Gösele, U.; Nielsch, K. *J. Am. Chem. Soc.* **2007**, *129*, 9554.
- Daub, M.; Knez, M.; Gösele, U.; Nielsch, K. *J. Appl. Phys.* **2007**, *101*, 09J111.
- Bachmann, J.; Escrig, J.; Pitzschel, K.; Moreno, J. M. M.; Jing, J.; Görlitz, D.; Altbir, D.; Nielsch, K. *J. Appl. Phys.* **2009**, *105*, 07B521.
- Rudolph, A.; Soda, M.; Kiessling, M.; Wojtowicz, T.; Schuh, D.; Wegscheider, W.; Zweck, J.; Back, C.; Reiger, E. *Nano Lett.* **2009**, *9*, 3860.
- Chong, Y. T.; Görlitz, D.; Martens, S.; Yau, M. Y. E.; Allende, S.; Bachmann, J.; Nielsch, K. *Adv. Mater.* **2010**, *22*, 2435.
- Albrecht, O.; Zierold, R.; Allende, S.; Escrig, J.; Patzig, C.; Rauschenbach, B.; Nielsch, K.; Görlitz, D. *J. Appl. Phys.* **2011**, *109*, 093910.
- Escrig, J.; Bachmann, J.; Jing, J.; Daub, M.; Altbir, D.; Nielsch, K. *Phys. Rev. B* **2008**, *77*, 214421.
- Bleszynski-Jayich, A. C.; Shanks, W. E.; Peaudecerf, B.; Ginossar, E.; von Oppen, F.; Glazman, L.; Harris, J. G. E. *Science* **2009**, *326*, 272.
- Jang, J.; Ferguson, D. G.; Vakaryuk, V.; Budakian, R.; Chung, S. B.; Goldbart, P. M.; Maeno, Y. *Science* **2011**, *331*, 186.
- Banerjee, P.; Wolny, F.; Pelekhov, D. V.; Herman, M. R.; Fong, K. C.; Weissker, U.; Mühl, T.; Obukhov, Yu.; Leonhardt, A.; Büchner, B.; Hammel, P. C. *Appl. Phys. Lett.* **2010**, *96*, 252505.
- Lee, S.; Moore, E. W.; Hickman, S. A.; Longenecker, J. G.; Marohn, J. A. *J. Appl. Phys.* **2012**, *111*, 083911.
- Chui, B. W.; Hishinuma, Y.; Budakian, R.; Mamin, H. J.; Kenny, T. W.; Rugar, D. *Transducers, 12th Int. Conf. Solid-State Sensors, Actuators Microsyst.* **2003**, *2*, 1120.
- Rugar, D.; Mamin, H. J.; Guethner, P. *Appl. Phys. Lett.* **1989**, *55*, 2588.
- Xue, F.; Peddibhotla, P.; Montinaro, M.; Weber, D. P.; Poggio, M. *Appl. Phys. Lett.* **2011**, *98*, 163103.
- Stoner, E. C.; Wohlfarth, E. P. *Philos. Trans. R. Soc. London, Ser. A* **1948**, *240*, 599.
- Kittel, C. *Introduction to Solid-State Physics*, 8th ed.; Wiley: New York, 2005.
- Li, S. P.; Peyrade, D.; Natali, M.; Lebib, A.; Chen, Y.; Ebels, U.; Buda, L. D.; Ounadjela, K. *Phys. Rev. Lett.* **2001**, *86*, 1102.

### ■ NOTE ADDED AFTER ASAP PUBLICATION

This paper was published ASAP on November 9, 2012. J. Arbiol has been added as a contributing author. The revised version posted on November 16, 2012.



**Publication B-II: Reversal Mechanism of an Individual Ni Nanotube Simultaneously Studied by Torque and SQUID Magnetometry**

A. Buchter, J. Nagel, Daniel Ruffer, F. Xue, D. P. Weber, O. F. Kieler, T. Weimann, J. Kohlmann, A. B. Zorin, E. Russo-Averchi, R. Huber, P. Berberich, A. Fontcuberta i Morral, M. Kemmler, R. Kleiner, D. Koelle, D. Grundler, and M. Poggio

*Phys. Rev. Lett.*, 2013, 111, 067202  
doi: 10.1103/PhysRevLett.111.067202

*Reprinted with permission from Phys. Rev. Lett.*, 2013, 111, 067202.  
*Copyright 2013 American Physical Society.*

I participated actively in the discussion and interpretation and conducted the micromagnetic simulations. The experiment and the modeling were done by Arne Buchter, Martino Poggio and Dennis Weber, who wrote the majority of the manuscript.

## Reversal Mechanism of an Individual Ni Nanotube Simultaneously Studied by Torque and SQUID Magnetometry

A. Buchter,<sup>1</sup> J. Nagel,<sup>2</sup> D. Ruffer,<sup>3</sup> F. Xue (薛飞),<sup>1</sup> D. P. Weber,<sup>1</sup> O. F. Kieler,<sup>4</sup> T. Weimann,<sup>4</sup> J. Kohlmann,<sup>4</sup> A. B. Zorin,<sup>4</sup> E. Russo-Averchi,<sup>3</sup> R. Huber,<sup>5</sup> P. Berberich,<sup>5</sup> A. Fontcuberta i Morral,<sup>3</sup> M. Kemmler,<sup>2</sup> R. Kleiner,<sup>2</sup> D. Koelle,<sup>2</sup> D. Grundler,<sup>5,6,\*</sup> and M. Poggio<sup>1,†</sup>

<sup>1</sup>Department of Physics, University of Basel, 4056 Basel, Switzerland

<sup>2</sup>Physikalisches Institut and Center for Collective Quantum Phenomena in LISA+, Universität Tübingen, 72076 Tübingen, Germany

<sup>3</sup>Laboratoire des Matériaux Semiconducteurs, Institut des Matériaux, Ecole Polytechnique Fédérale de Lausanne, 1015 Lausanne, Switzerland

<sup>4</sup>Fachbereich 2.4 "Quantenelektronik", Physikalisch-Technische Bundesanstalt, 38116 Braunschweig, Germany

<sup>5</sup>Lehrstuhl für Physik funktionaler Schichtsysteme, Physik Department E10,

Technische Universität München, 85747 Garching, Germany

<sup>6</sup>Institut des Matériaux, Faculté Sciences et Technique de l'Ingénieur, Ecole Polytechnique Fédérale de Lausanne, 1015 Lausanne, Switzerland

(Received 14 May 2013; revised manuscript received 14 July 2013; published 8 August 2013)

Using an optimally coupled nanometer-scale SQUID, we measure the magnetic flux originating from an individual ferromagnetic Ni nanotube attached to a Si cantilever. At the same time, we detect the nanotube's volume magnetization using torque magnetometry. We observe both the predicted reversible and irreversible reversal processes. A detailed comparison with micromagnetic simulations suggests that vortexlike states are formed in different segments of the individual nanotube. Such stray-field free states are interesting for memory applications and noninvasive sensing.

DOI: 10.1103/PhysRevLett.111.067202

PACS numbers: 75.60.Jk, 07.55.Jg, 75.80.+q

Recent experimental and theoretical work has demonstrated that nanometer-scale magnets, as a result of their low dimensionality, display magnetic configurations not present in their macroscopic counterparts [1–3]. Such work is driven by both fundamental questions about nanometer-scale magnetism and the potential for applying nanomagnets as elements in high-density memories [4], in high-resolution imaging [5–7], or as magnetic sensors [8]. Compared to nanowires, ferromagnetic nanotubes are particularly interesting for magnetization reversal as they avoid the Bloch point structure [9]. Different reversal processes via curling, vortex wall formation, and propagation have been predicted [10–13]. Because of their inherently small magnetic moment, experimental investigations have often been conducted on large ensembles. The results, however, are difficult to interpret due to stray-field interactions and the distribution in size and orientation of the individual nanotubes [12,14–18]. In a pioneering work, Wernsdorfer *et al.* [19] investigated the magnetic reversal of an individual Ni nanowire at 4 K using a miniaturized SQUID. Detecting the stray magnetic flux  $\Phi$  from one end of the nanowire as a function of magnetic field  $H$ ,  $\Phi$  was assumed to be approximately proportional to the projection of the total magnetization  $M$  along the nanowire axis. At the time,  $M(H)$  of the individual nanowire was not accessible and micromagnetic simulations were conducted only a decade later [9]. Here, we present a technique to simultaneously measure  $\Phi(H)$  and  $M(H)$  of a single low-dimensional magnet. Using a scanning nanoSQUID and a cantilever-based torque magnetometer

(Fig. 1) [20], we investigate a Ni nanotube producing  $\Phi(H)$  with a nearly square hysteresis, similar to the Ni nanowire of Ref. [19].  $M(H)$ , however, displays a more complex behavior composed of reversible and irreversible contributions, which we interpret in detail with micromagnetic simulations. In contrast to theoretical predictions, the experiment suggests that magnetization reversal is not initiated from both ends. If nanomagnets are to be optimized for storage or sensing applications, such detailed investigations of nanoscale properties are essential.

We use a direct current nanoSQUID formed by a loop containing two superconductor-normal-superconductor Josephson junctions (JJs) [21–23] [Fig. 1(a)]. Two T-shaped superconducting Nb arms are sputtered on top of each other separated by an insulating layer of SiO<sub>2</sub>. The Nb arms are connected via two planar 225 nm thick Nb/HfTi/Nb JJs each with an area of 200 × 200 nm<sup>2</sup>. These JJs and the 1.8 μm long Nb leads form a SQUID loop in the  $xz$  plane [shown in yellow in Fig. 1(a)], through which we measure  $\Phi$ . Atomic layer deposition of Ni is used to prepare the nanotube around a GaAs nanowire template grown by molecular beam epitaxy [24,25]. The GaAs core supports the structure, making it mechanically robust. The polycrystalline nanotube, which does not exhibit magneto-crystalline anisotropy, has a 140 ± 20 nm outer diameter, a 70 ± 10 nm inner diameter, and a 6.0 ± 0.5 μm length. The error in the diameters results from the roughness of the Ni film [23]. The Ni nanotube is affixed to the end of an ultrasoft Si cantilever [25], such

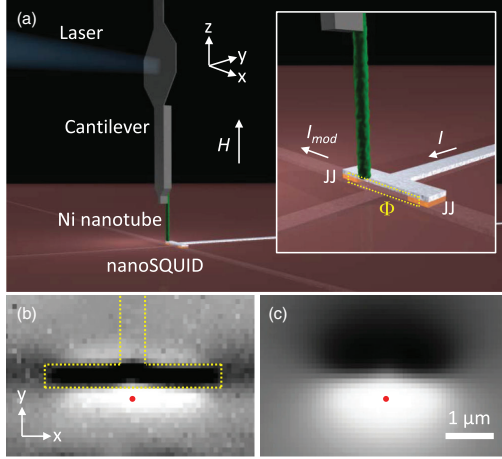


FIG. 1 (color). (a) Sketch of the apparatus (inset: zoomed-in view; dashed line indicates SQUID loop). Gray-scale maps of (b)  $\Delta f(x, y)$  and (c)  $\Phi(x, y)$  taken simultaneously at a distance  $z = 280$  nm with  $H = 0$ .  $\Delta f$  ( $\Phi$ ) ranges from  $-170$  to  $430$  Hz ( $-0.08$  to  $0.08\Phi_0$ ). Dashed lines indicate the T-shaped SQUID arm and dots the operating position.

that it protrudes from the tip by  $4 \mu\text{m}$ . The cantilever is  $120 \mu\text{m}$  long,  $4 \mu\text{m}$  wide and  $0.1 \mu\text{m}$  thick. It hangs above the nanoSQUID in the pendulum geometry, inside a vacuum chamber (pressure  $< 10^{-6}$  mbar) at the bottom of a cryostat. A 3D piezoelectric positioning stage moves the nanoSQUID relative to the Ni nanotube and an optical fiber interferometer is used to detect deflections of the cantilever along  $\hat{y}$  [26]. Fast and accurate measurement of the cantilever's fundamental resonance frequency  $f_c$  is realized by self-oscillation at a fixed amplitude. An external field  $\mu_0\mathbf{H}$  of up to 2.8 T can be applied along the cantilever axis  $\hat{z}$  using a superconducting magnet. At 4.3 K and  $\mu_0H = 0$ , the cantilever, loaded with the Ni nanotube and far from any surfaces, has an intrinsic resonance frequency  $f_c = f_0 = 3413$  Hz, a quality factor  $Q = Q_0 = 3.4 \times 10^4$ , and spring constant of  $k_0 = 90 \pm 10 \mu\text{N/m}$ . The magnetic flux due the Ni nanotube  $\Phi_{\text{NN}}(H)$  is evaluated from  $\Phi_{\text{NN}}(H) = \Phi(H) - \Phi_{\text{ref}}(H)$ , where the flux  $\Phi(H)$  is measured with the nanotube close to the nanoSQUID, while  $\Phi_{\text{ref}}(H)$  is measured with the nanotube several  $\mu\text{m}$  away such that the stray flux is negligible. Therefore,  $\Phi_{\text{ref}}(H) \propto H$ , due to the small fraction of  $\mathbf{H}$  that couples through the nanoSQUID given its imperfect alignment with  $\hat{z}$ . Once calibrated, we also use  $\Phi_{\text{ref}}(H)$  to measure the  $\mu_0H$  axis of our plots, removing effects due to hysteresis in the superconducting magnet. Such a field calibration was not possible for the integrated SQUID of Ref. [19]. We also perform dynamic-mode cantilever magnetometry [27], which is sensitive to the dynamic component of the magnetic torque acting between  $\mathbf{H}$  and the

magnetization  $\mathbf{M}$  of the Ni nanotube. In order to extract  $M(H)$ , we measure the field-dependent frequency shift  $\Delta f(H) = f_c(H) - f_0$ . Micromagnetic simulations are performed with NMAG [28] which provides finite-element modeling by adapting a mesh to the curved inner and outer surfaces of the nanotube. We simulate 30 nm thick nanotubes of different lengths  $l$  and the same 70 nm inner diameter. We assume magnetically isotropic Ni consistent with earlier studies [24], a saturation magnetization  $M_S = 406$  kA/m [29], and an exchange coupling constant of  $7 \times 10^{12}$  J/m [30].

We first scan the nanoSQUID under the cantilever with the attached Ni nanotube, to map the coupling between them. To ensure that the scan is done with the nanotube in a well-defined magnetic state, we first saturate it along its easy axis ( $\hat{z}$ ). Scans are then made at  $H = 0$  in the  $xy$  plane at a fixed height  $z$ , i.e., for a fixed distance between the top of the SQUID device and the bottom end of the Ni nanotube.  $\Delta f(x, y) = f_c(x, y) - f_0$  and  $\Phi(x, y)$  are measured simultaneously, as shown in Figs. 1(b) and 1(c), respectively.  $\Delta f(x, y)$  is proportional to the force gradient  $\partial F_y / \partial y$  acting on the cantilever and is sensitive to both the topography of the sample and to the magnetic field profile in its vicinity. Raised features such as the T-shaped top-electrode of the nanoSQUID are visible.  $\Phi(x, y)$  shows a bipolar flux response. The change in sign of  $\Phi(x, y)$  occurs as the Ni nanotube crosses the  $xz$  plane (defined by the SQUID loop) above the nanoSQUID, matching the expected response. Such images allow us to identify the nanoSQUID and to position the Ni nanotube at a maximum of  $|\Phi(x, y)|$ . Given a constant  $z$ , the nanotube stray flux optimally couples through the nanoSQUID loop at such positions, resulting in the maximum signal-to-noise ratio for flux measurements.

At one such position, indicated by the dot in Fig. 1, we record  $\Phi(H)$  by sweeping  $\mu_0H$  from 41 to  $-41$  mT and vice versa. A representative hysteresis curve  $\Phi_{\text{NN}}(H) = \Phi(H) - \Phi_{\text{ref}}(H)$  is shown in Fig. 2(a) where  $\Phi(H)$  is measured at  $z = 450$  nm.  $\mu_0|H|$  is incremented in steps of 0.2 mT with a wait time of 1 s before each acquisition. The hysteresis has an almost square shape with a maximum flux  $\Phi_{\text{NN}} = 75 \text{ m}\Phi_0$  coupled into the nanoSQUID. The loop appears similar to stray-field hysteresis loops obtained from a bistable Ni nanomagnet [31] and the Ni nanowire of Ref. [19], where  $H$  was collinear with the long axis. Such a shape may suggest that at  $H = 0$  the remanent magnetization  $M_R \approx M_S$ . Increasing  $H$  from zero [see red branch in Fig. 2(a)], we first observe a nearly constant flux, then a variation by about 30% along with tiny jumps in a small field regime, and finally, a large jump occurring near 30 mT. Similar to Ref. [19], our SQUID data suggest that almost all magnetic moments are reversed at once near 30 mT via a large irreversible jump, i.e., via domain nucleation and propagation.

We now turn to cantilever magnetometry, which is sensitive to  $M(H)$ .  $\Delta f$  is first measured simultaneously with



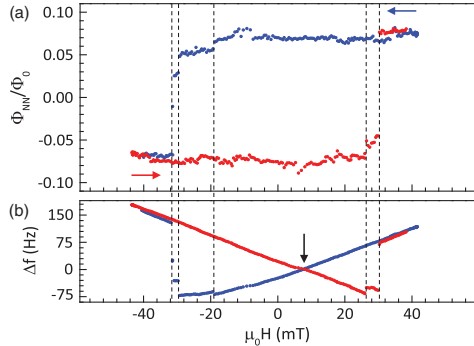


FIG. 2 (color). Simultaneously measured hysteresis loops of (a)  $\Phi_{\text{NN}}(H)$  and (b)  $\Delta f(H)$  at  $z = 450$  nm. Red (blue) points represent data taken while sweeping  $H$  in the positive (negative) direction. Dashed lines indicate discontinuities (magnetic switching fields  $H_{\text{sw},e}$ ) appearing in both  $\Phi_{\text{NN}}(H)$  and  $\Delta f(H)$ .

$\Phi(H)$  at  $z = 450$  nm, as shown in Fig. 2(b). The torque measured via  $\Delta f$  is found to exhibit tiny jumps and large abrupt changes at exactly the same switching fields  $H_{\text{sw},e}$  as  $\Phi_{\text{NN}}(H)$ . We note that switching fields vary from sweep to sweep [23] as was observed in the Ni nanowire of Ref. [19]; such behavior is expected if nucleation is involved, given its stochastic nature. Importantly, there is always a one-to-one correspondence between switching fields observed in  $\Delta f$  and flux  $\Phi_{\text{NN}}$  as highlighted by the dashed lines in Fig. 2. This correlation confirms that the changes in  $\Delta f$  and  $\Phi_{\text{NN}}$  have a single origin: the reversal of magnetic moments within the Ni nanotube.

In order to analyze  $\Delta f(H)$  in terms of  $M(H)$ , it is important to retract the Ni nanotube from the nanoSQUID by several  $\mu\text{m}$ . Therefore, we avoid magnetic interactions with both the diamagnetic superconducting leads and the modulation current of the nanoSQUID. These interactions lead to an enhanced  $\Delta f$  and a branch crossing [indicated by an arrow in Fig. 2(b)] occurring at finite  $H$  rather than at  $H = 0$  as was reported in Ref. [24]. After retracting the nanotube from the nanoSQUID, we measure  $\Delta f(H) = f_c(H) - f_0$  as shown in Fig. 3. We start the acquisition at a large positive field ( $\mu_0 H = 2.8$  T), where the nanotube is magnetized to saturation, and then reduce  $H$  to zero as shown in Fig. 3(a). In large fields, the nanotube behaves as a single-domain magnetic particle; i.e., it is magnetized uniformly and  $M$  rotates in unison as the cantilever oscillates in the magnetic field. Based on this assumption, we fit the results with an analytical model for  $\Delta f(H)$  [25]. The volume of the Ni nanotube  $V_{\text{Ni}}$ ,  $\omega_0$ , and  $k_0$  are set to their measured values, while the saturation magnetization  $M_S = 300 \pm 200$  kA/m and the anisotropy parameter  $K = 40 \pm 20$  kJ/m<sup>3</sup> are extracted as fit parameters. The error in these parameters is dominated by the error associated with the measurement of the nanotube's

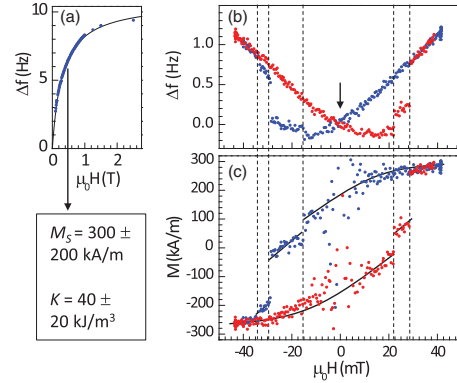


FIG. 3 (color). (a) Cantilever magnetometry (points) and fit (solid line) in large magnetic fields. (b) Cantilever magnetometry at small fields. (c) Volume magnetization  $M$  extracted from (b) according to (1). Solid lines guide the eye. Red (blue) points represent data taken while sweeping  $H$  in the positive (negative) direction. Dashed lines highlight switching fields  $H_{\text{sw},e}$ . The error in  $M$  scales with  $1/|H|$ , explaining the scatter near  $H = 0$ .

exact geometry and therefore of  $V_{\text{Ni}}$  [23].  $M_S$  is consistent with the findings of Ref. [25] on similar nanotubes and with 406 kA/m, known as the saturation magnetization for bulk crystalline Ni at low temperature [29].

Figure 3(b) shows  $\Delta f(H)$  taken in the low-field regime. In an opposing field, we observe discrete steps in  $\Delta f(H)$  indicating abrupt changes in the volume magnetization  $M$ . As expected, the branch crossing (arrow) occurs at  $H = 0$  and the overall behavior is consistent with measurements of similar nanotubes [25]. To analyze the low field data, we adapt the analytical model to extract the dependence of the volume magnetization  $M$  on  $H$ , i.e., the field dependence of magnetization averaged over the entire volume of the nanotube. Solving the equations of Ref. [25] describing the frequency shift for  $M$ , we find

$$M = \frac{2k_0 l_e^2 K \Delta f}{H(KV_{\text{Ni}} f_0 - k_0 l_e^2 \Delta f)}, \quad (1)$$

where  $l_e = 85$   $\mu\text{m}$  is the effective cantilever length for the fundamental mode.  $M(H)$  extracted from Fig. 3(b) is plotted in Fig. 3(c). In both field sweep directions, the magnetization is seen to first undergo a gradual decrease as  $|H|$  decreases. Starting from  $\sim 300$  kA/m at  $+40$  mT,  $M$  reduces to  $\sim 200$  kA/m at 0 mT. We find  $M_R \approx 0.65 M_S$ , in contrast with the SQUID data suggesting  $M_R \approx M_S$ . However, this gradual change of  $M$  at small  $|H|$  in the initial stage of the reversal is consistent with the gradually changing anisotropic magnetoresistance observed in a similar nanotube of larger diameter in nearly the same field regime [24]. At  $-15$  mT, just before the first of three discontinuous jumps,  $M$  is only  $\sim 100$  kA/m. Note that

jumps are seen after the magnetization has decreased to a value of about  $0.3M_S$ . Two further jumps occur at  $\mu_0 H_{sw,e} = -28$  and  $-33$  mT. For  $\mu_0 H < -40$  mT, the nanotube magnetization is completely reversed. We observe a somewhat asymmetric behavior at positive and negative fields. This asymmetry may be due to an antiferromagnetic NiO surface layer providing exchange interaction with the Ni nanotube [32,33]. Irreversible jumps in  $M$  are observed for  $15 \text{ mT} < \mu_0 |H_{sw,e}| < 35 \text{ mT}$  in Fig. 3, in perfect agreement with the range over which jumps occur in  $\Phi_{NN}$  with the nanotube close to the nanoSQUID in Fig. 2.

The observed magnetization steps suggest the presence of 2 to 4 intermediate magnetic states or 2 to 4 segments in the nanotube that switch at different  $H$ . Calculations for ideal nanotubes [10] suggest that the intermediate states should be multidomain, consisting of uniform axially saturated domains separated by azimuthal or vortexlike domain walls. The preferred sites for domain nucleation are expected to be the two ends of the nanotube [9,10]. As the field is reduced after saturation, magnetic moments should gradually curl or tilt away from the field direction. The torque magnetometry measurements, which show both gradual and abrupt changes in  $M(H)$ , are consistent with such gradual tilting; the SQUID data, showing only abrupt changes in  $\Phi_{NN}(H)$ , are not. In the following, we present micromagnetic simulations performed on Ni nanotubes of different lengths  $l$  to further analyze our data.

In Fig. 4(a), we show simulated hysteresis loops  $M(H)$  with  $\mathbf{H}$  applied along the long axis of nanotubes with  $l$  between 250 nm and  $2 \mu\text{m}$ . For  $l = 2 \mu\text{m}$  the  $M(H)$  loop is almost square, but the switching field is  $\sim 8$  mT. This value is much smaller than the regime of  $H_{sw,e}$  observed experimentally. Nanotubes with  $250 \text{ nm} < l < 1 \mu\text{m}$  are consistent with  $15 \text{ mT} < \mu_0 |H_{sw,e}| < 35 \text{ mT}$ . For  $l = 500 \text{ nm}$  the simulation provides a switching field  $\mu_0 H_{sw} = 28$  mT. At the same time,  $M$  is almost zero for  $|H|$  just below  $|H_{sw}|$ . Such behavior is consistent with the overall shape of the measured  $M(H)$  loop in Fig. 3(c), where the largest jumps in  $M$  take place at about  $\pm 30$  mT. Comparing Figs. 4(a) and 3(c), we conclude that the superposition of a few segments with  $250 \text{ nm} < l < 1 \mu\text{m}$  could account for the measured  $M(H)$ . For such segments, Figs. 4(b) and 4(c) (right panels) show characteristic spin configurations (cones) well above and near  $H_{sw}$ , respectively. We observe the gradual tilting of spins at both ends in Fig. 4(b) and two tubularlike vortex domains with opposite circulation direction in Fig. 4(c) [34]. Between the domains, a Néel-type wall exists. For each  $l$  and  $M(H)$ , we simulate the relevant stray field at the position of the nanoSQUID [red squares in the left panels of Figs. 4(b) and 4(c)] providing the predicted  $\Phi_{NN}(H)$  [23]. The shapes of the simulated  $\Phi_{NN}(H)$  are nearly proportional to, and thus closely follow, the shape of  $M(H)$  shown in Fig. 4(a). Thus, the simulations allow us to explain the measured torque magnetometry data, although they are inconsistent with the nanoSQUID data.

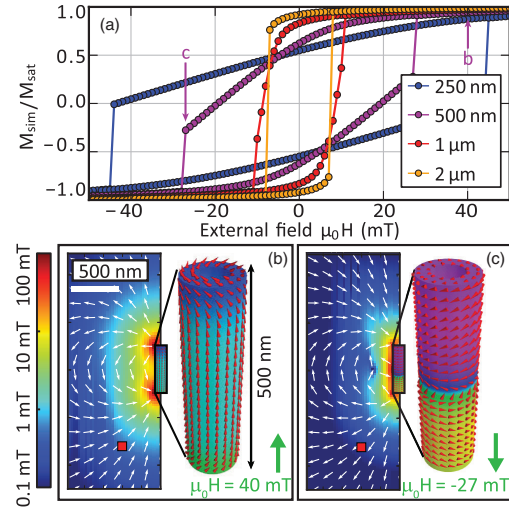


FIG. 4 (color). (a) Simulated hysteresis loops  $M(H)$  for nanotubes of four different  $l$ .  $H_{sw}$  increases with decreasing  $l$ . Magnetic configurations (right) and stray-field distribution (left) for  $l = 500 \text{ nm}$  at (b)  $40 \text{ mT}$  and (c)  $-27 \text{ mT}$  as indicated by the labels in (a). Cones (arrows) indicate the local direction of the magnetic moments (stray field). The stray fields  $H_{str}$  are color coded as depicted. The red squares indicate the position of the center of the nanoSQUID loop.

The contrast between hysteresis traces obtained by the nanoSQUID and torque magnetometry shows that  $\Phi(H)$  is not the projection of  $\mathbf{M}$  along the nanotube axis. This finding contradicts the assumption of Ref. [19]; we attribute this discrepancy to the fact that while cantilever magnetometry measures the entire volume magnetization, the nanoSQUID is most sensitive to the magnetization at the bottom end of the nanotube, as shown in calculations of the coupling factor  $\phi_\mu = \Phi/\mu$  (flux  $\Phi$  coupled to nanoSQUID by a pointlike particle with magnetic moment  $\mu$ ) [20]. Still, we find a one-to-one correspondence between switching fields  $H_{sw,e}$  detected by either the nanoSQUID or cantilever magnetometry. This experimentally verified consistency substantiates the reversal field analysis performed in Ref. [19]. In Fig. 2(a), we find no clear evidence for curling or gradual tilting at small  $H$ . Thus, the reversal process does not seem to start from the end closest to the nanoSQUID, but rather from a remote segment. This is an important difference compared to the ideal nanotubes considered thus far in the literature, in which both ends share the same fate in initiating magnetization reversal. The unintentional roughness of real nanotubes might be relevant here. In an experiment performed on a large ensemble of nanotubes, one would not have been able to judge whether a gradual decrease in  $M(H)$  [17] originated from a very broad switching field distribution

or from the gradual tilting of magnetic moments in the individual nanotubes. Thus, our combination of nanomagnetometry techniques represents a powerful method for unraveling hidden aspects of nanoscale reversal processes. In order to optimize nanotubes for sensing and memory applications, such understanding is critical.

In summary, we have presented a technique for measuring magnetic hysteresis curves of nanometer-scale structures using a piezoelectrically positioned nanoSQUID and a cantilever operated as a torque magnetometer. This dual functionality provides two independent and complementary measurements: one of local stray magnetic flux and the other of volume magnetization. Using this method we gain microscopic insight into the reversal mechanism of an individual Ni nanotube, suggesting the formation of vortexlike tubular domains with Néel-type walls.

A. B., J. N., and D. R. contributed equally to this work which was funded by the Canton Aargau, the SNI, the SNF under Grant No. 200020-140478, the NCCR QSIT, the DFG via the Project No. SFB/TRR 21, and the ERC via the advanced Grant SOCATHES. Research leading to these results was funded by the European Community's Seventh Framework Programme (FP7/2007-2013) under Grant No. 228673 MAGNONICS. J. N. acknowledges support from the Carl-Zeiss-Stiftung.

\*grundler@ph.tum.de

†martino.poggio@unibas.ch

- [1] Z. K. Wang, M. H. Kuok, S. C. Ng, D. J. Lockwood, M. G. Cottam, K. Nielsch, R. B. Wehrspohn, and U. Gösele, *Phys. Rev. Lett.* **89**, 027201 (2002).
- [2] R. Streubel, J. Thurmer, D. Makarov, F. Kronast, T. Kosub, V. Kravchuk, D. D. Sheka, Y. Gaididei, R. Schäfer, and O. G. Schmidt, *Nano Lett.* **12**, 3961 (2012).
- [3] R. Streubel, V. P. Kravchuk, D. D. Sheka, D. Makarov, F. Kronast, O. G. Schmidt, and Y. Gaididei, *Appl. Phys. Lett.* **101**, 132419 (2012).
- [4] S. S. P. Parkin, M. Hayashi, and L. Thomas, *Science* **320**, 190 (2008).
- [5] S. Khizroev, M. H. Kryder, D. Litvinov, and D. A. Thompson, *Appl. Phys. Lett.* **81**, 2256 (2002).
- [6] M. Poggio and C. L. Degen, *Nanotechnology* **21**, 342001 (2010).
- [7] H. Campanella, M Jaafar, J. Llobet, J. Esteve, M. Vázquez, A. Asenjo, R. P. del Real, and J. A. Plaza, *Nanotechnology* **22**, 505301 (2011).
- [8] M. M. Maqableh, X. Huang, S.-Y. Sung, K. S. M. Reddy, G. Norby, R. H. Victora, and B. J. H. Stadler, *Nano Lett.* **12**, 4102 (2012).
- [9] R. Hertel and J. Kirschner, *J. Magn. Magn. Mater.* **278**, L291 (2004).
- [10] P. Landeros, O. J. Suarez, A. Cuchillo, and P. Vargas, *Phys. Rev. B* **79**, 024404 (2009).
- [11] P. Landeros and Á. S. Núñez, *J. Appl. Phys.* **108**, 033917 (2010).
- [12] J. Escrig, J. Bachmann, J. Jing, M. Daub, D. Altbir, and K. Nielsch, *Phys. Rev. B* **77**, 214421 (2008).
- [13] P. Landeros, S. Allende, J. Escrig, E. Salcedo, D. Altbir, and E. E. Vogel, *Appl. Phys. Lett.* **90**, 102501 (2007).
- [14] J. Bachmann, J. Jing, M. Knez, S. Barth, H. Shen, S. Mathur, U. Gösele, and K. Nielsch, *J. Am. Chem. Soc.* **129**, 9554 (2007).
- [15] M. Daub, M. Knez, U. Goesele, and K. Nielsch, *J. Appl. Phys.* **101**, 09J111 (2007).
- [16] J. Bachmann, J. Escrig, K. Pitzschel, J. M. Montero Moreno, J. Jing, D. Görlitz, D. Altbir, and K. Nielsch, *J. Appl. Phys.* **105**, 07B521 (2009).
- [17] O. Albrecht, R. Zierold, S. Allende, J. Escrig, C. Patzig, B. Rauschenbach, K. Nielsch, and D. Görlitz, *J. Appl. Phys.* **109**, 093910 (2011).
- [18] J. Escrig, S. Allende, D. Altbir, and M. Bahiana, *Appl. Phys. Lett.* **93**, 023101 (2008).
- [19] W. Wernsdorfer, B. Doudin, D. Mailly, K. Hasselbach, A. Benoit, J. Meier, J.-Ph. Ansermet, and B. Barbara, *Phys. Rev. Lett.* **77**, 1873 (1996).
- [20] J. Nagel, A. Buchter, F. Xue, O. F. Kieler, T. Weimann, J. Kohlmann, A. B. Zorin, D. Ruffer, E. Russo-Averchi, R. Huber, P. Berberich, A. Fontcuberta i Morral, D. Grundler, R. Kleiner, D. Koelle, M. Poggio, and M. Kemmler, [arXiv:1305.1195](http://arxiv.org/abs/1305.1195).
- [21] J. Nagel, O. F. Kieler, T. Weimann, R. Wölbing, J. Kohlmann, A. B. Zorin, R. Kleiner, D. Koelle, and M. Kemmler, *Appl. Phys. Lett.* **99**, 032506 (2011).
- [22] R. Wölbing, J. Nagel, T. Schwarz, O. Kieler, T. Weimann, J. Kohlmann, A. Zorin, M. Kemmler, R. Kleiner, and D. Koelle, *Appl. Phys. Lett.* **102**, 192601 (2013).
- [23] See Supplemental Material at <http://link.aps.org/supplemental/10.1103/PhysRevLett.111.067202> for a description of the experimental methods, further flux hysteresis loops, discussion of the simulations, and a description of the detection of simultaneous switching events.
- [24] D. Ruffer, R. Huber, P. Berberich, S. Albert, E. Russo-Averchi, M. Heiss, J. Arbiol, A. Fontcuberta i Morral, and D. Grundler, *Nanoscale* **4**, 4989 (2012).
- [25] D. P. Weber, D. Ruffer, A. Buchter, F. Xue, E. Russo-Averchi, R. Huber, P. Berberich, J. Arbiol, A. Fontcuberta i Morral, D. Grundler, and M. Poggio, *Nano Lett.* **12**, 6139 (2012).
- [26] D. Rugar, H. J. Mamin, and P. Guethner, *Appl. Phys. Lett.* **55**, 2588 (1989).
- [27] B. C. Stipe, H. J. Mamin, T. D. Stowe, T. W. Kenny, and D. Rugar, *Phys. Rev. Lett.* **86**, 2874 (2001).
- [28] T. Fischbacher, M. Franchin, G. Bordignon, and H. Fangohr, *IEEE Trans. Magn.* **43**, 2896 (2007); <http://nmag.soton.ac.uk/nmag/>.
- [29] C. Kittel, *Introduction to Solid-State Physics* (Wiley, New York, 2005), 8th ed.
- [30] A. Knittel, Ph.D. thesis, University of Southampton, 2011.
- [31] G. Meier, D. Grundler, K.-B. Broocks, Ch. Heyn, and D. Heitmann, *J. Magn. Magn. Mater.* **210**, 138 (2000).
- [32] P. Zhang, F. Zuo, F. K. Urban III, A. Khabari, P. Griffiths, and A. Hosseini-Tehrani, *J. Magn. Magn. Mater.* **225**, 337 (2001).
- [33] M. Gierlings, M. J. Prandolini, H. Fritzsche, M. Gruyters, and D. Riegel, *Phys. Rev. B* **65**, 092407 (2002).
- [34] A.-P. Chen, J. M. Gonzalez, and K. Y. Guslienko, *J. Appl. Phys.* **109**, 073923 (2011).



# Curriculum Vitae

## Daniel Ruffer

*Dipl.-Phys., PhD cand.*

Rue du Caudray 3  
1020 Renens  
Switzerland  
☎ +41 (0)78 627 48 10  
✉ mail@danielrueffer.de



[www.danielrueffer.ch](http://www.danielrueffer.ch)



### Personal Information

Date of birth 11.01.1985  
Place of birth Friedrichshafen, Germany  
Nationality German

### Experience

Jan. 2010– Aug. 2014 **Doctoral Research Assistant**, *École Polytechnique Fédérale de Lausanne*, CH.  
Magnetic states and spin-wave modes in single ferromagnetic nanotubes  
Oct. 2008– Nov. 2009 **Research Assistant / Master Student**, *Walther-Meißner-Institut*, Garching, DE.  
Non-local Phenomena in Metallic Nanostructures - On the Search for the Spin Hall Effect  
July–Dec. 2007 **Intern**, *EPCOS AG, SAW R&D Department*, Munich, DE.  
Mar.–Apr. 2006 **Intern**, *Lindauer Dornier GmbH, R&D Speciality Machinery*, Lindau, DE.  
2005–2009 **Student Assistant**, *Technical University Munich*, DE.

### Education

Jan. 2010–Present **PhD candidate in physics**, *École Polytechnique Fédérale de Lausanne*, CH.  
**Anticipated Graduation:** Oct. 2014  
2003–2009 **Diplomstudiengang Physik**, *Technical University Munich*, DE.  
(**Master of Science in Physics**)  
2003 **European Baccalaureate**, *European School Munich*.

### Languages

German	Native	Spanish	Limited working proficiency (B2)
English	Full professional proficiency (C1)	French	Elementary proficiency (A2/B1)